Genetically encoded fluorescent biosensors for detection of ligands and protein-protein interactions

by

Sheng Yi Wu

A thesis submitted in partial fulfillment of the requirements for the degree of

Doctor of Philosophy

Department of Chemistry
University of Alberta

Abstract

Fluorescence imaging enables direct visualization of cellular activities with remarkable resolutions supported by advancing technologies. The fluorescent markers for biomolecules complement the hardware and software for imaging a specific target in detail. Genetically encoded fluorescent proteins enable imaging in live cells with a spatiotemporal resolution and can be targeted to a specific subcellular region of a cell or a specific cell type of a tissue. While most biomolecules can be visualized with a fused fluorescent protein, more sophisticated biosensors are required to report a specific small molecule or ion (e.g., Ca^{2+} biosensors), protein-protein interactions (e.g., Split GFP), or enzymatic activity (e.g., kinase biosensor). These biosensors are valuable tools that have revolutionized the way scientists investigate biological questions.

Well aligned with the expertise of the Campbell lab in genetically encoded indicator development, my thesis focuses on genetically encoded biosensors to detect ligands including potassium ion (K^+), insulin, and the brain derived neurotropic factor (BDNF); and protein-protein interactions with dimerization-dependent fluorescent proteins (ddFPs) and FRET pairs of DipdTFP (*Discosoma* peripheral dTFP) and dTomato. The proposals of biosensors are based on two criteria: the potential impact and feasibility. All the projects listed above can potentially make a difference in biological research. Potassium ion is one of the most abundant biological ions that has many implications in human; abnormal level of K^+ concentration has been reported in various diseased conditions. Insulin is a major biomolecule for blood glucose regulation and is associated with diabetes, a common and uncurable metabolic condition. BDNF is a nerve growth factor that has implications in neurological diseases. Protein-protein interactions are commonly investigated in biology. The feasibility of biosensor development largely relies on the availability of binding proteins: potassium binding protein (Kbp), human insulin receptor (hIR), insulin degrading

enzyme (IDE), and BDNF pre-peptide. The ddFPs and FRET based DipdTFP/dTomato pair uses engineered interface interaction to detect protein-protein interactions.

The main projects in this thesis are on the K^+ biosensor development. KIRIN1 and GINKO1 were developed for intracellular K^+ detection as described in Chapter 2. GINKO1 was further optimized to GINKO2a and GINKO2b in Chapter 3, with greatly improved sensitivity and specificity. In Chapter 4, I describe the effort towards tackling the major obstacle of the K^+ biosensor project, developing a functional extracellular displayed version.

The ddFP optimization work in Chapter 5 was a continuous effort to further improve the previous development ddFPs in the Campbell lab. The optimization led to some improvements in ddRFP brightness but not sufficiently brighter to show a difference in the mammalian system. The work on ddGFP did not yield variants much brighter.

In Chapter 6, a DipdTFP/dTomato FRET pair was engineered by replacing the exterior residues of dTFP with that of dTomato. The surface residue engineering successfully allows heterodimer to form, but with a high affinity. More work is required to weaken this interaction for proper protein-protein interaction detection.

Finally, the appendix chapter describes my attempt on prototyping insulin and BDNF biosensors. The designed prototype indicators were constructed and tested with the corresponding ligands, further investigations and optimizations is required to for the development of functional biosensors.

Preface

The work on genetically encoded K^+ indicators, described in Chapter 2, 3, and 4, was a collaborative work among the Campbell lab and external collaborators. The work in Chapter 2 was led by Dr. Yi Shen and published as Yi Shen, Sheng-Yi Wu, Vladimir Rancic, Abhi Aggarwal, Yong Qian, Shin-Ichiro Miyashita, Klaus Ballanyi, Robert E. Campbell, Min Dong in *Communications Biology* in 2019 with a title of "Genetically encoded fluorescent indicators for imaging intracellular potassium ions"[1]. YS performed design and construction of the indicators. YS, SYW, and AA performed *in vitro* characterization. YS, SYW, and SIM performed plasmid construction. YS and SYW performed live imaging in mammalian cell lines. VR and YQ performed imaging in dissociated neurons. YS, KB, REC, and MD supervised the research. YS, REC, and MD wrote the manuscript.

The work in Chapter 3 is being written for submission as Sheng-Yi Wu, Yurong Wen, Abhi Aggarwal, Vladimir Rancic, Brian Taylor, Terence Hwa, Klaus Ballanyi, M. Joanne Lemieux, Yi Shen, Robert E. Campbell. SYW and YS performed plasmid construction. YW performed X-ray crystallography. SYW performed GINKO optimization with site directed mutagenesis and directed evolution. SYW performed protein purification and *in vitro* characterization. SYW and VR performed mammalian cell imaging. AA performed the stopped flow. BT performed the *E. coli* growth experiment. TH, KB, JL, YS, and REC supervised the research. SYW, YS, and REC wrote the manuscript.

In the work described in Chapter 4, SYW performed plasmid construction, GINKO optimization with site directed mutagenesis and directed evolution, *in vitro* characterization, and mammalian cell imaging.

In Chapter 5 and 6, SYW performed protein engineering of dimerization dependent fluorescent proteins (ddFPs) and the FRET-based DipdTFP and dTomato pair and *in vitro* characterization.

Acknowledgment

I would like to take the opportunity to thank my family, friends, and colleagues for support during my PhD. My parents have been my backbone for many years of my post secondary studies: They not only have been the most understanding and loving parents, but also provided a safety net for me, so I know I don't have to worry about financial shortage in the worst scenario. I would like to specially thank my grandmother who told me her story of fighting for an education. She reminded me that there was a time that educations for females were not supported by their family or community. Even today, many people, not necessarily females, are prevented or discouraged from accessing the education opportunities. I am fortunate to be surrounded by my supportive family and friends. I hope I have made my loved ones proud. Admittedly, my PhD program did not go all smoothly. I thank my colleagues who helped me emotionally and technically during the up and downs. I thank Dr. Robert E. Campbell for accepting me as his student and guiding me during my PhD. I thank Dr. Yi Shen who has been an incredibly patient and knowledgeable mentor in whom I could see who I want to become in the future. I thank Yan Li, who has been a great company in the years of my PhD. I thank Drs Woodside, Macauley, and Williams for being my supervisory committee members during my program. In addition, I thank Drs. Dodani and Kurata for agreeing to attend my defense as a committee member.

I also would like to acknowledge the funding agencies who made my PhD research possible. My PhD program was supported generously by graduate scholarships provided by National Science and Engineering Research Council (NSERC), Alberta Innovates-Technology Future (AITF), and the University of Alberta. The research conducted in the Campbell lab was supported by NSERC, Canadian Institute of Health Research (CIHR), National Institute of Health (NIH), and Brain Canada. My travels to trainings, conferences, and exchange at Dr Jin Zhang's lab at

UCSD was kindly supported by the Graduate Student Association and the Faculty of Graduate Studies at the University of Alberta, as well as the Michael Smith Foreign Studies Supplement.

Table of contents

List of tables

List of figures

Figures in the Appendix

List of Abbreviations

αCT	12 amino acids at the C terminus of the α subunit of human insulin receptor
ATP	Adenosine triphosphate
BAPTA	1,2-bis(*o*-aminophenoxy) ethane-*N*,*N*,*N*′,*N*′-tetraacetic acid
BDNF	Brain-derived neurotropic factor
BFP	Blue fluorescent protein
BON	Bacterial OsmY and nodulation
B-PER	Bacterial protein extraction reagent
BRET	Bioluminescence resonance energy transfer
BV	Biliverdin
CaM	Calmodulin
C. elegans	*Caenorhabditis elegans*
CFP	Cyan fluorescent protein
CCD	Charge-coupled device
ChR	Channelrhodopsin
cp	circularly permuted (or circular permutation)
CR	cysteine-rich domain
Cys	cysteine
DipdTFP	*Discosoma* peripheral dimer TFP
DidTFP	*Discosoma* interface dimer TFP
ddFP	dimerization-dependent fluorescent protein
DMEM	Dulbecco's modified Eagle medium
DMSO	dimethyl sulfoxide
DTT	1,4-Dithiothreitol
EC (or ε)	Extinction coefficient
E. coli	*Escherichia coli*
EDTA	Ethylenediaminetetraacetic acid
EGFP	Enhanced green fluorescent protein
EGTA	Ethylene glycol tetraacetic acid
Em	Emission
Ex	Excitation

FBS	Fetal bovine serum
FPLC	fast protein liquid chromatography
FPX	fluorescent protein exchange
FMN	Flavin mononucleotide
FnIII	fibronectin type III domain
FP	Fluorescent protein
FRET	Förster resonance energy transfer
GA	Green ddFP A copy
GB	Green ddFP B copy
GECI	Genetically-encoded Ca^{2+} indicator
GECO	Genetically-encoded Ca^{2+} indicator for optical imaging
GFP	Green fluorescent protein
GINKO	Green indicator for K^+ optical imaging
Gly	Glycine
GPI	Glycosylphosphatidylinositol
hIR	human insulin receptor
His	Histidine
HHBSS	Hank's buffer with HEPES
IDE	insulin degrading enzyme
Kbp	potassium binding protein
K_d	Dissociation constant
KIRIN	K^+ ion ratiometric indicator
L1 (L2)	Leucin-rich repeat domain 1 (2)
LB	Luria-Bertani
LED	Light-emitting diode
LysM	Lysine motif
mL	millilitre
mm	millimetre
mM	millimolar
MOPS	3-(*N*-morpholino) propanesulfonic acid
ncp	non-circularly permuted

NES	Nuclear exclusion sequence
NIR	Near-infrared
NLS	Nuclear localization sequence (or signal)
nm	nanometre
nM	nanomolar
PDGFR	platelet derived growth factor receptor
PBS	Phosphate buffered saline
PCR	Polymerase chain reaction
PDB	Protein data bank
PKA	Protein kinase A
PPI	Protein-protein interaction
QY (or Φ)	Quantum yield
RA	Red ddFP A copy
RB	Red ddFP B copy
RCF	Relative centrifugel force
RFP	Red fluorescent protein
SEP	super ecliptic pH biosensor
Ser	Serine
s.e.m	Standard error of the mean
s.d	Standard deviation
SNR	Signal to noise ratio
Tyr	Tyrosine
μm	micrometer
μM	micromolar
UV	Ultraviolet
YA	Yellow ddFP A copy
YB	Yellow ddFP B copy
YFP	Yellow fluorescent protein

Chapter 1 Indicators for imaging monoatomic ions in biology

1.1 Abstract

Monoatomic ions play critical roles in biology: maintaining the fluid balance, transmitting signals, catalyzing redox reactions, and many more diverse functions. Our ability to measure the local concentration, and detect dynamic changes in concentration, of monoatomic ions is essential to understand their biological functions. Imaging technology allows such detections but requires suitable indicators. Genetically encoded and small synthetic indicators are both effective types of indicators. In this chapter, we will provide a guideline for potential users to choose an appropriate indicator for their application and an overview for indicator developers to identify unexplored opportunities or seek approaches to improve existing indicators.

1.2 Introduction

Life is composed of, and made possible by, a combination of organic and inorganic substances. The macromolecular organic substances are defined as substances containing the elements of carbon and hydrogen and can be roughly categorized into four classes: carbohydrates, lipids, proteins, and nucleic acids. The small biological molecules include vitamins (e.g., biotin and niacin), neurotransmitters (e.g., dopamine and acetylcholine), and metabolites (e.g., lactate and melanin). Examples of inorganic substances include water, calcium phosphate in bones and shells, and ions. Some ions are essential inorganic nutrients just like some vitamins are essential organic nutrients. The most highly abundant monoatomic ions include sodium (Na^+), potassium (K^+), calcium (Ca^{2+}), iron (Fe^{2+}/Fe^{3+}) and chloride (Cl^-). The trace ions include zinc (Zn^{2+}), molybdenum (Mo^+), cobalt (Co^+), copper (Cu^{2+}/Cu^+), and manganese (Mn^{2+})[2]. They all have important roles in physiology: Some serve as electrolytes that play roles in maintenance of osmotic

pressure and pH; some are involved in neuronal activities; and some are incorporated into a larger structure such as a cofactor or an enzyme to facilitate catalysis[3]. To better understand their roles in cellular functions, researchers have been actively measuring their concentrations, investigating their locations within tissues and cells, and tracing the dynamic concentration change during cellular activities.

A variety of methods have been developed to measure concentration of metal ions, whether they are bound or free. These include flame or graphite furnace atomic absorption spectroscopy (AAS) and inductively coupled plasma mass spectrometry (ICP-MS)[4–6]. The elemental analysis by AAS is performed one element at a time, while ICP-MS can quantitatively measure multiple elements at a time. Although these methods can detect the metals with very high sensitivity (parts per billion for AAS and parts per trillion for ICP-MS), they cannot distinguish the bound and free ions or provide any insight into localization in tissue or the dynamics of ion concentration changes. Knowing the free ion concentration is important because the bound ions cannot be translocated across organelle or plasma membrane through ion channels or transporters, therefore considered inaccessible to ion dynamics. Adapting mass spectrometry with fixed biological samples has enabled elemental mapping at a cellular or subcellular level[7]. Yet, these techniques fail to provide dynamic information because they are destructive and cannot be used on living tissue.

Dynamic changes are a key to life and fluxes of ions are the foundation of many important intra- and intercellular processes. Moreover, the dynamics can also reflect a cellular response to an environmental perturbation. The ability to image ion concentrations allows us to study how ions are regulated and transported after a certain stimuli or condition. Tools that enable such measurements in live cells are of particularly of interest, especially for neurons where the ion changes are transient and localized. Ion-specific electrodes are one of the methods that are

commonly used for electrophysiology of activatable cells. It can provide real-time measurements at a single cell level. On the other hand, it is very challenging, or often impractical, to use electrodes to measure multiple cells simultaneously or measure ion concentrations at a subcellular level. For many applications, light microscopy is an indispensable and advantageous technique that allows direct visualization of ion dynamics in multiple cells at once, and with subcellular resolution, when using appropriate indicators.

Fluorescent or bioluminescent indicators are today's mainstream indicators. They not only allow dynamic measurements with sensitivity and selectivity, but also allow higher throughput and subcellular measurements. The imaging can be complemented with simultaneous electrode measurement in some cases. The indicators can be either small molecule-based synthetic indictors or genetically encoded indicators. The synthetic dyes are usually brighter and more photostable, but they can be complicated by issues of loading and subcellular or cell-specific targeting[8]. Genetically encoded indicators can usually be conveniently expressed by the cellular machineries and specifically displayed on the cell membrane with a leader peptide fused to N terminus of the indicator. However, they are often placed at disadvantage due to their low brightness, low photostability, and/or pH sensitivity. In this chapter, we will look at these indicators in detail.

1.3 Ca^{2+} indicators

1.3.1 The role of Ca^{2+} in cell physiology

Ca^{2+} is involved in many important physiological activities including the roles as a second messenger and a neurotransmitter[9,10]. As a second messenger in all types of cells, Ca^{2+} can regulate many cellular activities, including motility involving cytoskeleton, enzymatic activity via phosphorylation and dephosphorylation, and secretion of biomolecules such as neurotransmitters. In neurons, the voltage sensitive Ca^{2+} channel opens during an action potential to allow Ca^{2+} to

enter along the concentration gradient[10]. The Ca^{2+} ions can bind to many intracellular Ca^{2+} binding proteins including calmodulin, which leads to neurotransmitter release and signal propagation. Because Ca^{2+} undergoes dramatic changes in localization and local concentration during signalling events with a much larger net movements than other biological ions, being able to measure Ca^{2+} concentration dynamics is particularly of interest.

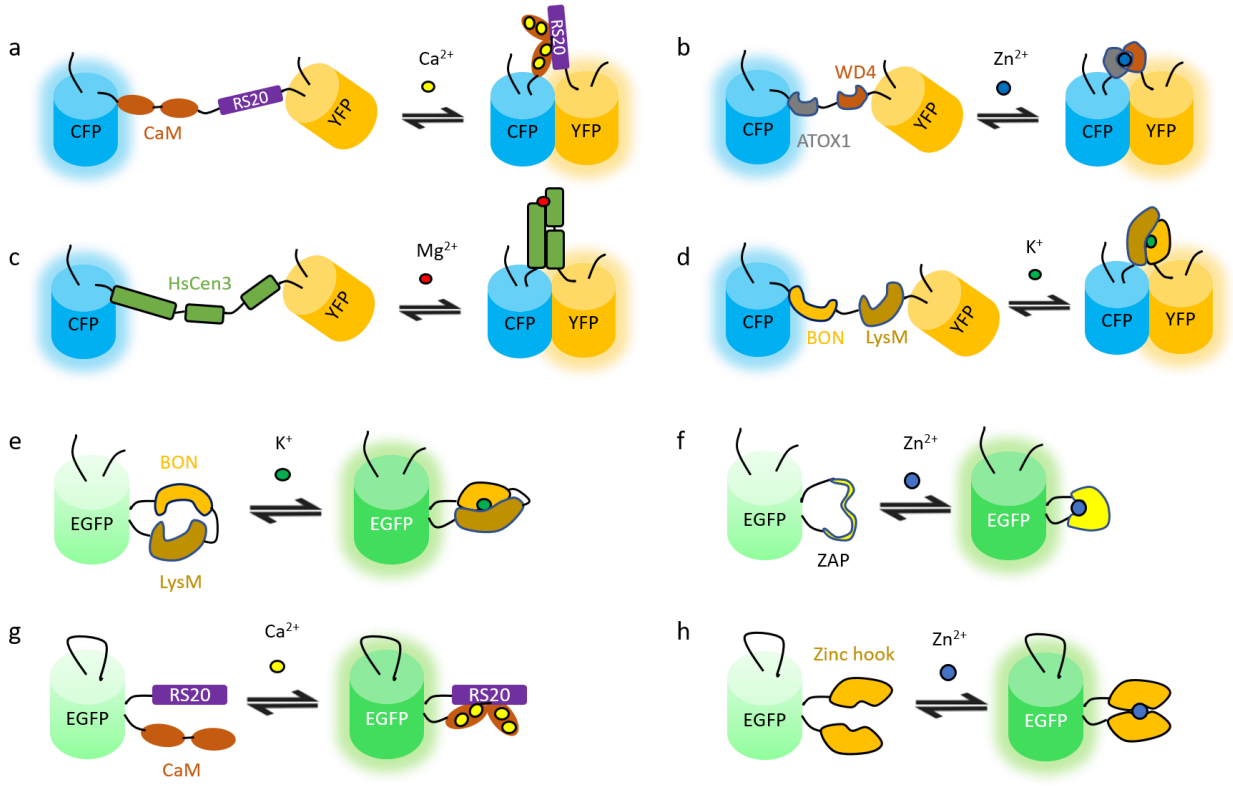

Figure 1.1. Schematic representations of selected genetically encoded indicators.

The (a–d) FRET-based and (e–g) single FP-based genetically encoded ion indicators. The indicators illustrated include (a) cameleon, (b) CALWY, (c) MagFRET, (d) KIRIN, (e) GINKO, (f) ZIGB1, (g) GCaMP/G-GECO, and (h) ZIGB2.

The local concentration of Ca^{2+} varies from nM to mM in cells. At resting state, the intracellular level is usually kept as low as 100 nM[11]. Ca^{2+} is being actively pumped out to extracellular space or into endoplasmic reticulum or mitochondria by Ca^{2+} pump or Na^{+}/Ca^{2+} exchanger for storage. Extracellular Ca^{2+} is maintained at 1 mM, 10000-fold of its intracellular concentration. Because of the importance of Ca^{2+}, being able to detect Ca^{2+} becomes vital to many different research fields. To accommodate the different ranges of Ca^{2+} in a variety of environments, sensors with different affinities are also in demand. The diversity of Ca^{2+} sensors created thus far has contributed to and facilitated the research enormously, which will be described in detail.

1.3.2 Synthetic small molecules for Ca^{2+} detection

Small molecule-based Ca^{2+} indicators usually contain a fluorophore and a Ca^{2+} chelator. The indicators function through photo-induced electron transfer (PET) — the fluorescence of fluorophore is modulated by the electron-rich or electron-withdrawing group nearby[12]. The electron rich Ca^{2+} chelator quenches the fluorescence of the fluorophore in absence of Ca^{2+} and the quenching is disrupted once Ca^{2+} binds to the chelator.

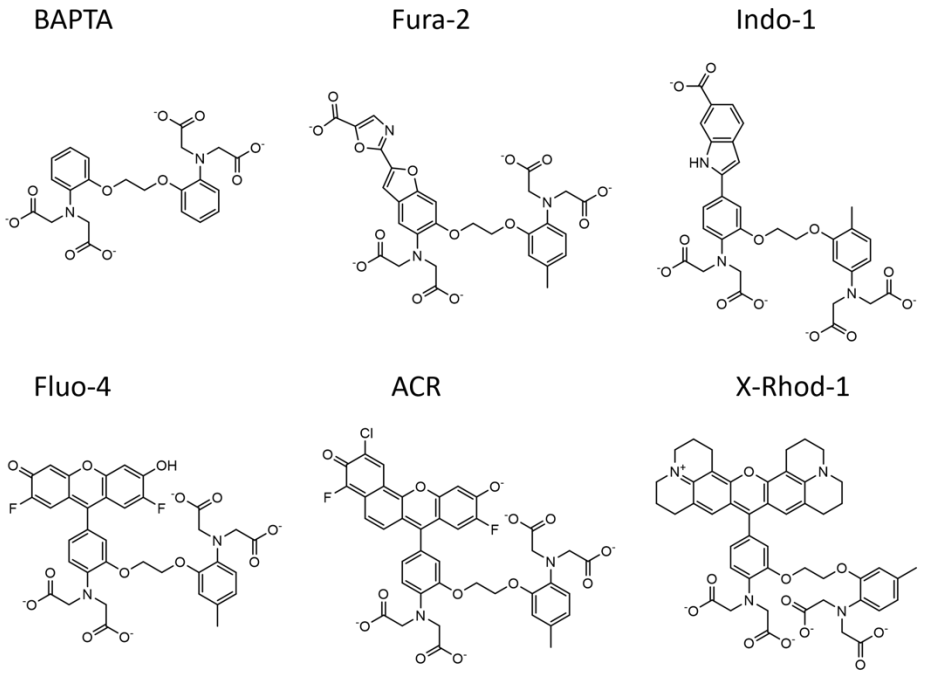

Figure 1.2. Molecular structures of selected small molecule-based Ca^{2+} indicators.

1.3.2.1 BAPTA and BAPTA-based Ca^{2+} indicators

The development of BAPTA (1,2-bis(*o*-aminophenoxy) ethane-*N*,*N*,*N*′,*N*′-tetraacetic acid) by Roger Tsien and his coworkers in 1980 is a milestone in the history of synthetic fluorescent Ca^{2+} indicators[13]. Many later synthetic fluorescent Ca^{2+} indicators are based on BAPTA, an EGTA (ethylene glycol-bis(β-aminoethyl ether)-*N*,*N*,*N*′,*N*′-tetraacetic acid) analog. EGTA is a Ca^{2+} chelator that prefers Ca^{2+} over other cations such as Mg^{2+}. Like EGTA, BAPTA interacts with Ca^{2+} with coordination through the four carbonyl oxygens, as well as two ether oxygens and the nitrogen of tertiary amine groups. BAPTA has a K_d of 1.1×10^{-7} M and has a selectivity for Ca^{2+} 10^5 times greater than that for Mg^{2+}. Structurally, BAPTA differs from EGTA by replacing the methylenes between the nitrogen and the ether oxygen with a benzene ring. The delocalized electrons of the aromatic rings allow the compound to fluoresce. Upon Ca^{2+} binding, the nitrogen atoms are bent away from the same plane of the nearby benzene ring due to the structural constraint.

This results in a major shift in the absorbance spectrum. The absorbance peaks are at 254 nm ($\varepsilon = 1.6 \times 10^4\ M^{-1}cm^{-1}$) and 287 nm ($\varepsilon = 5.6 \times 10^3\ M^{-1}cm^{-1}$) in absence of Ca^{2+} and they are at 274 nm ($\varepsilon = 4.2 \times 10^3\ M^{-1}cm^{-1}$) and 203 nm ($\varepsilon = 4.1 \times 10^4\ M^{-1}cm^{-1}$) with 1 mM Ca^{2+}. The emission peaks at 363 nm, with fluorescence intensity lowered by the presence of Ca^{2+}.

BAPTA was a great innovation at the time because the compound can be easily modified to adjust the affinity to its ligand Ca^{2+}, as well as its major competitor Mg^{2+}. The affinity can be increased by an electron-releasing group (e.g., methyl group) on the benzene rings and decreased by an electron-withdrawing group (e.g., bromide group) on the rings. BAPTA was later modified more intensively to create better Ca^{2+} sensors.

Derived from BAPTA, quin-2 is a green fluorescent indicator providing a positive response upon Ca^{2+} binding[14]. Its maximum excitation wavelength is at 339 nm and maximum emission wavelength is at 492 nm. The K_d of the indicator is 115 nM for Ca^{2+} and is suitable for the cytosolic Ca^{2+} detection. Its K_d for Mg^{2+} is in the range of mM, making quin-2 selective for Ca^{2+}. Quin-2 has an extinction coefficient $<5000\ M^{-1}cm^{-1}$ and quantum yield from 0.03–0.14. As quin-2 is not membrane-permeable, the compound was modified with addition of an acetoxymethyl (AM) group on its carboxylic groups to allow it for cell entry. The acetoxymethyl groups will be cleaved by the esterase in the cytosol to convert quin-2 AM to the functional quin-2.

With the success of quin-2, more derivatives of BAPTA were explored to create better Ca^{2+} indicators. Noticeably, indo-1 and fura-2 were better indicators that have brighter fluorescence and provide ratiometric measurements[15]. Both indicators have a K_d around 250 nM, slightly larger than that of quin-2. Indo-1 emits cyan light at 485 nm in Ca^{2+} free environment and violet light at 410 nm in Ca^{2+} rich environment, with excitation spectra peak at 349 nm and 331 nm, respectively. The ratiometric changes in emission spectra upon Ca^{2+} binding allows more sensitivity in detection.

Contrarily, fura-2 is green fluorescent with a minor shift in emission peak from 512 nm to 505 nm with increasing Ca^{2+} concentration. The excitation peak, however, undergoes a blue shift from 362 nm to 335 nm, which provides an opportunity for ratiometric excitation. The quantum yield increases from 0.23 to 0.49. The single-colour emission of fura-2 is convenient for applications with a fluorescence microscope with a single or dual-excitation setup. Fura-2 has a low affinity for Mg^{2+} with K_d of 1-2 mM that allows intracellular Ca^{2+} imaging in various animal cells[16]. The membrane-permeable dyes were made in the same way as quin-2 AM by the addition of acetoxymethyl groups. Because these two indicators are both bright and sensitive to Ca^{2+}, they are still commonly used today.

1.3.2.2 Fluorescein-based Ca^{2+} indicators

Fluorescein were used to make green indicators include fluo-1, fluo-2, fluo-3, fluo-4, fluo-8 series, Oregon green BAPTA-1 (OGB1), and Cal-520 (Refs. 17–19). These green fluorescent indicators are generally more sensitive, have faster kinetics, and bind Ca^{2+} with different affinities that allow detection in different environments[19]. For example, Cal-520 responds to Ca^{2+} faster and provides a good signal with low SNR in subcellular regions of neurons. Fluo-8 series have variants with high and low affinities: fluo-8H has a K_d of 232 nM and fluo-8L has a K_d of 1.8 μM.

1.3.2.3 Rhodamine-based Ca^{2+} indicators

Red-shifted Ca^{2+} indicators provide a unique advantage as red colours penetrate deeper in tissues and can be used simultaneously with other green indicators. Rhod2 is excited by light at 553 nm and emits light at 576 nm[17]. The compound utilizes the BAPTA with incorporation of a rhodamine structure to induce the red shift. The quantum yield is from 0.03 (Ca^{2+} free) to 0.102 (excess of Ca^{2+}) and K_d is 0.52 μM. Later variants rhod4, rhod5N, Asante Calcium Red (ACR), and X-Rhod-1 have a superior sensitivity to $Ca^{2+}$and some are more red-shifted[19]. Rhod5N has a

maximum 150-fold change. ACR is excited at 537 nm and emits at 654 nm[20]. The indicator is also compatible with two-photon excitation at 780 nm.

1.3.3 Genetically encoded Ca^{2+} indicators (GECIs)

Synthetic Ca^{2+} dyes provide opportunities for the Ca^{2+} related studies, but also display some intrinsic shortcomings that make it undesirable in some applications. The loading procedure may lead to artifacts in the experiment: for example, uneven distribution of the dye in the sample tissue. Dyes cannot be targeted to specific cell types in tissue or a specific cell compartment in a cell. These issues are well addressed by the genetically encoded Ca^{2+} indicators (GECIs).

GECIs, except for aequorin, share a general design that consists of a binding domain and a reporter domain. The choices for binding domains include calmodulin (CaM)/RS20 (a.k.a. M13) pair and troponin-C. The reporter domains are usually fluorescent proteins (FPs) or bioluminescent proteins. Fluorescent proteins form a chromophore with three amino acids (e.g., Ser65, Tyr66, and Gly67 in GFP) in their sequence[21]. We currently have a large set of GECIs: the variety in colour and affinity provides enormous opportunities for applications. The mechanism for all these biosensors involves an event, usually a conformational change of the binding domain, that causes a signal change of the reporter domain, allowing us to monitor the Ca^{2+} concentration dynamics.

1.3.3.1 Bioluminescent and BRET-based Ca^{2+} biosensors

Compared to fluorescence, bioluminescence allows better sensitivities as it requires no excitation light, thus reducing photodamage of the tissue, photobleaching of the biosensors, and background autofluorescence. Because of this, bioluminescent protein-based biosensors present superior performance especially when used simultaneously with optogenetic tools. The drawback of bioluminescence is its requirement of a luciferin, which usually needs to be added manually[22].

In cases where sensitivity is the priority, bioluminescent and bioluminescence resonance energy transfer (BRET)-based Ca^{2+} biosensors can be the key to the success in detection.

Found in 1962, aequorin is the first genetically encoded Ca^{2+} biosensor[23]. It is a Ca^{2+} activatable bioluminescent protein found in *Aequorea victoria*. The protein is complexed with a luminophore coelenterazine, which can be oxidized by O_2 to coelenteramide in an aerobic environment, emitting blue light. Aequorin has three binding sites with different binding affinities for Ca^{2+}, which leads to a wide range of detection from 100 nM to 100 μM[24]. However, the low signal level due to slow catalysis limits its applications.

BRET-based Ca^{2+} biosensor couples the bioluminescent protein with a fluorescent protein, providing a variety of colours for detection. Aequorin has been reported to couple with GFP and mRFP[25,26]. Later, brighter BRET-based Ca^{2+} biosensors utilize a brighter bioluminescent protein (e.g., *Renilla* luciferase and NanoLuc luciferase) and Ca^{2+} binding calmodulin/RS20 in place of aequorin to couple with a fluorescent protein[27]. There are three different designs — based on split luciferase, proximity, and single FP GECI — for the BRET based Ca^{2+} biosensors. In the split-luciferase design, the ligand binding will bring the split bioluminescent protein parts together to form a function bioluminescent protein in a reversible fashion. The examples are RLuc8-based nano-lantern and NanoLuc-based GeNL series[28,29]. Compared to the low affinity of aequorin-based biosensors ($K_d \sim 10$ μM), these BRET biosensor using calmodulin/RS20 displayed higher affinities: The K_d of BRAC is 1.9 μM and that of nano-lantern and GeNL variants are in the range from tens of nM to hundreds of nM[28–30]. The split-luciferase-based GECIs are intensiometric, making the concentration of luciferin a noticeable varying factor to the response level. Ratiometric BRET GECIs described below can address this issue. In proximity-based biosensors, Ca^{2+} binding at the binding domain will change its conformation, leading to a reduction of distance between the

bioluminescent protein and the fluorescent protein and thus yielding a better BRET efficiency. BRAC, for example, uses *Renilla* luciferase (RLuc8) and a yellow fluorescent protein, Venus[30]. CalfluxVTN is another example that uses troponin-C for Ca^{2+} binding, NanoLuc for bioluminescence, and Venus as the BRET receptor[31]. CalfluxVTN has a dynamic range of 7.7 and a K_d of 1.1 μM. The BRET GECI can also use a bioluminescent protein and an existing GECI. LUCI-GECO, as an example, uses NanoLuc as the chemiluminescent part, but ncpGCaMP6s (ncpEGFP and calmodulin/RS20) for the BRET receptor and Ca^{2+} binding. LUCI-GECO has a maximum ratiometric response of 5.0 and a nM affinity (K_d = 285 nM) for cytosolic Ca^{2+} detection.

1.3.3.2 FRET-based Ca^{2+} biosensors

The development of fluorescent biosensors was benefited by the expansion of fluorescent proteins, discovered from nature or engineered from natural fluorescent proteins. Till today, we are fortunate to have fluorescent proteins that cover the colour spectrum, allowing developed biosensors to show a diversity in colours. FRET-based Ca^{2+} biosensors use a two-fluorescent-protein FRET pair to report the Ca^{2+} concentration. The emission spectrum of the FRET donor should be well aligned with the excitation spectrum of the FRET acceptor for a reasonable FRET efficiency.

Cameleon series were among the first genetically encoded fluorescent Ca^{2+} biosensors developed. The binding domain of calmodulin/RS20 is inserted in between the flanking FPs, EBFP/EGFP or ECFP/EYFP[32]. The cameleon with the ECFP/EYFP pair is named YC (yellow cameleon) and is further engineered for both performance: The biphasic binding of YC2.1 to Ca^{2+} is removed in YC3.1 by E104Q on the calmodulin domain[33]. YC3.1 also demonstrated to have a more appropriate detection range for intracellular Ca^{2+} detection when YC2.1 signal is saturated due to a higher affinity in histamine stimulated HeLa cells. Noticeably, YC series were the first

genetically encoded biosensors tested in a living organism. In 2000, Kerr and coworkers published their work in which recombinant YC2.1 and YC3.1 was expressed in *Caenorhabditis elegans* and resulted a detectable FRET signal when the pharynx muscle of the transgenic *C. elegans* contracted[34]. The YC2.1 and YC3.1, despite being a success, were limited by the presence of environmental binding partners to calmodulin. Further engineered YC6.1 had inserted CKKP into calmodulin instead of fusing a R20 to the C terminus of calmodulin[35]. The insertion of CKKP in a split calmodulin leads to a shorter distance between the N and C termini in the Ca^{2+} bound form. The resulting YC6.1 has a suitable dynamic range (R_{max} = 2.50, R_{min} = 1.18) and affinity (K_d = 110 nM) for intracellular Ca^{2+} detection. VC6.1, based on YC6.1, replaced YFP with a Venus through directed evolution. VC6.1 is more sensitive to Ca^{2+} change in a cellular environment.

Parallel to the first publication of cameleon series, another FRET-based Ca^{2+} biosensor with a similar design to cameleons, FIP-CB_{SM} , was developed independently by Romoser and colleagues[36]. Instead of using both calmodulin and RS20, it only uses RS20 between the flanking FPs. The Ca^{2+} bound endogenous calmodulin will bind to RS20 of the biosensor. With a BFP/ RFP FRET pair, this indicator demonstrated a 5-fold dynamic range of $F_{505\ nm}/F_{440\ nm}$ ratio and a K_d of 0.4 nM.

Calmodulin is not the only choice for the binding domain: troponin was another reasonable choice that leads to the development of TN-L15, XL, and XXL[37–39]. The series adopts the design where troponin C (TnC) is inserted in a pair of CFP and citrine. Calmodulin used in cameleons and FIP-CB_{SM} have many native binding partners that make their in-cell response not as substantial as the *in vitro* response. TnC, on the other hand, is only native to skeletal and cardiac muscles and has far fewer numbers of cellular molecules that may interfere with its Ca^{2+} binding. The TN series developed demonstrated a wide range of affinities (K_d from 470 nM to 29 μM) and suitable

dynamic ranges (e.g., ~160% for TN-L15)[37–39]. TN-XXL was later engineered into the Twitch series with the full-length TnC replaced by a minimal domain of TnC[40]. Twitch-1 has a maximum response of 400% and K_d of 250 nM *in vitro*. Directed evolution was carried out to make better Twitch variants with varying maximum response and affinity. K_d was increased while the maximum response was increased during the optimization. With K_d ~ 100–200 nM, Twitch 1, 2, 3 are more suitable for a lower Ca^{2+} environment, such as the intracellular space. Twitch 4, 5 have a much larger K_d and maximum response, making them ideal in a higher Ca^{2+} environment. They were tested in neurons and Twitch-3 displayed a better response in stimulated neurons in comparison to its counterpart, YC3.6.

In general, the most effective FRET-based GECIs use a pair of cyan (CFP and mCerulean) and yellow (YFP, cpVenus, and mCitrine) fluorescent proteins to report FRET signal changes. The binding domains can be calmodulin or TnC-based. As important members of the GECI tool set, they have been demonstrated to be robust and effective in dissociated neurons and animal models.

1.3.3.3 Single FP-based Ca^{2+} biosensors

Single FP-based Ca^{2+} biosensors are the gems of the GECIs. They are usually smaller in size, making them easier for transfection and packaging into a virus. Compared to FRET GECIs, their narrower spectra make them ideal for multiplex imaging. With extensive engineering, they can achieve a remarkable dynamic range (e.g., jGCaMP7c has a dynamic range over 20-fold) that a FRET-based GECI can hardly achieve. Selected single FP-based GECI are included in **Table 1.1**.

1.3.3.3.1 Circular permuted and non-circular permuted FPs for biosensor design

Before introducing the single FP GECIs, it is important to address the ways in which a single FP can be incorporated into a reporter sensitive to the changes of the binding domain. The circular permuted (cp) FP and non-circular permuted (ncp) FP are the two strategies commonly

used for biosensor development. Both strategies involve splitting FPs into two parts in the primary protein structure, usually near the chromophore and two parts folding into a complete β-barrel shaped FP of which the chromophore is in proximity to the ligand binding domain. The binding event changes the conformation of the binding domain, which subsequently influences the chromophore environment, leading to a fluorescence signal change that we can monitor.

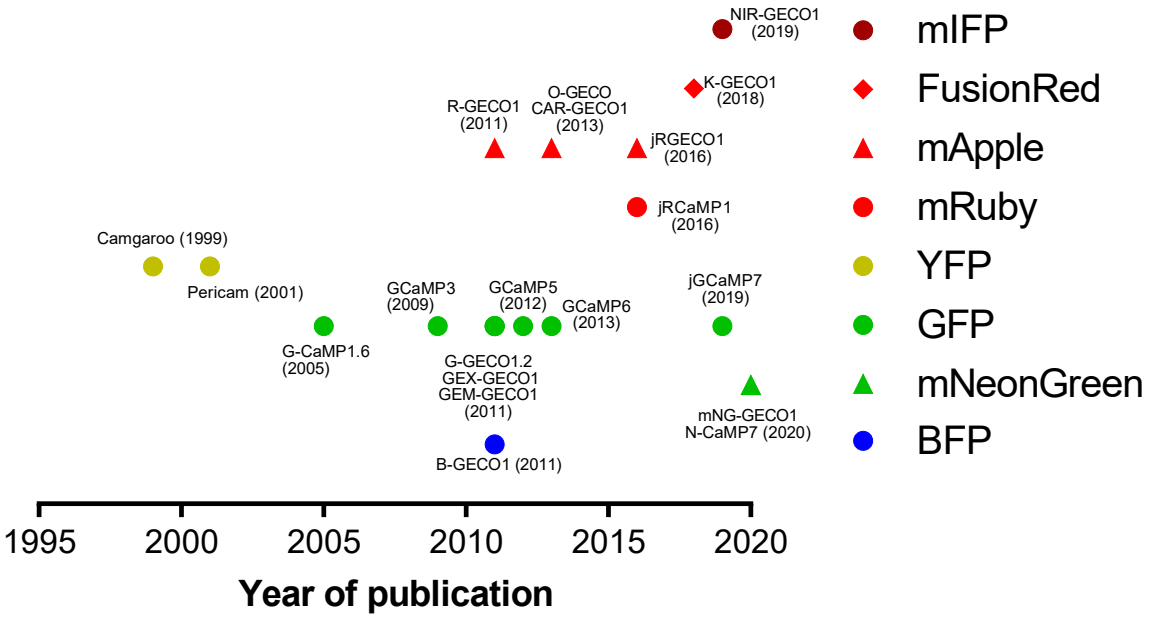

Figure 1.3. The journey of GECI development.

The selected GECIs are plotted with the time they were published. All of them utilized CaM/RS20 as the binding domains. The FPs incorporated include YFP, GFP, mApple, mRuby, FusionRed, mIFP, and BFP.

Circular permutation is one well-thought design to rearrange the primary sequence of the FP such that the newly created N- and C-termini are located close to the chromophore. Baird *et al*. first described the design of cpEGFP, cpEYFP, and cpECFP in 1999 (Ref. 41). The shared primary sequence is FP(145–238)-GGTGGS-FP(1–144). GGTGGS serves as the linker to connect the

original N- and C-termini and the new termini are created between residue 144 and 145. All three cpFP retain their original colours of fluorescence while increasing their pK_a. When designing a biosensor with cpFP, connecting the binding domain to the terminus is a routine approach to ensure maximum influence of ligand-binding induced conformational change in immediate vicinity to the chromophore.

Non-circular permutation is also seen in many biosensor designs. The binding domain is inserted in between the split FP. The split site, like the new termini of cpFP, is usually located close to the chromophore on the β-barrel, allowing the binding to affect the chromophore environment.

In both cases, optimizations on the position of the split site and linker regions, are usually required for optimal responses. Advanced screening systems were invented and developed for such work in bacteria, mammalian cells, or neurons. Here we summarized the collection of the single FP GECIs designed with cp or ncpFP designs during the last two decades in **Figure 1.1**.

1.3.3.3.2 Camgaroos and Pericams

Camgaroos and pericams are the first developed GECIs utilized ncpFP and cpFP, respectively. The development of these two types of biosensors provided many strategies used in later biosensor development. **Figure 1.2** shows the schemes of cp- or ncpFP-based genetically encoded ion indicators.

The history of single FP-based GECI started with camgaroos in 1999, in which the YFP was split into two parts with a calmodulin inserted in between[41]. The biosensor adopted the non-circular permutated sensor design with a primary sequence described as EYFP(1–144)-GGT-Calmodulin-EL-EYFP (146–238).The F/F_0 for this YFP-based GECI can be as big as 20-fold in ionomycin treated cells.

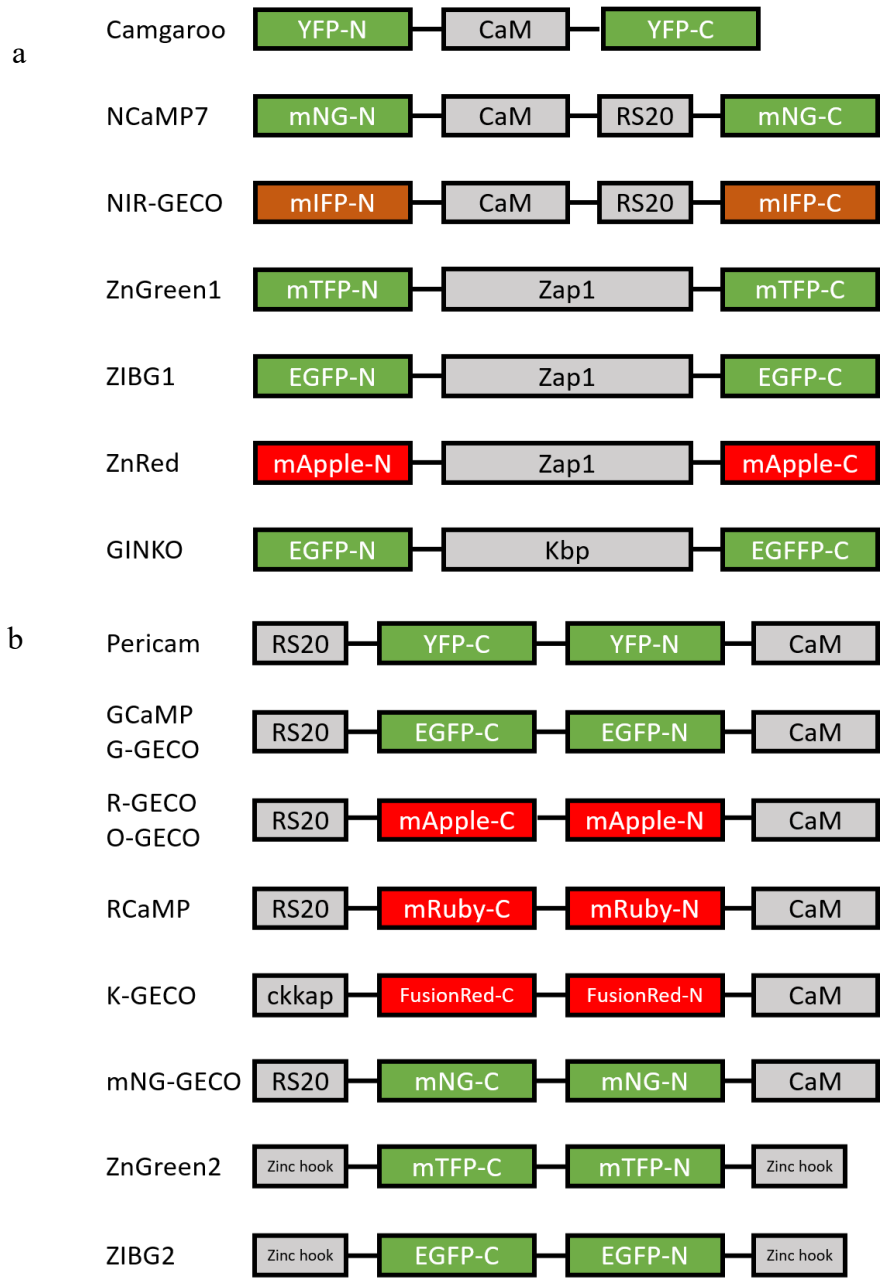

Figure 1.4. The schematic illustrations of cp and ncpFP-based indicators.

The (a) ncpFP-based indicators include Camgaroo, NCaMP7, NIR-GECO, ZnGreen1, ZIBG1, ZnRed, and GINKO. The FP is split into two parts and fused to the N- and C-termini of the binding domain. The (b) cpFP indicators include pericam, GCaMP, G-GECO, R-GECO, O-GECO, RCaMP, K-GECO, mNG-GECO, ZnGreen2, and ZIBG2. The cpFPs were made with new N- and C- termini.

In 2001, pericams was developed by Nagai and his coworkers with circular permeable YFP in which the primary sequence of YFP was rearranged in a sequence of EYFP (145–238)-GGTGGS-EYFP (1–144)[42]. The tertiary structure of pericams are similar to that of camgaroos, with a new N- and C- termini connecting to CaM and RS20, respectively, and the original termini connected by the new linker GGSGG. Nagai *et al* described three pericams: flash-pericam, inverse-pericam, and ratiometric-pericam. Flash-pericam was the developed with M13 to the N terminus and CaM to the C terminus of cpYFP. The two linker sequences are SAG and GTG between RS20 and cpYFP and between cpYFP and CaM, respectively. Ratiometric-pericam was engineered from flash-pericam with changes of linkers and amino acid mutations. The linker between the original N- and C- termini was replaced to VDGGSGGTG and the linker between the cpYFP and CaM has been shortened by one amino acid. Two mutations H148D and Y203F were also introduced. The inverse-pericam was discovered during the engineering for ratiometric-pericam. H148T and Y203F made it an inverse sensor, which has a higher signal in absence of Ca^{2+}. The *in vitro* fold changes are 8 times, 10 times (ratio of excitation intensities at 494 nm and 415 nm), and 7-fold, for flash-, ratiometric-, and inverse-pericams, respectively[42]. In the engineering of FP-based biosensors, linkers play important roles and sometimes mutations on the linkers are sufficient to inverse the signals.

1.3.3.3.3 GCaMP/G-GECO

Green-colour genetically encoded Ca^{2+} biosensors are widely used and intensively optimized by biosensor developers. Nakai and coworkers published the first EGFP-based GECI in 2001 around the same time of the EYFP-based GECIs[43]. They tried both cpEGFP and ncpEGFP like camgaroo and pericam described above[43]. The green GECI with cpEGFP showed better response to Ca^{2+} and was named GCaMP1 after some optimizations. GCaMP1 contains a cpEGFP

with EGFP (149–238) fused to EGFP (1–144) with a linker of GGSGGT. The linker between RS20 and cpEGFP has a sequence of LE and the linker between cpEGFP and CaM has a sequence of TR. Three amino acids MVD were also added to the N terminus of RS20. GCaMP displayed 4.5-fold change to Ca^{2+}, a Hill coefficient of 3.3, and a K_d of 235 nM to Ca^{2+}.

GCaMP2 and its precursor GCaMP1.6 addressed the major deficiencies of GCaMP1: low brightness and instability at 37°C. Ohkura *et al*. introduced two mutations on cpEGFP: V163A and S175G, as well as a His Tag at the N terminus: these mutations greatly improved the brightness by almost 40 times[44]. The resulted GCaMP1.6 also show better stability at 37°C for both purified protein and the protein expressed in HEK cells. Ohkura and coworkers tested specificity of GCaMP1 and GCaMP1.6 as well. Except for Mg^{2+}, all other tested divalent cations (Ni^{2+}, Mg^{2+}, Co^{2+}, Zn^{2+}, Mn^{2+}, Cd^{2+}, Sr^{2+}, and Ba^{2+}) triggered a GCaMP1 or GCaMP1.6 response at 1 mM. Ba^{2+} and Sr^{2+} generated GCaMP responses similar to the level of Ca^{2+} response, but their affinities were much lower than that of Ca^{2+} (K_d values of Ba^{2+} and Sr^{2+} were 260 and 370 μM for GCaMP1 and 80 and 460 μM for GCaMP1.6)[44]. Using GCaMP1.6 as the template, Tallini and coworkers introduced D180Y and V93I by random mutagenesis and a 35-amino-acid long polyHis-RSET N terminal sequence, leading a 6-times brighter new variant, GCaMP2 (Ref. 45). Tallini and coworkers also expressed GCaMP2 in mice and observed GCaMP2 activity in its spontaneous beating and paced heart. Imaging the heart expressing GCaMP2 and loaded with Rhod2, a red Ca^{2+} dye, showed that GCaMP2 has about 3 times of the dynamic range of that of Rhod2 (Ref. 45).

Despite the success of GCaMP2, GECIs were still not a competitor to the small molecule-based chemical Ca^{2+} dyes in terms of brightness (the product of quantum yield and extinction coefficient), photostability, and well-tuned affinities. GCaMP3 was the first of many GCaMP series developed by GENIE project at the Janelia research campus. GCaMP3 was developed via

both structure-guided site directed mutagenesis at sites close to the chromophore and semi-rational library screening: the resulted GCaMP3 presented a brightness of 4 times of that of GCaMP2, a dynamic range of 3 times of that of GCaMP2, and a reduced Hill coefficient ($n_H = 2.1$)[46]. GCaMP3 was able to provide a noticeable signal with one signal action potential, making it a more useful indicator for neuroscience than previous GECIs.

In 2011, Zhao and coworkers developed G-GECO, B-GECO, GEM-GECO, and GEX-GECO based on GCaMP3 using directed evolution and gene shuffling[47]. G-GECO doubles the dynamic range of GCaMP3 but has a lower brightness at the brighter Ca^{2+} bound state. The Hill coefficient of G-GECO1.2 is 2.1. A blue variant, B-GECO, was developed with a GFP Y66H that was previously used to convert EGFP into EBFP. GEM-GECO and GEX-GECO were also identified after gene shuffling of B-GECO, G-GECO, and F-pericam1.2. They both respond to Ca^{2+} with ratiometric changes: GEM-GECO1 present a 110-fold change of emission ratio ($I_{455\ nm}$ to $I_{511\ nm}$); GEX-GECO1 presents a 26-fold change of excitation ratio ($I_{482\ nm}$ to $I_{390\ nm}$). The large ratiometric changes allow these two GECOs to be sensitive to Ca^{2+} with dual channel imaging.

To generate GCaMP5 variants, site directed mutagenesis and library screening were performed at the RS20/cpGFP linker, cpGFP/CaM linker, at the interface of CaM and cpEGFP on the crystal structure, on RS20, and near the third Ca^{2+} binding site of CaM[48]. Compared to GCaMP3, GCaMP5 increased the dynamic range to 17, 18, and 31 for GCaMP5A, 5D, and 5G, respectively. Although the only GCaMP5G has a dynamic range that outperform that of G-GECO1.2, the baseline fluorescence of GCaMP5 variants is brighter, which is important in cases with low biosensor expression. The Hill coefficients are 2.7, 2.5, and 2.5 for GCaMP5A, 5D, and 5G, respectively.

Prior to GCaMP6, all GCaMPs or GECOs were screened in *E. coli* system. As a well-established and robust organism for molecular biology, *E. coli* allow easy transformation and efficient protein expression. Working with *E. coli* is a convenient and cost-effective in comparison to alternative biological systems, making *E. coli* the top choice for screening for a long time. The effectiveness of *E. coli* system was demonstrated by the drastic improvement of GCaMPs and GECOs over time. The first GCaMP only had a Ca^{2+}- bound brightness of 0.07 (Ref. 44) and that of GCaMP5G was 33 (Ref. 48), comparable with the brightness of EGFP. The dynamic range (F_{max}/F_{min}) was improved from 4.5 (GCaMP1) to 33 (GCaMP5G), but the test in mammalian system, such as HEK cells, exhibited a much smaller dynamic range (5.5 for GCaMP5G)[48]. The noticeable performance discrepancy in bacteria and mammalian cells led to screening in a mammalian system. Because prevalent usage of GECI in neuroscience, dissociated neurons became an ideal system for screening.

GCaMP6 variants were screened in rat hippocampal neurons. Mutagenesis was performed at the interface of cpGFP and CaM for better sensitivity and the interface of CaM and RS20 for affinity tuning[49]. Neurons were transfected with the mutants and nuclear mCherry control and subject to screening. This method led to remarkable GCaMP6 variants that substantially outperform previous GECIs in neurons where fast and sensitive detection is required. GCaMP6s is the most sensitive variant: the dynamic range of GCaMP6s is 63.2 with purified protein from *E. coli* and a fluorescence increase of 23%.was observed with one action potential in neurons[49]. In comparison, one action potential can only lead to a 3.6% increase for GCaMP5K[48]. The substantial improvement of GCaMP6 made it a useful and popular tool in the neuroscience community.

To optimize GCaMP6 further for different applications, jGCaMP7 was developed by Dana and coworkers and published in 2019 with variants that exhibit optimized sensitivity, kinetics,

Ca^{2+} affinity, or brightness[50]. In the work, jGCaMP7s (sensitive) and jGCaMP7f (fast) have improved sensitivity and kinetics for single action potential imaging: jGCaMP7s provides the biggest response to one action potential with a 65.6% increase in fluorescence; jGCaMP7f responses to 10 actions potentials with a half-rise time of 75 ms and half-decay time of 520 ms, comparable to those of GCaMP6f (a half-rise time of 80 ms and half-decay time of 335 ms)[49,50]. jGCaMP7b (bright) is a good choice for cells with lower protein expression level as it has a 40.6% increase in response to one action potential and 50% increase in resting fluorescence compared to GCaMP6s. jGCaMPc (contrast) displays the biggest dynamic range of 145 and the lowest brightness in absence of Ca^{2+} with purified protein characterization, making it an ideal choice for experiments with more scattering.

1.3.3.3.4 mNeonGreen-based GECI

The improvement on GCaMPs and G-GECOs is largely limited by the brightness of EGFP. mNeonGreen is the brightest monomeric green fluorescent protein so far, which is 2.8 times as bright as EGFP[51]. Zarowny et. al. and Subach et. al. independently developed mNeonGreen-based GECI named mNG-GECO1 and NCaMP7, respectively. mNG-GECO1 used an unpublished ncp REX-GECO scaffold and replaced the EGFP with mNeonGreen[52]. The Ca^{2+} bound state brightness of mNG-GECO1 is 59% higher than that of GCaMP6s. Its dynamic range of 45, comparable to that of GCaMP6. The sensitivity of mNG-GECO1 is only about half of that of GCaMP6s in neurons. NCaMP7 used GCaMP6s as a template, hence, adopted its cp design[53]. The brightness of NCaMP7 is 70% higher than that of GCaMP6s and the dynamic range of NCaMP7 is 89. NCaMP7 is sensitive to Mg^{2+} and the dynamic range is reduced to 27 with 1 mM Mg^{2+} in the solution. The sensitivity of NCaMP7 is comparable to that of GCaMP6s in neurons, but with a slower kinetics. Neither mNG-GECO or NCaMP7 surpassed GCaMP6s as a tool in neuron imaging. Yet, we shall

keep in mind that the sensitive GCaMP6s and GCaMP7s were obtained after almost two decades of work on the GFP-based GECI, while optimizations of the mNeonGreen-based GECI started recently.

1.3.3.3.5 Red, far-red, and near-infrared GECI

The depth of imaging is one of the concerns with the green and blue coloured indicators. As biological samples absorb and scatter incoming light (characterized by the absorption coefficient μ_a and the scattering coefficient μ_s'), the percentage of photons decreases with increasing sample depth. μ_a and μ_s' are wavelength dependent: absorption and scattering are more severe with photons of shorter wavelength[54]. In the brain tissue, μ_a generally decreases as the wavelength of the incoming light increases (0.01–3.51 for 420 nm light, 0.02–3.84 for 532 nm light, 0.02–0.05 for 630 nm light, 0.11–0.17 for 760 nm light, and 0.078–0.089 for 780 nm light)[55]. μ_s' decreases with increasing wavelength of the incoming light (18.75–55.83 for 420 nm light, 0.10–46.3 for 532 nm light, 3.72–21.97 for 630 nm light, 4.0–10.5 for 760 nm light, and 8.42–9.16 for 780 nm light). Thus, the red-shifted GECIs are more suitable for deeper sample imaging. Another advantage of red shifted GECI is its compatibility with channelrhodopsin-based optogenetics tools, which are usually activated by blue light.

R-GECO was developed by replacing cpEGFP with cpmApple in G-GECO[47]. After a few rounds of directed evolution, R-GECO1 was able to present a 16-fold Ca^{2+} response. The brightness of R-GECO1 is 10.2 at its brighter Ca^{2+} bound state. Further engineering of R-GECO1 led to different variants: R-GECO1.2, O-GECO1, REX-GECO1, and CAR-GECO1 (Refs. 56,57). R-GECO1.2 is twice as sensitive as R-GECO1 but has a higher K_d at 1200 nM. O-GECO1 was created by site directed mutagenesis on sites previously used to generate mOrange from DsRed followed by directed evolution[56]. The resulted O-GECO1 is blue-shifted with an excitation

wavelength at 543 nm (Ca^{2+} bound)/545 nm (Ca^{2+} unbound) and an emission wavelength at 564 nm (Ca^{2+} bound)/570 nm (Ca^{2+} unbound). Its dynamic range is 146 *in vitro* and 41 in HeLa cells treated with histamine followed by ionomycin/Ca^{2+} and ionomycin/EGTA. The remarkable sensitivity of O-GECO1 is accompanied by a large K_d of 1500 nM. Directed evolution on R-GECO1 for red-shifted variant led to CAR-GECO1 with excitation and emission wavelengths at 560 and 609 nm, respectively. CAR-GECO1 has a dynamic range of 27 and a K_d of 490 nM *in vitro*. REX-GECO1 is a long Stokes shift red indicator with ratiometric excitation developed through *E. coli* screening with two excitation filters: 438/24 nm and 542/27 nm[57]. The resulted REX-GECO1 has a blue shifted excitation: the one-photon excitation is at 480 nm and the two-photon excitation is at 960 nm. Because tissues are most transparent to light in the range of 700 to 1000 nm, REX-GECO1 is more advantageous than other red GECIs, which usually requires excitation at an excitation wavelength over 1000 nm for two-photon imaging. REX-GECO1 has a 100-fold ratiometric change *in vitro* and a K_d of 240 nM. Although effective, these mApple-based GECIs all suffers with photobleaching, as well as photoactivation by blue light, which complicates co-imaging with channelrhodopsin-based optogenetic tools.

To make an alternative red GECI addressing the issues of R-GECO1, Akerboom and coworkers used mRuby to make the GCaMP3-based RCaMP[58]. RCaMP1f and RCaMP1h are sensitive to Ca^{2+} *in vitro* with a dynamic range of 12.3 and 10.5. The dynamic ranges in HEK cells are smaller at 1.8 and 2.0, which is smaller than that of R-GECO1 at 2.5. RCaMP1f and 1h also present a larger K_d at 1900 and 1300 nM. On the hand, With a brightness of 28 and 33, RCaMP1f and 1h are much brighter than R-GECO1.They are also brighter with two-photon excitation at 1070 nm: RCaMP1f and 1h has a peak brightness of 9.2 $mM^{-1}cm^{-1}$and 8.1 $mM^{-1}cm^{-1}$, while that of R-GECO1 is 3.8 $mM^{-1}cm^{-1}$. Akerboom and coworkers also demonstrated that RCaMP1 can be

used with ChR2, suggesting RCaMP1 variants are more suitable for multi-colour imaging with optogenetic tools.

Inoue and coworkers replaced RS20 with CaM-dependent kinase kinase peptide ckkap to address the low affinity of RCaMP1 (Ref. 59). The resulted RCaMP2 reduced the K_d from a μM level to 69 nM. RCaMP2 respond to Ca^{2+} fast enough for one action potential detection in neurons with a rise half time of 0.06, a decay half time of 0.15s and an amplitude increase of 60%. Despite its good performance in neurons, RCaMP2 presents worse brightness and dynamic range than RCaMP1 *in vitro*, suggesting that a suitable affinity and kinetics may be more important for neuronal imaging.

Dana and coworkers optimized the RCaMP1h and R-GECOs for neuronal imaging as well[60]. Instead of replacing RS20 with CaMKK-α, they focused on mutagenesis on the residues on the interface between the RFP (mRuby or mApple) and CaM, between CaM and RS20-, and in CaM. The variants were screened in dissociated neurons. jRGECO1a generated from R-GECO1 is the most sensitive one with a dynamic range of 11.6 *in vitro*. Its performance in neuron is comparable to that GCaMP6f, most likely due to its smaller K_d at 148 nM. However, jRGECO1a inherited the photoswitchable property of DsRed derived mApple, disabling dual imaging with blue light activated optogenetic tools. jRCaMP1a and 1b are much improved with smaller K_d at 214 nM and 712 nM compared to 1.3 μM for that of RCaMP1 (Ref. 58). jRCaMP1b respond to one action potential with a larger signal than jRCaMP1a. Although neither is more sensitive than jRGECO1a, they are both 2-fold brighter than jRGECO1a and allow simultaneous photo-stimulation of ChR2 and imaging of jRCaMP1a/b.

To bypass the obvious flaws of R-GECOs and RCaMPs, Shen and coworkers used the low cytotoxic variant of mKate2, FusionRed, to build a new red GECI called K-GECO[61]. K-GECO

was built with cpFusionRed circular permuted at Ser143 and ckkap in place of RS20 as previously used for RCaMP2 (Ref. 59). Linker optimization and directed evolution lead to K-GECO1, which addressed both the brightness and affinity issues from R-GECOs and RCaMPs, respectively. K-GECO1 has a K_d to Ca^{2+} at 165 nM and a brightness of 27 (Ref. 61). In neurons, K-GECO1 responds with action potentials with better ΔF/F than most red GECIs except jRGECO1a. It also displays a reasonable signal-to-noise ratio and kinetics. K-GECO1 has negligible blue-light photoactivation as well. Unfortunately, K-GECO1 shows much lower expression than jRGECO1a and jRCaMPs *in vivo*, suggesting more screening in dissociated neurons is required.

The red shift of GECI is limited by the β-barrel FPs (β-FPs) because they do not cover the near infrared region of the spectrum. Another class FPs, biliverdin (BV)-binding FPs (BV-FPs) provide far-red to near infrared (NIR) fluorescence needed for red shifted GECI. NIR-GECO1 was the first NIR GECI developed with mIFP, a BV-FP. The design of NIR-GECO contains a split mIFP sandwiching CaM and RS20 (Ref. 62). The authors, Qian and coworkers, created a dual expression vector pcDuEx to express NIR-GECO in both *E. coli* and mammalian cells for screening in both systems. The resulted NIR-GECO1 performs well *in vitro* with an 8-fold inverse change and a K_d of 885 nM. The brightness of NIR-GECO1 is 0.06 at the Ca^{2+} unbound state and 0.02 at the Ca^{2+} bound state. The low brightness is due to the low quantum yield inherited from mIFP, which is only 0.1. The brightness of this BV-FP-based GECI is further limited by the amount of available BV in the tissue as BV unbound NIR-GECO1 is not fluorescent. Testing in the sensorimotor cortex of mice with paw stimuli revealed a response of only 0.3% for NIR-GECO1 whereas the same condition could lead to 10-fold greater fluorescence changes for GCaMP6s.

Further engineering on NIR-GECO1 leads to NIR-GECO2 and NIR-GECO2G[63]. The most pronounced improvement is the stronger affinity to Ca^{2+} with K_d values of 331 nM (NIR-GECO2) and 480 nM (NIR-GECO2G), in comparison to K_d of 885 nM for NIR-GECO1; while the sensitivity and brightness of the new variants remain similar to NIR-GECO1. The stronger affinity alone is sufficient for a substantially increased -ΔF/F (16%, 17%, and 4.5% for NIR-GECO2, NIR-GECO2G, and NIR-GECO1). The Ca^{2+} response levels of NIR-GECO2 and NIR-GECO2G are comparable to those of GCaMP6f (19%) and jRCaMP1a (15%). However, NIR-GECO2 and 2G show slow kinetics (3.0 s^{-1} for NIR-GECO2 and 3.7 s^{-1} for NIR-GECO2G) and low brightness (4.0 $mM^{-1}cm^{-1}$ for NIR-GECO2 and 4.5 $mM^{-1}cm^{-1}$ for NIR-GECO2G). A better variant can be achieved in the future with more engineering of NIR-GECO or using a brighter and more photostable BV-FP for a new NIR GECI.

1.4 Zn^{2+} ion indicators

1.4.1 The roles of Zn^{2+} in cell physiology

Zinc (Zn^{2+}) is an essential trace metal element in biology. Although not involved in redox reactions, Zn^{2+} is incorporated in over 300 enzymes that play important biological functions including regulation of small, taste, and appetite; synthesis of DNA and RNA; hormonal regulation; immune functions; and antioxidation[64]. Zn^{2+} is transported mainly by albumin in the blood and is maintained at a concentration of 1–10 μM in human serum or plasma[64]. The concentration of Zn^{2+} in cells are higher at a few hundreds of micromolar, but most Zn^{2+} are tightly bound, leaving free Zn^{2+} in the picomolar level. Free Zn^{2+} distribute in cell heterogeneously: 1 pM in the endoplasmic reticulum and the Golgi apparatus, 0.1 pM in the mitochondrial matrix, 180 pM in the cytosol, and 200 pM in the nucleus[12]. Zn^{2+} dynamics are important: Zn^{2+} secretion, for example, is associated

with insulin secretion of human pancreatic β-cells[65]. Zn^{2+} is suggested to a play important role in brain for its Ca^{2+}-dependant release from synaptic vesicles[66]. Small molecule-based and genetically encoded Zn^{2+} indicators are developed to quantitively measure the concentration and dynamics of Zn^{2+} in biological samples.

1.4.2 Small molecule-based Zn^{2+} indicators

Like Small molecule-based Ca^{2+} indicators, small molecule-based Zn^{2+} indicators are also consisted of a Zn^{2+} chelator and a fluorophore. Common fluorophores include quinoline, fluorescein, 4-aminoapthalimide, and BODIPY[12]. The small molecule-based Zn^{2+} has been comprehensively reviewed previously by Carter and coworkers[12].

1.4.2.1 BAPTA-based Zn^{2+} indicators

As Zn^{2+} and Ca^{2+} are both divalent cations, existing Ca^{2+} indicators provided a template for making excellent Zn^{2+} indicators. By removing one or more chelating moieties on the BAPTA-based Ca^{2+} indicators, Gee and coworkers created indicators that have lower affinity for Ca^{2+} and much higher affinity for Zn^{2+} (Ref. 67). These indicators include FluoZins, IndoZin, FuraZin, RhodZin, X-RhodZin, and NewPort Green PDX. Among these indicators, FuraZin and IndoZin are ratiometric indicators similar to their templates Fura-2, and Indo-1. FuraZin shows ratiometric excitation at 378 nm and 330 nm; IndoZin shows ratiometric emission at 480 nm and 390 nm. FluoZin-1 and FluoZin-3 are extremely sensitive to Zn^{2+} with a dynamic range of 200. RhodZin and X-RhodZin also have big dynamic ranges of 150 and 100, respectively. FluoZin-3 and NewPort Green PDX are most specific to Zn^{2+} with no response to Ca^{2+}. Because Ca^{2+} indicators are optimal with K_d in the nanomolar to micromolar range, the affinities of these BAPTA based Zn^{2+} indicators usually fall into the same range, which are not ideal for physiological Zn^{2+} detection. NewPort Green PDX, for example, has a K_d of 40 μM, which is too high for Zn^{2+}

detection. FluoZin-3 has the highest affinity to Zn^{2+} with a K_d of 15 nM and FluoZin-3-AM is the most sensitive dye for intracellular Zn^{2+} with a $\Delta F/F$ of 50.

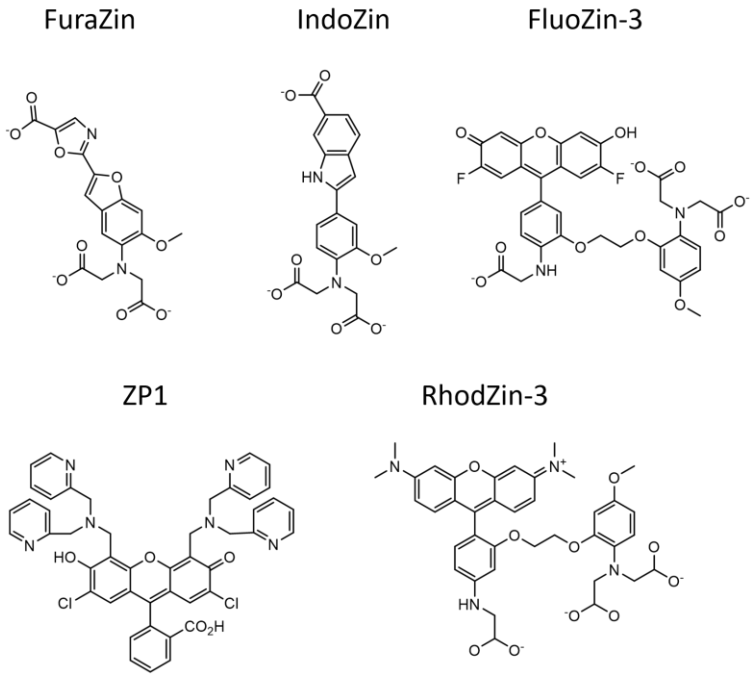

Figure 1.5. Molecular structures of selected small molecule-based Zn^{2+} indicators.

1.4.2.2 Fluorescein-based Zn^{2+} indicator

The green fluorescence dye fluorescein has been used for building the Zinpyr (ZP), ZnAF, Zinspy (ZS), and QZ families of Zn^{2+} indicators. ZP indicators contain a di-2-picolylamine (DPA) Zn^{2+} chelator and a fluorescein moiety. ZP1 is cell permeable and has no measurable response to Ca^{2+} or Mg^{2+} (Ref. 68). It binds $Zn^{2+}$with a brightness of 68 $M^{-1}cm^{-1}$, a dynamic range of 3.1, and K_d of 700 pM. Further improvement led to ZP3 with a brightness of 78 $M^{-1}cm^{-1}$ at Zn^{2+}-bound state, a dynamic range of 6, and a K_d of 700 pM[69]. Instead of a symmetrical fluorescein platform with two DPA groups in ZP1–3, ZP4 employed an asymmetrical fluorescein platform with a Zn^{2+} chelator of one DPA and an additional aniline group[70]. ZP4 exhibits a dynamic range of 5 and K_d of 650 pM; however, this probe does not enter cells efficiently like previous ZP indicators. Better

ZP variants were created with modification on the electron-withdrawing groups on either the fluorophore or the chelator. ZP8, for example, has a dynamic range of 11 and K_d of 600 pM[71]. ZP9 and 10 adopted a pyrrole group or a *N*-methypyrrole group in the asymmetrical Zn^{2+} chelator, which lowered the affinity substantially (K_d of ZP9 is 690 nM and that of ZP10 is 1.9 μM)[72].

ZnAF probes were developed with the DPA moiety attached to different positions on the benzoic acid of fluorescein. ZnAF probes show lower background fluorescence than ZP probes. Among this family, ZnAF-2, ZnAF-1F, and ZnAF-2F exhibit high dynamic ranges of 51, 69, and 60 (Refs. 73,74).

With a pyridine-amine-thioether as the Zn^{2+} chelator, ZS indicators address the specificity issue present in ZP indicators: ZP indicators also bind to Fe^{2+} and Cu^{+}. The thioether was replaced by thiophene to lower the background fluorescence and improve the dynamic range. ZSF7 has a low background brightness of 1.7 $M^{-1}cm^{-1}$, a dynamic range of 42, and a K_d of 33 μM.

QZ family uses 8-aminoquinoline to bind Zn^{2+}. They show remarkably big dynamic ranges: 150 for QZ1 and 120 for QZ2. With an affinity of micromolar range, they were only suitable for detection of a large concentration of Zn^{2+}.

1.4.2.3 Other fluorophore-based indicators

Fluorophores such as boron dipyrromethene (BODIPY) and rhodamine provide different advantages to Zn^{2+} indicators. BDA[75], a BODIPY-based indicator, has a pK_a of 2.1 because BODIPY is much less sensitive to pH than fluorescein. BDA probe is a sensitive green Zn^{2+} indicator with a dynamic range of 10.5 and a K_d of 1 nM. These properties make BDA a good indicator in cases where pH fluctuates. Rhodamine is a photostable red fluorescent fluorophore that has been incorporated into indicators ZRL1 (Ref. 76), SiR-Zn[77], and ZIGIR[78]. The excitation and emission maxima of ZRL1 are at 569 nm and 595 nm, respectively. SiR-Zn incorporated a Si

atom in the chromophore and are more red-shifted than other rhodamine-based indicators with the excitation and emission maxima at 650 nm and 665 nm, respectively. The indicator is useful in intracellular Zn^{2+} detection with a nanomolar affinity and a dynamic range of 15. ZIGIR is a red Zn^{2+} indicator that is a sensitive (a dynamic range >100), cell-permeable, and granule-specific.

1.4.3 Genetically encoded Zn^{2+} biosensors

As previously described, most intracellular Zn^{2+} is bound to proteins or nucleic acids. The abundance of Zn^{2+} binding proteins allows us find suitable candidates for making genetically encoded zinc indicators (GEZIs). They include the CXXC-motif-containing metal binding domains Atox1/WD4 for CALWY family, yeast transcription factor Zap1 for Zap family, and yeast transcription factor Zif268 for Zif family.

Most of Zn^{2+} biosensors are FRET based. ZifCY2 with ECFP and mCitrine shows a dynamic range of 4.0 but is limited by a millimolar affinity[79]. Atox1/WD4 Zn^{2+} binding pair provides a stronger affinity: eCALWYs with Cerulean and Citrine exhibit affinities range from nanomolar to picomolar[80]. Zap indicators also exhibit strong Zn^{2+} affinity: ZapCY1 with ECFP and mCitrine shows a 3-fold fluorescence increase upon Zn^{2+} binding with a K_d of 2.5 pM; ZapCY2 shows a larger K_d of 810 pM and a smaller dynamic range of 1.5 (Ref. 81). There are different colour combinations for the FRET pairs: CFP/YFP pair, GFP/RFP pair, and OFP/RFP pair. In comparison to CFP/YFP pairs, other colour variants of Zap indicator show limited dynamics ranges upon Zn^{2+} binding: 1.1 for ZapSM2 with tSapphire and mKO, 1.2 for ZapSR2 with tSapphire and tagRFP, 1.1 for ZapOC2 with mOrange2 and mCherry, 1.1 for ZapOK2 with mOrange2 and mKate, and 1.5 for ZapCmR1.1 with Clover and mRuby2 (Ref. 82).

ZinCh and eZinCh indicators use a different approach. ZinCh-1 consisted of a Cerulean and Citrine pair with double mutations of Y39H and S208C on both Cerulean and Citrine[83]. The

histidine and cysteine form a Zn^{2+} binding pocket, leading to two binding sites on the FRET pair. After optimization with the sites for cysteine and histidine, eZinCh-2 was identified with 4-fold dynamic range and a K_d of 1 nM[84]. It contains a cysteine on position 208 and a histidine on position 206. Although it also binds Pb and Cd, eZinCh-2 is a useful intracellular GEZI that works in the cytosol, the ER, the mitochondria, and the vesicles.

Chen and coworkers developed single FP base GEZI with multiple designs[65,85]. The designs utilize either Zap1 or a zinc hook as the binding domain. *Pyrococcus furiosus* Rad50 zinc hook peptide undergoes homodimerization upon Zn^{2+} binding. The single FPs utilized include GFP, mApple, and mTFP in either cp or ncp form. ZnGreen1 is a GEZI consisted of a ncp-mTFP and Zap1 (Ref. 85). It shows superior performance than previous FRET-based GEZIs with a dynamic range as large as 26.3 and a K_d of 633 pM. ZnGreen2 with cpmTFP and two zinc hooks displays a K_d of 20 μM and a dynamic range of 8.7 (Ref. 85). ZnGreen1 and ZnGreen2 are both inverse indicators with a poor photostability possibly due to mTFP. To address this issue, Chen and coworkers replaced cpmTFP and ncp-mTFP with cpEGFP and ncp-GFP to create ZIGB2 and ZiGB1, respectively[65]. ZIGB1 and ZIGB2 both give positive response to Zn^{2+} binding. ZIGB1 has a dynamic range of 2.5 and a K_d of 2.81 μM; ZIGB2 has a dynamic range of 7 and K_d of 282 pM. A red GEZI was also created with mApple and Zap1 with a dynamic range of 3.8 and two K_d values of 166 pM and 20 μM according to the biphasic titration curve.

GZnPs are an alternative single FP-based GEZI series[86–88]. GZnPs incorporate two Zn^{2+} fingers of ZAP1 fused to the ends of cpGFP. The two Zn^{2+} fingers undergo conformational change upon Zn^{2+} binding. GZnP1 has a dynamic range (F_{max}/F_{min}) of 2.2 and a K_d of 34 pM . Engineering efforts on GZnP1 led to GZnP3 with weaker affinity (K_d =1.3 nM) and a larger dynamic range of 11. The reduced affinity is more appropriate for Zn^{2+} released from granules.

1.5 K^+ indicators

1.5.1 The roles of K^+ in cell physiology

Potassium (K^+) is most abundant ion in the intracellular space. Despite its role as an electrolyte for body fluid balance, K^+ also plays a pivotal role in excitable cells such as the ones in the heart and the nervous system[89]. At the resting state, it is sequestered into cells by Na^+/K^+ pump and other transporter actively to maintain a sharp concentration gradient with the intracellular K^+ concentration around 150 mM and the extracellular K^+ concentration around 5 mM. When cells are excited, K^+ effluxes through a variety of voltage-gated K^+ channels to repolarize cells after depolarization. The dynamic of K^+ fluxes, similar to that of Ca^{2+}, is indicative of neuronal and cardiac signal propagation and therefore is a valuable target for imaging in live cells.

1.5.2 Small molecule-based K^+ indicator

Potassium binding benzofuran isophthalate (PBFI) is the earliest small molecule-based K^+ indicator[90]. It is excited by UV light at 350 nm and 344 nm at K^+ unbound and bound forms, respectively. The indicator binds to Na^+ with a K_d of 21 mM and to K^+ with a K_d of 8 mM. Although the indicator is more selective to K^+, better selectivity is required to avoid signal contributed by Na^+, which has an intracellular concentration of 10–40 mM[90]. The low quantum yield of 0.024 and 0.072 at K^+ unbound and bound forms, respectively, led to low brightness. Later, Asante Potassium Green (APG) series show some attractive properties. APG-1 is more red-shifted than PBFI: it excites at 515 nm and emits at 540 nm[91]. APG-1 responds to K^+ with a maximum four-fold change. APG indicators have been applied in permeabilized Jurkat and U937 cells to visualize changes in intracellular K^+ concentration[92]. Recently, Ratiometric Potassium Sensor-1 (RPS-1).was developed by the Chang lab[93]. The dual-fluorophore dye contains a K^+-responsive fluorophore —

Potassium Sensor 525 (PS525) — and a non-responsive Coumarin 343 for internal calibration. The dye displays a maximum fluorescence change of 7-fold and an apparent K_d of 137 mM for intracellular K^+ imaging.

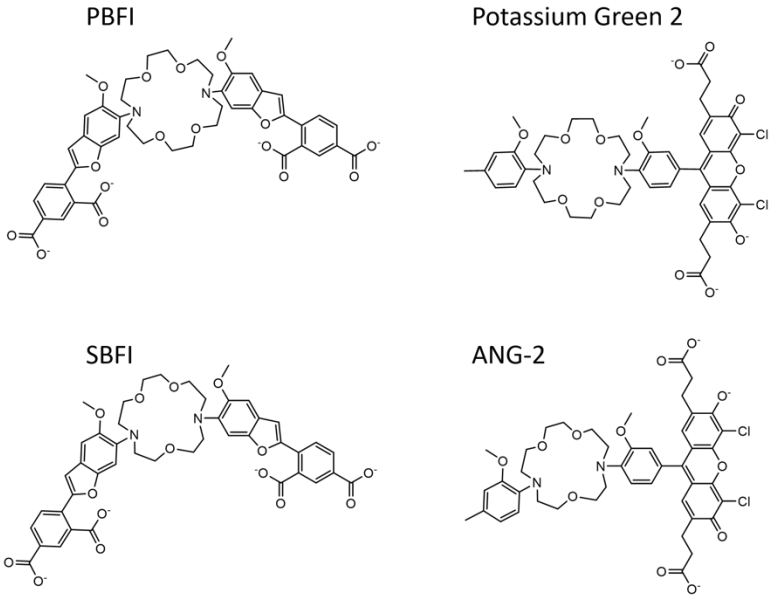

Figure 1.6. Molecular structures of selected small molecule-based K^+ (PBFI and Potassium Green 2) and Na^+ (SBFI and ANG-2) indicators.

1.5.3 Genetically encoded K^+ indicators

With the newly identified K^+ binding protein Kbp, Bischof *et al*. and Shen *et al*. both developed a FRET-based K^+ indicators named Genetically encoded potassium ion indicator (GEPII) and K^+ ion ratiometric indicator (KIRIN), respectively[94,1,95]. The two biosensors show comparable dynamic ranges and affinity: the mCerulean3-cpVenus-based KIRIN has a dynamic range of 1.5 and a K_d of 1.66; and the mseCFP-cpVenus-based GEPII has a dynamic range of 2.2 and a K_d of 0.42. Both FRET biosensors exhibit outstanding selectivity by not responding to Na^+

at all. Shen and coworkers also developed and characterized a green/red FRET K^+ biosensor KIRIN-GR with Clover and mRuby2[1]. KIRIN-GR shows a small dynamic range of 0.2 and a K_d of 2.56 mM. In addition to the FRET biosensors, Shen *et al*. also described a green indicator for K^+ optical imaging (GINKO1) that adopts a ncpEGFP as the fluorescent reporter. GINKO1 exhibits a dynamic range of 1.5 mostly contributed by the change in extinction coefficient. GINKO1 has a K_d of 0.42 mM for K^+ and a K_d of 153 mM for K^+. Although GINKO1 was responsive to Na^+, the discrimination for K^+ was big enough to avoid bias for measurements in biological samples. The work of KIRIN1, GINKO1, and further engineered variants will be described in detail in this thesis.

Genetically encoded K^+ indicators may be more suitable for experiments in complex environments such as tissues. They show superior selectivity than the small molecule-based synthetic dyes and they can also be targeted to subcellular organelles or to a specific cell type. However, the genetically encoded K^+ indicators currently face the challenges for membrane display. This prevents the applications of these indicators on the membrane for detection of transient extracellular K^+ changes during repolarization of neurons and abnormal level of extracellular K^+ concentration associated with many neurological conditions.

1.6 Mg^{2+} indicators

1.6.1 The roles of Mg^{2+} in cell physiology

Mg^{2+} is an essential metal ion that plays many pivotal roles in cellular processes and functions. Mg^{2+} serves as an important cofactor for almost every enzyme that needs ATP for catalysis; stabilizes nucleic acids for DNA and RNA synthesis and repair; and regulates mitochondrial Ca^{2+} transport and voltage gated Ca^{2+} and K^+ channels[96].

Most Mg^{2+} are bound intracellularly: the intracellular concentration of total Mg^{2+} is 17–20 mM and that of free Mg^{2+} is 0.25–1.5 mM[97,98]. Cells maintain a steady-state Mg^{2+} concentration through transporters such as Mrs2p, which transports Mg^{2+} into mitochondria for Mg^{2+} sequestration[99].

1.6.2 Small molecule-based Mg^{2+} indicators

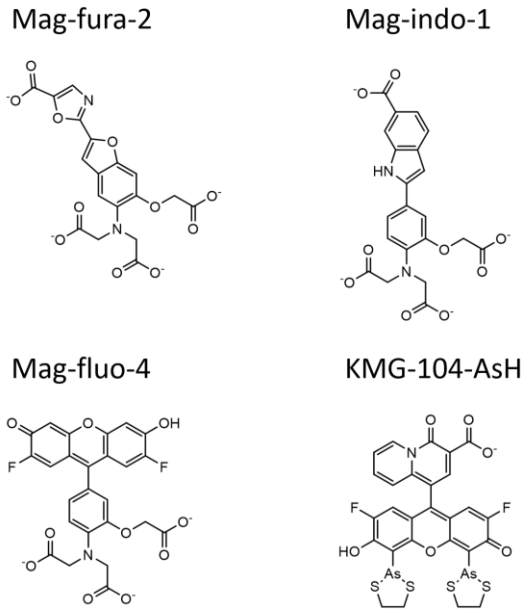

Figure 1.7. Molecular structures of selected small molecule-based Mg^{2+} indicators.

Many small molecule-based Ca^{2+} indicators also display an affinity to Mg^{2+}, therefore, they were made into Mg^{2+} indicators with the binding group *o*-aminophenol-*N*,*N*,*O*-triacetic acid (APTRA). Such examples include Mag-fura-2, Mag-indo-1, and Magnesium Green[100–102]. Mag-fura-2 is excited at 369 nm and Mag-indo-1 is excited at 349 nm[100]. The UV excitation photo-damages the tissue, which led to development of Mg^{2+} indicators excited at longer-wavelength light. The green indicators Magnesium Green and Mag-fluo-4 are excited at 506 nm and 490 nm, respectively[102,103]. The above indicators all have a millimolar affinity to Mg^{2+} and a micromolar

affinity to Ca^{2+}. The lack of Mg^{2+} selectivity over Ca^{2+} was addressed by FMg1 and FMg2, which measure Ca^{2+} and Mg^{2+} simultaneously with two-photon imaging[104].

Other binding motifs were sought to address the lack of Mg^{2+} selectivity over Ca^{2+} by APTRA. One of the motifs is the charged β-diketone. This binding motif is used in the KMG series, most of which have similar K_d values for Mg^{2+} and Ca^{2+}. KMG-104-AsH exhibits an outstanding selectivity with K_d values of 1.7 mM for Mg^{2+} and 100 mM for Ca^{2+} (Ref. 105). KMG-104-AsH is pH stable in the range of pH 5–6.5 and photostable for 10-min illumination. *In situ* experiments showed that KMG-104-AsH is membrane. The affinity, selectivity, stability, and membrane permeability of KMG-104-AsH all suggest it to be a more suitable for Zn^{2+} imaging than APTRA-based indicators.

1.6.3 Genetically encoded Mg^{2+} indicators

The main challenge for developing genetically encoded Mg^{2+} indicators is finding a suitable binding protein, because most Mg^{2+} binding proteins also bind Ca^{2+} with a much higher affinity. The first genetically encoded Mg^{2+} indicators MagFRET series incorporate a binding protein, the human centrin HsCen3, flanked by Cerulean and Citrine[106]. HsCen3 contains two binding sites that bind both Mg^{2+} and Ca^{2+}. MagFRET indicators all show a higher affinity for Ca^{2+} at the first ion binding. Some variants show much less dynamic range for the first ion binding: MagFRET1 has a dynamic range of 0.49 for Mg^{2+} and 0.19 for Ca^{2+}; MagFRET2 has a dynamic range of 0.33 for Mg^{2+} and 0.031 for Ca^{2+}. MagFRET1,2,7, and 8 show a K_d in the physiological range of Mg^{2+}.

MagIC is another ratiometric Mg^{2+} indicator incorporating a mCherry and a Mg^{2+}/Ca^{2+} sensitive cpVenus[27]. K_d values of MagIC are 5.1 mM for Mg^{2+} and 4.8 mM for Ca^{2+}. Its affinity for Mg^{2+} is too low for intracellular Mg^{2+}. The indicator has an *in vitro* dynamic range of 0.5 for

Mg^{2+}, which is similar to that for Ca^{2+}. Just like MagFRETs, the sensitivity of MagIC to Ca^{2+} is the major barrier for the genetically encoded Mg^{2+} indicators to be more widely applied.

MARIO1 is another FRET-based Mg^{2+} indicator incorporating a modified cytosolic Mg^{2+}-sensing domain of the *E. coli* Mg^{2+} transporter CorA (CorA-CD)[107]. Mario1 binds Ca^{2+} (K_d = 6.2 mM) and Mg^{2+} (K_d = 7.2 mM) with similar affinities. The dynamic range R_{max}/R_{min} for Mg^{2+} binding is 2.53.

1.7 Na^+ indicators

1.7.1 The role of Na^+ in cell physiology

As one of the most abundant ions in biology, Na^+ plays many important functions. It regulates osmotic pressure and fluid balance with kidney regulating its blood concentration[108]. Na^+ also play roles in the immune system by enhancing immune responses for pathogen clearance and affecting the differentiation and functions of immune cells[109]. In the nervous system, Na^+ influxes during depolarization phase of action potentials for signal propagation[110].

As a key to some of its functions, Na^+ concentration is around 10 mM intracellularly and over 100 mM extracellularly[111]. The large gradient across the membrane is maintained by Na^+/K^+ pump, which provides energy for the translocation of Ca^{2+} and other neurotransmitters and allows rapid Na^+ influxes in neurons during an action potential. A fluorescent Na^+ probe allows real-time imaging of action potentials. There are several small molecule-based Na^+ indicators developed, but none for genetically encoded indicators so far due to the lack of appropriate Na^+ binding protein.

1.7.2 Small molecule-based Na^+ indicators

Sodium binding benzofuran isophthalate (SBFI) is developed at the same time as PBFI with a good selectivity to Na^+. SBFI has a K_d of 7.4 for Na^+ and a K_d of 166 mM for K^+ (Ref. 90). The indicator provides a dynamic range of 2-fold. The loading of SBFI takes 40 min to 4 hours. A

drawback of SBFI is its low brightness due to its low quantum yield of 0.045 and 0.083 at Na^+ unbound and bound states, respectively. Sodium Green provides an alternative to SBFI with visible light excitation, shorter loading time (30 min), and brighter fluorescence in flow cytometry[112]. CoroNa Green and Asante NaTRIUM Green 2 (ANG-2) are two other green fluorescent dyes. CoroNa Green is excited at 492 nm and emits photons at 516 nm; ANG-2 is slightly red-shifted with excitation and emission maxima at 517 nm and 542 nm, respectively[113–115]. The dynamic range of CoroNa Green is 4 and that of ANG-2 is 20 (Ref. 114).

1.8 pH (H^+) indicators

1.8.1 Importance of pH in cell physiology

Proton (H^+) concentration is measured as pH ($-\log[H^+]$) for convenience. The pH values vary in different cellular compartments: 7.0–7.4 for cytoplasm, 7.2 for ER, 6.4 for Golgi, 5.0 for lysosomes, 5.4 for secretory granule, 6.2 for early endosomes, and 5.3 for late endosomes[116]. The pH values of organelles are maintained mainly by vacuolar H^+-ATPase (V-ATPase), which actively pumps H^+ against its concentration gradient with the energy from ATP[117]. The pH environment is important for the functions of the organelles. For example, the lysosomal low pH is important for the optimal functions of many enzymes in the lysosomes such as lysozyme. In other cases, proton gradient across organelle membrane or plasma membrane is used to provide energy to translocate other molecules, such as neurotransmitters accumulated into synaptic vesicles[118]. In cellular power house mitochondria, proton gradient is the source of energy for ATP synthesis[119]. The ability to measure pH in subcellular compartments of live cells becomes critical to investigate pH-related processes, especially the related channels and transporters.

1.8.2 Small molecule-based pH indicators

Tsien lab developed 2',7'-bis(carboxyethyl)-5,6-carboxyfluorescein (BCECF), the first fluorescent small molecule-based indicator for pH measurement[120]. BCECF has a pK_a at 6.98, ideal for intracellular pH measurement. The dye shows two peaks in the excitation spectrum: 505 nm and ~470 nm. The emission intensity exhibits a three-fold increase from pH 6.4 to pH 7.5. The isosbestic excitation wavelength of BCECF is at 440 nm, where the excitation leads to the pH-independent emission. Seminaphtharhodafluor (SNARF) is an alternative pH indicator with dual excitation and dual emission. SNARF-1, for example, has two excitation peaks in acidic environment at 515 nm and 544 nm; the excitation peak in basic environment is much red shifted at 573 nm[121]. The emission peak also shifts from 583 nm to 631 nm as pH increases. Carboxy SNARF-1 (C.SNARF-1) retains the spectral properties of SNARF-1, while its cell-permeant AM ester acetate aids loading into cells. The emission of SNARF is in the range of yellow to orange, which allows co-imaging with dyes fluoresces in the blue region such as Fura-2 (Ref. 122). SNARF-1 and SNARF-2 both have pK_a values above 7 (7.6 for SNARF-1, 7.5 for SNARF-2). SNARF-4 lowered the pK_a to 6.4 for pH detection in slightly acidic environment[123].

Other small molecule-based pH indicators provide alternatives. 8-Hydroxypyrene-1,3,6-trisulfonic acid (HPTS) is a ratiometric indicator with dual excitation at 405 nm and 450 nm[124]. Unlike BCECF and SNARF, HPTS is not membrane-permeable, therefore requires physical injection for intracellular imaging. The pH indicators pHrodo green and red (Thermo-Fisher) are ideal indicators to image endocytosis because of their low fluorescence signal at neutral pH; the dye is also cell-permeable[125,126].

1.8.3 Genetically encoded pH indicators

The development of genetically encoded pH indicators is largely benefited by the intrinsic pH sensitivity of fluorescent proteins because pH of the environment can influence the protonated state of the chromophore tyrosine, thus induce fluorescence changes. The pH sensitivity of EGFP and EYFP was observed two decades ago. EGFP shows dual excitation at approximately 390 nm and 480 nm and the two peaks changes ratiometrically in response to changes in pH[127]. When excited at 480 nm, EGFP shows an emission increases with pH increase. EYFP is more suitable for intracellular pH sensing than EGFP with its pK_a at 7.1 while that of EGFP is at 6.15 (Ref. 128). Other pH sensitive FPs are also available, such as pHvenus with a pK_a at 7.3 and mNectarine with a pK_a at 6.9 (Refs. 129,130).

Fusing a pH sensitive fluorescent protein to a FRET donor or acceptor leads to a FRET-based pH indicator. FluBpH used EcFbFP, a FMN binding fluorescent protein excited at 380 nm, and YFPs with different pK_a values, Citrine (pK_a at 5.7), EYFP (pK_a at 6.1), and EYFP-H148G (pK_a at 7.5), to generate FRET indicators covers different ranges of pH[131]. The ratio of 570nm (YFP emission) to 495 nm (EcFbFP emission) reflects the pH of the environment. Another FRET-based pH indicator is CFP YFP pH FRET sensor, which is excited at 410 nm and emits at 476 nm (CFP) and 535 nm (YFP)[132]. pHusion is a tandem concatenation of mRFP1 and the pH sensitive EGFP[133].

Engineering on EGFP resulted a variety of green pH indicators. One example is the ratiometric pH sensitive variant E^2GFP (EGFP with F64L/S65T/T203Y/L231H) with a pK_a around 7 (Ref. 134). E^2GFP shows ratiometric excitation and emission: the emission maximum is at 510 nm at low pH and red shift to 523 nm at high pH; the excitation maximum is at 424 nm at low pH and becomes two peaks at 401 nm and 515 nm at high pH. Another engineering work on EGFP

resulted in dual emission deGFPs that have a variety of pK_a values: deGFP1 variant (S65T/H148G/T203C, pK_a ~8.0), deGFP2 (S65T/C48S/H148C, pK_a ~7.2), deGFP3 (S65T/T203C, pK_a ~6.9), and deGFP4 (S65T/C48S/H148C/T203C, pK_a ~7.3)[135]. These different pK_a values are a result of the changes in the chromophore environment due to the mutations. Miesenböck and coworkers developed ratiometric pHluorin and ecliptic pHluorin by mutating key residues identified to affect Tyr66 protonation or excitation spectrum (Gln94, Arg96, His148, Ile167, Thr203, Ser205 and Glu222)[136]. With fixed emission wavelength at 508 nm, ratiometric pHluorin exhibits over a 3-fold excitation ratio (395 nm to 475 nm) change in the pH ranges from 5.5 to 7.5. Ecliptic pHluorin exhibits a remarkable 50-fold emission change in the pH range from 5.5 to 7.5. pHluorin2 improved upon ratiometric pHluorin with codon optimized for mammalian expression and F64L for better folding[137]. The modifications led to a substantially brighter pH indicator in the mammalian system with similar spectral properties. Similarly, superecliptic pHluorin introduced two mutations (F64L and S65T) on ecliptic pHluorin for better folding and brightness required for neuronal imaging[138].

Beside EGFP, other fluorescent proteins were utilized to generate a palette of pH indicators of different colours. pHRed is a red pH indicator based on mKeima with dual excitation at 440 nm and 585 nm[139]. pHRed has a pK_a of 6.5 and a dynamic range over 10. pHTomato is another red pH indicator resembles excitation and emission maxima (λ_{ex} = 550 nm, λ_{em} = 580 nm) of Tomato of mFruit series[140]. The indicator is originated from mRFP and mStrawberry with six mutations (F41T, F83L, S182K, I194K, V195T and G196D) relative to mStrawberry. It has a higher pK_a at 7.8 and a dynamic range over 2 in the pH range of 7.5 to 9.8. Based on mOrange, pHoran1–4 exhibits pK_a values of 6.7, 7.0, 7.4, and 7.5, respectively[141]. pHoran 4 shows a dynamic range of 17 and outstanding brightness with an extinction coefficient of 83,000 $M^{-1}cm^{-1}$ and quantum yield

of 0.66. pHuji is an mApple-based pH indicator with a dynamic range of 22 in the pH range of 5.5 to 7.5.

1.9 Cl^- indicators

1.9.1 The roles of Cl^- in cell physiology

Chloride (Cl^-) is an important anion in biology. It regulates proteins and genes including kinases (e.g., Cl^-dependent GTP-utilizing protein kinase, nucleoside diphosphate kinase (NDPK), and with-no-lysine kinase (WNK)), channels (e.g., Na^+-K^+-2Cl^- cotransporter), and receptors (e.g., glutamate ionotropic receptor kainate (GRIK))[142]. Cl^- in mammalian cells is maintained in a concentration range of 5 to 100 mM by transporters such as potassium chloride cotransporter 2 (KCC2). The serum Cl^- concentration is maintained at 100 mM by kidney. The gradient is used by chloride channels for cellular processes. For example, GABA type A receptor ($GABA_A$) conducts Cl^- upon GABA binding to allow signal propagations[143].

1.9.2 Small molecule-based Cl^- indicators

The small molecule-based chloride (Cl^-) indicators include 6-methoxy-*N*-(3-sulfopropyl) quinolinium (SPQ), *N*-(ethoxycarbonylmethyl)-6-methoxyquinolinium bromide (MQAE), 6-methoxy-*N*-ethylquinolinium iodide (MEQ), and lucigenin. These Cl^- indicators are quenched by Cl^- through collisional quenching. The rate of fluorescence quenching is accelerated by the presence of Cl^-. All of them are long Stoke shift dyes that are excited by UV lights and emits at a wavelength approximately 100 nm apart from the corresponding excitation maximum[144,145]. The sensitivity of the dyes are reflected by the Stern-Volmer constant K_{sv}, which is defined with the following equation where φ_0 is the quantum yield without quencher, φ is the quantum yield, [Cl^-] is the concentration of the quencher, Cl, and extinction coefficient ε is constant[-]:

$$\frac{\emptyset_0}{\emptyset} = 1 + K_{sv}[Cl^-]$$

K_{sv} values are 118 M^{-1}, 145 M^{-1}, 200 M^{-1}, and 390 M^{-1} for SPQ, MEQ, MQAE, and lucigenin, respectively. Lucigenin has the highest φ_0 in addition to the highest K_{sv}[144,145]. When applied in cells, SPQ and MQAE shows severe photobleaching[144,146]. MEQ required an additional modification for cell permeability; 6-methoxy-*N*-ethyl-1,2-dihydroquinoline (diH-MEQ) converts to MEQ after cell entry within 10 min[144]. MEQ is much less prone to photobleaching than MQAE in Swiss 3T3 fibroblasts[147]. Lucigenin, however, is incompatible for intracellular imaging for the reactivity of its 9-position in biological samples[145].

1.9.3 Genetically encoded Cl^- indicators

The genetically encoded Cl^- indicators include Clomeleons, ClopHensor, and other YFP-based indicators. The sensitivity of YFP to Cl^- was first found by Wachter and Remington[148]. YFP decreases its fluorescence by 40% with 150 mM Cl^- at pH 7.0. Cl^- is speculated to binds near chromophore and disfavours the deprotonated form of the chromophore due to charge repulsion. This also leads to elevated pK_a (5.2 without Cl^-, and 7.0 with Cl^-). T203Y is present in all the YFPs tested and is identified as the key mutation for Cl^- binding[148,149]. Since then, YFP has been intensively engineered to generate better Cl^- indicators. H148Q lowers the K_d from 777 mM to 100 mM and increases the response to 50% reduction in fluorescence in presence of Cl^- (Ref. 150). I152L was introduced to reduce the K_d to 85 mM for Cl^- (Ref. 151). A further engineered variant mCl-YFP (EYFP-F46L/Q69K/H148Q/I152L/V163S/S175G/S205V/A206K) has a higher affinity and a lowered pH sensitivity[152]. These Cl^- sensitive FPs also responds to other halides.

Ratiometric Cl^- indicators provide good dynamic range. Kuner and Augustine developed the first ratiometric Cl^- biosensor Clomeleon based on CFP and YFP, where YFP is the only component affected by Cl^- concentration[153]. Clomeleon undergoes a near 80% decrease of F_{527nm}/F_{485nm} ratio in presence of Cl^- *in vitro* and a maximum 2-fold change in hippocampal

neurons. Clomeleon has a K_d of 167 mM for Cl^-, which leads to a low response in more physiological relevant applications. Introducing H148Q, I152L, V163S to Clomeleon led to a K_d of ~30 mM[154]. SuperClomeleon is an improved version with a K_d of 8.1 mM and a dynamic range of 6.9 (Ref. 155). SuperClomeleon was engineered with changes in the linker between CFP and YFP; beneficial mutations such as S30R, Q69T and V163A; and Cerulean replacing CFP.

ClopHensor is a dual biosensor for pH and Cl^- that addresses complications raised by the pH sensitivity of YFP[156]. The sensor is a fusion of pH sensing E^2GFP and DsRed monomer. E^2GFP can be excited at 488 nm for pH dependent Cl^- measurement or 458 nm for pH independent Cl^- measurement. The wavelength of 458 nm is an isosbestic point based on the pH titration of E^2GFP. DsRed is excited at 543 nm with no overlapping signal from E^2GFP. Its signal is affected by neither pH nor Cl^- concentration. Hence, measurements with excitation at 458 nm, 488 nm, and 548 nm allow simultaneous measurement of pH and Cl^-.

Other fluorescent proteins were explored for alternative Cl^- biosensors with some attractive properties. The jellyfish *Phialidium sp* phiYFP was identified as a naturally occurring Cl^- sensitive ratiometric indicator[157]. phiYFP can be excited at 400 nm or 480 nm and emits photon at 540 nm. When excited at 480 nm, the fluorescence of phiYFP decreases modestly as Cl^- concentration increases. When excited at 400 nm, phiYFP shows a maximal 3.5-fold increase of fluorescence with 400 mM Cl^-. This allows phiYFP to be a turn-on indicator. Recently, mNeonGreen was identified as another turn-on Cl^- indicator with a 21-fold dynamic range and a K_d of 9.8 mM[158]. These two alternatives, unlike the other genetically encoded and small molecule-based Cl^- indicators mentioned above, are turn-on indicators, which are less influenced background signals at the apo state.

1.10 Cu^+ indicators

1.10.1 The roles of Cu^+ in cell physiology

Copper is an essential nutrient to human health. It has implications in cardiovascular[159], immune[160], and nervous systems[161]. The element exists in two forms in biology: the monovalent Cu^+ and the divalent Cu^{2+}. The two different oxidation states of copper are exploited by enzymes that catalyze redox reactions (e.g. cytochrome c oxidase and NADH dehydrogenase)[162]. Many of these metalloenzymes are located on the membranes of compartmented organelles in eukaryotic cells. Mitochondria, in particular, contain many copper-dependent enzymes for energy production[163]. Most copper ions are incorporated as cofactors in enzymes, leading to low free Cu^+ concentrations. Excess copper is toxic as free Cu^+ can generate free radicals in cells and destabilize iron-sulfur clusters; therefore, regulated trafficking is required to prevent cell damages[164–166]. Fluorescent copper indicators enable monitoring of free Cu^+ concentration, thus allow us to better understand Cu^+ dynamics and localizations under stimuli or stress.

1.10.2 Small molecule-based Cu^+ indicators

CTAP-1 is the first synthetic fluorescent indicator for Cu^+ with a 4.6-fold enhancement of fluorescence upon Cu^+ binding[167]. The indicator consists of a tetrathiaza crown ether Cu^+ binding motif and a pyrazoline fluorophore. The tetrathiaza crown ether allows specific binding to Cu^+ over other ions including Cu^{2+}, and monovalent ions K^+ and Na^+. The K_d value is 40 nM. The pyrazoline fluorophore enables the UV excitation and the emission at 480 nm. CTAP-1 is membrane permeable and allows the detection of Cu^+ localization in NIH 3T3 cells grown in medium supplemented with Cu^+. CTAP-1 showed aggregation, which was addressed by the improved version, CTAP-2 (Ref. 168). CTAP-2 also presents a dynamic range of 65.

Coppersensor-1 (CS1) is another synthetic Cu^+ indicator with a BODIPY fluorophore and an azatetrathia binding domain[169]. The indicator displays a dynamic range of 10 and excitation and emission maxima of 540 nm and 566 nm, respectively. CS3 is a more sensitive and brighter version with a dynamic range of 75 (Ref. 170). The improvement enabled visualization of Cu^+ concentration at basal and depleted levels and was used to identify Ca^{2+}-dependent Cu^+ redistribution.

Some synthetic Cu^+ indicators were developed for more specific purposes. Mito-CS1 was targeted to mitochondria via a triphenylphosphonium moiety to enable Cu^+ imaging in mitochondria[171]. RCS1 was a ratiometric indicator that enables estimation of Cu^+ in situations with variations in indicator concentration[172]. It has a 20-fold maximum ratio change and emission peaks at 505 nm and 570 nm. ACu1 can be excited two-photons at 750 nm and was used to image Cu^+ in the hippocampal slice at depths ranging from 90 to 220 μm[173]. Cao Cu-3 incorporates a tricarbocyanine scaffold to fluoresce at near infrared[174]. It also provides a maximum 9.6-fold fluorescence change.

1.10.3 Genetically encoded Cu^+ indicators

The apparent Cu^+ affinities of the synthetic Cu^+ indicators range from 10^{-8} to 10^{-14} M and are usually too low for the basal concentration of Cu^+ in the cell. The low Cu^+ affinity was addressed by the genetically encoded Cu^+ indicators.

FRET-based genetically encoded Cu^+ indicators were developed with several different Cu^+ binding moieties. Wegner and coworkers developed Ace1-FRET, Mac1-FRET, and Amt1-FRET[175,176]. Amt1-FRET uses a Cu^+-responsive transcriptional regulator, Amt1, as the binding domain and CFP/YFP as the FRET pair[175]. The indicator has a high affinity ($K_d = 2.5 \times 10^{-18}$ M) that allows visualization fo the tightly controlled Cu^+ availability. Ace1-FRET and Mac1-FRET

was designed with yeast copper regulators Ace1 and Mac1, respectively[176]. The two indicators show opposing responses to Cu^+: Mac1-FRET decreases FRET efficiency upon Cu^+ binding and Ace1-FRET increases FRET efficiency upon Cu^+ binding. Ace1-FRET has a K_d of $4.7 \times 10^{-18} \pm 8.8 \times 10^{-19}$ M and Mac1-FRET has a K_d of $9.7 \times 10^{-20} \pm 1.3 \times 10^{-20}$ M for Cu^+. Zn^{2+} indicator eCALWY was also modified for Cu^+ binding[80,177]. The Zn^{2+} binding domains used in eCALWY are Cu^+ chaperones ATOX1 and WD4, which contains CXXC Zn^{2+} binding motifs[80]. By mutating several Cys to Met in the CXXC motifs, Zn^{2+} binding was abolished while Cu^+ binding was retained[177]. The resulting eCALWY-C2M/C3M shows specific binding to Cu^+ over Zn^{2+} and no binding to Co^{2+}, Cu^{2+}, or Ni^{2+}.

Some Cu^+ binding domains were also used for single FP-based Cu^+ indicators. Amt1 Cu^+ binding moiety was used to develop EGFP-145Amt1 (Ref. 178). The indicator was designed with Amt1 inserted in between residues 145 and 146 of EGFP. YFP-Ace1 used a similar design with Ace1 as the binding moiety and YFP as the reporter[179]. YFP-Ace1 was optimized by adding GGS linkers of different lengths before Asn146 of YFP. The resulting variants were named YAGn where n denotes the number of Gly-Gly-Ser repeats in the linker. YFP-Ace1 and YAG1 are excitation ratiometric at 440 nm and 496 nm. The longer linker abolished the ratiometric change. YFP-Ace1 exhibited the best sensitivity with 38% fluorescence intensity change. The Cu^+ affinity increases with increasing linker length (K_d for YFP-Ace1, YAG1, YAG2, YAG3, and YAG4 are $(8.2 \pm 1.2) \times 10^{-18}$, $(2.0 \pm 0.8) \times 10^{-18}$, $(1.2 \pm 1.0) \times 10^{-18}$, $(4.6 \pm 1.2) \times 10^{-19}$, and $(3.3 \pm 0.9) \times 10^{-19}$).

1.11 Indicators for toxic ions (Pb^{2+}, Cd^{2+}, As^{3+} and Hg^{2+})

Indicators for toxic ions, Pb^{2+}, Cd^{2+}, As^{3+} and Hg^{2+} were also developed to understand the mechanism of their toxicity in cells. Many of these toxic ions can hijack the transporters for

essential ions and thus disrupt their normal functions. Pd^{2+} can be imported through Ca^{2+} channels and *N*-methyl-D-aspartate (NMDA) receptor[180,181]. Pb^{2+} interferes with iron incorporation of hemoglobin and acts as a Ca^{2+} or Zn^{2+}analog to disrupt Ca^{2+}-dependent signalling pathway and Zn^{2+}-dependent activities[182]. Similarly, Cd^{2+} mimics Ca^{2+} and Zn^{2+} to cause detrimental effect on multiple organs[183]. Mercury and mercury compounds are extremely toxic for their reactivity to the thiol group of the amino acid cysteine and thus causes detrimental effect on a variety of key enzymes[184]. Arsenic can react with reduced thiol group to disrupt protein metabolism in general; arsenic in the forms of arsenite and arsenate are particularly toxic to the nervous system and cardiovascular system by disrupting voltage-gated K^+ channels[185]. Small molecule-based and genetically encoded fluorescent indicators are thus valuable tools to investigate the toxicity of these elements. Among these indicators, synthetic fluorescent indicators for Pb^{2+}, Cd^{2+}, and Hg^{2+} have been reviewed previously by Kim and coworkers[186].

SenALiB is a genetically encoded FRET indicator for As^{3+} (Ref. 187). The indicator was designed with an *E. coli* arsenic sensing domain ArsR flanked by CFP and YFP. Further optimized variant SenALiB-676n achieved higher affinity for As^{3+} with a K_d of 0.676×10^{-6} M whereas the K_d of SenALiB is 2.6×10^{-5} M. The indicator exhibited maximum 10% increase in FRET ratio.

Pb^{2+} indicators include leadfluor-1 (LF1) and leadglow and the protein-based Met-lead 1.59 (Ref. 188). LF1 combines a fluorescein-like scaffold and a dicarboxylate pseudocrown binding moiety[189]. The indicator is sensitive with a dynamic range of 18 and selective to Pb^{2+} over Li^+, Na^+, K^+, Mg^{2+}, Ca^{2+}, Mn^{2+}, Fe^{2+}, Co^{2+}, Ni^{2+}, Cu^{2+}, Zn^{2+}, Cd^{2+}, and Hg^{2+}. Leadglow is another sensitive and selective synthetic Pb^{2+} indicator[190]. Because Pb^{2+} usually presents in low concentration in the environment, the practicality of these two indicators are limited by their low affinity to Pb^{2+} (LF1: $K_d = 23 \pm 4$ μM; Leadglow: $K_d = 217$ nM). The genetically encoded Met-

lead 1.59 provide a better alternative for low Pb^{2+} concentration. It is a FRET-based indicator with *Cupriavidus metallidurans* CH34 Pb^{2+} binding protein PbrR flanked by CFP and YFP[191]. The indicator exhibited emission ratios (YFP/CFP) of 3.3-5.7 and two K_d values of 69 nM and 22.081 μM.

Cd^{2+} indicators include small molecule-based Liu Cd-1, Peng Cd-1, and Cheng Cd-1, as well as genetically encoded Cd-FRET. Liu Cd-1 consists of a fluorescein and a thiosemicarbazide, and responds to Cd^{2+} with a maximum 2.5-fold fluorescence intensity change[192]. Peng Cd-1 used BODIPY as the fluorophore and presented ratiometric emission (655 nm in Cd^{2+} free environment and 597 nm in Cd^{2+} rich environment)[193]. Cheng Cd-1 is another BODIPY-based Pb^{2+} indicator with superior sensitivity and affinity[194]. The fluorescence intensity of Cheng Cd-1 is enhanced by maximum 195-fold with linear detection of Cd^{2+} in nanomolar range. Cd-FRET was created by modifying Zn^{2+} indicator ZinCh-9 with a new $(Cys)_4$ metal binding motif at the interface of the FPs[195]. Met-cad 1.57 is another genetically encoded FRET-based Cd^{2+} indicator with a Cd^{2+} binding protein CadR flanked by CFP and YFP[196].

Various Hg^{2+} indicators were developed to detect Hg^{2+}. Among these indicators, Zhao Hg-1 and Lin Hg-1 demonstrated remarkable dynamic ranges of 1200 and 1000, respectively[197,198]. Rhodamine spirolactam-based Zhao Hg-1 is nonfluorescent unless bound to Hg^{2+}, which converts the spirolactam to a ring-open amide form reversibly[197]. Lin Hg-1 used a thiolspirolactam in a similar manner to achieve the high sensitivity[198]. The molecular structural change upon Hg^{2+} binding allows the rhodamine to fluoresce. Zhao Hg-1 and Lin Hg-1 bind Hg^{2+} with K_d values of 4.6×10^{-7} M and 2.5×10^{-5} M, respectively. Compared to these indicators, BODIPY-based 8H-BDP and Mercuryfluor-1 (MF1) bind Hg^{2+} with a stronger affinity (8H-BDP: $K_d = 6.3 \times 10^{-19}$ M; MF1: $K_d = 7.0 \times 10^{-11}$ M) and a lower dynamic range of 27 (Ref. 199).

1.12 Conclusions

The decades of work on monoatomic ion indicators have yielded many useful tools with diverse spectral properties, sensitivity, specificity, affinity, and brightness. In general, a useful indicator displays following properties:

(1) A large dynamic range that allow signal change to be conveniently monitored;

(2) High brightness that enables signal detection at a low concentration of the indicator;

(3) Suitable affinity that is compatible with the compartment where the ligand concentration is being measured;

(4) Fast kinetics that enable the detection of transient changes;

(5) Specific targeting that allows measurement in the specific cell types, cell compartments, or extracellular membrane;

(6) Colour variety that enables multiplex or quantitative measurement.

Criteria for making a successful indicator include **(1)** finding an appropriate ligand binding moiety and a bioluminescent or fluorescent reporter, **(2)** exploring and testing different indicator designs, **(3)** and extensive optimizations. The properties of the ligand binding moiety and the reporter are assessed before initiating an indicator development: The binding moiety provides the binding properties to the ligand of interest, such as affinity, specificity, and Hill coefficient; the bioluminescent or fluorescent reporter provides spectral properties. Availability of new binding moieties can open the door for a new indicator. Potassium binding protein (Kbp) enabled the development of genetically encoded potassium biosensor with a superior selectivity for K^+ over Na^+ (Refs. 1,94,200). Improving existing indicators sometimes involves choosing an alternative ligand binder or reporter. The green fluorescent mNeonGreen, for example, has been used to replace EGFP in Ca^{2+} indicators[52,53] and also used as a single fluorescent protein Cl^- indicator[158].

The brighter mNeonGreen allows an increased maximum brightness for mNeonGreen-based indicators accordingly. The initial development of indicators usually requires multiple designs. The pH indicators SNARFs, for example, were developed with multiple derivatives that exhibit different spectral properties and pK_a values[121]. Creating a new single FP-based indicator usually involves attempts with cp and ncp designs to increase the probability of obtaining a ligand sensitive design. NIR-GECO, for examples, only responds to Ca^{2+} in the ncp form[62]. The initial construct of genetically encoded indicators rarely responds with optimal performance and thus requires further optimizations. The best example is the optimization of GCaMP series that lasted for about two decades. The optimizations include site saturations on identified important sites and directed evolution. The screenings of variants were performed in *E. coli* and later hippocampal neurons. Early GCaMPs evolved in *E. coli* usually show inferior performance in neurons, necessitating screenings in neurons, which led to state-of-the-art GECIs[49].

The future of monoatomic ion indicators largely relies on new binding moieties and fluorescent proteins. For example, new binding moieties for Na^+ is the key to a Na^+ indicator surpasses the currently available ones. The small molecule-based Na^+ indicators are facing a specificity issue for Na^+ over K^+. The lack of appropriate Na^+ binding proteins results in no genetically encoded Na^+ indicators. The potential impact of a specific and sensitive Na^+ indicator can be enormous when used in combination with a Ca^{2+} indicator and/or a K^+ indicator for neuroscience.

1.13 The scope of the thesis

Small molecule-based and genetically encoded ion indicators have enabled imaging of ion dynamics in live cells, which is important to understand the roles of these ions. Fluorescent proteins (FPs) are widely used for the development of genetically encoded ion indicators, such as

GCaMP6s[49], a state-of-the-art Ca^{2+} indicators. In this thesis, I will introduce my work on some new FP-based tools for imaging molecules and activities in lived cells: genetically encoded K^+ indicators, as well as tools for protein-protein interactions (PPIs).

The structure determination of the *E. coli* Kbp[94] opened the door to genetically encoded indicators[1,200]. In this thesis, several genetically encoded K^+ indicators are described.

In Chapter 2, two FRET-based K^+ indicators, KIRIN and KIRIN-GR, and a GFP-based K^+ indicator GINKO1 are developed and demonstrated in the cytosol of live cells. The CFP/YFP-based KIRIN allows ratiometric detection with a dynamic range (R_{max}/R_{min}) of 2.3. The GFP-based GINKO1 is excitation ratiometric with a maximum R_{max}/R_{min} of 3.5. The dynamic range (F_{max}/F_{min}) of GINKO emission is around 2.

The optimizations on GINKO1 was described in Chapter 3. GINKO2a and 2b were developed with crystal structure guided optimizations and ten rounds of directed evolution. GINKO2a and 2b are more sensitive and selective than GINKO1. Their maximum intensiometric changes are around 10 and they do not respond to Na^+ at a concentration up to 150 mM.

Chapter 4 focuses on the efforts on targeting GINKO to the membrane for extracellular K^+ detection. Fzd7 leader peptide was identified for secretion, but the membrane tethered GINKO2a did not respond to K^+ added to the imaging buffer. Post-translational modifications were found irrelevant to the functional loss. Tagging purified GINKO2a to the membrane with the SpyTag-SpyCatcher system led to substantial decrease in the K^+ response, suggesting membrane environment might be partially responsible for the functional loss.

In additional to the K^+ indicators described in Chapter 2–4, FPs for detecting protein-protein interactions were also engineered as described in Chapter 5 and 6. In Chapter 5, I optimized ddFPs for better brightness. In Chapter 6, DipdTFP was engineered to form a heterodimer with

dTomato. The FRET efficiency is remarkably high, but the affinities between the heterodimers and homodimers need to be addressed for this dTomato-DipdTFP pair to become an effective FRET-based ddFPs.

Table 1.1. Spectral properties, affinity, and sensitivity of selective GECIs in presence and absence of Ca^{2+}.

The parameters listed are maximum absorbance wavelength (λ_{abs}), extinction coefficient (ε), maximum emission wavelength (λ_{em}), quantum yield (φ), brightness (the product of ε and φ), dissociation constant (K_d), Hill coefficient (n_H), *in vitro* dynamic range (F_{max}/F_{min}), fluorescence range for single action potential, and acid dissociation constant (pK_a). Some parameters were provided at both Ca^{2+}-free and Ca^{2+}-rich states.

name	Ca^{2+}	λ_{abs} (nm)	ε (M^{-1} cm^{-1})	λ_{em} (nm)	φ	brightness ($mM^{-1}cm^{-1}$)	K_d (nM)	n_H	F_{max}/F_{min}	$\Delta F/F$ for 1 AP	pK_a	References
Flash-pericam	-	403	26800	514	0.04	1.07	700	0.7	8	NR	NR	42
		488	6300	NR	NR	NR						
	+	410	21200	514	0.2	4.24					NR	
		494	16900	NR	NR	NR						
Ratiometric-pericam	-	418	24100	511	0.3	7.23	1700	1.1	10	NR	NR	42
		494	4100	NR	NR	NR						
	+	415	20500	517	0.18	3.69					NR	
		494	10300	NR	NR	NR						
Inverse-pericam	-	503	59000	515	0.64	37.76	200	1	7	NR	NR	42
	+	490	44000	513	0.44	19.36					NR	
G-CaMP	–	409	1100	NR	NR	NR	235	3.3	4.5	NR	8.1	43
		488	570	510	0.03	0.02						
	+	410	690	NR	NR	NR					7.1	
		487	1400	510	0.05	0.07						
G-CaMP1.6	–	404	5800	NR	NR	NR	146	3.8	4.9	NR	8.8	44
		489	1100	510	0.56	0.62						
	+	403	5200	NR	NR	NR					8.2	
		488	3800	509	0.79	3.00						
G-CaMP2	–	400	11100	NR	NR	NR	146	NR	~5	NR	NR	45
		491	5200	511	0.7	3.64						
	+	401	5800	NR	NR	NR					NR	
		487	19000	508	0.93	17.67						
GCaMP3	-	399	36000	NR	NR	NR	405	2.1	12.3	NR	8.4	46
		496	11000	513	0.2	2.20						
	+	399	20000	NR	NR	NR					7.0	
		496	50000	513	0.44	22.00						
GCaMP5A	-	NR	NR	NR	NR	NR	307	2.7	17.4	NR	8.7	48
	+	497	56100	NR	0.65	36.47					6.8	
GCaMP5D	-	NR	NR	NR	NR	NR	730	2.5	22.0	NR	8.9	48
	+	497	25300	NR	0.67	16.95					7.4	

GCaMP5G	-	NR	NR	NR	NR	NR	460	2.5	32.7	NR	9.1	48
	+	497	49300	NR	0.67	33.03					7.0	
G-GECO1.2	-	402	37000	NR	NR	NR	1150	2.1	23.0	NR	10.4	47
		498	2000	513	0.25	0.50						
	+	402	22000	NR	NR	NR					7.2	
		498	33000	513	0.36	11.90						
GEM-GECO1	-	397	34000	511	0.31	10.20	340	2.9	110.0	NR	6.2	47
	+	390	36000	455	0.18	6.50						
GEX-GECO1	-	392	32000	NR	NR	NR	318	2.8	26.0	NR	6.7	47
		482	0	512	0.21	6.70						
	+	390	32000	506	0.19	6.08					6.1	
		482	2500	506	0.39	0.98						
B-GECO0.1	-	378	22000	446	0.02	0.44	164	2.6	7.0	NR	5.0	47
	+	378	23000	446	0.18	4.10					5.6	
GCaMP6s	-	505	2910	NR	NR	NR	144	2.9	63.2	0.23	9.8	49
	+	497	68500	515	0.61	41.79					6.2	
GCaMP6m	-	505	20700	NR	NR	NR	167	3.0	38.1	0.13	8.7	49
	+	497	38200	515	0.61	23.30					6.9	
GCaMP6f	-	505	2800	NR	NR	1.65	375	2.3	51.8	0.19	8.8	49
	+	497	61900	515	0.59	36.52					6.3	
jGCaMP7s	-	NR	5554	NR	0.58	3.22	68	2.5	40.4	0.657	7.7	50
	+	NR	70117	NR	0.65	45.58					6.4	
jGCaMP7f	-	NR	2358	NR	0.47	1.11	174	2.3	30.2	0.316	7.9	50
	+	NR	56028	NR	0.59	33.06					6.5	
jGCaMP7b	-	NR	5668	NR	0.59	3.34	82	3.1	22.1	0.406	7.8	50
	+	NR	56562	NR	0.6	33.94					6.4	
jGCaMP7c	-	NR	1541	NR	0.5	0.77	298	2.4	145.6	0.223	8.7	50
	+	NR	49566	NR	0.59	29.24					6.7	
mNG-GECO1	+	496	102000	513	0.69	70.38	807	NR	45	NR	NR	52
NCaMP7	-	402/406	46600	520	0.048	2.2368	96	2.2	89	NR	5.4/6.6	53
	+	509/512	110000	522	0.52	57.2	NR				6.18	
R-GECO1	-	445	22000	NR	NR	NR	482	2.06	16.0	NR	8.9	47
		577	15000	600	0.06	0.72						
	+	445	9000	NR	NR	NR					6.6	
		561	51000	589	0.2	10.20						
R-GECO1.2	-	564	2800	595	0.16	0.45	1200	2.79	33.0	NR	8.9	56
	+	556	52000	585	0.29	15.10					6.0	
O-GECO1	-	545	1400	570	0.07	0.10	1500	2.06	146.0	NR	9.4	56
	+	543	65000	564	0.22	14.30					6.1	
CAR-GECO1	-	565	2500	620	0.11	0.28	490	2.01	27.0	NR	9.1	56
	+	560	36000	609	0.21	7.60					5.7	
REX-GECO1	-	582	26000	600	0.06	1.60	240	1.8	100.0	NR	6.5	57
	+	480	28000	585	0.23	6.40						
RCaMP1f	-	574	17400	597	0.11	1.91	1900	2.80	12.3	NR	4.6	58
	+	572	58900	592	0.48	28.27					5.3	

RCaMP1h	-	575	18700	602	0.14	2.62	1300	2.50	10.0	NR	3.2/4.7/6.5	58
	+	571	65100	594	0.51	33.20					4.9	
RCaMP2	-	445	28288	NR	NR	NR	69	1.2	4.8	0.09	8.7	59
		576	14200	591	0.11	1.59						
	+	445	16600	NR	NR	NR					6.1	
		563	48100	583	0.23	11.2						
jRCaMP1a	-	~575	33800	~600	NR	NR	214	0.86	3.2	0.15	5.6	60
	+	~570	54100	~595	NR	NR					6.4	
jRCaMP1b	-	~575	25300	~600	NR	NR	712	1.6	7.2	0.09	6.4	60
	+	~570	53400	~595	NR	NR					5.5	
jRGECO1a	-	~580	61800	~600	NR	NR	148	1.9	11.6	0.3	8.6	60
	+	~570	53300	~590	NR	NR					6.3	
K-GECO1	-	568	19000	594	0.12	2.28	165	1.12	12	NR	NR	61
	+	565	61000	590	0.45	27.45					NR	
NIR-GECO1	-	678	62000	704	0.063	3.906	885	1.03	8	0.045	6.03	62
	+	678	20000	704	0.019	0.38					4.68	
NIR-GECO2	-	NR	67000	NR	0.059	3.953	331	0.94	NR	0.16	5.26	63
	+	NR	18000	NR	0.014	0.252					4.85	
NIR-GECO2G	-	NR	74000	NR	0.061	4.514	480	0.78	NR	0.17	5.34	63
	+	NR	21000	NR	0.021	0.441					4.84	

Table 1.2. Physical properties of selected small molecule-based Mg^{2+} indicators.

The parameters listed are maximum absorbance wavelength (λ_{abs}), extinction coefficient (ε), maximum emission wavelength (λ_{em}), and dissociation constant (K_d) for Mg^{2+} and Ca^{2+}. Some parameters were provided at both Mg^{2+}-free and Mg^{2+}-rich states.

name	Mg^{2+}	λ_{abs} (nm)	ε ($M^{-1}cm^{-1}$)	λ_{em} (nm)	K_d for Mg^{2+} (mM)	K_d for Ca^{2+} (μM)	References
mag-fura-2	-	369	22,000	511	1.5	53	201,202
	+	330	24,000	491			
mag-fura-5	-	369	23,000	505	2.3	28	203,204
	+	332	25,000	482			
mag-indo-1	-	349	38,000	480	2.7	35	101
	+	330	33,000	417			
mag-fluo-4	-	490	74,000	NR	4.7	22	103,205
	+	493	75,000	517			
Magnesium Green	-	506	77,000	531	1.0	6	102,103
	+	506	75,000	531			
	+	578	82,000	603			
KMG-104-AsH	-	520	NR	540	1.7	100	105
	+	521	NR	540			

Table 1.3. Physical properties of selected small molecule-based and genetically encoded pH indicators

The parameters listed are maximum absorbance wavelength (λ_{abs}), extinction coefficient (ε), maximum emission wavelength (λ_{em}), quantum yield (φ), isosbestic wavelength (λ_{iso}), dissociation constant (K_d), Hill coefficient (n_H), and *in vitro* dynamic range (F_{max}/F_{min}). Some parameters were provided at both acidic and basic conditions.

name	pH	λ_{abs} (nm)	ε ($M^{-1}cm^{-1}$)	λ_{em} (nm)	φ	λ_{iso} (nm)	pK_a	n_H	F_{max}/F_{min}	References
Small molecule-based pH indicators										
BCECF	acidic	470	NR	NR	NR	440	6.98	NR	NR	[120]
		505	NR	535	NR					
	basic	470	NR	NR	NR					
		505	NR	520	NR					
SNARF-1	acidic	515	17700	583	0.03	521	7.62	NR	NR	[121]
		544	21600							
	basic	573	44100	631	0.09					
SNARF-2	acidic	518	20500	584	0.03	530	7.43, 7.50	NR	NR	[121]
		550	24400							
	basic	576	46400	633	0.16					
C.SNARF-1	acidic	518	23200	585	0.047	534	7.6	NR	NR	[121]
		548	25700							
	basic	575	44900	637	0.09					
C.SNARF-2	acidic	516	26200	585	0.02	524	7.70, 7.78	NR	NR	[121]
		550	29800							
	basic	577	51500	635	0.11					
Genetically encoded pH indicators										
EGFP	/	480	NR	510	NR	NR	6.15	0.7	NR	[127]
EYFP	/	514	NR	527	NR	NR	7.1	1.1	NR	[128]
mNecterine	/	558	NR	578	NR	NR	6.9	0.78	NR	[130]
E^2GFP	acidic	424	31560	510	0.22	NR	7	NR	NR	[134]
	basic	401	28180	523	0.91					
		515	22400	527	NR					
dEGFP1	acidic	400	28700	NR	NR	NR	8.02	NR	NR	[135]
	basic	504	54800	516	0.49					
dEGFP2	acidic	398	21700	NR	NR	NR	7.25	NR	NR	[135]
	basic	496	38200	517	0.55					
dEGFP3	acidic	396	26700	NR	NR	NR	6.86	NR	NR	[135]
	basic	508	45900	518	0.57					

dEGFP4	acidic	400	26900	NR	NR	NR	7.37	NR	NR	[135]
	basic	509	50800	518	0.27					
r-pHluorin	/	395	NR	508	NR	NR	NR	NR	3 (pH 5.5–7.5)	[136]
	/	475	NR							
e-pHluorin	/	395	NR	508	NR	NR	NR	NR	6 (pH 6–7.5)	[136]
pHRed	/	440	NR	610	NR	NR	6.5	NR	>10	[139]
pHTomato	/	550	NR	580	NR	NR	7.8	NR	>3 (pH 7.5–9.8)	[140]
pHuji	/	556	NR	598	NR	NR	7.7	NR	22 (pH 5.5–7.5)	[141]
SE-pHluorin	/	495	NR	512	NR	NR	7.2	1.90	50 (pH 5.5–7.5)	[138,141]
pHoran1	/	547	NR	564	NR	NR	6.7	0.87	10 (pH 5.5–7.5)	[141]
pHoran2	/	549	NR	563	NR	NR	7.0	0.89	12 (pH 5.5–7.5)	[141]
pHoran3	/	551	NR	566	NR	NR	7.4	0.87	15 (pH 5.5–7.5)	[141]
pHoran4	/	547	NR	561	NR	NR	7.5	0.92	17 (pH 5.5–7.5)	[141]

Table 1.4. Physical properties of genetically encoded Cl^- indicators.

The parameters listed are maximum absorbance wavelength (λ_{abs}), extinction coefficient (ε), maximum emission wavelength (λ_{em}), quantum yield (φ), brightness (the product of ε and φ), dissociation constant (K_d), Hill coefficient (n_H), *in vitro* dynamic range (F_{max}/F_{min}), and acid dissociation constant (pK_a). Some parameters were provided at both Cl^--free and Cl^--rich states.

name	Cl^-	λ_{abs} (nm)	ε ($M^{-1}cm^{-1}$)	λ_{em} (nm)	φ	brightness ($mM^{-1}cm^{-1}$)	K_d (mM)	n_H	F_{max}/F_{min}	pK_a	References
mNeonGreen	-	400	NR	NR	NR	NR	9.8	0.72	21	5.7	158
		505	10021	520	0.18	1.80					
	+	400	NR	NR	NR	NR				4.7	
		505	26884	520	0.4	10.75					
YFP	/	514	NR	527	NR	NR	777	NR	1.6	NR	148
Clomeleon	/	NR	NR	NR	NR	NR	167	NR	4.9	NR	153
SuperClomeleon	/	NR	NR	NR	NR	NR	8.1	NR	6.9	NR	155
YFP-H148Q	/	NR	71000	NR	0.59	NR	100	NR	2	6.7	150
YFP-H148Q/I152L	/	NR	52200	NR	0.6	NR	85	NR	2	6.92	151
phi-YFP	-	480	NR	540	0.44	NR	384	0.9	3.5	4.9	157
		400	NR	540	0.02	NR					
	+	480	NR	540	0.49	NR				5.4	
		400	NR	540	0.06	NR					

Chapter 2 Genetically encoded fluorescent indicators for imaging intracellular potassium ions

2.1 Abstract

Potassium ion (K^+) homeostasis and dynamics play critical roles in regulating various biological activities, and the ability to monitor K^+ spatial and temporal dynamics is critical for the understanding of these biological functions. Here we report the development of three genetically encoded indicators for fluorescence imaging of dynamic changes in K^+ concentration. KIRIN1 (potassium (K) ion ratiometric indicator) and KIRIN1-GR are Förster resonance energy transfer (FRET)-based indicators constructed by inserting a bacterial cytosolic K^+ binding protein (Kbp) between the fluorescent protein (FP) FRET pairs, mCerulean3/cp173Venus and Clover/mRuby2, respectively. Changes in FRET efficiency due to binding of K^+ induce emission ratiometric changes ($\Delta R/R_{min}$) of 130% and 20%, respectively. GINKO1 (green indicator of K^+ for optical imaging) is a single fluorescent protein-based K^+ indicator constructed by insertion of Kbp in to EGFP. KIRIN1, KIRIN1-GR, and GINKO1 are suitable for detection of K^+ at physiologically relevant concentrations *in vitro* and are highly selective toward K^+ over Na^+. We demonstrate that KIRIN1 enables imaging of pharmacologically induced depletion of cytosolic K^+ in live cells, and optical tracing of K^+ efflux and reuptake in neurons upon glutamate stimulation in cultured cortical neurons. GINKO1 enabled dual-color imaging of ion concentration changes in neurons, in conjunction with red fluorescent Ca^{2+} indicator K-GECO1. These results demonstrate that KIRIN1 and GINKO1 are useful tools for imaging intracellular K^+ dynamics.

2.2 Introduction

Intracellular and extracellular potassium ion (K^+) concentration affects all aspects of cellular homeostasis, and therefore techniques that enable the visualization of K^+ in biological tissues are of high importance[206]. Normal levels of K^+ concentration (~150 mM for intracellular K^+; ~5 mM for extracellular K^+) are vital for the maintenance of neuronal[207,208], cardiovascular[209], as well as immune system function[210–212]. Abnormal K^+ concentration levels are often associated with disease conditions[213,214]. Measuring K^+ concentration has predominantly relied upon K^+-specific glass capillary electrodes[215]. Although sensitive and accurate, such electrode-based measurements are invasive, time consuming, and low throughput. Electrode-based measurements also provide little to no spatiotemporal information on K^+ dynamics in biological samples. Alternatively, synthetic small molecule-based K^+-sensitive fluorescent dyes have been developed to measure K^+ concentration, but these dyes usually have poor selectivity, as they also bind to Na^+ with similar affinity[90,91]. Although K^+-sensitive dyes with improved selectivity have been reported[216,217], the use of synthetic dyes still involves complications including cumbersome loading and washing steps. In addition, synthetic dyes cannot be targeted to specific cells in a tissue.

Much as genetically encoded calcium ion (Ca^{2+}) indicators have revolutionized the study of cell signalling and Ca^{2+} biology *in vivo*, so to might genetically encoded K^+ indicators revolutionize the study of K^+ homeostasis and dynamics in live cells and *in vivo.* Such indicators would allow accurate measurement of K^+ concentration levels in specific cell types or cellular organelles with spatial and temporal resolution. The key to designing such an indicator is to identify or develop a suitable sensing domain with a high degree of specificity toward K^+ and sufficient levels of conformational change upon binding to K^+. Recently, an *E. coli* K^+ binding

protein (Kbp) was identified and structurally characterized[94]. Kbp is a small (149 residues, 16 kDa) cytoplasmic protein with highly specific K^+ binding properties. Kbp contains two domains: BON (bacterial OsmY and nodulation)[218] at the N-terminus and LysM (lysin motif)[219] at the C-terminus. Importantly, small-angle X-ray scattering (SAXS) structural analysis of Kbp has revealed that the protein exhibits a global conformational change upon K^+ binding[94], bringing BON and LysM closer to each other to stabilize Kbp. This high K^+ specificity and large conformational change are ideal properties for constructing a genetically encoded K^+ indicator.

Genetically encoded indicators are widely used tools for studying biochemical activities in live cells[220,221]. Among these indicators, intramolecular Förster resonance energy transfer (FRET)-based indicators are particularly useful for the detection of binding-induced protein conformational change[222]. The design principle of such indicators is straightforward and well-established: a sensing domain is attached to two fluorescent proteins (FPs) as a single polypeptide chain. Upon analyte binding, the conformational change of the sensing domain affects the FRET efficiency between the attached fluorophores, altering the ratiometric fluorescence emission[223]. FRET ratio change is independent from protein expression level therefore can be useful for quantitative imaging in live cells. However, FRET-based indicators have large fluorescence spectrum width due to the employment of two FPs, which limits their applications in multiplexed imaging experiments. Single FP-based indicators typically utilize the conformational change of the sensing domain to allosterically alter the FP chromophore environment, resulting in an intensiometric change in fluorescence[41]. With narrower spectral profiles, single FP-based indicators are more easily used for multiparameter imaging[47].

The development of FP-based genetically encoded indicators, including for Ca^{2+}, Zn^{2+}, Mg^{2+}, ATP, neurotransmitters, membrane voltage, and various enzyme activities, has opened new

avenues for biological studies and led to numerous new biological insights[79,106,224–230]. However, analogous indicators for monovalent metal cations including sodium (Na^+) and potassium (K^+) ions have been noticeably absent from this toolkit until the recent report of FRET-based K^+ indicators, known as GEPIIs (genetically encoded potassium ion indicators), based on Kbp and mseCFP/cpVenus FRET pair. GEPIIs were successfully used to semi-quantify subcellular K^+ concentration in HeLa cells and visualize K^+ level changes INS-1 cells. Purified GEPII protein was also used to quantitatively assess the K^+ concentration in biological samples *in vitro*[200].

Here we report an independent and parallel effort to engineer and characterize genetically encoded K^+ indicators based on Kbp. We describe both cyan-yellow (KIRIN1) and green-red (KIRIN1-GR) FRET-based K^+ indicators, as well as a single FP-based green fluorescent K^+ indicator (GINKO1). Considering their independent origins, KIRIN1 and GEPII are remarkably similar in terms of design and performance, although a different donor FP was utilized in KIRIN1 versus in GEPIIs. KIRIN1-GR offers spectral distinction with the same FRET design, while GINKO1 represents a new type of K^+ indicator. With these indicators, we imaged intracellular K^+ level in live mammalian cell lines and dissociated neurons as a proof-of-principle demonstration.

2.3 Results

2.3.1 Engineering and characterization of FRET-based K^+ indicators

We designed genetically encoded K^+ indicators by inserting Kbp between a FP FRET pair (**Fig. 1a**). We expected that, upon binding of K^+, the Kbp sensing domain would undergo a conformational change, increasing FRET efficiency between the FP donor and acceptor (**Fig. 1b**). Accordingly, we would observe a ratiometric fluorescence change with donor emission fluorescence decrease and acceptor emission fluorescence increase. We constructed a fusion protein consisting of the cyan FP (CFP) mCerulean3 as the FRET donor[231] and a circularly

permutated variant of yellow FP (YFP), cp173Venus[232], as the FRET acceptor. The donor, mCerulean3, is the brightest CFP currently available[233] with an exceptionally high quantum yield at 0.80. The acceptor, cp173Venus, is a bright FRET acceptor with an orientation factor optimized for a CFP-based donor[232]. mCerulean3 is linked to the N-terminus of Kbp (residues 2–149) and cp173Venus is attached to the C-terminus (**Fig. 2.1a, b**). The resulting construct was designated KIRIN1 (potassium (K) ion ratiometric indicator).

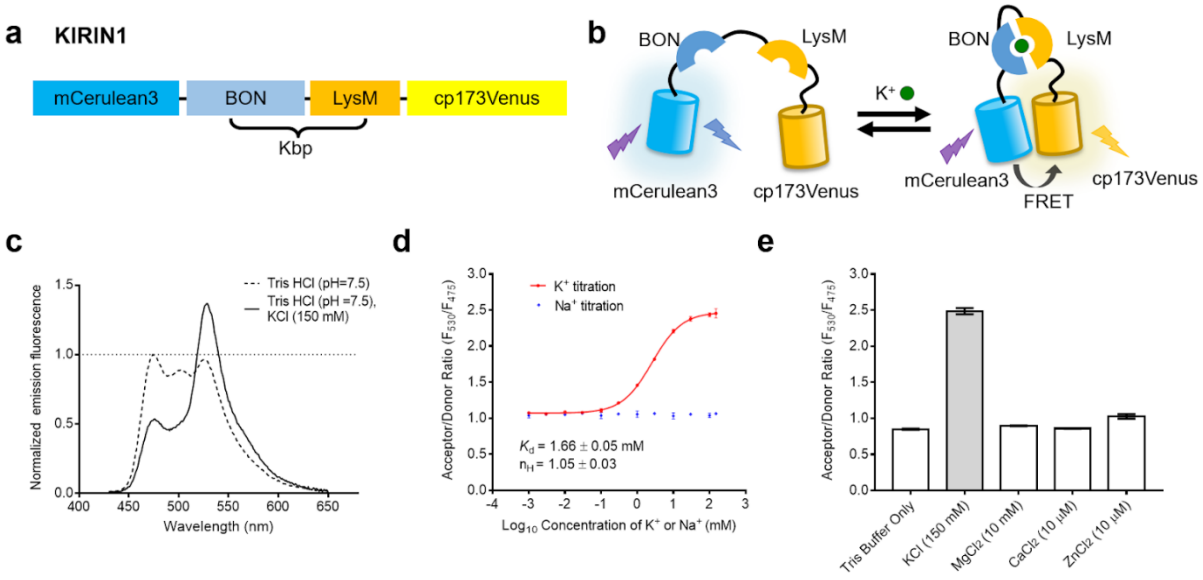

Figure 2.1. Design and *in vitro* characterization of KIRIN1.

(a) Design and construction of the genetically encoded K^+ indicator KIRIN1. mCerulean3 (residues 1–228) at the N-terminus is linked with Kbp (residues 2–149), followed by cp173Venus (full length) at the C-terminus. (b) Schematic demonstration of the molecular sensing mechanism of KIRIN1. Binding of K^+ induces a structural change in the Kbp protein, increasing the FRET efficiency between mCerulean3 and cp173Venus in KIRIN1. (c) KIRIN1 emission fluorescence spectrum (excitation 410 nm, emission 430 nm to 650 nm) in Tris HCl buffer with (red) and without (blue) K^+. (d) FRET acceptor-to-donor fluorescence ratio (F_{530}/F_{475}) of purified KIRIN1 protein at various concentrations (1 μM to 150 mM) of K^+ (red) and Na^+ (blue) solutions. (e) FRET acceptor-

to-donor fluorescence ratio of purified KIRIN1 protein upon addition of various physiologically relevant ions including Mg^{2+} (10 mM), Ca^{2+} (10 μM), and Zn^{2+} (10 μM).

To investigate the potential utility of KIRIN1 as a K^+ indicator, the protein was purified and characterized *in vitro*. To determine the K^+-induced FRET efficiency change, we first measured the emission spectrum (430 nm to 650 nm) of KIRIN1 protein in Tris buffer (**Fig. 2.1c**). Upon the addition of 150 mM K^+, the mCerulean3 emission (~475 nm) decreased by ~50% and cp173Venus (~530 nm) emission increased by ~30%, indicating an increase in FRET efficiency resulting from the K^+-induced structural compaction of Kbp. The maximum FRET acceptor and donor fluorescence emission intensity ratio ($R = F_{530}/F_{475}$) change ($\Delta R/R_{min}$) was 130%, which is comparable to highly optimized CFP-YFP-based FRET indicators[232,234].

To determine the K^+ affinity of KIRIN1, we measured the mCerulean3 and cp173Venus fluorescence emission ratio (F_{530}/F_{475}) in the presence of K^+ concentrations ranging from 1 μM to 150 mM (**Fig. 2.1d**). The indicator showed FRET ratio changes over the range from 0.1 mM to 100 mM K^+, which overlaps the physiologically relevant concentrations. The K^+ titration curve was fitted with a one-site saturation model, yielding an apparent dissociation constant (K_d) of 1.66 ± 0.05 mM and an apparent Hill coefficient (n_H) of 1.05 ± 0.03 (**Fig. 2.1d**). To test the selectivity for K^+ relative to Na^+, we incubated KIRIN1 with Na^+ over the physiological concentration range from 1 μM to 150 mM. The emission ratio remained unchanged upon the addition of concentrations of Na^+ up to 150 mM (**Fig. 2.1d**), indicating that KIRIN1 has an excellent selectivity for K^+ over Na^+. The indicator exhibited no significant FRET ratio change upon the addition of other physiologically relevant ions including Mg^{2+} (10 mM), Ca^{2+} (10 μM), and Zn^{2+} (10 μM) (**Fig. 2.1e**), further confirming the specificity of KIRIN1 for K^+. Kinetics characterization,

using stopped-flow fluorescence, revealed a k_{on} of 28.5 ± 0.8 $mM^{-1}s^{-1}$ and a k_{off} of 105.5 ± 5.3 s^{-1} for K^+ binding to KIRIN1, indicating that KIRIN1 has a rapid kinetic response to changes in K^+ concentration (**Fig. 2.2a**).

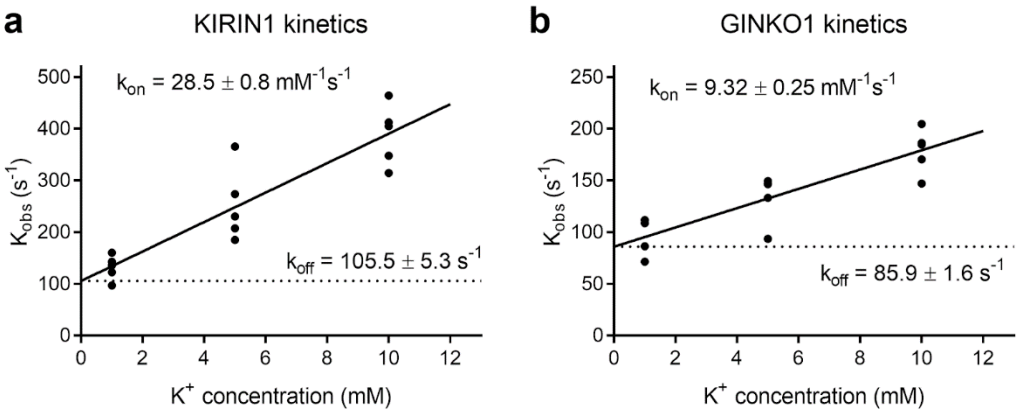

Figure 2.2. Stopped-flow kinetic characterization of genetically encoded K^+ indicators. Observed rate constants (k_{obs}) are plotted as a function of K^+ concentration for (a) KIRIN1 and (b) GINKO1. Rate constants of association and dissociation (k_{on} and k_{off}) were determined by fitting linear regression to the equation $k_{obs} = k_{on}[K^+] + k_{off}$.

In a parallel effort, we constructed a red-shifted FRET-based K^+ indicator using the Clover green FP (GFP) and the mRuby2 red FP (RFP) pair[235] (**Fig. 2.3a, b**). The resulting indicator, KIRIN1-GR (KIRIN1 with GFP and RFP), exhibited a K_d of 2.56 ± 0.01 mM for K^+ binding. Like KIRIN1, it also showed a strict selectivity toward K^+. However, the *in vitro* K^+ binding–induced FRET ratio change ($\Delta R/R_{min}$) was limited to 20%, which is much smaller than the 130% ratio change of KIRIN1 (**Fig. 2.3c, d, e**).

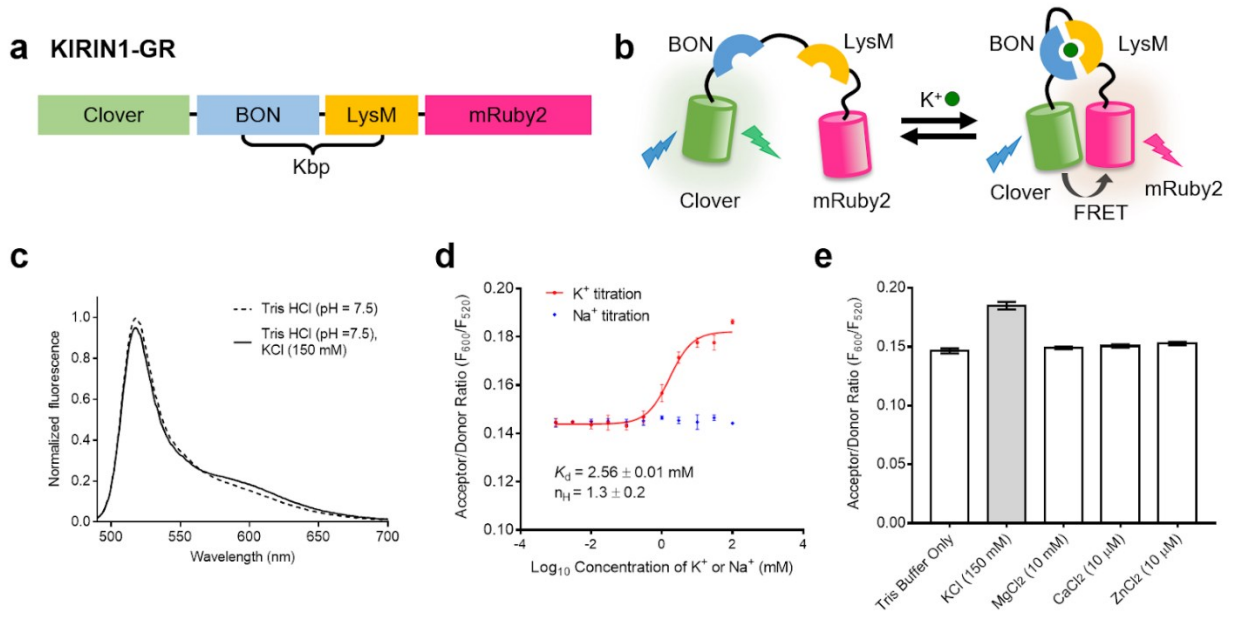

Figure 2.3. Design and *in vitro* characterization of KIRIN1-GR.

(a) Design and construction of the genetically encoded K^+ indicator KIRIN1-GR. (b) Schematic of the molecular-sensing mechanism of KIRIN1-GR. (c) Emission fluorescence spectrum of KIRIN1-GR with (red) and without (blue) K^+. (d) K^+ titration curve (red) and Na^+ titration (blue) of KIRIN1-GR according to FRET acceptor-to-donor fluorescence ratio (F_{600}/F_{520}). (e) FRET acceptor-to-donor fluorescence ratio of the genetically encoded K^+ indicator elicited by adding different physiologically relevant ions including Mg^{2+} (10 mM), Ca^{2+} (10 μM), and Zn^{2+} (10 μM).

2.3.2 Engineering and characterization of a single fluorescent protein-based K^+ indicator

Building upon the development of FRET-based K^+ indicators KIRIN1 and KIRIN1-GR, we sought to engineer a single FP-based K^+ indicator. We first attempted to engineer such an indicator based on a circularly permutated (cp) EGFP scaffold similar to the design of GCaMP[236] series of Ca^{2+} indicators. In this design, the BON and LysM domains of Kbp were split and fused to the N/C termini of cpEGFP respectively. The resulting protein exhibited green fluorescence, but this fluorescence did not change upon addition of K^+, possibly due to a disruption of Kbp protein

function. In order to keep Kbp protein fully intact, we explored an alternate indicator topology and inserted the Kbp domain into the FP. This topology was first used in the camgaroo Ca^{2+} indicator[41] and has recently been used for non-circularly permutated (ncp) Ca^{2+} indicator[237] and glutamate indicators[238]. Insertion of Kbp into the EGFP scaffold of GCaMP6s at residue 144 yielded a functional green fluorescent indicator for K^+ (**Fig. 2.4a, b**), designated as GINKO1 (green indicator of K^+ for optical imaging).

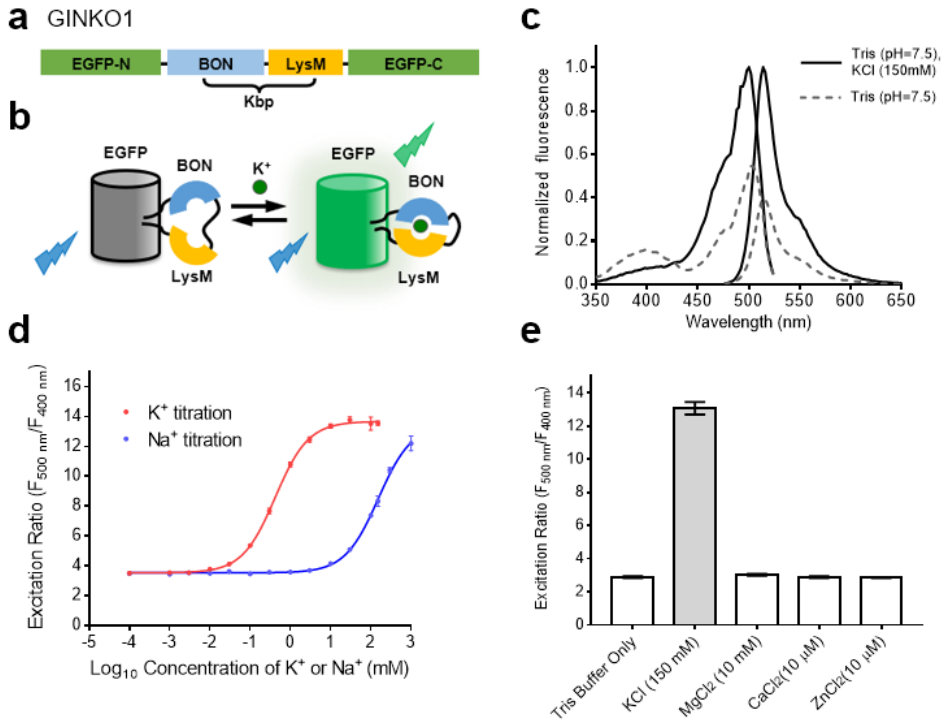

Figure 2.4. Design and *in vitro* characterization of GINKO1.

(a) Design and construction of the genetically encoded K^+ indicator GINKO1. (b) Schematic demonstration of the molecular sensing mechanism. (c) GINKO1 excitation and emission fluorescence spectrum in buffer with (red) and without (blue) K^+. (d) Excitation ratio of purified GINKO1 protein at various concentrations of K^+ (red) and Na^+ (blue) solutions. (e) Excitation fluorescence ratio of purified GINKO1 protein upon addition of various physiologically relevant ions.

To characterize GINKO1, we first measured the fluorescence excitation and emission spectrum of purified GINKO1 in Tris buffer with and without K^+ (**Fig. 2.4c**). Upon the addition of 150 mM K^+, the green fluorescence emission (~515 nm) intensity increased to ~250% of its initial intensity. GINKO1 also exhibited a K^+-dependent excitation ratio change (F_{500}/F_{400}) from 3.5 (without K^+) to 13.5 (with K^+), making it an excitation ratiometric indicator (**Fig. 2.4c, d**). To determine the K^+ affinity of GINKO1, we measured the green fluorescence excitation ratio (F_{500}/F_{400}) over K^+ concentrations ranging from 1 μM to 150 mM (**Fig. 2.4d**). The K^+ titration curve revealed an apparent K_d of 0.42 ± 0.03 mM and apparent Hill coefficient (n_H) of 1.05 ± 0.03 (**Fig. 2.4d**). To test the selectivity for K^+ relative to Na^+, we also titrated Na^+ over the concentration range from 1 μM to 1 M (higher concentrations of Na^+ lead to sensor protein precipitation). GINKO1 fluorescence excitation ratio (F_{500}/F_{400}) changed to 12 upon addition of 1 M Na^+. Fitting of the Na^+ titration curve revealed an apparent K_d of 153 ± 8 mM and an apparent n_H of 1.04 ± 0.05 (**Fig. 2.4d**). The binding affinity for K^+ is over 350 times higher than that for Na^+, indicating that GINKO1 is highly selective towards K^+ over Na^+. GINKO1 exhibited no significant excitation ratio change upon the addition of other ions including Mg^{2+} (10 mM), Ca^{2+} (10 μM), or Zn^{2+} (10 μM) (**Fig. 2.4e**), confirming its K^+ specificity. Stopped-flow kinetic characterization of GINKO1 revealed k_{on} = 9.32 ± 0.25 $mM^{-1}s^{-1}$ and k_{off} = 85.9 ± 1.6 s^{-1} for K^+ binding, similar to the kinetic constants for KIRIN1 (**Fig. 2.2b**)

2.3.3 Imaging of intracellular K^+ depletion in cell lines with KIRIN1

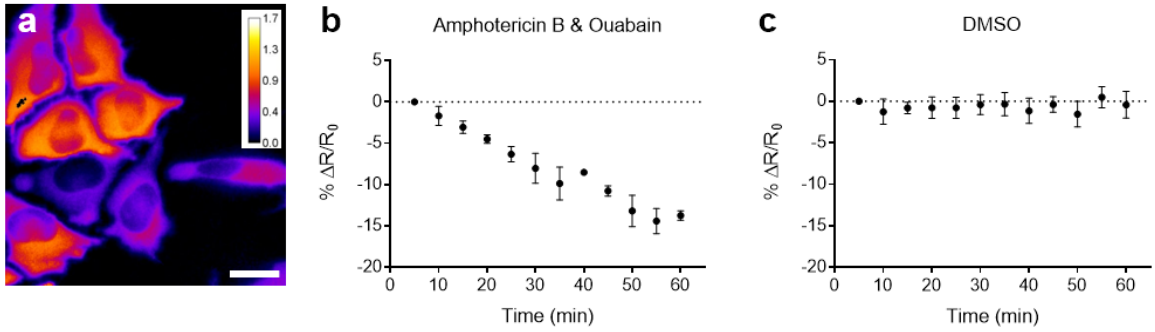

Figure 2.5. Imaging intracellular K^+ depletion using KIRIN1.

(a) Representative FRET acceptor (excitation 438/24 nm, emission 544/24 nm) to donor (excitation 436/20 nm emission 483/32 nm) fluorescence ratio ($R = F_{acceptor}/F_{donor}$) image of live HeLa cells expressing KIRIN1 (scale bar = 20 μm). (b) Trace of FRET acceptor-to-donor fluorescence percentage ratio change ($\Delta R/R_0$) after treatment of live HeLa cells expressing KIRIN1with 5 μM amphotericin B and 10 μM ouabain (n = 7). (c) Trace of FRET acceptor-to-donor fluorescence percentage ratio change ($\Delta R/R_0$) without chemical treatment (n = 13) on live HeLa cells expressing KIRIN1.

The *in vitro* characterization suggested that Kbp-based genetically encoded K^+ indicators are promising candidates for visualization of intracellular K^+ dynamics in live cells. To test the performance of KIRIN1 in cells, immortalized human cervical cancer cells (HeLa) were transfected with the plasmid encoding KIRIN1. Changes in intracellular K^+ concentrations were then induced pharmacologically by Amphotericin B, an antifungal drug that induces K^+ efflux, and ouabain, an inhibitor of sodium-potassium ion pump (Na/K-ATPase). Addition of both amphotericin B and ouabain to HeLa cells has been reported to deplete intracellular K^+ concentration[239,240]. Cells were imaged in both the CFP (excitation 436/20 nm emission 483/32 nm) and FRET (excitation 438/24 nm, emission 544/24 nm) channels, and the FRET ratio image

of KIRIN1 was calculated by dividing the FRET channel image by the CFP channel image (**Fig. 2.5a**). Upon treatment with 5 μM amphotericin B and 10 μM ouabain, the indicator exhibited a gradual decrease of 15% in FRET ratio over a period of ~60 minutes, signaling a decrease of K^+ concentration in the cells (**Fig. 2.5b**). The control experiment using KIRIN1-expressing cells treated with DMSO vehicle revealed no significant change in FRET ratio over the same time period (**Fig. 2.5c**). These findings demonstrate that KIRIN1 is capable of monitoring intracellular K^+ changes across a population of live cells in real time.

2.3.4 Imaging intracellular K^+ dynamics in primary neurons with KIRIN1

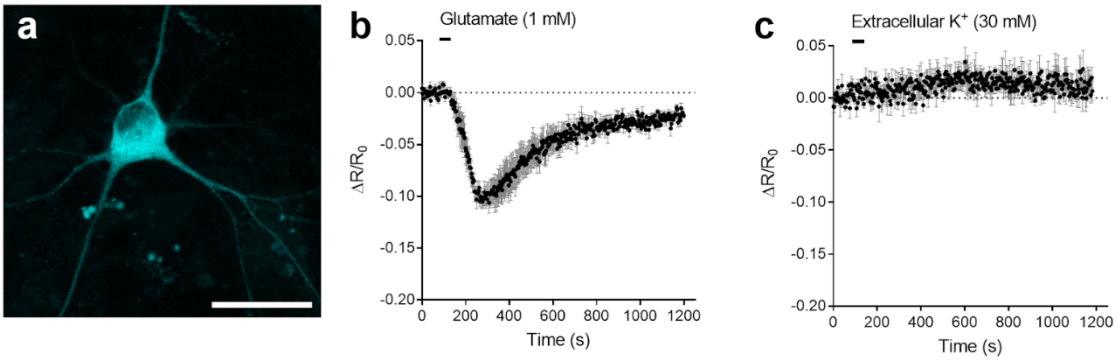

Figure 2.6. Imaging neuronal K^+ dynamics using KIRIN1.

(a) Representative CFP channel fluorescence image of dissociated cortical neuron expressing KIRIN1 (scale bar = 30 μm). (b) FRET acceptor-to-donor fluorescence percentage ratio change time course with the treatment of glutamate (n = 6). (c) FRET acceptor-to-donor fluorescence percentage ratio change time course with treatment with a high concentration of extracellular K^+ (n = 3).

K^+ plays an essential role in maintaining the proper membrane potential of neurons. Neuron activities are associated with K^+ efflux and influx. Repeated activation of neurons can induce larger efflux and influx. We examined whether these changes in intracellular K^+ can be detected optically

using KIRIN1. We utilized primary neurons cultured from the rat cortical region, a well-established neuronal model. KIRIN1 was expressed in neurons via transient transfection, and its fluorescence appeared to distribute evenly throughout the cell, filling the cell bodies and processes (**Fig. 2.6a**). Previous studies[241–245] using electrode-based measurements of extracellular K^+ concentration revealed that activation of ionotropic acetylcholine, A-type γ-aminobutyric acid (GABA) or glutamate receptors, mediates a strong K^+ efflux from neurons, resulting in efflux of intracellular K^+. After perfusion of glutamate (1 mM) for a short period (30 s), neurons expressing KIRIN1 underwent a 10% decrease in FRET ratio within 120 s; after washing out glutamate, the FRET ratio of KIRIN1 returned to baseline after ~600 s, suggesting a slow re-equilibration of intracellular K^+ concentration in neurons (**Fig. 2.6b**). The observed FRET change is consistent with previous measurements using both electrode[242] and synthetic fluorescent dye[91].

To further confirm that the FRET ratio change was due to K^+ concentration changes, rather than other cellular changes associated with neuronal activities, we performed the same set of experiments but replaced glutamate stimulation with high extracellular concentrations of K^+ (30 mM)[246]. This condition depolarizes neurons but does not cause a major K^+ efflux, possibly due to the fact that the K^+ gradient across the membrane is reduced and thus the driving force for outward K^+ current is attenuated[241–245]. Under these conditions, neurons expressing KIRIN1 did not undergo any detectable decrease in FRET ratio (**Fig. 2.6c**), confirming that KIRIN1 FRET changes specifically reflect K^+ dynamics during neuronal activity.

2.3.5 Imaging intracellular K^+ dynamics in primary neurons and glial cells with GINKO1

One of the advantages of single FP-based indicators is that, relative to FRET-based indicators, they can be readily combined with other colours of FP for multiparameter imaging. To explore whether GINKO1 could be used with a red fluorescent Ca^{2+} indicator for imaging of K^+

and Ca^{2+} dynamics in the same cell, we co-expressed GINKO1 and K-GECO1 (Ref. 247) in cultured dissociated cortical neurons (**Fig. 2.7a, b**). Neuronal activity was evoked by a short exposure (30 s) to glutamate (500 μM). Following this treatment, the red fluorescence from K-GECO1 rapidly increased by an average of 188% within 10 s, followed by a gradual decrease back to baseline in 300 s (n = 10) (**Fig. 2.7c,** pink trace). The green fluorescence of GINKO1 followed a relatively slow, but significant decrease of 43% in 120 seconds, and then recovered back to baseline level after 900 s (n = 10) (**Fig. 2.7c,** green trace), consistent with the results from KIRIN1 in neurons with glutamate stimulation.

We further imaged neuronal K^+ and Ca^{2+} changes with stimulation using high extracellular concentrations of K^+ (30 mM). Cultured dissociated cortical neurons were perfused for 60 s with 30 mM extracellular K^+. Following the stimulation, a 28% increase in K-GECO1 red fluorescence was observed due to neuronal depolarization and Ca^{2+} influx (n = 7) (**Fig. 2.7d,** pink trace). In the same cells, GINKO1 green fluorescence exhibited a 9% increase (**Fig. 2.7d,** green trace), indicating a K^+ influx. This K^+ influx was not detected by KIRIN1 under the same experimental conditions, suggesting that GINKO1 is a more sensitive indicator for reporting intracellular K^+ concentration elevation.

Building upon this insight, we continued to explore the K^+ and Ca^{2+} dynamics in (astrocytic) glial cells using GINKO1 and K-GECO1. Compared to neurons, glial cells have relatively hyperpolarized resting membrane potentials and that glia display large and selective K^+ permeability[248,249]. These electrophysiological properties of glial cells contribute to their function in maintaining and regulating extracellular K^+ concentration. Accordingly, an elevated extracellular K^+ concentration should trigger the K^+ uptake by glial cells, leading to an increase in intracellular K^+ concentration[243,244,250,251]. Glial cells expressing both GINKO1 and K-GECO1

were stimulated using 30 mM extracellular K^+ for 60 s. Upon treatment, GINKO1 green fluorescence intensity increased by 53% (n = 4) (**Fig. 2.7e,** green trace), a more substantial increase than the 9% increase observed for identically treated neurons. K-GECO1 red fluorescence showed a slight increase of 4% (n = 4) (**Fig. 2.7d,** pink trace), which is substantially less than the 28% increase in neurons. These results support the notion that glial cells regulates extracellular K^+ homeostasis[252], also revealed a differential response of glial cells versus neurons in handling K^+ and Ca^{2+} under depolarized conditions.

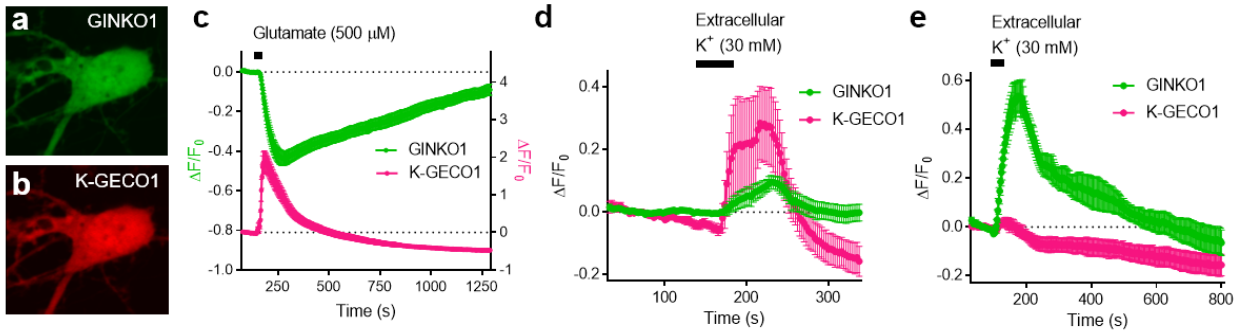

Figure 2.7. Dual-Color imaging of K^+ and Ca^{2+} dynamics in cultured cortical dissociated neurons and glial cells.

(a) Representative GFP channel fluorescence image of dissociated neuron expressing GINKO1. (b) Representative RFP channel fluorescence image of dissociated neuron expressing K-GECO1 (scale bar = 5 μm). (c) Normalized fluorescence intensity change ($\Delta F/F_0$) time course of GINKO1 and K-GECO1 with stimulation (30 s, 500 μM) of glutamate on neurons (n = 10). (d) Normalized fluorescence intensity change ($\Delta F/F_0$) time course of GINKO1 and K-GECO1 with stimulation by a high concentration of extracellular K^+ on neurons (n = 7). (e) Normalized fluorescence intensity change ($\Delta F/F_0$) time course of GINKO1 and K-GECO1 with stimulation by a high concentration of extracellular K^+ on glial cells (n = 4)

2.4 Discussion

We have developed a genetically encoded FRET-based K^+ indicator, KIRIN1, based on bacterial Kbp and the FRET pair of mCerulean3 and cp173Venus. Characterization of KIRIN1 revealed that the FRET efficiency changes over the physiologically relevant range of K^+ concentrations. The dynamic range (based on FRET emission ratio) of KIRIN1 *in vitro* is 230%, comparable to some highly optimized FRET-based ion indicators[40,253,254]. Importantly, KIRIN1 is much more selective for K^+ than Na^+, due to the inherent K^+ selectivity of Kbp[94]. Our findings on KIRIN1 are largely consistent with the similarly designed K^+ indicator, GEPII1.0, which also uses Kbp and the cyan/yellow FRET pair[200]. The main difference between GEPII1.0 and KIRIN1 is the use of mseCFP versus mCerulean3, respectively, as FRET donors. Both indicators use Kbp as a sensing domain and cp173Venus as a FRET acceptor. In addition to KIRIN1, we constructed another K^+ indicator, KIRIN1-GR, based on the green and red FP FRET pair Clover/mRuby2. However, the change in FRET ratio of KIRIN1-GR is substantially smaller than that of KIRIN1, which is likely due to the relatively low quantum yield of mRuby2 (0.38) as FRET acceptor[255] and the absence of a weak dimerization effect, which is present in the CFP/YFP pair[256,257]. Nonetheless, due to its red shifted spectrum and large difference in fluorescence hue between donor and acceptor, the GFP/RFP FRET-based KIRIN1-GR may offer a high signal-to-background ratio with minimal spectral bleed-through. Future efforts to increase the KIRIN1-GR FRET change could be directed at replacing the Clover/mRuby2 FRET pair with brighter GFPs such as mClover3 or mNeonGreen, and brighter RFPs such as mRuby3 or mScarlet[51,235,258]. This work provides further support for the conclusions of Bischof *et al.*[200], that Kbp-based FRET K^+ indicators are well-suited for sensing K^+ *in vitro* and in live cells.

We have also developed a single FP-based green fluorescent K^+ indicator, GINKO1, which utilizes a distinctly different design relative to the FRET-type indicators. By inserting the Kbp domain into a single fluorescent protein (EGFP scaffold), K^+ binding-induced conformational changes of Kbp and modulated the FP fluorescence. This fluorescence intensity modulation is most likely associated with alteration of the equilibrium between the protonated and deprotonated forms of the EGFP chromophore[259]. This design enables the detection of K^+ dynamics based on single emission wavelength fluorescence intensity changes. Characterization of GINKO1 revealed that it has 2.5-fold fluorescent intensity change (F_{max}/F_{min}) upon K^+ binding. Single-FP based indicators offer various advantages over their FRET-based counterparts. Specifically, they can more easily be used for simultaneous multiparameter imaging with minimal spectral bleed-through. In addition, single FP-based indicators have the potential to be engineered for larger intensity-based fluorescence changes, as suggested by the development and optimization of the GCaMP series of Ca^{2+} indicators[46,48,49]. Beyond these typical advantages of single FP-based indicators, GINKO1 is also excitation ratiometric. With approximately 4-fold K^+-binding induced excitation ratio change (R_{max}/R_{min}), GINKO1 can also be used for ratiometric imaging. Ratiometric imaging is preferable for quantitative imaging enables experimental correction for intensity differences that are due to variability in protein expression levels. For these reasons, GINKO1, with further engineered variants, could ultimately serve as a more versatile tool for K^+ imaging, compared with its FRET-based counterpart KIRIN1.

Single FP-based GINKO1, FRET-based KIRIN1, and the previously reported FRET-based GEPIIs[33], are indicators with large dynamic range and high specificity, making them promising probes for K^+ imaging. Our imaging experiments in cell lines and dissociated neurons have demonstrated that both KIRIN1 and GINKO1 are useful for imaging K^+ dynamics intracellularly.

The advent of Kbp-based K^+ biosensors will open new avenues for investigation of cellular signaling associated with normal or abnormal K^+ dynamics. As they are genetically encoded, these indicators are compatible with *in vivo* expression in animal models (either with viral vectors or through transgenic technology). Important application areas include imaging of neuronal activity, cardiovascular activity, and innate immunity activation, at the single-cell level or across large cell populations, and ultimately achieving a deeper understanding of the role of K^+ dynamics *in vivo*.

2.5 Methods

Plasmid DNA construction

DNA encoding KIRIN1 was synthesized and cloned into the pET28a+ expression vector by GenScripts. For KIRIN1-GR, the Kbp sequence was synthesized by Integrated DNA Technologies (IDT) as a double-stranded DNA fragment; DNA encoding Clover and mRuby2 was obtained from Addgene (plasmid #49089). For GINKO1, the DNA sequence was synthesized by Integrated DNA Technologies (IDT) as a double-stranded DNA fragment. DNA fragments were PCR amplified using Phusion polymerase and then cloned into the pBAD/His-B expression vector (Thermo Fisher Scientific) using Gibson assembly (New England Biolabs). KIRIN1, KIRIN1-GR, and GINKO1 genes were PCR amplified, digested, and ligated into the mammalian expression vector pcDNA3.1 (Thermo Fisher Scientific). pcDNA 3.1-NES-KIRIN1 was constructed by PCR with the primer containing the nuclear exclusion signal (NES) encoding the sequence (LALKLAGLDIGS). All constructs were verified by DNA sequencing.

In vitro characterization

The indicator proteins were expressed as His-tagged recombinant proteins in *E. coli*, with an induction temperature of 30°C overnight. Bacteria were centrifuged at 10,000 rpm, 4°C for 10 min, resuspended in Tris-Cl buffer (20 mM Tris at pH 7.4), lysed using sonication, and then

clarified at 14,000 rpm for 30 min. The protein was purified from the supernatant by Ni-NTA affinity chromatography (McLab) according to the manufacturer's instructions: supernatant was loaded onto the column prepared with 2-4 mL Ni-NTA beads, washed with approximately with 15 mL wash buffer (50 mM Tris, 300 mM NaCl, 20 mM imidazole), and eluted with the elution buffer (50 mM Tris, 300 mM NaCl, 300 mM imidazole). The eluted samples were buffer exchanged using a PD-10 (GE Healthcare Life Sciences) desalting column to a K^+ and Na^+ free buffer according to the manufacturer's instructions. For K^+ K_d determination, purified protein was diluted into a series of buffers with K^+ concentration ranging from 0 to 150 mM. The fluorescence spectrum of the KIRIN1 in each solution (100 μL) was measured using a Tecan Safire2 microplate reader with excitation at 410 nm and emission from 430 nm to 650 nm. The fluorescence spectrum of the KIRIN1-GR in each solution (100 μL) was measured using a Biotek microplate reader with excitation at 470 nm and emission from 490 nm to 700 nm. The fluorescence spectrum of the GINKO1 in each solution (100 μL) was measured using a Tecan Safire2 microplate reader. The emission spectra were measured with fixed excitation at 460 nm; the excitation spectra were measured with fixed emission at 540 nm. Titration experiments were performed in triplicate. The FRET ratios for KIRIN1 and KIRIN1-GR or excitation ratios for GINKO1 were plotted as a function of K^+ concentration. Data was analyzed using Graphpad Prism to obtain apparent K_d and the apparent Hill coefficient. Stopped-flow kinetic measurements were performed on SX20 Stopped-Flow Reaction Analyzer (Applied Photophysics). For KIRIN1, the excitation wavelength was 430 nm with 2 nm bandwidth and collected emitted light at 530 nm through a 10 mm path. For GINKO1, the excitation wavelength for was 488 nm with 2 nm bandwidth and collected emitted light at 520 nm through a 10 mm path. A total of 200 data points was collected over 5 replicates throughout the reaction and the fluorescence changes were examined for 250 ms.

Reactions were initiated by mixing equal volumes of diluted purified protein in Tris buffer (100 mM, pH = 7.50) and varying concentrations of KCl (2, 10, and 20 mM) at 20°C. Data was analyzed with Graphpad Prism to obtain the observed rate constant K_{obs} and determine rate constants of association k_{on} and dissociation k_{off}.

Live cell imaging

For mammalian cell line imaging, HeLa or HEK293 cells were maintained in Dulbecco's modified Eagle medium (DMEM) supplemented with 10% fetal bovine serum (FBS, Thermo Fisher Scientific), Penicillin-Streptomycin (Thermo Fisher Scientific), and GlutaMAX (Thermo Fisher Scientific) at 37°C with 5% CO_2. Cells with 60–70% confluence on 35-mm glass-bottom dishes (In Vitro Scientific) were transfected using Polyjet (SignaGen), Turbofect (Thermo Fisher Scientific), or Lipofectamine 2000 (Thermo Fisher Scientific) according to the manufacturer's instructions. Cells were imaged 24 h after transfection. Immediately prior to imaging, medium was replaced with 1 mL of 20 mM HEPES buffered HBSS (HHBSS). Cell imaging was performed with a Zeiss Axiovert 200 microscope with a 40× objective. HeLa or HEK293 cell images were processed using ImageJ.

For imaging of cultured dissociated neurons and (likely astrocytic) glial cells, dissociated E18 Sprague Dawley cortical neurons were grown on 35-mm glass-bottom dishes (In Vitro Scientific) containing NbActiv4 medium (BrainBits LLC) supplemented with 2% FBS and Penicillin-Streptomycin (Thermo Fisher Scientific). Half of the culture medium was replaced every 4–5 days. Neurons were transfected on day 8 using Lipofectamine 2000 (Thermo Fisher Scientific), according to the manufacturer's instructions, with the following modifications. Briefly, 1–2 μg of plasmid DNA and 4 μL of Lipofectamine 2000 (Thermo Fisher Scientific) were added to 100 μl of NbActive4 medium to make the transfection medium. Half of the neuron-glia culture

medium was removed from each neuron dish and combined with an equal volume of fresh NbActiv4 medium to make a 1:1 mixture and incubated at 37°C and 5% CO_2. All dishes were replenished with freshly conditioned (at 37°C and 5% CO_2) NbActiv4 medium. Following the addition of transfection medium, neurons and glial cells were incubated for 2–3 h. The medium was then replaced using the conditioned 1:1 mixture medium. Cells were imaged 36–72 h after transfection. Fluorescence imaging was performed in HHBSS buffer using a Zeiss microscope with a 40× objective or Olympus FV1000 microscope with a 20× objective. Neuron images were processed using Olympus FluoView.

Statistical analysis

All data are expressed as mean ± s.e.m. Sample sizes (n) are listed for each experiment.

Chapter 3 Improved genetically-encodable green fluorescent biosensors for imaging potassium ion

3.1 Abstract

Potassium ion (K^+) plays a central role in electrolyte homeostasis in all biological systems. In mammals, it is particularly critical in activable cells such as neurons, heart cells, and muscle cells. The ability to image potassium ion (K^+) dynamics is essential to understand the related processes under normal or pathological cellular conditions. Genetically encoded fluorescent K^+ biosensors, KIRIN1, GINKO1, and GEPII, were reported to be useful tools to monitor K^+ dynamic in live cells. In this paper, we present improved green fluorescent K^+ biosensors, GINKO2a and GINKO2b, with enhanced sensitivity and specificity. We also tested GINKO2 with proof-of-concept applications in multiple biological systems.

3.2 Introduction

Potassium ion (K^+) is one of the most abundant cations in biological systems. Its involvement has been implicated in a variety of cellular activities in organisms expanding from prokaryotes to multicellular eukaryotes[260–263]. Potassium ion is a target of interest for biomedical research for its roles in the nervous[207,208], the cardiovascular[209], and the immune systems[210–212]. Our ability to study K^+ in biology is limited by the currently available detection tools. Applying synthetic K^+ dyes, such as PBFI[264], often involve multiple steps of loading and washing that can introduce artifacts during an experiment. Electrode-based methods present good sensitivity and selectivity, but lack through-put and subcellular level detection[215]. Genetically encoded fluorescent biosensors, as an alternative method, empower K^+ detection in subcellular level as well as in

targeted cells of a tissue in real-time imaging, and allow the capture of K^+ concentration dynamics with a spatiotemporal resolution and to better understand K^+ related cell activities[1,200].

As a parallel example of powerful cation biosensors, the calcium ion (Ca^{2+}) biosensors, such as GCaMP and GECO series[46–49], have provided numerous opportunities in science. When used in combination with other fluorescent probes[1] or electrophysiology[49], it enables major advances in biological studies, especially the field of neuroscience where Ca^{2+} plays a central role in indicating neuronal activities. Considering the research achievement facilitated by state-of-the-art Ca^{2+} indicators[49,50], we foresee that imaging K^+ can become more practical with a more robust K^+ biosensor in studies across multiple biological disciplines including, but not limited to neuroscience.

In our recent work of K^+ biosensors, we demonstrated that both the FRET-based KIRIN1 and the GFP-based GINKO1 are effective tools for intracellular K^+ detection[1]. GINKO1 is especially of interest due to its single colour that better facilitates multiplex imaging. The biosensor has a F_{max}/F_{min} of 2.5 and a stronger affinity to K^+ (K_d = 0.42 ± 0.03 mM) than Na^+ (K_d = 153 ± 8 mM). In this work, we combined structure-guided engineering and directed evolution to optimize GINKO1 to achieve greater sensitivity and specificity. We apply the second-generation variants, GINKO2a and GINKO2b, in a variety of biological systems to show their advantages.

3.3 Results

3.3.1 The X-ray crystal structure of GINKO1

Protein structures provide valuable information for sensor optimization[48].To pinpoint key sites for improvement, Dr. Yurong Wen, our X-ray crystallographer collaborator, solved the structure of GINKO1 at a resolution of 1.85 Å with X-ray crystallography (**Fig. 3.1c**). The Kbp

region of GINKO1 aligns well with the Kbp NMR solution structure solved previously by Ashraf *et. al*[94]. Interestingly, Ashraf and coworkers had to switch to the NMR due to failed crystal growth for X-ray crystallography, while we managed to obtain crystals of GINKO1 in the buffer supplemented with 150 mM K^+ as illustrated in **Fig. 3.1b**. It suggested that fusing Kbp to EGFP may have increased the stability of Kbp protein.

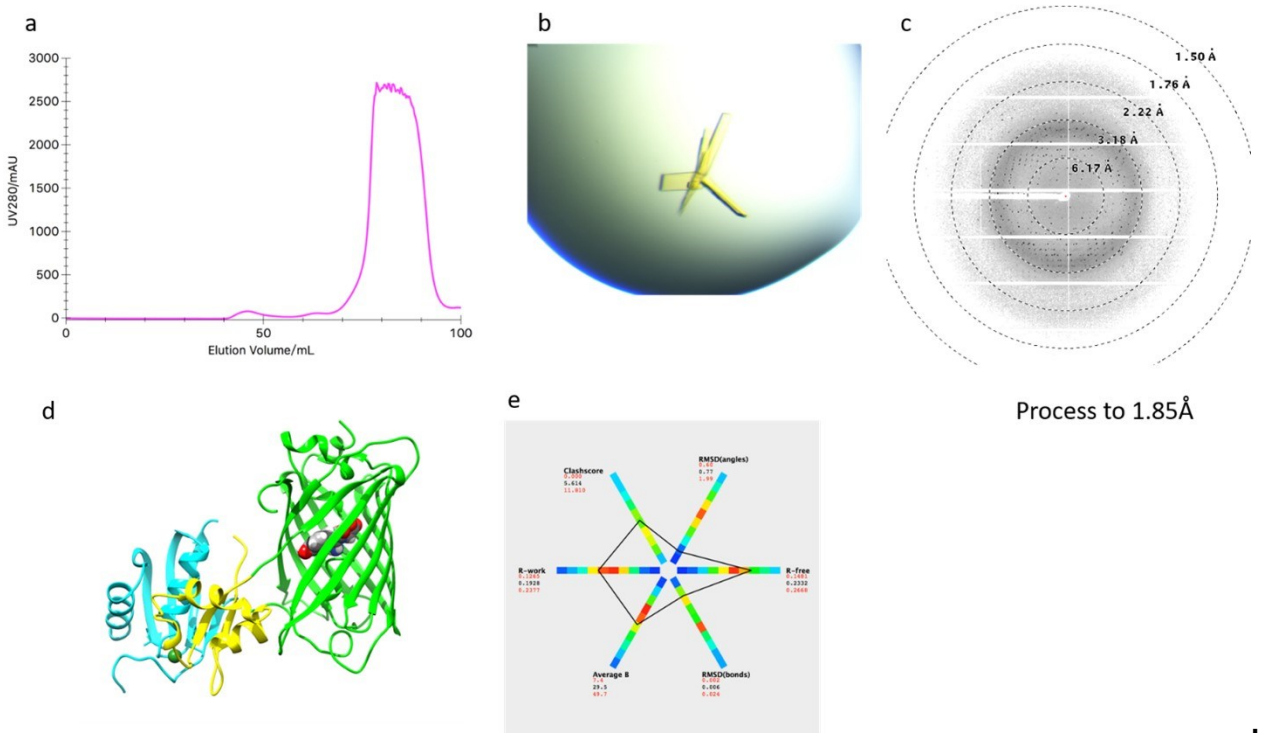

Figure 3.1. Solving the crystal structure of GINKO1.

(a) Size exclusion chromatography was used to confirm monomeric GINKO (b) the image of crystals of GINKO in TBS supplemented with 150 mM KCl (c) The X-ray diffraction pattern of GINKO1 (d) the crystal structure of GINKO1. Domains of GINKO is colour-coded: cyan for BON domain, yellow for LysM domain, and green for EGFP (e) The validation of the GINKO crystal structure represented by a polygon. The six axes are the clash score, RMSD (angles), R-free, RMSD (bonds), average B, and R-work. The red numbers indicate the ranges of selected PBD

entries with a similar resolution, the black numbers indicate the values for the GINKO1 structure, which are also represented by the polygon outlined in black.

Our X-ray crystal structure is the first of such to identify the location of K^+ binding site of Kbp that was missing in the previous NMR structure[94]. The K^+ binding site is in the BON domain and close to the interface of BON and Lys domains. The location of K^+ binding site is consistent with the previous work by Ashraf and coworkers in which the BON domain of Kbp was identified as the K^+ binding domain and the binding affinity is increased by the presence of LysM domain according to the isothermal calorimetry results[94]. In the GINKO1 crystal structure, all six binding residues (Val154, Lys155, Ala157, Gly222, Ile224, and Ile227) are from BON domains and they coordinate the K^+ ion through their backbone carbonyl oxygens, similar to the K^+ coordination modes of K^+ channels which usually adopt octahedral carbonyl coordination instead (**Fig. 3.2a**). The binding pocket is further stabilized by a network of hydrogen bonds through the surrounding residues as well as two water molecules included in the crystal structure (**Fig. 3.2b**). One of the water molecules is 3.08 Å away from the K^+ ion, which suggests it may also be directly involved in K^+ coordination.

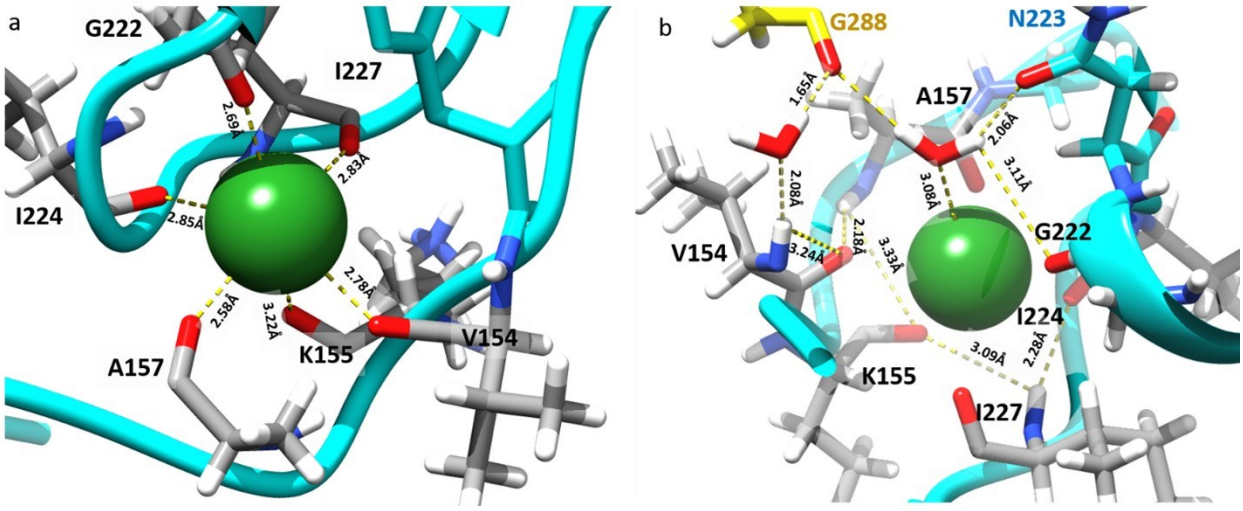

Figure 3.2. K^+ binding site of Kbp was first solved in this work.

The residues from the BON domain is coloured cyan and the ones from the LysM domain is coloured yellow. Potassium ion is represented by a green sphere. (a) The potassium ion is coordinated by carbonyl backbones of six residue shown in sticks with grey carbons (b) The binding pocket is stabilized by a network of hydrogen bonds by surrounding residues and water molecules.

3.3.2 The structure-guided optimization of GINKO1

To look at potential sites for optimization, we aligned the structure of GINKO1 with that of GCaMP6 (**Fig. 3.3a**)[265]. GINKO1 E295 aligns well with GCaMP6 R376 (**Fig. 3.3b**). Both residues are located at the interface of the binding domain and EGFP; and in proximity to the chromophore of EGFP. The residue on this location may be able to alter the sensitivity and brightness of the biosensor by influencing the chromophore environment. We hypothesized that the basic residues at this site can stabilize the anionic form, which is also the brighter state, of the chromophore through the electrostatic interaction. To further explore E295, site-directed mutagenesis was performed to obtain oppositely charged variants E295R and E295K, as well as hydrophobic variants E295W, E295Y, E295P, E295L, and E295F. Characterization of these variants showed that bulky hydrophobic residues like tyrosine and phenylalanine perform better with a dynamic range of 2.9 and 3.0, respectively (**Fig. 3.3c**). E295F was named GINKO1.1 for further improvement (**Fig. 3.5b**). Interestingly, substituting acidic glutamic acid at residue 295 with a basic residue, arginine or lysine, led to variants with only about 60% and 80% of signal change of GINKO1, respectively (**Fig. 3.3c**).

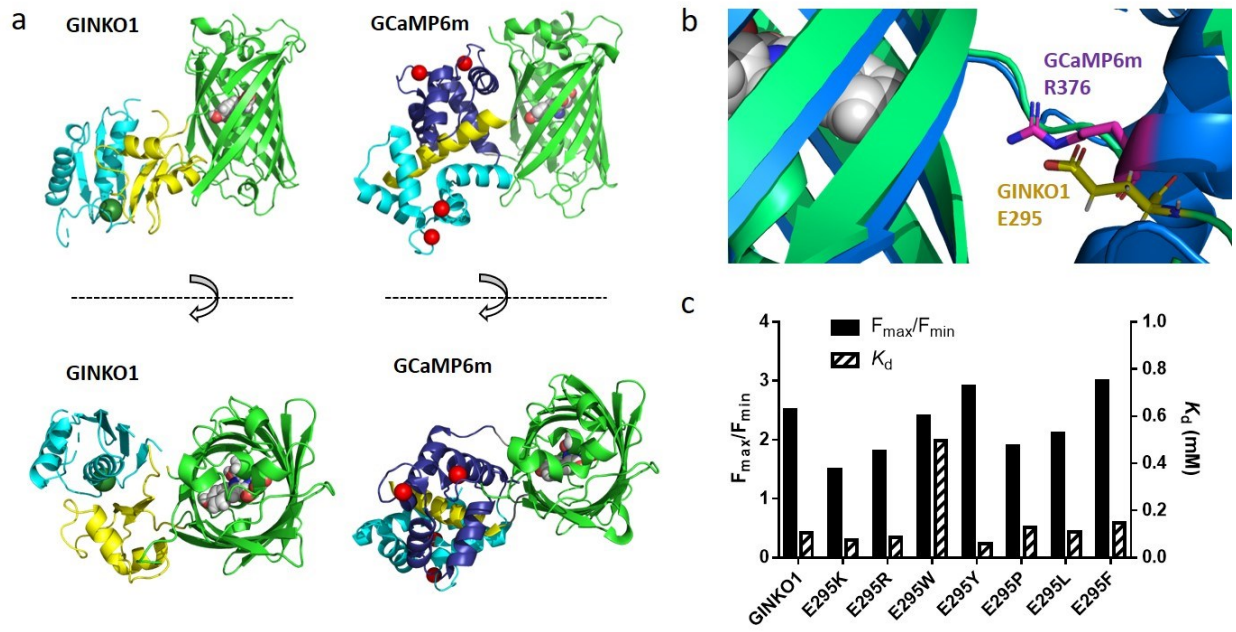

Figure 3.3. Structure-based GINKO optimization.

(a) Crystal structure of GINKO1 and GCaMP6m. Both structures contain a EGFP barrel (green) and a binding domain. (b) Alignment of R376 (magenta sticks) of GCaMP6m (PDB: 3WLC) to E295 (yellow sticks) of GINKO1. GINKO1 is represented by green ribbons and GCaMP6m is represented by blue ribbons. They both point towards the chromophore of the EGFP (in white sphere). (c) Comparison of E295 variants. The bulky hydrophobic residues Y and F lead to a better fold change.

Another observation of the K^+-bound GINKO1 structure is that the linker regions connecting Kbp to EGFP creates grooves that are exposed to the aqueous environment (**Fig. 3.4**). We speculate that a bulky hydrophobic residue at residue 295 fills the grooves and stabilizes the K^+ bound state of GINKO1, leading to a better dynamic range.

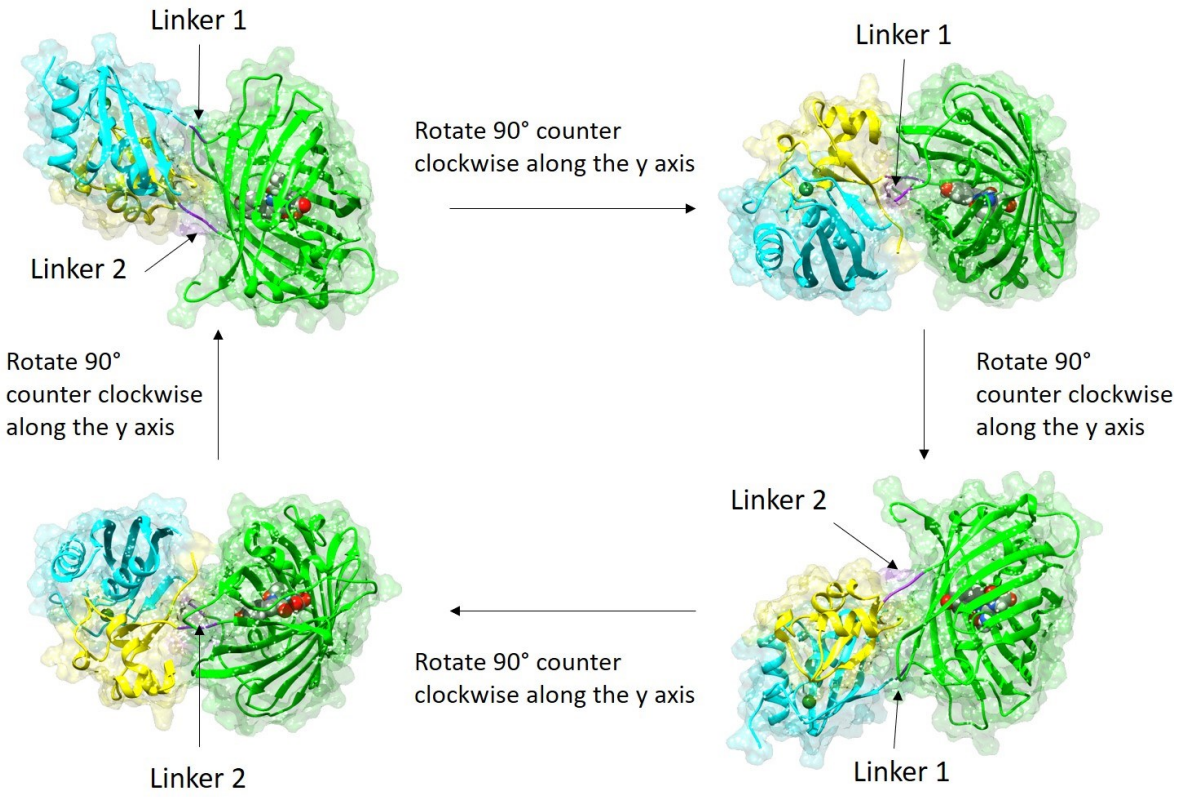

Figure 3.4. The surface representation for GINKO1 shows big grooves in the linker regions.

To rationally improve the linkage between EGFP and Kbp, we randomized the linker regions to screen for better-responding variants. There were no better variants generated by randomizing the first linker LPDG. The second linker library yielded a variant with a linker sequence AAN, which has a 30% improvement in the dynamic range (**Fig. 3.5c**).

3.3.3 Directed evolution of GINKO generated a biosensor with high dynamic range

We then continued optimization with directed evolution in *E. coli* (**Fig. 3.5d**). We generated libraries with random mutations and picked variants with fluorescence intensity that ranges from medium to high from libraries, as *E. coli* cells have a high intracellular K^+ concentration. We extracted the protein through physical freeze and thaw because detergents in the chemical lysis buffer were found to compromise the function of the K^+ biosensor in lysate. We

obtained substantial improvement in dynamic range after 4 rounds of screening, and such improvement plateaued in Rounds 9 and 10 (**Fig. 3.5e**). Finally, we identified two best variants with improved dynamic range and named them GINKO2a and GINKO2b.

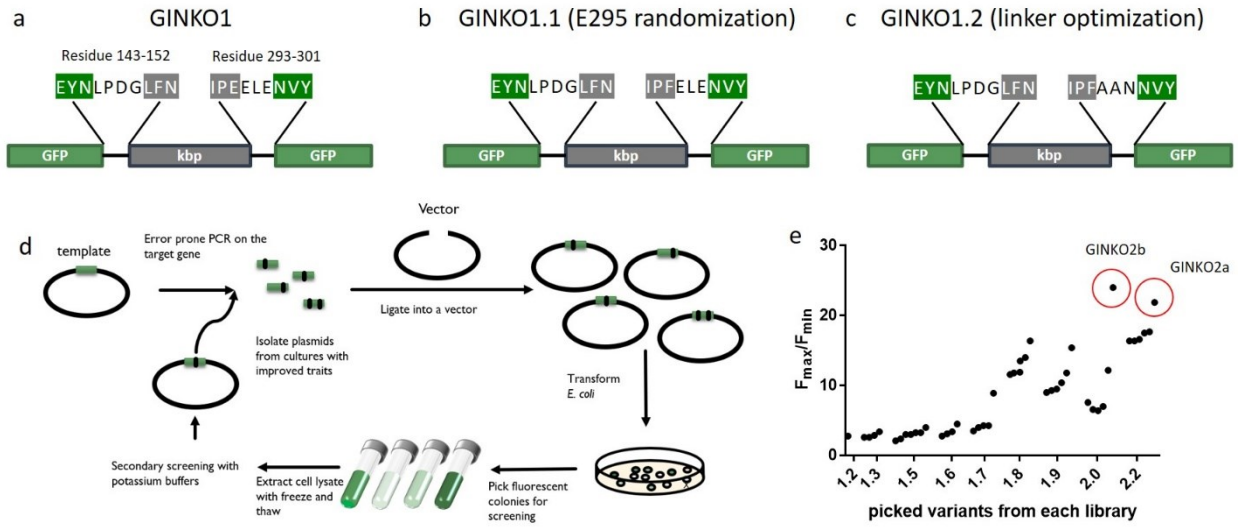

Figure 3.5. Linker optimization and directed evolution.

Sequences of linker regions of (a) GINKO1, (b) GINKO1.1, and (c) GINKO1.2. (d) The optimization on GINKO was performed with directed evolution. The procedure includes error-prone PCR, selecting colonies on plates, and further screening with cell lysate samples. (e) Maximum fold changes of picked variants (~5 per round) after lysate assays show improvement during the rounds of directed evolution. The variants selected for characterization and applications are circled in red.

3.3.4 In vitro characterization of GINKO2 variants showed better dynamic range and specificity

Measurements of quantum yield and extinction coefficient of GINKO variants in K^+ free buffer and the buffer containing 150 mM KCl allowed us to calculate the molecular brightness of the variants in both K^+ free and K^+ saturated states. In K^+ unbound state, GINKO2a and GINKO2b have a low brightness of 1.0 $mM^{-1}cm^{-1}$ and 1.3 $mM^{-1}cm^{-1}$, respectively, in comparison to that of

GINKO1 (4.4 $mM^{-1}cm^{-1}$)[1]. In K^+ bound state, GINKO2a and GINKO2b have a much higher brightness value of 15.5 $mM^{-1}cm^{-1}$ and 11.0 $mM^{-1}cm^{-1}$, respectively, whereas the brightness of GINKO1 is 8.5 $mM^{-1}cm^{-1}$ (Ref. 1). The results suggested that a brighter ligand bound state and a dimmer unbound state both contribute to a greater dynamic range.

Titrations on purified GINKO2a and 2b with K^+ showed consistent results to the brightness measurements in terms of dynamic range and provided more information regarding the ligand affinity and hill coefficient. GINKO2a has a larger dynamic range than GINKO2b (**Fig. 3.6a and Fig. 3.7a**). In terms of affinity, the K_d value of GINKO2b is 9.3 mM for K^+, which is smaller than K_d of GINKO2a (15.3 mM); but both are larger than K_d of GINKO1 which was previously reported as 0.42 mM[1].

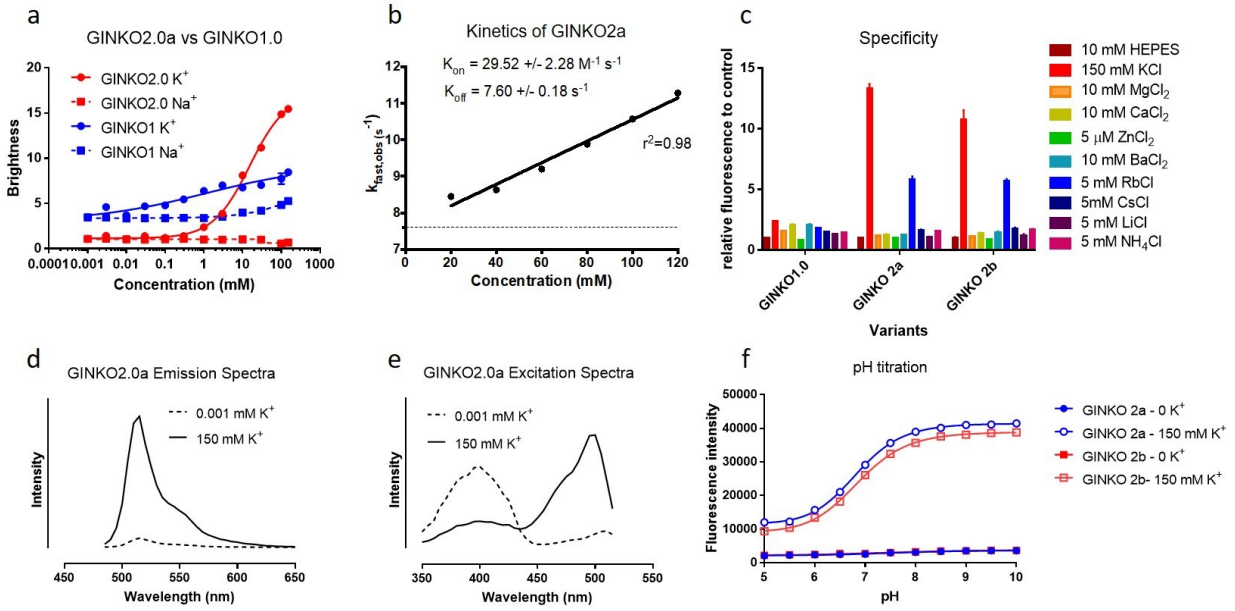

Figure 3.6. Characterization of the second generation GINKOs.

(a) K^+ and Na^+ titration of GINKO2a and GINKO1 (b) Kinetics of GINKO2a (c) Specificity test with cations. (d) Emission spectra and (e) excitation spectra of GINKO with high (solid line) and low (dash line) K^+ concentration. (f) pH titration of GINKO2a and 2b ranges from pH 5 to 10.

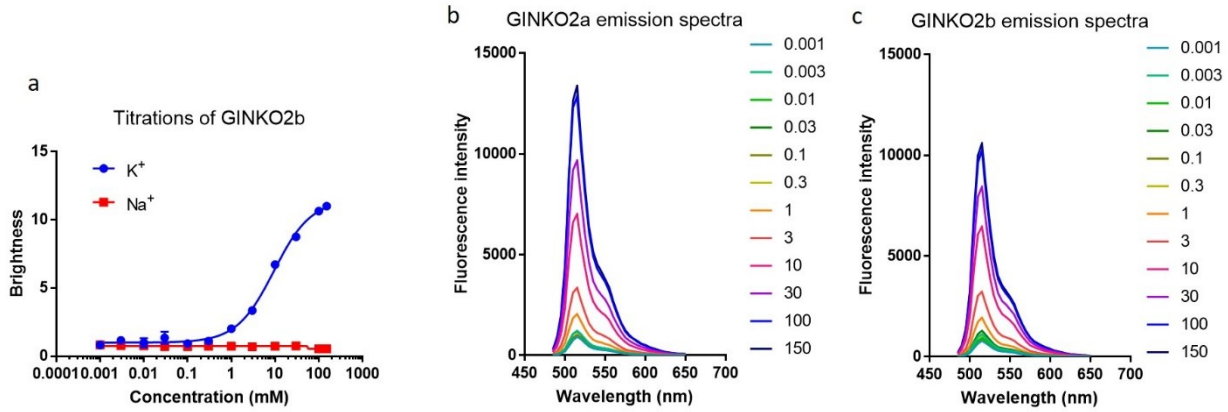

Figure 3.7. Titration curves and spectra for GINKO2a and GINKO2b.

(a) K^+ and Na^+ titration curves of GINKO2b (b) Emission spectra of GINKO2a at different concentrations of K^+ (c) Emission spectra of GINKO2b at different concentrations of K^+.

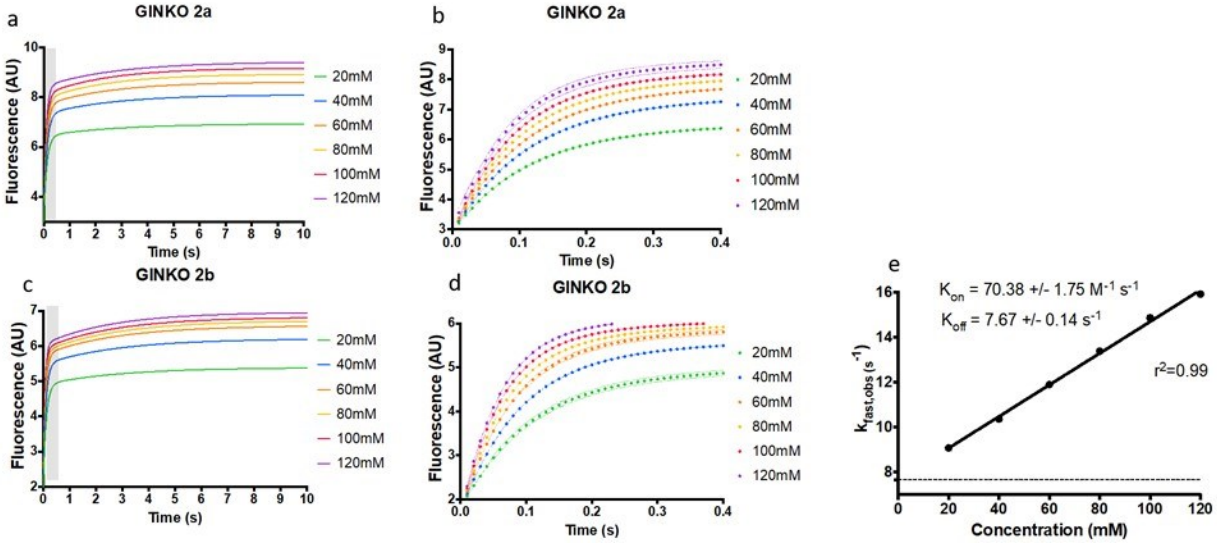

Figure 3.8. Kinetics for GINKO2a and 2b.

The fluorescence reading of GINKO2a to different concentration of K^+ in the first 10 s (a) and 0.4 s (b) of the reaction. The fluorescence reading of GINKO2b to different concentration of K^+ in the first 10 s (c) and 0.4 s (d) of the reaction. (e) k_{on} and k_{off} of GINKO2b.

As sodium sensitivity was one of the major concerns for GINKO1, we performed a NaCl titration with the new biosensors. The results were surprisingly satisfactory that GINKO2a and 2b do not respond Na^+ of concentrations up to 150 mM (**Fig. 3.6a and Fig. 3.7a**).

The excitation and emission spectra of the GINKO2 variants were obtained at K^+ rich and K^+ free environments. With excitation wavelength fixed at 465 nm, the emission spectra show an intensiometric increase of about 15-fold change for GINKO2a and peak around 515 nm (**Fig. 3.6d**). The excitation spectra displayed ratiometric change: the anionic form (B band, peak at 500 nm) dominates in K^+ bound form and the protonated form (A band, peak at 400 nm) dominates in K^+ unbound form (**Fig. 3.6e**). This allows ratiometric imaging in situations where ratiometric measurement is more suitable (i.e., growing bacterial culture with continuous biosensor production). We also noticed the minor peak shift for B band: it peaks at 510 nm in absence of K^+ and 500 nm in presence of K^+(**Fig. 3.6e**).

We measured the kinetics of the biosensors with stopped-flow measurements. GINKO2a has a k_{on} of 29.5 ± 2.3 $M^{-1}s^{-1}$ and k_{off} of 7.6 ± 0.2 s^{-1} (**Fig. 3.6b**). GINKO2b has a slightly larger k_{on} of 70.4 ± 1.8 $M^{-1}s^{-1}$ and similar k_{off} of 7.7 ± 0.1 s^{-1} (**Fig. 3.8e**). In comparison to GINKO1 whose k_{on} is 9.32 ± 0.25 mM^{-1} s^{-1} and k_{off} is 85.9 ± 1.6 s^{-1}, the new variants have smaller k_{on} and k_{off}[1]. Although slower, GINKO2a and 2b still bind to and dissociate from K^+ fast enough for most imaging experiments.

To test whether the new biosensors would respond to cations beside K^+ and Na^+, we tested them with $ZnCl_2$, $MgCl_2$, $CaCl_2$, $BaCl_2$, CsCl, RbCl, LiCl, and NH_4Cl. GINKO2a and 2b are unresponsive to most cations except for Rb^+ (**Fig. 3.6c**). However, substantial concentrations of Rb^+ are not normally present in biological systems, though it is often used as a substitute of K^+ in

experimental settings[266]. The specificity test suggested that the biosensors can be applied in cells without concerns of unspecific binding to other cations in the environment.

Fluorescent protein-based biosensors are often pH sensitive thus limiting their applicability. We performed a pH titration to examine our biosensors. The results suggested GINKO2a and 2b are both very sensitive to pH with a pK_a of 6.8 (**Fig. 3.6f**). This will unavoidably bring complications to the application of the biosensors in cases where pH fluctuates, thus need to be addressed. Therefore, we constructed a pHuji-GINKO2a fusion to measure K^+ and pH changes simultaneously. Alternatively, approaches to reduce the pH sensitivity of GINKO2 at the physiological pH, such as engineering GINKO with less pH-sensitive FP or optimizing GINKO to achieve a different p*K*a, may provide a better GINKO in the future.

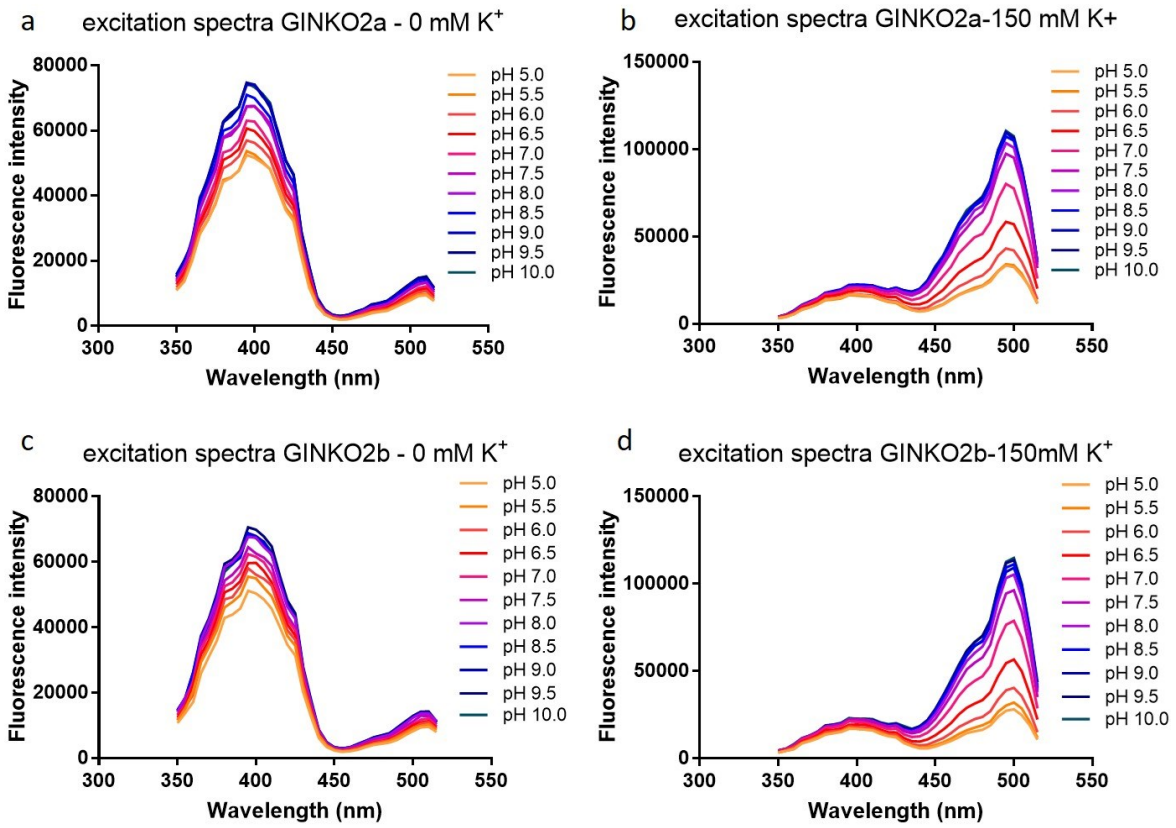

Figure 3.9. Excitation spectra of pH titrations of GINKO2a and GINKO2b.

The spectra for GINKO2a (a) and 2b (c) in absence of K^+ show minor increase in the intensity at both 400 nm and 510 nm. The spectra for GINKO2a (b) and 2b (d) in presence of 150 mM K^+ show an increasing 500 nm peak as pH increases.

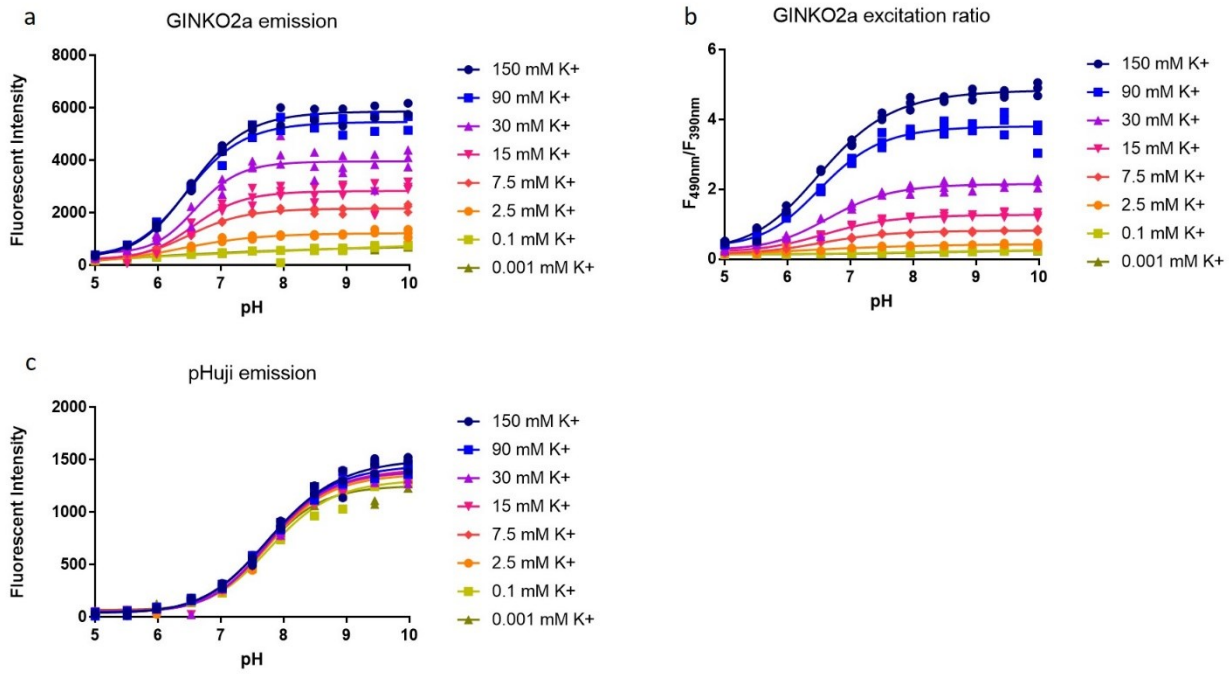

Figure 3.10. K^+ and pH titrations for pHuji-GINKO2a.

The pH titrations of GINKO2a at different concentrations of K^+ are represented as emission intensity (a) and excitation ratio of 490 nm over 390 nm (b). (c) The pH titrations of pHuji at different concentrations of K^+.

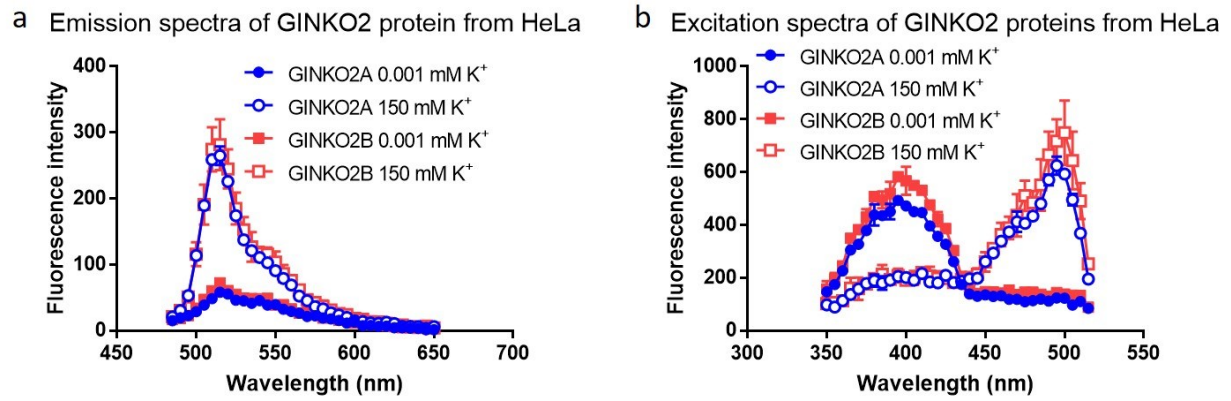

Figure 3.11. Spectral information of GINKO2a/b extracted from HeLa cells.

Intracellular GINKO2a and 2b expressed by HeLa was extracted to determine its (a) emission spectra and (b) excitation spectra.

3.3.5 Testing GINKO2a and 2b in HeLa cells

To test the new variants in a mammalian system, we expressed them in HeLa cells. Extracted protein shows similar excitation and emission spectra to those of the protein samples from *E. coli* (**Fig. 3.11**).

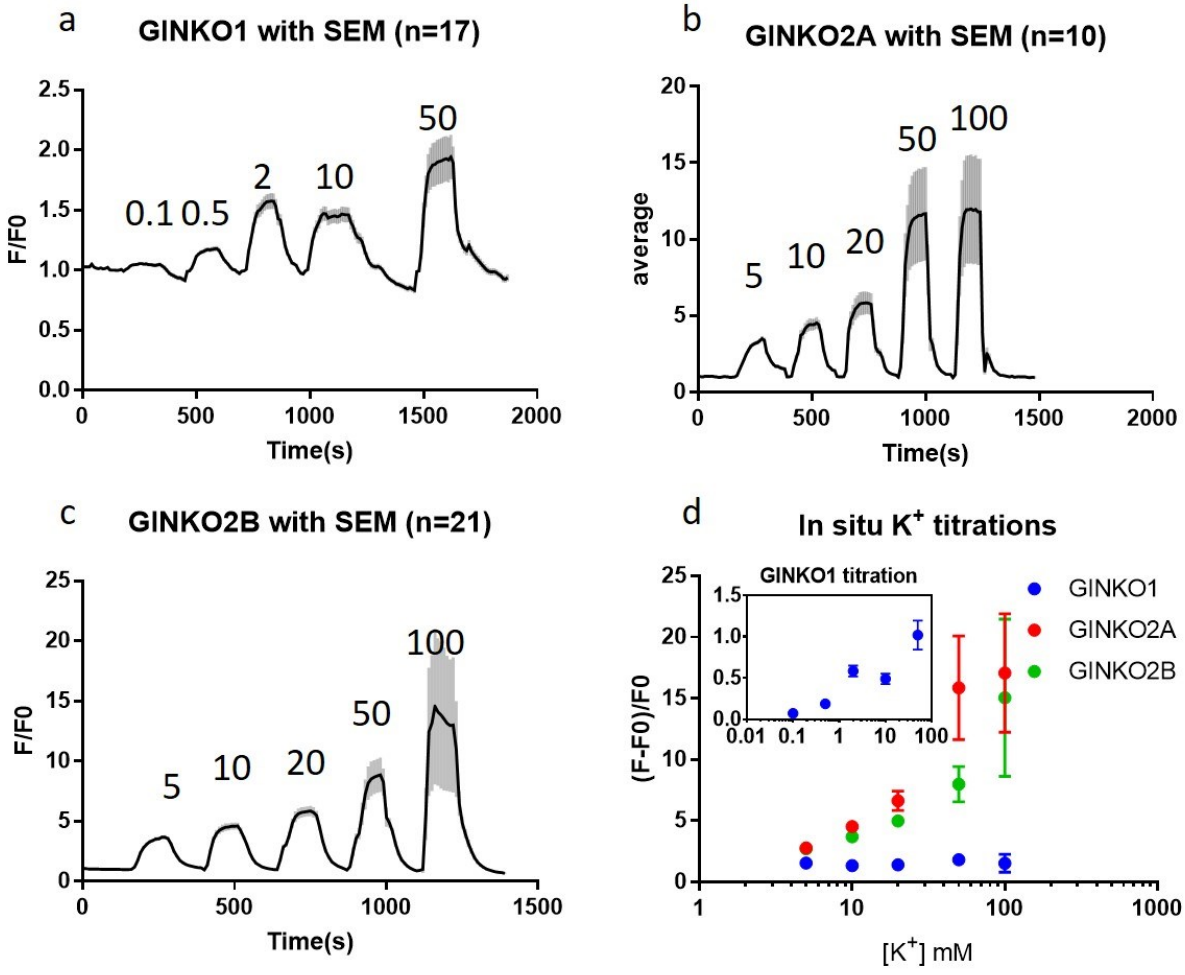

Figure 3.12. *In situ* K^+ titration with digitonin-permeabilized HeLa cells.

(a) GINKO1 is sensitive to a K^+ concentration less than 50 mM. GINKO2a (b) and 2b (c) are both sensitive in the range up to 100 mM. (d) Calibration curve based on titration results. GINKO1 calibration curve from 0.1 to 50 mM K^+ was shown in the inset.

We performed K^+ titrations on HeLa cells expressing GINKO1, GINKO2a, or GINKO2b. We permeabilized the cells with digitonin prior to perfusing with different concentrations of K^+ ranging from 0.4 mM to 100 mM. The response of GINKO variants in these permeabilized cells well aligns with the results from purified proteins. GINKO2a and GINKO2b are sensitive in the range of 5–100 mM K^+, while GINKO1 is more sensitive in a lower range under 50 mM K^+ (**Fig. 3.12a–d**).

3.3.6 Applications of GINKO2a in E. coli

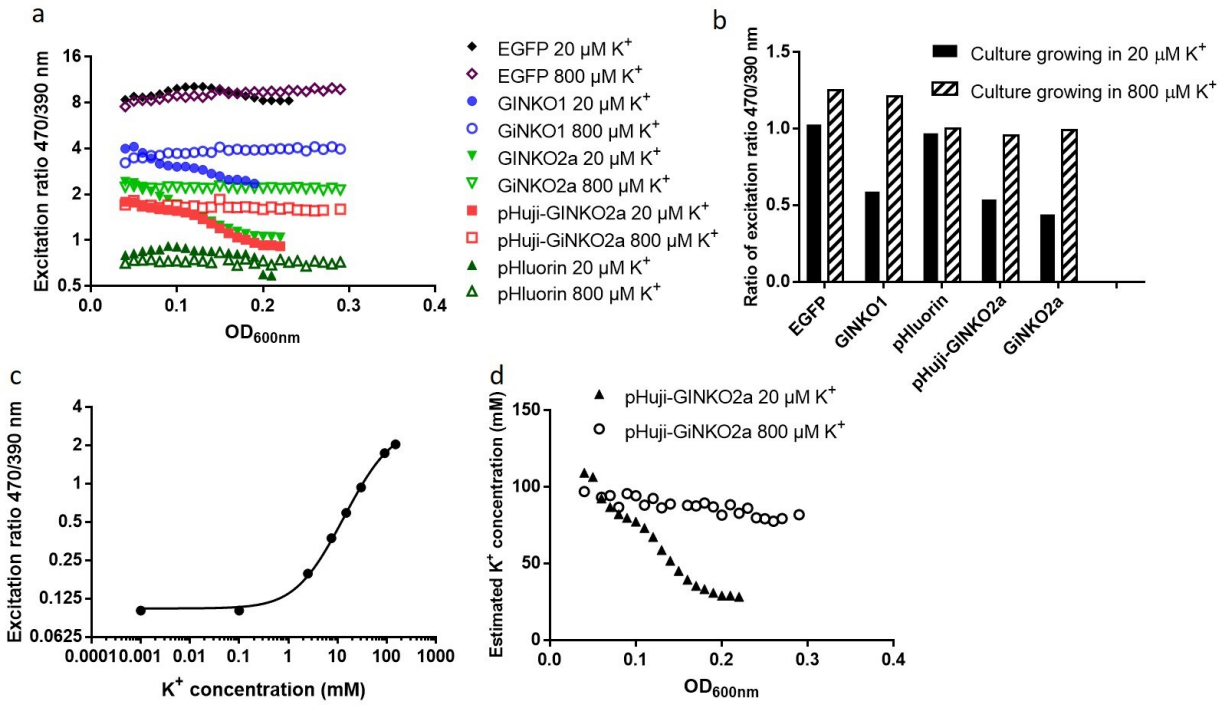

Figure 3.13. Testing the effect of K^+ concentration in the growth medium on *E. coli* intracellular K^+.

(a) Excitation ratio of 470 nm/390 nm of GINKO variants in *E. coli* growing in medium supplemented with 20 μM (solid symbols) or 800 μM (empty symbols) KCl at pH 7. (b)The ratio of excitation ratio at OD_{600nm} 0.19 to that at OD_{600nm} 0.04. (c) Excitation ratio (470 nm to 390 nm) curve of purified pHuji-GINKO2a at pH 7 (d) The change in K^+ concentration can be estimated with the curve in (c). The intracellular K^+ drops from 100 mM to 25 mM when *E. coli* grows from OD_{600nm} from 0.04 to over 0.2.

K^+ is important for the growth of *E. coli* and deficiency in K^+ resulted in slower growth[267,268]. Although the extracellular K^+ in the growth medium can be easily controlled, monitoring the intracellular K^+ is challenging until GINKOs. Because the growing *E. coli* shows increasing fluorescence as the number of cells increases, the excitation ratio becomes a better parameter for K^+ measurement. The excitation ratio was measured for *E. coli* transformed with GINKO1, GINKO2a, pHuji-GINKO2a, pHluorin, and EGFP in minimal medium with K^+ concentration of 20 or 800 μM (**Fig. 3.13a**). pHluorin and EGFP are the controls and the flat lines suggest that the density of *E. coli* does not interfere with GFP excitation ratio and pH value does not change. Monitoring cells expressing GINKO1, GINKO2a, or pHuji-GINKO2a, we found the excitation ratio stays relatively stable for cells growing in 800 μM K^+, while it decreases for *E. coli* growing in 20 μM K^+. **Fig. 3.13b** shows the ratio of the excitation ratio of sample at OD_{600nm} 0.19 to that at OD_{600nm} 0.04. The ratio is about 0.59, 0.54, and 0.44 for *E. coli* expressing GINKO1, GINKO2a, and pHuji-GINKO2a, respectively. An *in vitro* titration was performed on purified pHuji-GINKO2a in **Fig, 3.13c** to estimate the K^+ concentration. The dynamic range of excitation ratio of 470 nm to 390 nm is ~20× (ratio is 2.04 at 150 mM K^+; ratio is 0.10 at 0.001 mM K^+) (**Fig. 3.13c**). The estimated intracellular K^+ concentration over the growth period is plotted in **Fig. 3.13d**. The results indicate that the intracellular K^+ concentration starts around 100 mM and is reduced in

growing cells to 28 mM at O_{600nm} of 0.22 in medium containing 20 μM K^+ and to approximate 80 mM in medium containing 800 μM K^+. This suggests that *E. coli* growing in a K^+-depleted environment are capable of transporting K^+ into the cells against the concentration gradient, but the K^+ transport efficiency decreases when cells are competing with increasing number of cells in the surrounding.

3.4 Discussion

3.4.1 Mutations generated by the directed evolution

In this work, we developed improved GINKO1-based potassium biosensors, GINKO2a and GINKO2b, with better sensitivity and specificity. GINKO2 variants were generated through rational designs based on the newly obtained GINKO1 crystal structure and linker optimizations, as well as random mutagenesis approach with directed evolution. Rational approaches provided some but limited improvement. On the other hand, directed evolution was demonstrated to be a much more powerful method that generated a better K^+ biosensor GINKO2a with approximately 15-fold change from GINKO1.2.

There are 8 amino acid changes accumulated in GINKO2b and 14 in GINKO2a. A few mutations were at important sites of the crystal structure. K356R, for example, is the only mutation in GINKO1.7 that is absent in its template GINKO1.6 (**Fig. 3.14a**). This mutation, located at the interface of the Kbp and GFP, was able to double the dynamic range. It was suggested previously that arginine offers more stability than lysine due to its geometry, as its side chain can point to three different directions[269]. It is possible that K356R allows the K^+- bound GINKO to be more stable, which may subsequently improve the dynamic range. Another case is mutations on a pair of lysines facing each other: K259N and K102E on Kbp and GFP, respectively (**Fig. 3.14b**). They first appeared in two different variants in GINKO1.5 library and provided small improvement.

When using both variants as templates to generate GINKO1.6 library of a 5000–10,000 colonies, K259N and K102E were simultaneously incorporated in the selected GINKO1.6.15 variant, which provided an improvement of dynamic range from ~3.5 to 4.5. The double mutations remove the repulsive force and provide a new hydrogen bond to stabilize the interaction between Kbp and GFP. All the mutations mentioned above can be rationally explained for their observed functional importance by examining their positions on the crystal structure.

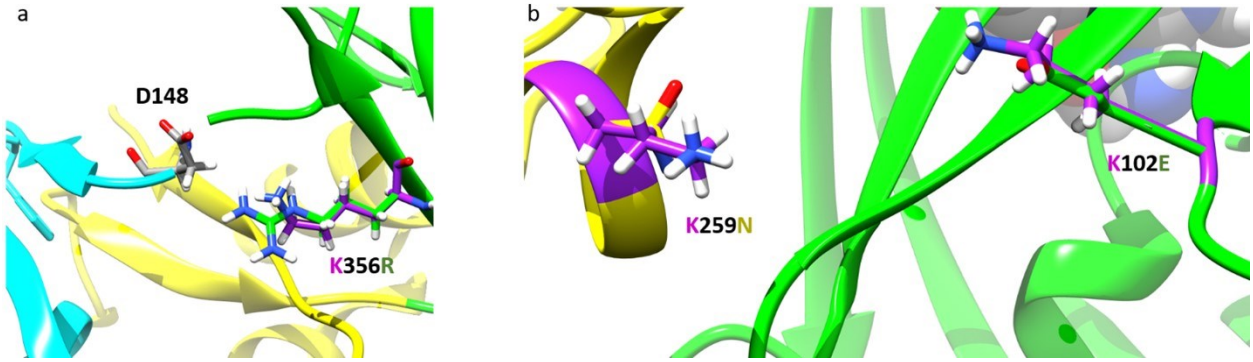

Figure 3.14. Selected mutations generated by directed evolution shown in the GINKO1 structure.

The original residue is shown in purple (a) K356 is in proximity to D148 to form electrostatic interaction. The two carboxyl oxygens of D148 side chain are 4.91Å and 6.54Å away from the amine nitrogen of K356. The distances of these two oxygens to the closest guanidine nitrogen of R356 are 4.19 Å and 5.82 Å. (b) K102 and K259 are 10.16 Å (measured with side chain amino nitrogens) apart on the GINKO1 structure and the pair of mutations may possibly bring the two side closer.

On the other hand, we find it difficult to explain the importance of most mutations in the selected variants given their locations on the crystal structure. Noticeably, N183H on Kbp is the only mutation in GINKO2b from its template. The residue side chain points toward the aqueous

environment and does not have any structure implication to the potassium binding site or the GFP-Kbp interaction. Yet, the improvement is visible. There are many other mutations on structurally non-important sites: S31Y, I94T, K127E, Q307E, and K388M on GFP and T205A on Kbp. They can possibly improve the protein folding for better stability. Some mutations may be non-relevant to optimization: Y40N and F151S appeared in GINKO1.3 and were reversed in later generations, indicating these mutations most likely does not contribute to the functional improvement.

3.4.2 In vitro performance of GINKO2a and GINKO2b indicates their advantages and limitations

GINKO2a and GINKO2b display superior sensitivity and specificity. A dynamic range of approximately 15 allows better detection than GINKO1. GINKO2a and 2b shows no sensitivity to Na^+, which is a major improvement over GINKO1, especially when Na^+ is another abundant cation in biology. The biosensors perform consistently when expressed intracellularly in *E. coli* and mammalian cells. The application of GINKO2a in *E. coli* allows a kinetic tracing of intracellular K^+ in K^+-depleted environment. While *E. coli* grows in an environment with micromolar K^+, they were able to accumulate K^+ in millimolar concentration. When *E. coli* cells are growing in 20 μM K^+, the intracellular K^+ drops substantially as mother cells shared their K^+ with their daughter cells in cell division[270] and K^+ uptake from the environment is insufficient to replenish K^+ stock. The decrease of K^+ for cells growing in 800 μM K^+ is much less substantial, probably due to sufficient uptake from the environment.

Although the new GINKO variants are more powerful than GINKO1, there are some limitations that need to be further addressed. One of the major limitations is their pH sensitivity. The pK_a of 6.8 is very close to physiological pH. Any fluctuation in pH during an experiment can induce an unwanted signal change that can be confused with the change induced by K^+. The pHuji-

GINKO fusion construct provided a way to co-measure pH and K^+ with dual-color imaging. Yet, this method requires some additional calculations due to the complications raised by multiple potential contributing factors to the green fluorescence signal: a pH change needs to be calculated first based on the information from the red channel, with which the green fluorescence signal change due to pH change can be estimated, and the discrepancy between this calculated number and the observed fluorescence signal change attribute to a K^+ change.

We also noticed an increased K_d of the new variants, which is a challenge for detection of K^+ dynamics at low concentrations found in the mammalian extracellular fluid. A K_d of 9.3 mM (GINKO2b) or 15.3 mM (GINKO2a) is less ideal for detecting extracellular K^+, which is usually around 5 mM in mammalian cells. We aim to engineer GINKO in the future to create better-affinity GINKO in the future for the extracellular K^+ detection.

While the K_d is suitable for intracellular K^+ concentration, the number of applications is limited in mammalian systems because physiological influx or efflux of K^+ in most cellular activities are only a small fraction of the large basal level of intracellular K^+ concentration. Large K^+ effluxes often lead to cell death. They were reported in NLRP3 inflammasome mediated immune response[271], cancer cell apoptosis[272], and under drug influence[273–275].

3.5 Conclusion

In this work, we report two improved genetically encoded green fluorescent potassium biosensors GINKO2a and 2b based on previously reported GINKO1. The new K^+ indicators displayed better sensitivity and specificity that open new avenues to applications *in vitro*, *in situ*, and in *E. coli*. While GINKO2a and 2b are valuable tools for intracellular K^+ detection, we hope to further expand its applications with membrane displayed version for extracellular K^+ measurement. So far, this remains a major challenge in further development of genetically encoded

K^+ sensor. We have actively worked on this and the effort is detailed in the next chapter of this thesis.

3.6 Methods

Crystallization and X-ray diffraction data collection

The His-tag affinity purified GINKO recombinant protein was further applied on the size exclusion chromatography Superdex200 (GE Healthcare) column pre-equilibrated with 25mM Tris pH 7.5, 150 mM KCl buffer. The main fractions of monodisperse protein were concentrated to around 25 mg/mL for further crystallization trials.

Crystallization experiments were set up in sitting drop geometry with 0.5 µL of protein sample with 0.5 µL of reservoir from commercially available screen kits at room temperature. This led to the crystals growing in multiple hits, the final diffraction quality crystals were grown in 0.1 M MES pH 6.0, 20% PEG6000 after several round of crystallization optimization. For data collection, the crystals were transferred to crystal stabilization buffer containing reservoir supplemented with 10–15% PEG400 or Glycerol and flash frozen in liquid nitrogen. X-ray diffraction data collection were collected at APS Synchrotron beamline and were initially processed with beamline supplemented software package. The X-ray diffraction data was further integrated and scaled with XDS suite[276]. The data collection details and statistics are summarized in crystallographic **Table 3.1**.

Structure determination and refinement

The GINKO structure was determined with maximum-likelihood molecular replacement program implemented in the Phaser program[277], using the GFP (6GEL) and the potassium binding domain protein structure (5FIM) as search model[94,278]. The linker and the potassium ions density were observed after initial refinement, the missing residues manual model rebuilding and

refinement were carried out with the COOT program and PHENIX suite[279,280]. The GINKO structure was solved at 1.85 Å in P1 space group with the unit cell dimension a=46.8 Å, b=49.3 Å, c=83.7 Å and α=89.96°, β=89.97°, γ= 80.95°. The final structure model was refined to a R_{work}/R_{free} value of 0.1947/0.2252. The model contains two GINKO molecules each occupying one potassium ion, and 892 water molecules in the asymmetric unit cell. The structure exhibited favorable Ramachandran plot and demonstrated good stereochemistry. The detailed structure refinement statistics are supplemented in crystallographic **Table 3.1**.

Plasmid construction and cloning

pBAD and pcDNA plasmid containing the gene encoding GINKO1 and KIRIN from our previous work were used as the templates for this work. XhoI and HindIII cutting sites were previously designed at the two ends of the gene for cloning. FastDigest restriction enzymes (Thermo Fisher Scientific), T4 DNA ligase (Thermo Fisher Scientific), Gibson assembly mix (made in the lab) were used to clone the genes to pBAD, pcDNA, pUAST, and pCAG vectors. Gene fragments and primers for this work were ordered from integrated DNA technology (IDT).

Linker optimizations and directed evolution

Manipulations of the linker residues were achieved with Quikchange lightning kit (Agilent). The linker residues were randomized with multiple NNKs at the linker regions. The Quikchange reaction and subsequent DpnI digestion were performed as described in the manufacturer's manual.

Directed evolution was performed using Taq polymerase with standard buffer from New England Biology (NEB). We followed the manufacturer's instruction with imbalanced dNTP (0.2 mM dATP, 0.2 mM dTTP, 1 mM dGTP, and 1 mM dCTP for the final concentrations) and modifications of $MnCl_2$ and $MgCl_2$ concentrations. We added 5.5 mM (final concentration) $MgCl_2$ in addition to 1.5 mM $MgCl_2$ in supplier's standard reaction buffer. $MnCl_2$ were added to a final

concentration of 0.15 mM and 0.30 mM to generate libraries with low-frequency and high-frequency mutations, respectively. 2% (v/v) DMSO was added to stabilize the unmatched nucleotide pairs during the synthesis of the gene.

The PCR products were then purified on a 1% agarose gel and digested with XhoI and HindIII (Thermo Scientific FastDigest) to create the sticky ends. They were ligated with pBAD backbone vector cut with the same pair of restriction enzymes using T4 DNA ligase (Thermo Scientific).

Screening

The transformation of the Quikchange products or ligation products was performed with electrocompetent DH10B (Invitrogen). We have about 5,000–10,000 colonies for each library. We pick 40–80 colonies with bright to medium fluorescence and inoculate them at 37°C overnight. They were pelleted down, resuspended in 200 µL of 10 mM HEPES buffer, and lysed by four cycles of freeze and thaw by liquid nitrogen and 42°C water bath, respectively. We centrifuged the lysates for 5 min and transferred 100 µL supernatant of each sample to a 96-well plate. The fluorescence response was read by a Tecan Safire2 microplate reader with excitation at 465 nm. We then add 10 µL of 1 M KCl into each well and repeat the measurements with the same parameters. The fold changes of sample fluorescence were calculated, and the winners were picked for further validation with another round of screening with triplicate samples for each variant, as well as a K^+ titration to verify the fold change and examine the K_d. The winner(s) was subject to the next round of optimization.

Culture growth and protein preparation

We picked a colony from an agar plate with *E. coli* DH10B transformed with pBAD GINKO variants to a growth vessel containing 200 – 500 mL of LB supplemented with 100 µg/mL

ampicillin and 0.02% (w/v) L-(+)-arabinose. The cells were inoculated at a speed of 200 rpm at 37°C for 16–20 hours.

GINKO variants expressed in *E. coli* DH10B were purified as previously described[281]. The cells were pelleted down by centrifugation at 6000 rpm for 10 minutes and lysed by sonication. The protein was purified through affinity chromatography with Ni-NTA beads. The beads were then washed with the wash buffer containing 20 mM imidazole and GINKO was eluted from the beads with the elution buffer containing 500 mM imidazole. The eluent was then subject to buffer exchange to 10 mM HEPES at pH 7.4 by PD-10 columns (GE Healthcare Life Sciences) following the manufacturer's instruction.

Titrations and Characterization

The purified GINKO variants were titrated with K^+ and Na^+ to determine the dynamic range, the fold change, as well as the affinity. The buffers were prepared in 10 mM HEPES at pH 7.4 with addition of 0.001, 0.003, 0.01, 0.03, 0.1, 0.3, 1, 3, 10, 30, 100, and 150 mM KCl or NaCl. The buffers for specificity test were also prepared in 10 mM HEPES at pH 7.4. pH titrations were performed with 10 mM HEPES buffers at pH 5.5, 6, 6.5, 7, 7.5, 8, 8.5, 9, 9.5, 10 with no K^+ presence or addition of 150 mM KCl. The pH of the buffers was adjusted with NaOH or HCl. The measurements were performed in a Tecan Safire2 microplate reader. The excitation wavelength was set at 460 nm for the emission scan from 485 to 650 nm and the emission wavelength was set at 540 nm for the excitation scan from 350 to 515 nm.

The quantum yield and extinction coefficient were determined to quantify the brightness of GINKO variants as described previously[281]. GINKO variants were measured in 150 mM KCl or K^+-and-Na^+ free buffer with 10 mM HEPES at pH 7.4. To determine extinction coefficients, Backman Coulter DU 800 spectrophotometer was used to measure the absorbance and quantify

the chromophores in the sample with addition of 0.5 M NaOH. The quantum yield was determined with GINKO1 as the standard. Fluorescence was measured with the Tecan Safire2 microplate reader.

Transfection in mammalian cells and imaging

HeLa cells were cultured in the complete medium, Dulbecco's Modified Eagle Medium (DMEM) from Gibco supplemented with 10% fetal bovine serum from Gibco and 200 U/mL penicillin-streptomycin solution from Thermo-Fisher Scientific.

The HeLa cells were transfected with pcDNA GINKO variants by TurboFect transfection reagent (Thermo Scientific) as instructed by the manufacturer when they reach 50 – 70% confluency on a 35 mm imaging dish (In Vitro Scientific). The cells were ready for imaging after 18–24-hour incubation. GINKO imaging was performed with a Zeiss Axiovert 200 microscope with a 40× objective. Molecular Devices MetaMorph and ImageJ were used for image acquisition and processing, respectively.

In situ titration with permeabilized HeLa cells

The transfected cells were first treated with 10 nM digitonin for about 15 min in the imaging buffer containing (in mM): 120 NaCl, 1.5 $CaCl_2$, 1.5 $MgSO_4$, 1.25 NaH_2PO_4, 26 $NaHCO_3$ and 10 D-Glucose (pH adjusted to 7.4). The cells were then imaged on an upright FV1000 confocal microscope equipped with FluoView software and a 20× XLUMPlanF1 water immersion objective (NA 1.0) with a flow rate of 10 mL/min using a peristaltic pump (Watson-Marlow). The cells were excited with a 488-nm laser and emissions were collected in the channel from 500 to 520 nm. The perfusion buffer was made in different K^+ concentrations (in mM) with imaging buffers: 0.1, 0.5, 2, 5, 10, 20, 50, and 100. *N*-methyl-D-glucamine (NMDG) was supplemented to make a 100 mM combined final concentration with K^+.

Kinetics measurements by stopped flow

Rapid kinetic measurements of GINKO2a/b interaction with K^+ were made using an Applied Photophysics SX20 Stopped-Flow Reaction Analyzer using fluorescence detection. The dead time of the instrument was 1.1 ms**.** The excitation wavelength used was 488 nm with 2 nm bandwidth and emitted light was collected at 520 nm through a 10 mm path. A total of 1000 data points were collected over three replicates at increments of 0.01 s for 10 seconds. Reactions were initiated by mixing equal volumes of diluted protein of GINKO2a and GINKO2b in Tris HCl 100 mM pH 7.20 and varying concentrations of KCl (20, 40, 60, 80, 100, 120 mM) at 20°C. Tris HCl 100 mM buffer was used as a blank. Graphpad Prism was used to fit the increase in fluorescence intensity observed over time to a single exponential function. The k_{obs} determined from this fit is the rate constant for dissociation of K^+ with units of s^{-1}. The slope of k_{obs} and K^+ concentration was used to determine the k_{on} rate (in the units of $s^{-1}M^{-1}$) and the y-intercept of the plot is used to determine is the k_{off} rate (in the units of s^{-1}).

E. coli growth in K^+ depleted environment

Cells were grown in a minimal medium with 20 mM NaH_2PO_4, 60 mM Na_2HPO_4, 10 mM NaCl, 10 mM NH_4Cl, 0.5 mM Na_2SO_4, 0.4% arabinose and micronutrients[282]. KCl was added as 800 µM or 20 µM as specified. Ampicillin was added to LB cultures at 100 µg/mL and in minimal medium cultures at 20 µg/mL.

Cells were picked from single colonies from LB agar plates and cultured in LB medium for 35 hours at 37°C in a water bath shaker at 240 rpm. Cells were then diluted 1000 times into arabinose minimal medium (800 µM KCl) and grown at 37°C in a water bath shaker at 240 rpm overnight. Cells were washed once in minimal media with the same potassium concentration as

the final condition and diluted 500× into 96 well plates with 200 µL of arabinose minimal media in each well (20 or 800 µM KCl).

The 96-well plates were incubated at 37°C in a Tecan Spark Plate reader. Every 7 minutes a loop would run with the following actions. First, the plate was shaken for 200 seconds on "Orbital" mode with amplitude 4.5 mm and 132 rpm. Then optical density was measured at 600 nm. Fluorescence was measured at two wavelength settings: excitation of 390 nm, emission 520 nm (Ex390) and excitation 470 nm, emission 520 nm (Ex470).

Background florescence was subtracted from wild-type NCM3722 control matched by binning into the nearest 0.01 of OD and averaging florescence.

Data Analysis

Microsoft Excel was used for data analyses of GINKO characterization and titrations. Graphpad Prism was used to create figures. The data are represented as mean ± s.d., except for the permeabilized HeLa titration, which are represented as mean ± s.e.m.

Table 3.1. X-ray data collection and refinement statistics.

Crystal	GINKO1
Data collection	
Spacegroup	P1
a, b, c (Å)	46.8, 49.3, 83.7
α, β, γ (°)	89.96, 89.97, 80.95
Resolution (Å)	42.08–1.85 (1.92–1.85)
R_{merge}	0.080 (0.834)
R_{meas}	0.109 (1.13)
Multiplicity	1.9 (1.9)
CC(1/2)	0.993 (0.591)
CC*	0.998 (0.862)
I/σ(I)	6.3 (1.1)
Completeness (%)	93.53 (81.64)
Wilson B-factor (Å^2)	16.71
Refinement	
Total Reflections	108186 (11513)
Unique Reflections	56403 (5152)
R_{work}/R_{free}	0.1947/0.2252
Number of atoms:	
Protein	5765
Ligands	46
Water	892
Average B-factor (Å^2)	25.54
Protein ADP (Å^2)	24.78
Ligands (Å^2)	10.71
Water	31.24
Ramachandran plot:	
Favored/Allowed (%)	96.8/3.0
Root-Mean-Square-Deviation:	
Bond lengths (Å)	0.008
Bond Angles (°)	1.25

Table 3.2. Mutations accumulated during directed evolution.

The mutations appeared in the template are in black and the new mutations are in red. The variants in bold were used as templates for the next round of directed evolution. The selected variants in Library 1.4 failed to yield better variants than GINKO$_{1.3.10}$ and were mixed as templates for Library 1.5. Similarly, the mix of GINKO1.5 variants was used as the template mix to generate Library 1.6.

Variant	Mutations
1	NA
1.2	E295F, E296A, L297A, E298N
1.3.10	Y40N, F151S, E295F, E296A, L297A, E298N
1.3.11	Q211L, E295F, E296A, L297A, E298N
1.3.25	K235E, E295F, E296A, L297A, E298N
1.5.6	Y40N, F151S, N152D, E295F, E296A, L297A, E298N
1.5.20	Y40N, F151S, K171E, V204L, E295F, E296A, L297A, E298N
1.5.21	Y40N, F151S, G167C, K201R, V261A, A265D, E295F, E296A, L297A, E298N, N299Y
1.5.36	Y40N, F151S, T205A, K259N, E295F, E296A, L297A, E298N
1.5.38	K102E, K201R, K235E, E295F, E296A, L297A, E298N, F373Y
1.5.41	Y40N, F151S, K284R, E295F, E296A, L297A, E298N
1.6.7	Y40N, F151S, V154A, T205A, K259N, E295F, E296A, L297A, E298N
1.6.8	K102E, D130N, I187F, K201R, K235E, E295F, E296A, L297A, E298N,F373Y
1.6.15	S31Y, K102E, T205A, K259N, E295F, E296A, L297A, E298N
1.6.40	V2A, Y40N, D130G, F151S, N152D, E295F, E296A, L297A, E298N, E385V
1.7.7	S31Y, K102E, T205A, K259N, E295F, E296A, L297A, E298N, K356R
1.7.8	S31Y, K102E, N194D, T205A, K259N, E295F, E296A, L297A, E298N
1.9.8	S31Y, I94T, K102E, T205A, N266D, K259N, E295F, E296A, L297A, E298N, K356R
1.9.13	S31Y, K102E, T205A, K259N, E295F, E296A, L297A, E298N, K356R, M383R
1.9.15	S31Y, K102E, D173V, Q174L, T205A, K259N, E295F, E296A, L297A, E298N, K303Q, K356R
1.9.20	S31Y, K102E, N183H,T205A, K259N, E295F, E296A, L297A, E298N, K312R, K356R
2.0.17	S31Y, I94T, K102E, T205A, T241A, N266D, K259N, E295F, E296A, L297A, E298N, K356R
2.0.29	S31Y, I94T, K102E, N183H, T205A, N266D, K259N, E295F, E296A, L297A, E298N, K356R
2.1.5	S31Y, I94T, K102E, K127E, N183H, T205A, N266D, K259N, E295Y, E296A, L297A, E298N, K356R
2.2.25	S31Y, I94T, K102E, K127E, N183H, Q179R, I197V, T205A, N266D, K259N, E295Y, E296A, L297A, E298N, Q307E, K356R, K388M

Table 3.3 Summary of GINKO *in vitro* characterization.

The extinction coefficient and the quantum yield of GINKO variants were measured to determine the brightness of GINKO variants in both apo- and K^+-bound states. The apparent K_d and n_H values of GINKO2a and 2b were determined by K^+ titrations. k_{on} and k_{off} were determined by stopped flow. pK_a values were determined by pH titrations. The values of K_d, n_H, k_{on}, k_{off} for GINKO1 were from Shen *et al* (2019)[1].

Name	[K^+] (mM)	ε (M^{-1} cm^{-1})	φ	brightness ($mM^{-1}cm^{-1}$)	K_d (mM)	n_H	k_{on} (mM^{-1} s^{-1})	k_{off} (s^{-1})	pK_a
GINKO1	0	10461	0.42	4.35	0.42 ± 0.03	1.05 ± 0.03	9.32 ± 0.25	85.9 ± 1.6	NA
	150	20744	0.41	8.45					
GINKO2a	0	3740	0.25	0.95	15.3 ± 1.1	0.91 ± 0.04	29.52 ± 2.28	7.60 ± 0.18	7.58 ± 0.14
	150	36880	0.42	15.46					6.83 ± 0.02
GINKO2b	0	4534	0.29	1.31	9.3 ± 0.6	1.02 ± 0.06	70.38 ± 1.75	7.67 ± 0.01	7.49 ± 0.14
	150	35595	0.31	11.00					6.87 ± 0.01

Chapter 4 Engineering cell surface targeted K^+ biosensors

4.1 Introduction

In Chapter 2 and 3, I described the engineering of genetically encoded K^+ indicators, KIRIN1, GINKO1, GINKO2a, and GINKO2b, for intracellular K^+ imaging[1]. To further expand the utility of genetically encoded K^+ indicators, we aim to target GINKO to the cellular surface for extracellular K^+ imaging. This can open new avenues to many K^+ related applications in mammalian system because of the implications of extracellular K^+ concentration in medical conditions such as epilepsy[283] and kidney failure[206]. In the nervous system, extracellular K^+ is an important electrolyte for action potentials during which a large K^+ efflux follows a Na^+ influx[263]. An extracellular targeted GINKO can be an important tool to capture the transient change of K^+ before the excess extracellular K^+ is re-uptaken by the neurons or absorbed by surrounding glia cells[284]. When displayed on the extracellular side of the membrane through a protein- or lipid-based membrane anchoring domain, GINKO can bind to extracellular K^+ and show fluorescence change that reflects K^+ dynamics.

Targeting genetically encoded tools to the extracellular membrane can be quite challenging as demonstrated by channel rhodopsin-based optogenetic tools[285]. The possibly post-translational modification of the *E. coli* originated K^+ binding domain Kbp added another layer of uncertainty[286]. Despite the challenges, we foresee the potential impact of membrane anchored GINKO and here we describe the effort toward targeting a functional GINKO to the extracellular membrane and fine-tuning the affinity to better fit the extracellular K^+ concentration.

4.2 Results

4.2.1 Targeting GINKO to the extracellular membrane with frizzled protein receptor 7 (Fzd7) leader peptide

The first challenge was to find an effective leader peptide and a membrane anchoring domain to facilitate GINKO secretion and anchoring to the membrane. We first tried pDisplay vector, a commercially available vector that has successfully displayed most fluorescent proteins on the mammalian cell membrane. The vector contains the IgK leader peptide for protein secretion and platelet derived growth factor receptor (PDGFR) for membrane anchoring, as shown in **Fig. 4.1a**. However, the resulted construct pDisplay GINKO did not show membrane localization. We then explored other potential options including CD59 glycoprotein leader peptide and a glycosylphosphatidylinositol (GPI) anchor, ER and Golgi export signal peptides in different combinations, as well as Fzd7 leader peptide. After testing the constructs in HeLa cells, I identified the leader peptide Frizzled protein receptor 7 leader peptide (Fzd7) and the GPI anchor achieved extracellular membrane anchoring for GINKO1.2 as shown in **Fig. 4.1b**. Later, I found the PDGFR transmembrane domain worked as well as the GPI anchor when combined with Fzd7 leader peptide (**Fig. 4.1d**). The localization was verified by acid quenching: the edges of a HeLa cell expressing Fzd7-GINKO1.2-GPI lost fluorescence far more substantially than the interior region, indicating the protein is exposed to the acidic extracellular environment (**Fig. 4.1c**). However, titrating the cells by adding K^+ to the imaging buffer showed that the performance of the membrane bound GINKO is indifferent from that of the EGFP control, indicating the sensor is not functional despite the correct membrane localization.

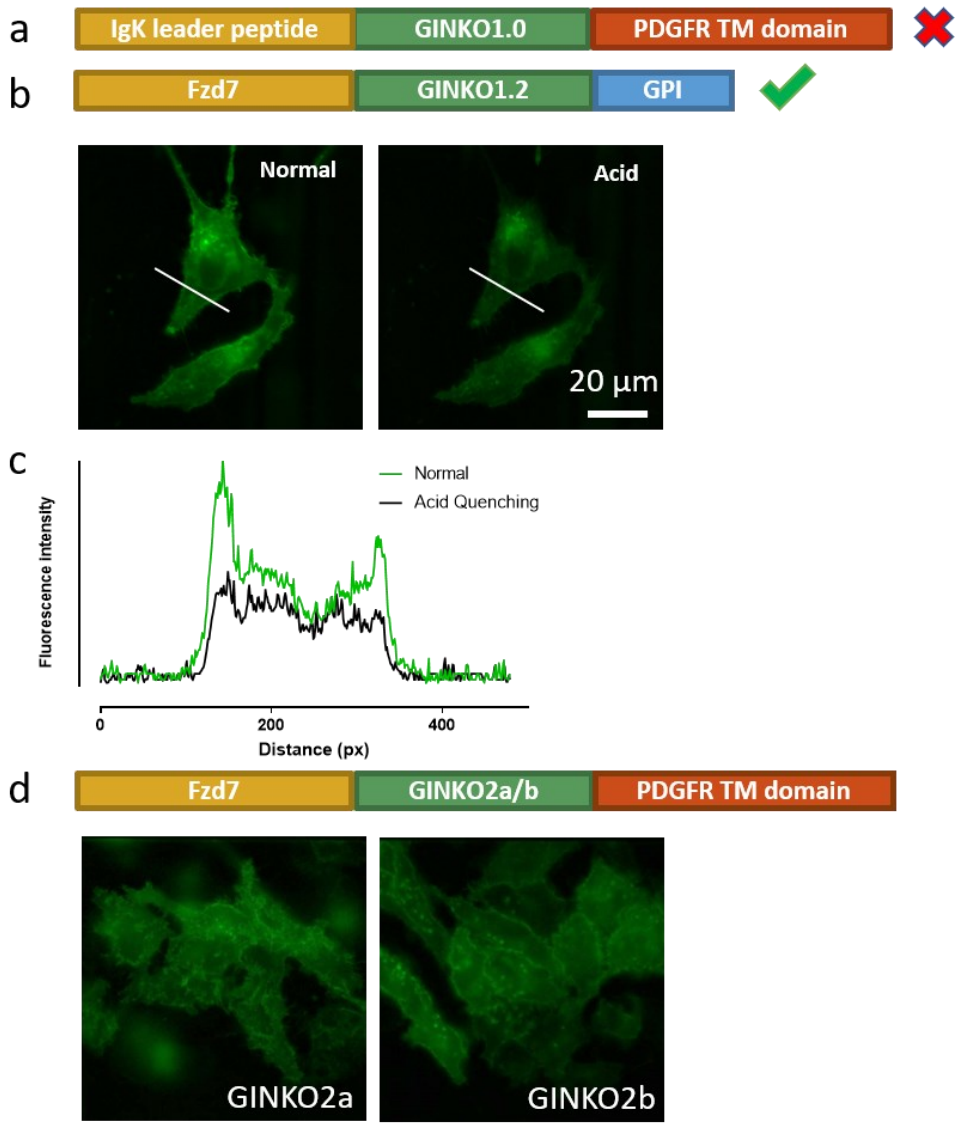

Figure 4.1. GINKO on the membrane.

(a) GINKO1 in a vector pDisplay with IgK leader peptide and PDGFR transmembrane domain (b) GINKO1.2 with Fzd7 leader peptide and GPI anchor. When expressed, GINKO1.2 is targeted on the membrane. An acid quenching experiment was performed to confirm the extracellular localization. (c) The fluorescence intensity is measured in a line across a cell. The fluorescence intensity drops more obviously at the edge of the cells. (d) Fzd7 leader peptide and PDGFR transmembrane domain can also make GINKO2a or GINKO2b membrane bound.

4.2.2 Fixing the cleavage in Kbp during the trafficking process

We first hypothesized the displayed GINKO is not functional due to the cleavage during trafficking process. This cleavage issue was previously observed when targeting FRET-based K^+ biosensor KIRIN (**Fig. 4.2a**) to the extracellular membrane with the same Fzd7 leader peptide. The expressed KIRIN in HeLa cells showed a lack of colocalization of mCerulean and cpVenus: mCerulean is on the membrane, but cpVenus is retained inside of cells (**Fig. 4.2b**). This is indicative of a cleavage during the trafficking.

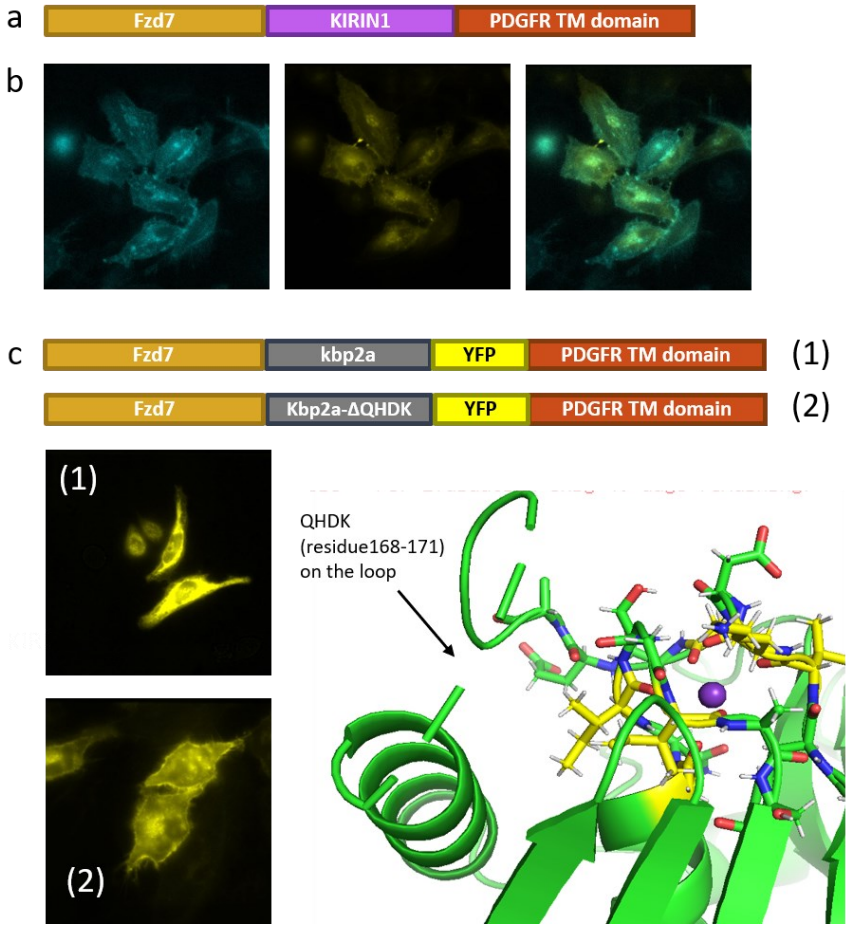

Figure 4.2. Finding and solving GINKO cleavage.

(a) Fzd7 and PDGFR transmembrane domain are used to target KIRIN1 to the extracellular membrane (b) The pictures of KIRINs were taken in the cyan and yellow channel. The cyan colour

is localized on the membrane and the yellow colour is localized in the cells. (c) Fzd7-Kbp from GINKO2a-cpVenus(YFP)-PDGFR transmembrane domain is used to find observe membrane localization. The Kbp2a (1) is ER localized and Kbp2a ΔQHDK (2) is membrane localized. The location of QHDK is on a flexible linker that was not resolved by X-ray crystallography.

In order to solve this unknown cleavage in the Kbp region, we exploited KIRINs with ten different Kbp homologues for various microbial species. These KIRIN variants, except the KIRIN with the original *E. coli* Kbp, showed perfect colocalization of mCerulean and cpVenus (**Fig. 4.4**). The results suggest this is a Kbp specific issue. We thus aligned Kbp with its homologues to find regions where Kbp sequence is different from the others (**Fig. 4.3**) and to mutate or delete them in a vector containing Fzd7-kbp-cpVenus-PDGFR. We identified ΔQHDK (Residue 168–171) allows cpVenus to be membrane anchored (**Fig. 4.2c**), which suggested Kbp-ΔQHDK remains intact during trafficking. We then continued to graft the deletion mutation onto GINKO, but unfortunately, GINKO-ΔQHDK remains nonresponsive to K^+ on the membrane, therefor other contributive factors must lead to the loss of GINKO function.

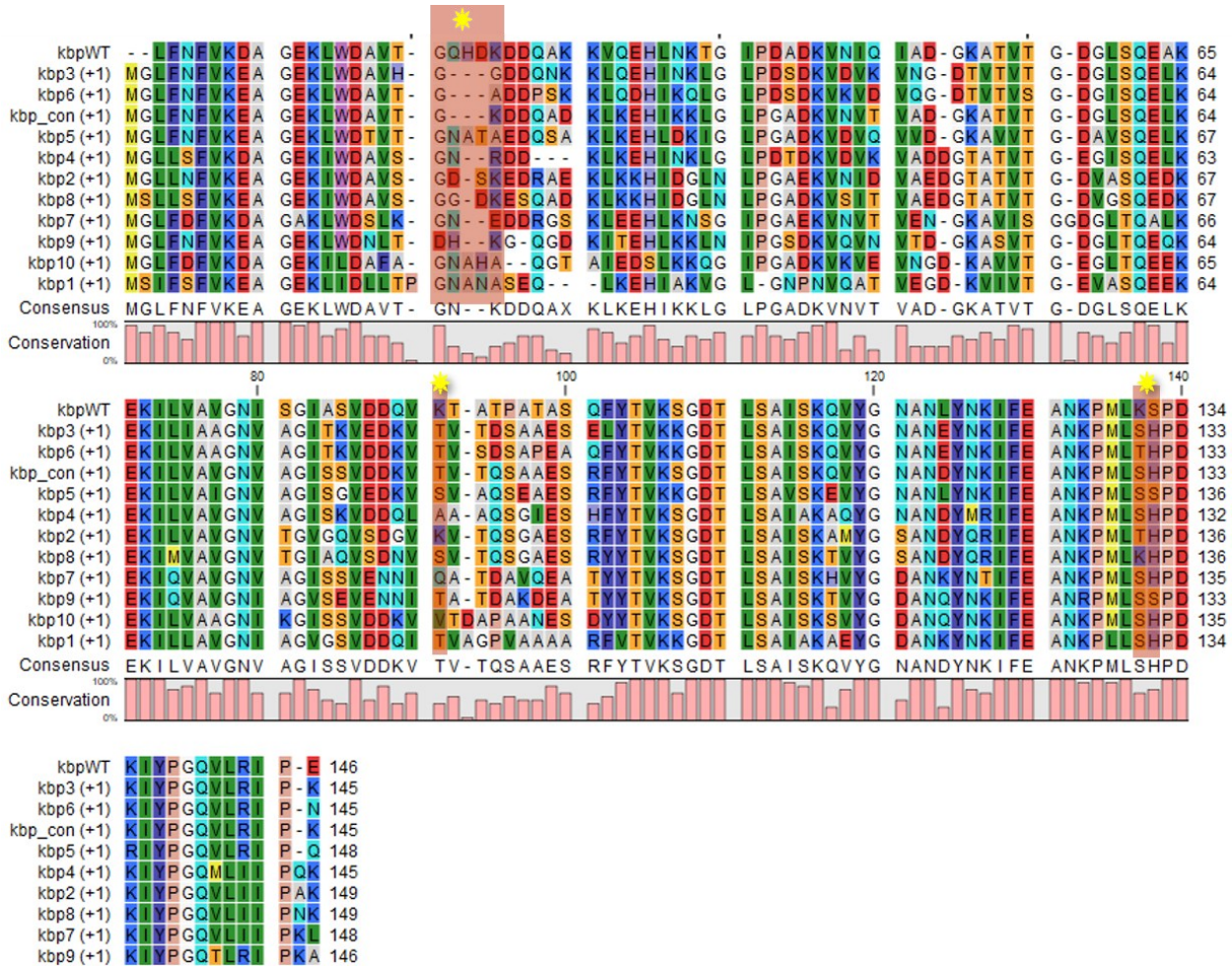

Figure 4.3. Alignment of Kbp WT and other homologues.

The sequences aligned include Kbp wildtype (*E. coli* Kbp), Kbp1–10, and the Kbp consensus sequence based on all 11 sequences. The regions highlighted with yellow stars are of interest as Kbp wildtype sequence at these regions is different from those of other homologues.

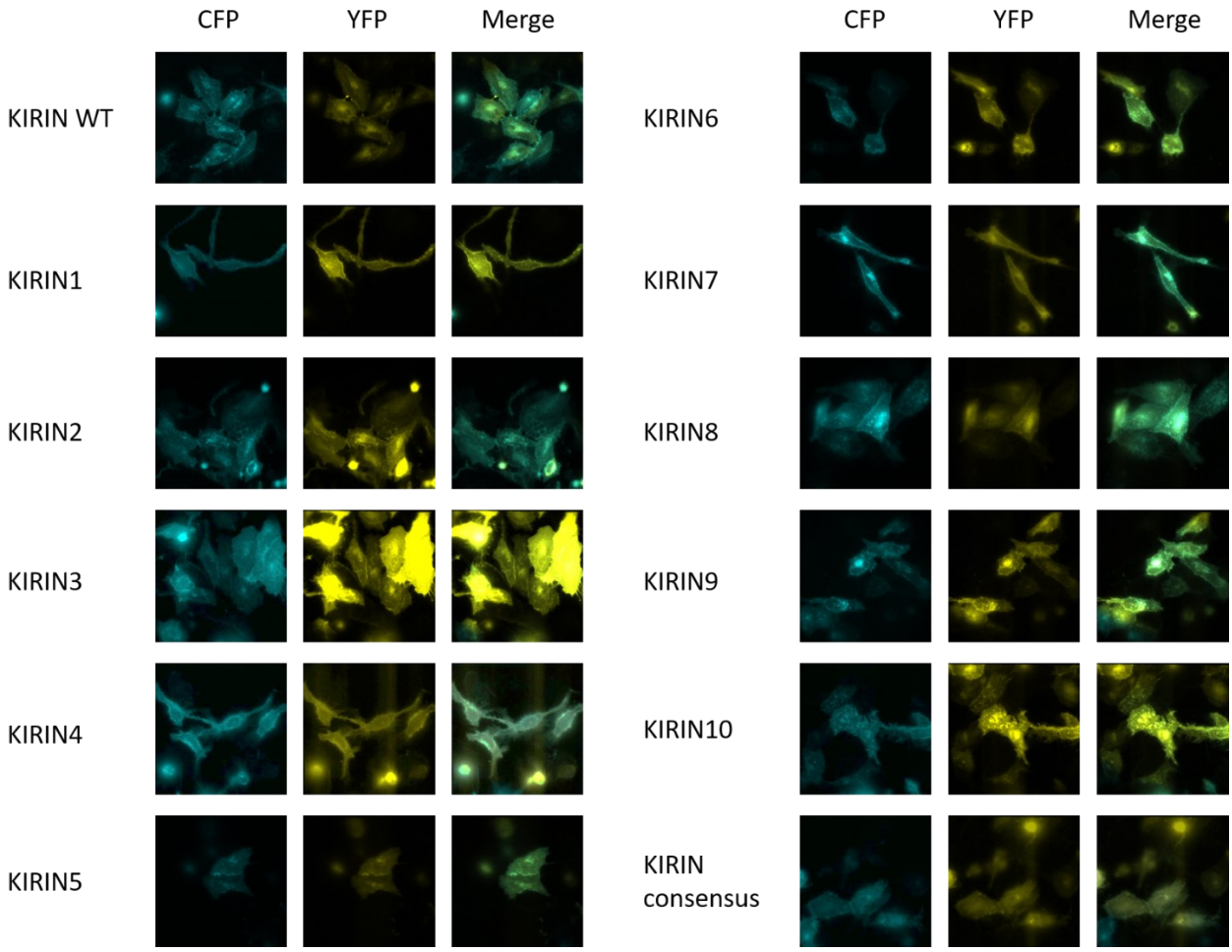

Figure 4.4. Images of KIRIN and KIRINs with Kbp homologues on the membrane.

Fzd7 leader peptide and PDGFR transmembrane domain were used for protein secretion and membrane anchoring, respectively. Images of CFP and YFP channels were taken and merged to show colocalization. All except for KIRIN wildtype have colocalization of YFP and CFP on the membrane

4.2.3 Search for possible post-translational modification

We then hypothesized that post-translational modifications may cause this loss of GINKO function because it is common for the mammalian system to modify proteins originated from

foreign sources in an unexpected way[286]. The common modifications include disulfide bonds[287], glycosylations[288], phosphorylations[289,290].

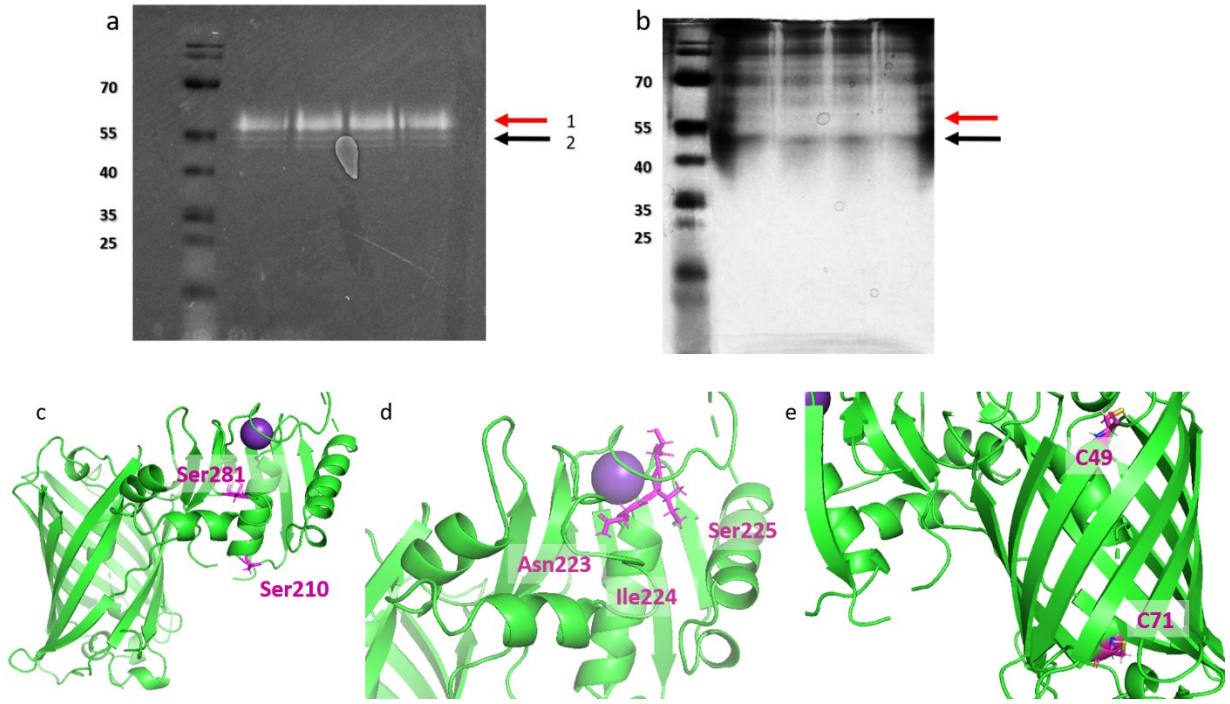

Figure 4.5. Examining possible post-translational modifications.

Gels for secreted GINKO2a and locations of possible post translational modifications. The (a) fluorescence image of the pseudonative gel of loaded with secreted GINKO2a in all four sample lanes and (b) an image of the same gel after silver staining. There are two sample bands on the fluorescence image: the thicker Band 1 (red arrow) right above the thinner Band 2 (black arrow). Band 2 is more visible on the silver stained gel. (c) The two phosphorylation sites Ser281 and Ser 210 in magenta. (d) The Asn-Ile-Ser *N*-glycosylation sequon is labelled by magenta sticks around K^+ ion in purple sphere. (e) The two cysteine residues C45 and C71 on EGFP are labelled in magenta.

To investigate in this direction, we purified secreted GINKO2a protein from HEK293 cells. The secreted GINKO2a fluoresces and shows two bands close to the expected size of 47 kDa: the

more fluorescent band is of less quantity according to the silver stained gel (**Fig. 4.5a**). The spectral reading suggests that the secreted GINKO2a is non-responsive to K^+. In collaboration with Carlos Gonzalez and David Gonzalez at University of California San Diego, we performed mass spectrometry on the bands cut out from the silver stained gel. The results not only verified the identity of the bands, but also suggested two phosphorylation sites, Ser210 and Ser291, which are both exposed to the aqueous environment according to their locations on the crystal structure, and therefore accessible to kinases (**Fig. 4.5c**). To eliminate these two phosphorylation sites, site-directed mutagenesis was performed to create variants: S210A, S281A, S210A/S281A, S210E, S281E, and S210E/S281E. Replacing serine with alanine removes the hydroxyl group phosphorylation while glutamic acid mimics phosphorylated serine[291]. Unfortunately, these mutations also failed to rescue the K^+ response of GINKO2a on the cellular membrane.

Although not shown in the mass spectrometry, we also searched for possible glycosylation via an online server (http://www.cbs.dtu.dk/services/NetNGlyc/). The server indicated a potential *N*-glycosylation site at Asn241 of Asn-Ile-Ser sequon at the K^+ binding pocket (**Fig. 4.5d**). Asn-X-Ser is a commonly recognized sequon for *N*-glycosylation. With site-directed mutagenesis, we created N241A, N241Q, and N241D, but all of them are dim and non-responsive to K^+ (**Table 4.1**). Asn241 may be of importance due to its location at the ligand binding site. As suggested by previous report, the second residue of Asn-X-Ser sequon can affect *N*-glycosylation efficiency: Tryptophan, glutamate, aspartic acid, and leucin can notably reduce the glycosylation[292]. However, variants of I242W, I242E, and I242D failed to respond to K^+; I242L is the only variant with very weak K^+ response (**Table 4.1**). We also treated the purified HEK-cell secreted GINKO2a ΔQHDK with PNGase-F *in vitro* to remove potential *N*-glycosylation, but the treated protein did not respond

to K^+, suggesting *N*-glycosylation may not be the cause for the functional loss of membrane-tethered GINKO2a.

The disulfide bond could not be detected in the regular mass spectrometry, therefore, is another possible post-translational modification worthy of investigation. There are three cysteine in the membrane bound GINKO2a sequence: one on Fzd7 leader peptide and two on the GFP. The cysteine on Fzd7 can potentially form disulfide bonds with other cysteines, because frizzled protein receptors have been reported to form critical disulfide bonds within their cysteine-rich N terminus[293]. To test whether the cysteine in Fzd7 leader test may lead to disulfide bond, I searched for other frizzled protein receptor leader peptides, specifically looking for the ones without cysteines. Fzd2 and Fzd4 were used to replace Fzd7 for the purpose and neither of them succeeded in membrane targeting. The two cysteine on GFP are Cys49 and Cys71 (**Fig. 4.5e**). They were mutated to alanine to create variant C49A/C71A, which is not fluorescent. The variant is dark. To rescue the brightness for testing K^+ response, we performed a round of directed evolution on the double mutant, but no bright colonies were found. To narrow the mutations to the sites of interest, I performed site saturation on the double mutant. The sequences of bright variants all contain a reverted cysteine. This suggest the cysteines are either important for the chromophore environment that is necessary for GFP fluorescence or essential for GFP folding and maturation. We also treated the secreted GINKO2a with β-mercaptoethanol to remove disulfide bonds. The result shows the treated samples have the same spectrum as the untreated control, suggesting that the disulfide may not be responsible for the loss of function.

Overall, the investigation of phosphorylation, *N*-glycosylation, and disulfide bonds suggested these post-translational modifications might be irrelevant to the functional loss of GINKO2a on the membrane and factors other than PTMs should be explored.

4.2.4. SpyTag-GINKO for anchoring purified GINKO from E. coli to the mammalian membrane

To investigate whether the membrane environment itself is the cause of the functional loss of GINKO2a, we purified GINKO from *E. coli* and attached it to the cell surface using SpyCatcher and SpyTag, which spontaneously form a covalent link in the aqueous environment. The SpyCatcher-mApple was expressed on the membrane of mammalian cells and SpyTag-GINKO2a was expressed by *E. coli* and purified. We first tested SpyTag-GINKO2a to confirm it perform consistently with GINKO2a *in vitro* (**Fig. 4.7a**). We then added the purified SpyTag-GINKO2a to HeLa cells expressing SpyCatcher-mApple by incubation followed with washing two times with HHBSS to remove the unattached SpyTag-GINKO2a in the solution. Cellular images suggest successful attached of SpyTag-GINKO2a to the cell membrane (**Fig. 4.6a**). In parallel, we used super ecliptic pHluorin pH biosensor (SEP) as a control (**Fig. 4.6b**). A time-lapse video was taken with increasing in K^+ concentration over time. GINKO2a shows an approximate 20% increase in green fluorescence and SEP remains mostly constant (**Fig. 4.6c and d**), while the mApple undergoes substantial photobleaching during the time course. The attached SpyTag-GINKO2a has a small fluorescence change at the low K^+ range but attenuated in the higher K^+ range (**Fig. 4.6e**). This small K^+ response suggests attached GINKO2a becomes partially functional on the membrane.

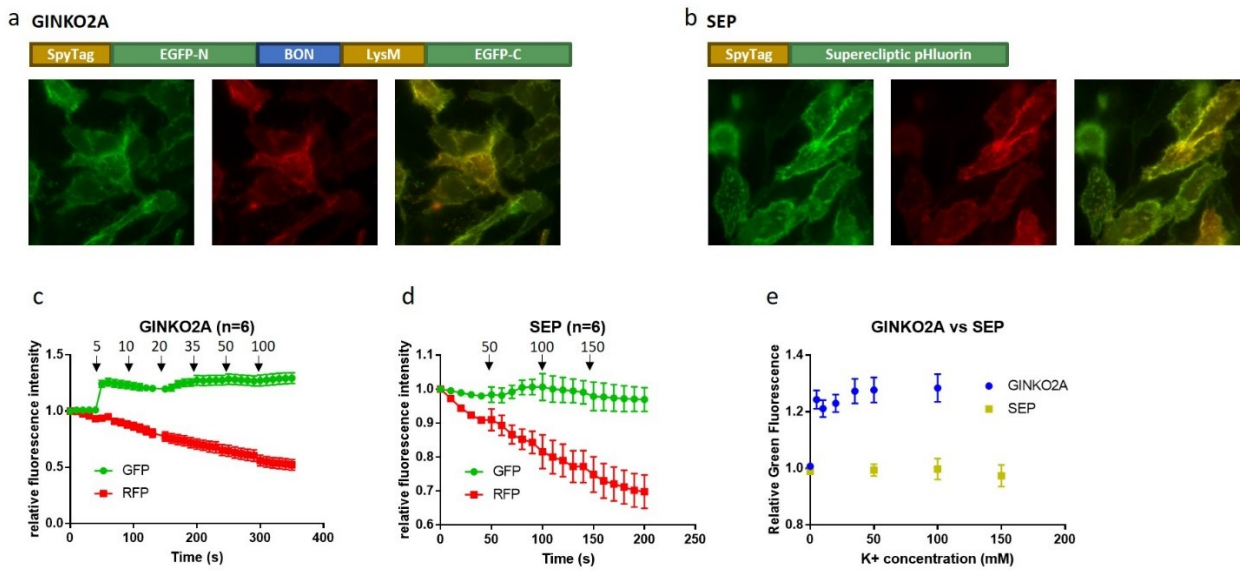

Figure 4.6. Tagging purified GINKO2a to membrane with SpyTag-SpyCatcher.

SpyTag was purified from *E. coli* and added to mammalian cells expressing SpyTag-mApple for spontaneous covalent linkage. The green, red, and merged images of SpyTag-mApple expressing HeLa cells incubated with (a) SpyTag-GINKO2a and (b) SpyTag SEP. Time lapse imaging measurement of both green and red fluorescence with increasing K^+ (additions indicated by arrows in mM) over time are represented in (c) and (d). The additions of K^+ are indicated by black arrows and final K^+ concentrations in mM are labeled above the arrows. (c) GINKO2a shows a small increase at the initial addition of K^+ to 5 mM, but (d) SEP does not. RFP signal decreases in both cases. (e) The relative fluorescence as a function of K^+ concentration.

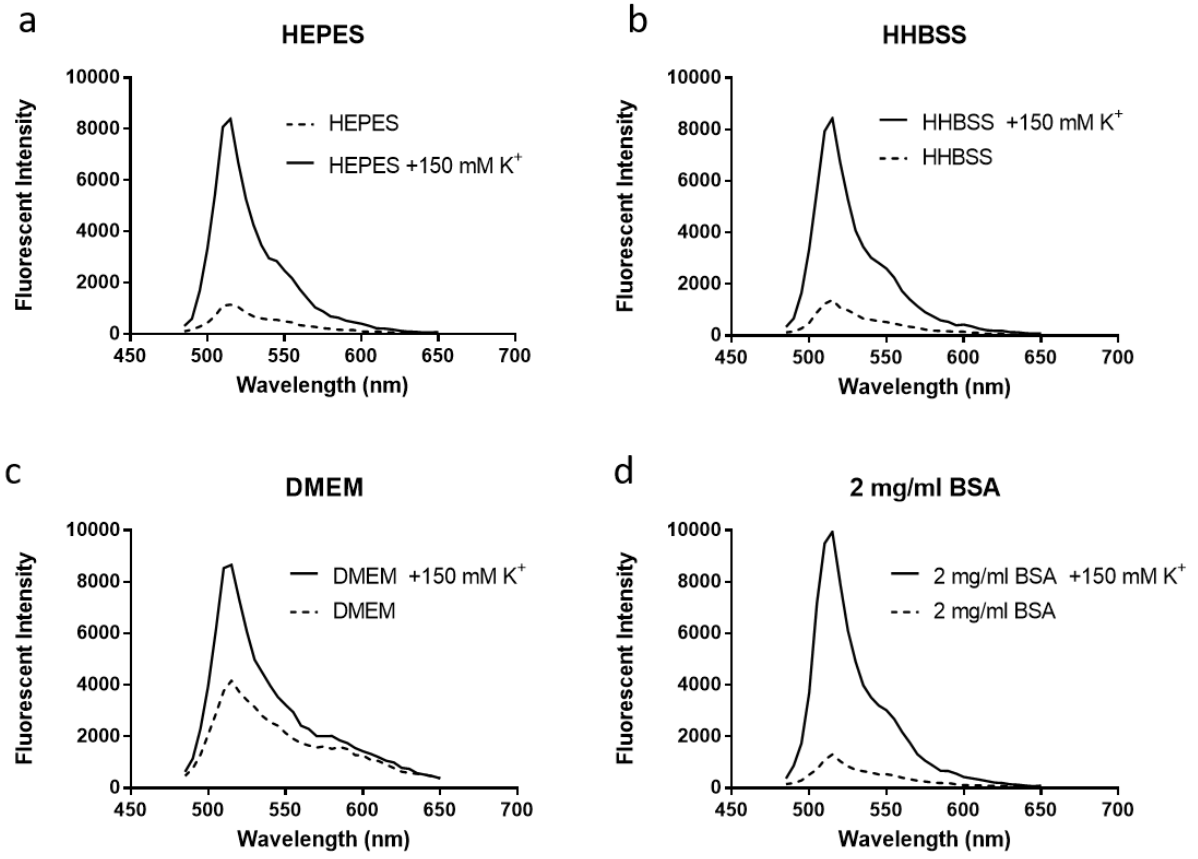

Figure 4.7. The impact of different aqueous environment to SpyTag-GINKO2a protein.

The fluorescence emission spectra of SpyTag-GINKO2a are measured with and without the addition of 150 mM K^+ in different background solutions. The spectra taken in (b) the imaging buffer HHBSS at pH 7.4 and (d) 2 mg/mL BSA are consistent to those in (a) 10 mM HEPES at pH 7.4. (c) The ones taken in the culture medium DMEM shows a slight elevated peak without the addition of K^+. This is consistent with ~5 mM K^+ in DMEM.

To investigate the possible impact of solution content, we tested SpyTag-GINKO2a in the imaging buffer HHBSS, the culture medium DMEM, as well as a solution containing 2 mg/mL BSA to test the effect of protein crowdedness. HEPES (pH 7.4), HHBSS (pH 7.4), and 2 mg/mL BSA appear to have no effect on K^+ response of purified SpyTag-GINKO2a (**Fig. 4.7b and d**);

DMEM has an elevated signal in the absence of additional K^+ due to the basal K^+ level in DMEM (**Fig. 4.7c**). Overall, these results suggested that GINKO2a is not influenced by a complex solution environment of HHBSS, DMEM, or elevated BSA concentration. Further investigation is required to understand the underlying cause of the GINKO2a function loss at the membrane.

4.2.5 Engineering towards a GINKO with higher K^+ affinity

The affinity of GINKO also need to be addressed as the K^+ concentration is much lower in the extracellular space than in the cytosol[294]. To generate a desired GINKO with a higher affinity, we examined the residues at the binding site. As the K^+ ion is coordinated by the backbone carbonyl of six amino acids as shown in **Fig. 4.8a**, it poses difficulties to rationally design residue mutations for affinity tunning. Instead, a proline scan was performed on the residues around the ligand binding site to understand how much these sites can tolerate perturbation[295]. Proline shows a detrimental effect on residue 224 to 228 but less so for residue 154 to 159 (**Table 4.2**). Except for V154, all of them are targets for site saturation that could be used to fine-tune the affinity. Ala228 was also investigated due to its proximity to Lys155. We proposed that mutating Ala228 to polar or oppositely charged residue can allow interactions that change the binding pocket: the two side chains may work as a clamp to influence the positions of the backbone carbonyl groups (**Fig. 4.8b**). The experimental data show the two side chains do not work in such way as A228S and A228D did not show much difference to GINKO2a (**Table 4.2**).

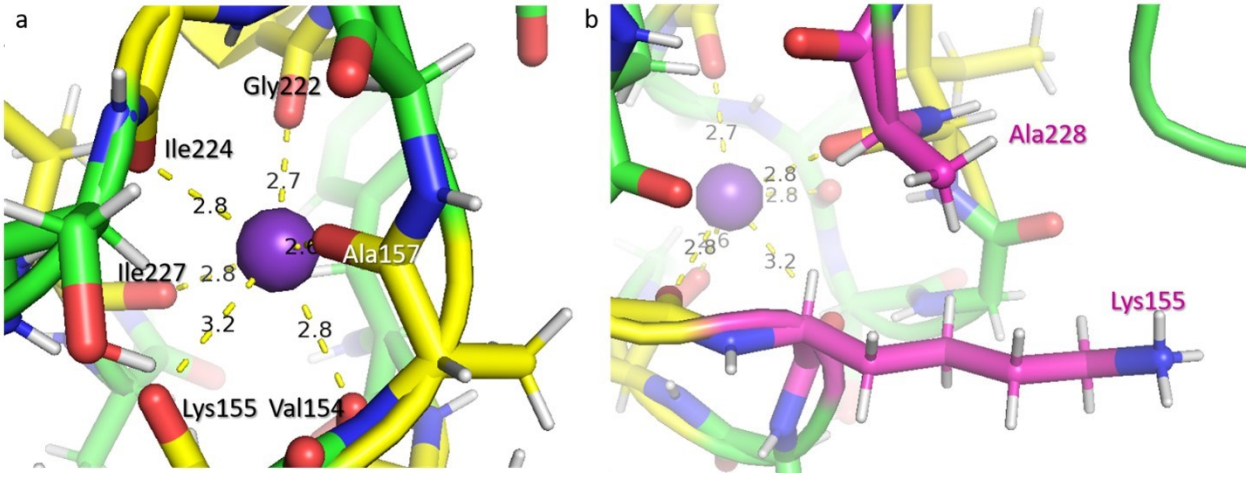

Figure 4.8. Altering GINKO affinity with sites around the K^+ binding site.

(a) The binding pocket for the K^+ ion. (b) The side chain of Lys155, a K^+ binding residue, is in proximity to the side chain of Ala228. Mutating the two residues to form interactions can potentially tighten the binding pocket like a clamp.

The deleted QHDK region was also investigated. Instead of deletion, they were mutated to DD and DDED for increased acidity to potentially attract K^+. Titrating the variants with K^+ shows that QHDK to DD variant has a lower K_d at 4.88 mM (**Fig. 4.9a** and **Table 4.3**). Both variants do not respond to Na^+. The pH profiles of both remain the same as well (**Fig. 4.9b**).

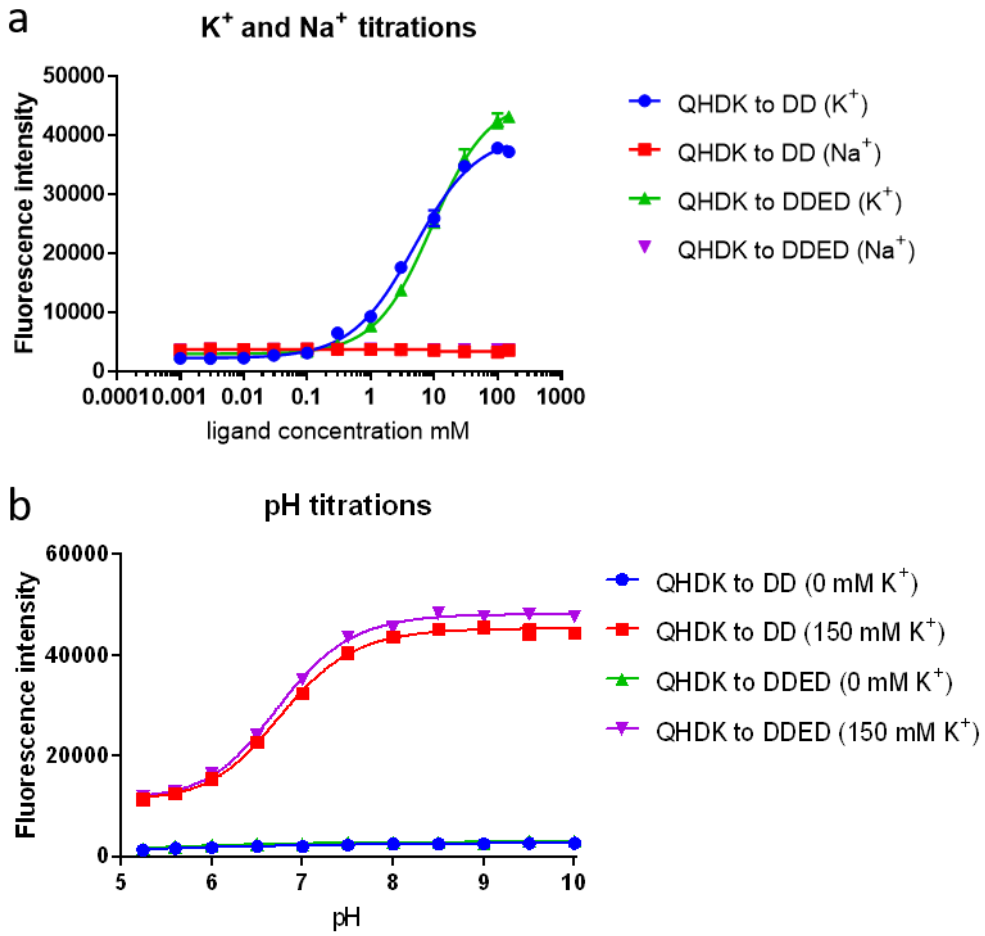

Figure 4.9. Titrations for variants replacing QHDK with DD or DDED.

(a) K^+ and Na^+ titrations and (b) pH titrations of variants with QHDK replaced by DD and DDED.

4.3 Conclusion and future work

The *E. coli* Kbp led to many challenges that prevented GINKO2a from being a successful membrane anchored K^+ biosensor. Although the Fzd7 leader peptide allowed GINKO2a secretion, the function of the membrane bound GINKO2a was lost. The troubleshooting included examining the cleavage in the secretory pathway and seeking for potential post-translational modifications. Later, SpyTag experiment showed the membrane environment may contribute to the loss of

function as well. Kbp may interact with the membrane lipid or sugar moieties; alternatively, it may be modified by enzymes on the membrane. The troubleshooting led to more questions than answers. As this project is still under active investigation, we will be further exploring other leader peptides. Despite the challenges so far, a successful membrane targeted K^+ indicator remains appealing to the user community where a membrane-displayed K^+ indicator will enable monitoring of key extracellular K^+ changes in tissue cultures or animal models for biomedical research of some diseased conditions.

4.4 Method

Plasmid DNA construction

Vectors of pDisplay and pAMEX were kindly provided by Dr Yi Shen and Dr Yusuke Nasu. ER and Golgi export tags and the GPI anchor were synthesized by Integrated DNA Technologies (IDT) as a double-stranded DNA fragment. Fzd7 sequence was provided by Dr Yi Shen. DNA fragments were PCR amplified using Q5 polymerase and then cloned into the pcDNA3.1, pDisplay, or pAMEX expression vector using Gibson assembly (New England Biolabs). All constructs were verified by DNA sequencing.

In vitro characterization

The indicator proteins were expressed as His-tagged recombinant proteins in *E. coli* and purified with Ni-NTA beads as described in Chapter 2 (Ref. 1). For K_d determination, purified protein was diluted into a series of buffers with K^+ concentration ranging from 0 to 150 mM. The fluorescence spectrum of the GINKO2a variants in each solution (100 μL) was measured using a Tecan Safire2 microplate reader with excitation at 410 nm and emission from 430 nm to 650 nm. Titration experiments were performed in triplicate. The fluorescence intensities were plotted as a

function of K^+ concentration. Data was analyzed using Graphpad Prism to obtain apparent K_d and the apparent Hill coefficient. The measurement of extinction coefficient and quantum yield was performed as describe[281]. The brightness was calculated as the product of these values with a unit of $mM^{-1}cm^{-1}$.

Live cell imaging

HeLa or HEK293 cells were maintained in Dulbecco's modified Eagle medium (DMEM) supplemented with 10% fetal bovine serum (FBS, Thermo Fisher Scientific), Penicillin-Streptomycin (Thermo Fisher Scientific), and GlutaMAX (Thermo Fisher Scientific) at 37°C with 5% CO_2. Cells with 60–70% confluence on 35-mm glass-bottom dishes (In Vitro Scientific) were transfected using Turbofect (Thermo Fisher Scientific) according to the manufacturer's instructions. Cells were imaged approximately 24 h after transfection. Immediately prior to imaging, medium was replaced with 1 mL of 20 mM HEPES buffered HBSS (HHBSS) at pH 7.4. Cell imaging was performed with a Zeiss Axiovert 200 microscope with a 40× objective. HeLa images were processed using ImageJ.

HEK293 cells were used to express Fz7-GINKO2a with a His tag for secretion. The cells at a 50% confluence on a 150 mm cultural dish or in a 75 cm^2 cultural flask were transfected with pcDNA Fz7-GINKO2a with Turbofect and incubated for 3–5 days in DMEM supplemented with 2–4% FBS, Penicillin-Streptomycin. The medium was collected and replaced with new medium every 1–2 days. The Fz7-GINKO2a in the medium was purified with Ni-NTA beads. The protein was run on pseudo-native gel[296] and stained with silver[297] as previously described.

Chapter 5 Optimizing dimerization-dependent fluorescent proteins

5.1 Introduction

Dimerization-dependent fluorescent proteins (ddFPs) are valuable tools for the development of biosensors as in previously reported Ca^{2+} indicator and Caspase activity indicator[298].They were created in the Campbell lab by Dr. Spencer Alford as tools for detection of protein-protein interactions and were further demonstrated in the fluorescent protein exchange (FPX) technology by Dr. Yidan Ding with which bi-colour biosensors can be created[298–300].

Dr Alford and coworkers developed three different colour variants of ddFPs: red (ddRFP), yellow (ddYFP), and green (ddGFP). Each pair consists of a bright A copy and a dark B copy[299,300]. A copies are named RA, GA, and YA for ddRFP, ddGFP, and ddYFP, respectively, while B copies are named RB, GB, and YB. The fluorescence brightness of A copy is enhanced when fused to a B copy by a short linker (**Fig. 5.1a and b**). The affinity of A copy to B copy is adjusted such that the dimerization does not occur spontaneously unless they are in proximity. When A copy and B copy are fused with different proteins of interest, ddFPs work like fridge magnets: if the proteins of interest interact with each other, the A and B copies will be brought sufficiently close, enabling dimerization and increasing the fluorescence intensity.

Incidentally, RB (B copy of ddRFP) was later found to have a reasonable affinity to both RA ($K_d = 40 \pm 8$ μM) and GA ($K_d = 40 \pm 8$ μM)[298]. Dr. Ding utilized this unique finding to design FPX where a B copy can swap its A copy from RA to RB or vice versa[298]. During changes in protein-protein interactions, this affinity provides ratiometric fluorescence intensity increase in one colour and respective decrease in the other. (**Fig. 5.1c**).

ddFPs were well expressed in HeLa cells and function as designed. However, when they are expressed in cells with reduced protein expression levels, such as neurons, the brightness can

be insufficient for some experiments and can be potentially be compensated for by brighter variants. With the goal of improving their brightness of ddFPs, I generated new ddFPs using directed evolution and tested the new variants *in vitro* and *in situ*.

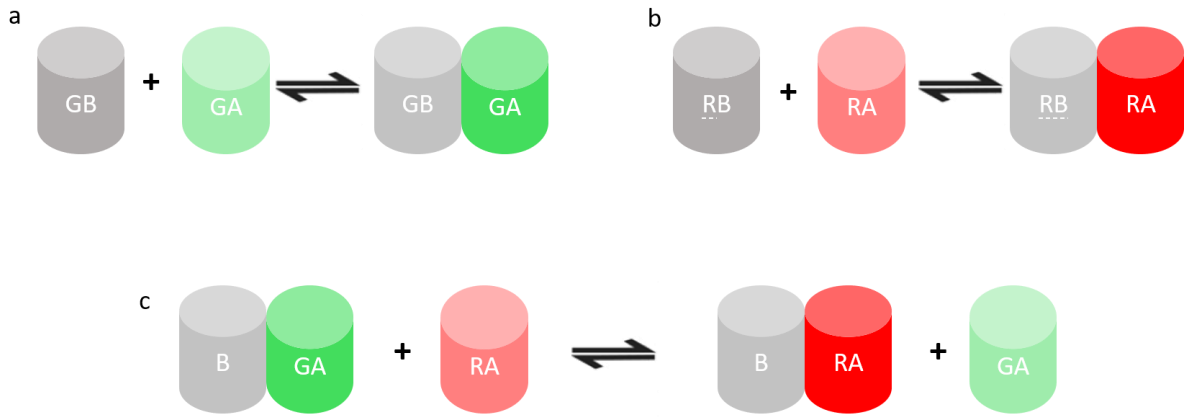

Figure 5.1. The general scheme of ddFPs.

The intensiometric ddFPs includes a (a) ddGFP and (b) ddRFP. The A copies are fluorescent, and the B copies are dark. The fluorescence intensity of an A copy is enhanced by heterodimerization. (c) RB can dimerization with both GA and RA. When ddRFP and ddGFP are used in combination, RB can change its dimerization partner, allowing ratiometric detection.

5.2 Results

Using directed evolution, I continued the work of Mr. Enterina of the Campbell lab in development of versions 1.7 and 1.4 for ddRFP and ddGFP, respectively. During the evolution, RB was unchanged to avoid mutations that can result in preferred dimerization to one of the A copies. Only the A copies were mutated for brightness improvement. Because RB is used for both RA and GA, I will denote RB as B for simplicity in the rest of the chapter.

Directed evolution for ddFPs was slightly modified from the original protocol (**Fig. 5.2a**). The error-prone PCR of the gene encoding A copies was performed in an A-copy-only pBAD vector to avoid PCR error from high sequence similarity between the A and B copies. The PCR fragments with mutations were ligated into a vector fusing the genes of the A copy libraries to the B copy via a linker containing a lysine residue for screening. I selected bright colonies seeking brighter heterodimers. Colonies were picked and screened with the lysate assay in which sample fluorescence was measured before and after the treatment with trypsin—which recognizes the lysine in the linker—to select variants that retain some reasonable intensity change (**Fig. 5.2b,c**).

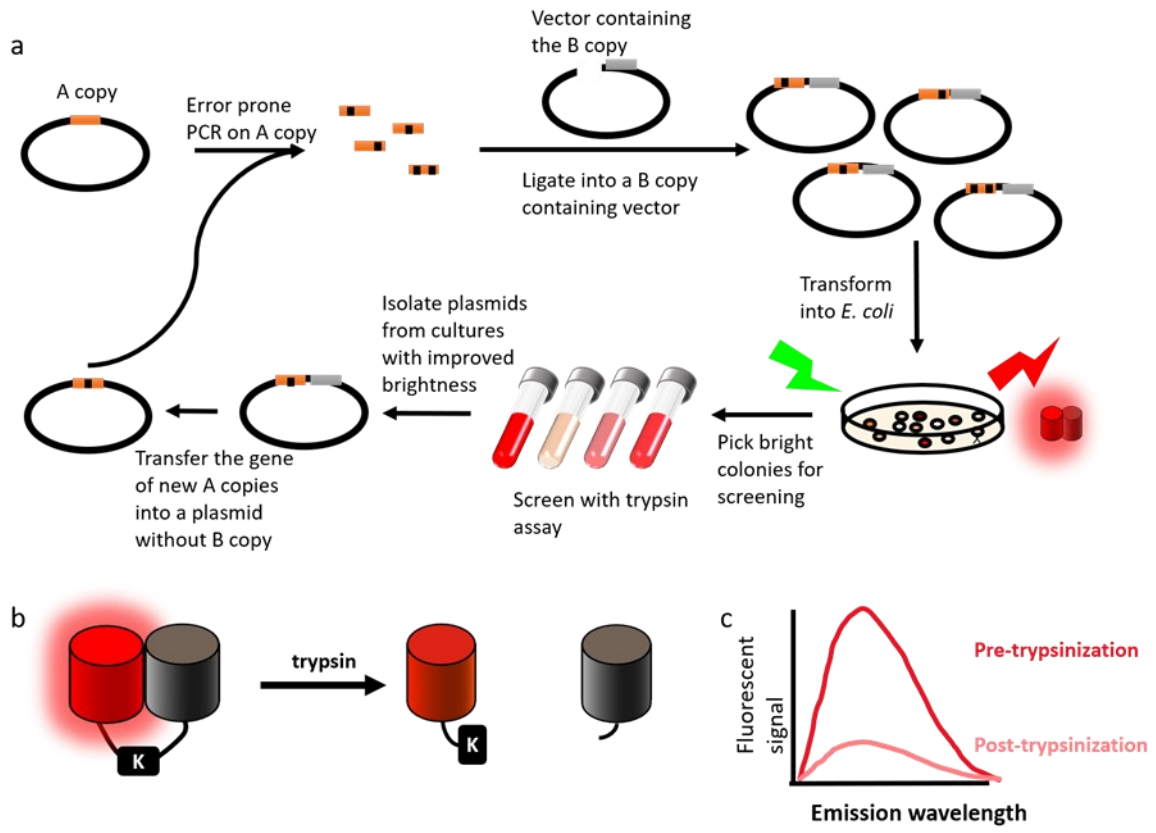

Figure 5.2. The directed evolution procedure for ddFPs.

(a) The error-prone PCR of ddFPs was performed on a pBAD vector containing only the A copy (RA or GA). The PCR fragments were digested then ligated into a vector containing a B copy (in

gray). *E. coli* DH10B cells transformed with the ligation products were plated and the bright colonies were picked for further screening in *E. coli* culture lysate screening. Winning variants were submitted for sequencing and used as the template for the next round of directed evolution. (b) The lysate assay used during directed evolution. The RA-B or GA-B fusion protein was treated with trypsin to cleave the linker. (c) The fluorescence readings were measured before and after the trypsin treatment to measure the intensity change.

The improvement for ddGFP is marginal. The streaked plate of *Escherichia coli* expressing ddGFPs, including GA_0, GA_0-B, $GA_{1.4.33}$, and $GA_{1.4.33}$-B, shows that $ddGFP_{1.4.33}$ failed to present substantial improvement when expressed (**Fig. 5.3a**). The numbering for the variants include three numbers: the first number is 1 in this work, indicating the variant is based on the first generation ddFP and not quite mature to be named as the second generation; the second number suggests the number of the library for screening; the third number is the colony number in the library. For example, GA1.4.33 means the 33rd colony in the 4th library of GA based on the first generation of GA. The heterodimers of $ddGFP_{1.4.33}$ and $ddGFP_{1.4.39}$ are approximately 50% brighter than the original $ddGFP_0$ heterodimer in the *E. coli* lysate assay. The dynamic range for $ddGFP_{1.3}$ and $ddGFP_{1.4.33}$ remained roughly 45, but that of $ddGFP_{1.4.39}$ was reduced to less than 10 (**Fig. 5.3b**). The lysate assay can be biased by incubation time and effectiveness of trypsin. To verify the results, I characterized purified ddFP dimers and monomers as shown in **Fig. 5.3e**. The brightness measurements showed $ddGFP_{1.4.33}$ and $ddGFP_{1.4.39}$ increased their dimer fluorescence intensities for 30% and 15%, respectively, which is consistent with the lysate assay results. The overall brightness, defined to be the product of extinction coefficient and quantum yield, of ddGFPs is below 10, much dimmer than the EGFP control (brightness = 37.5)[233]. The dynamic range, contrary to the lysate assay, was at a similar level to $ddGFP_0$ for both variants with a number that

ranges from 10 to 20. The overall results suggested that improvement of ddGFP were not observed. The discrepancy suggests possible increased expression levels for the new ddGFP variants.

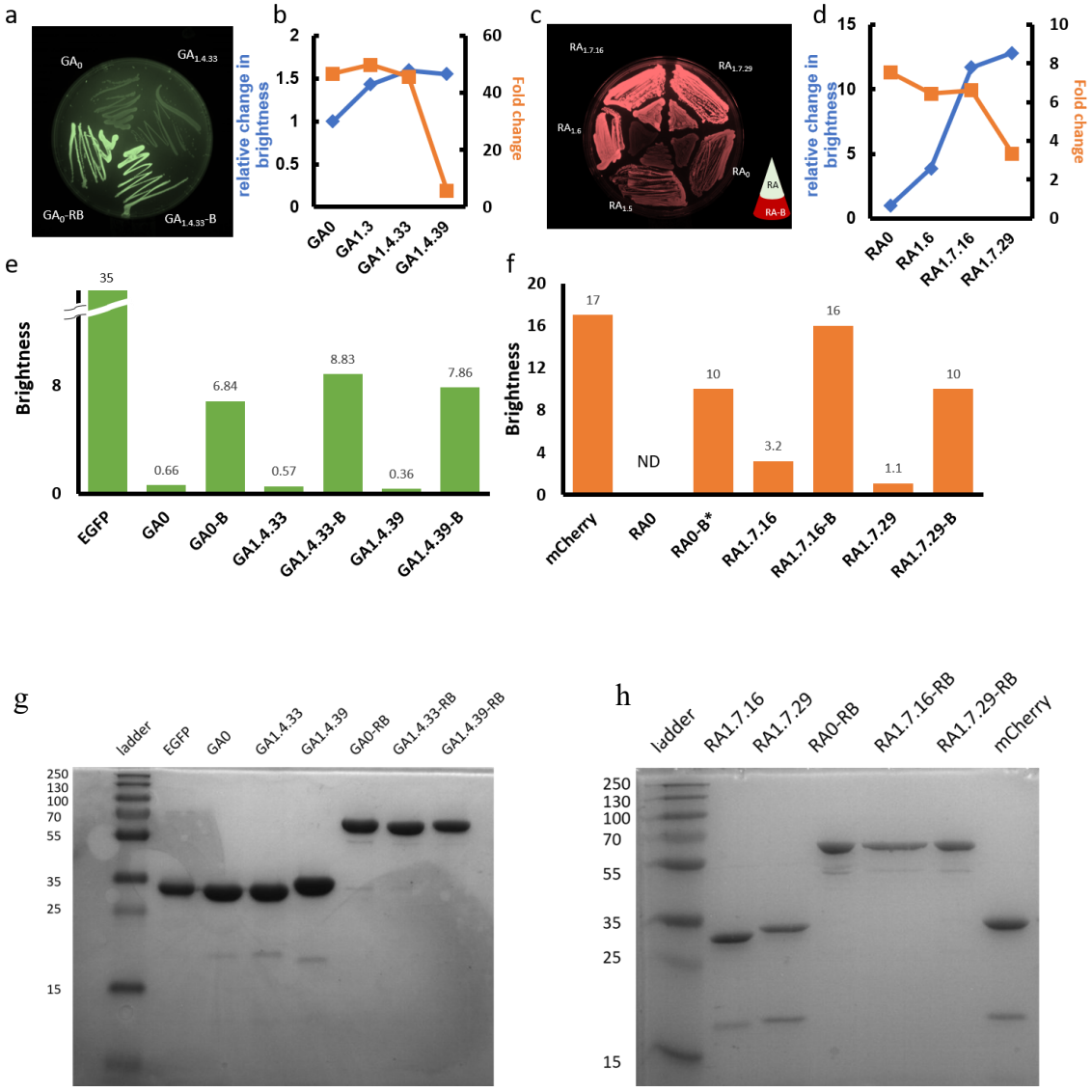

Figure 5.3. The preliminary data of brighter ddFP variants.

(a) *E. coli* expressing the brighter ddGFP variant $GA_{1.4.33}$ and GA_0 were plated in monomer and heterodimer forms. (b) The brightness of new green variants was 50% better than $ddGFP_0$; however, the fold change dropped substantially. (c) *E. coli* expressing ddRFP variants $RA_{1.7.16}$, $RA_{1.7.29}$, $RA_{1.6}$, $RA_{1.5}$ and RA_0 were plated with monomers in the middle of the plates and heterodimers in the outside circle. (d) The brightness increased substantially after directed

evolution and the dynamic range in intensity decreased dramatically. The comparison of green ddGFP (e) and ddRFP (f) in both monomer and heterodimer forms. The purified ddFP monomers and dimers were verified by SDS-PAGE.

Conversely, new ddRFP variants met the objective and showed brighter fluorescence. *E. coli* expressing selected variants, $ddRFP_{1.7.16}$, $ddRFP_{1.7.29}$, as well as $ddRFP_{1.6}$, are much brighter than the ones expressing $ddRFP_0$ on an agar plate (**Fig. 5.3c**). These results are congruent with the enhanced fluorescence of new variants shown in the lysate assay in **Fig. 5.3d**. The $ddRFP_{1.7.16}$ and $ddRFP_{1.6}$ retained a similar dynamic range as that of $ddRFP_0$, but $ddRFP_{1.7.29}$ dropped its fold change to 3. The purified protein characterization shows that there is 60% brightness improvement for $ddRFP_{1.7.16}$ and no improvement $ddRFP_{1.7.29}$ relative to $ddRFP_0$ (**Fig. 5.3f**). These results suggest that the increasing brightness observed on the agar plate and in the lysate assay are mostly likely due to an increase in protein expression level. The fold change is 5 for $ddRFP_{1.7.16}$ and 9 for $ddRFP_{1.7.29}$. Both are acceptable. This suggests that $ddRFP_{1.7.16}$ may be the only variant warranting further studies.

I tested the new ddFP variants in HeLa cells to see whether the new variants are truly brighter in a mammalian system. I used two previously published constructs[298]: a CaM-RS20 triple ddFP construct and a Caspase-3 triple ddFP construct as illustrated in **Fig. 5.4**. The equilibrium shifts towards to RA-B dimerization when Ca^{2+} binds to CaM-RS20 as described in **Fig. 5.4a** When histamine is applied to cells expressing caspase-3 triple ddFP, the intracellular Ca^{2+} fluctuates, leading to fluctuations of the ratio of red to green fluorescence[298]. To evaluate the improvement on the brightest of new ddFPs, one of RA_0 and GA_0 was replaced with a new version (**Fig. 5.4b**).The CaM-RS20 constructs with new ddFP variants exhibited small fluctuations in response to histamine treatment, which prevents comparisons of the new variants to the first

version. Similarly, caspase-3 cleaves at the DVED sequence when activated by TNF-α, which subsequently favours the dimerization of ddRFP as GA is cleaved off from the polypeptide (**Fig. 5.4c**)[298]. Due to cell-to-cell variation in expression level and caspase-induced ratiometric change, results were inconclusive and thus no solid conclusion can be interpreted from this data.

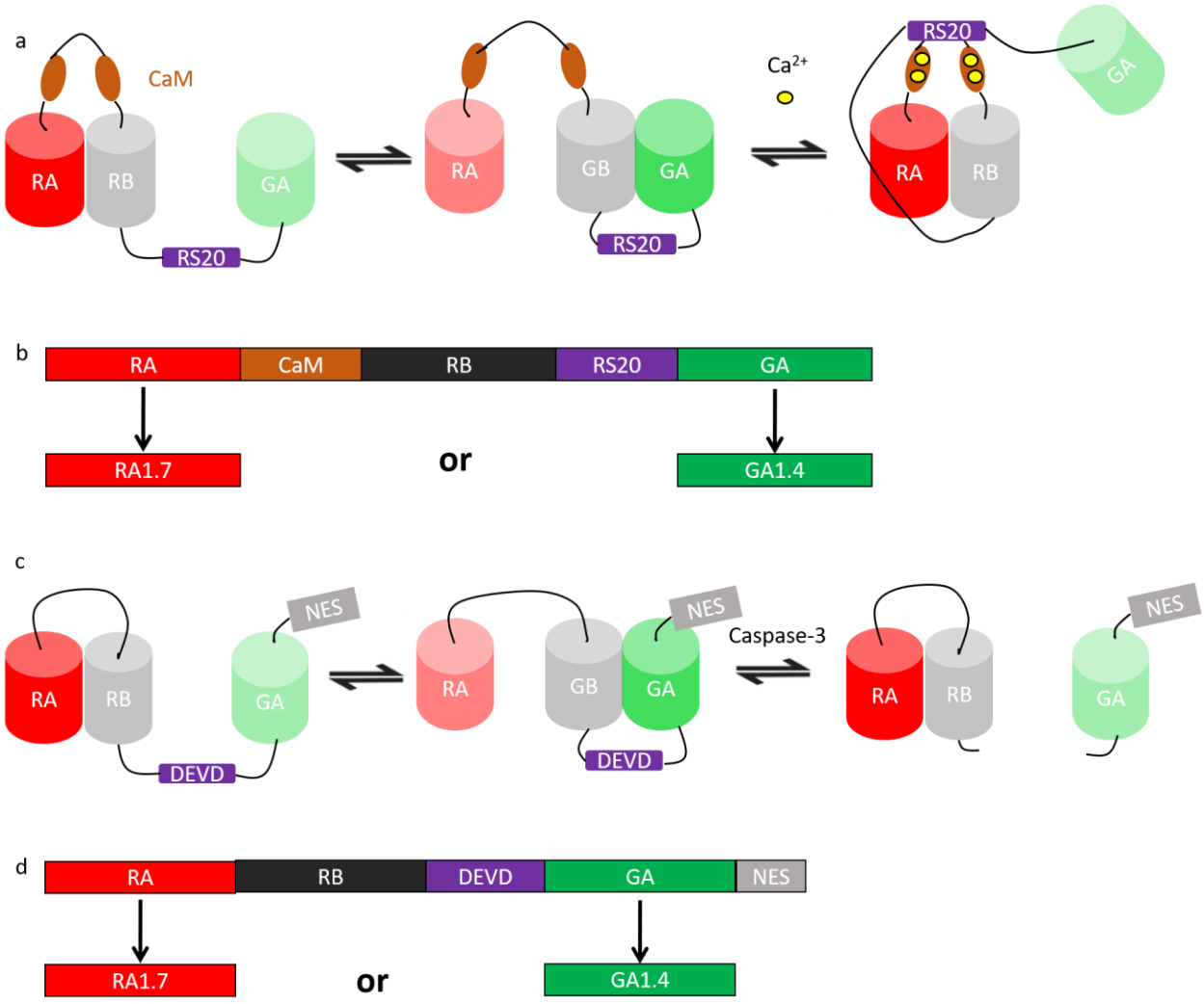

Figure 5.4. HeLa cell constructs to verify improvement of ddFPs.

(a) The scheme of CaM-RS20 triple FP construct. The red fluorescence is expected to increase in presence of Ca^{2+}. (b) The sequence topology of CaM-RS20 triple FP construct. (c) The scheme of Caspase-3 triple FP construct. (d) The sequence topology of Caspase-3 triple FP construct.

5.3 Conclusion

The engineering of ddGFP and ddRFP was conducted mainly by directed evolution to generate brighter variants. After thorough examination with the lysate assay and purified protein characterization, I determined that the new $ddGFP_{1.4.33}$ and $ddGFP_{1.4.39}$ did not display any substantially improved brightness. On the other hand, the apparent improvement in brightness of ddRFP new variants in the lysate assay were not as substantial with purified protein, though $ddRFP_{1.7.16}$ was 60% brighter. Further testing in HeLa cells showed inconclusive results. All these results suggest ddFPs require more engineering to improve their *in vitro* brightness first to fulfill my goal.

5.4 Methods

Directed evolution

The directed evolution procedure is modified from a previously described procedure in Ai *et al*. [281]. The error-prone PCR is performed on a pBAD vector containing only the A copy in duplicate with 15 and 30 μM $MnCl_2$. The different Mn^{2+} concentrations allow a library with two different mutation rates. Products of the two error-prone reactions are combined for ligation in a vector containing a B copy. The linker before B copy has a sequence of GTGSTKSGSSGT where K is designed to be cleaved by trypsin.

Lysate Assay

E. coli DH10B expressing library variants were cultured in LB with 100 μg/mL ampicillin and 0.02% arabinose at 37°C overnight. The cells were lysed with BPER reagent from Thermo Fisher at room temperature with vortexing. After spinning at 10,000 rpm for 20 min, the supernatant was transferred to a 96-well plate for the assay. Excess amount of trypsin is added to

the supernatant for 20 min at room temperature. Fluorescence readings were taken before and after trypsinization for comparison.

Protein purification and SDS-PAGE

ddFP monomers and heterodimers linked to a His tag were expressed by *E. coli* DH10B and purified with Ni-NTA as previously described[296]. The purified proteins were run on a 12.5% polyacrylamide gel with heat denaturation by DTT and boiling as previously described[301]. The prestained molecular weight marker (Bio-Rad) was used as a size standard. The gel was commassie-blue stained for band visualization.

Construct building for Caspase-3 triple ddFP and CaM-RS20 triple ddFP

The construct is based on Dr Ding's constructs[298]. The sequence of the CaM-RS20 triple ddF is *XhoI-RA-KpnI-Calmodulin-BamHI-B3-EcoRIRS20-KpnI-GA-NES-HindIII*. The sequence of the Caspase-3 triple ddFP is *HindIII-RA-KpnI-XhoI-B-BamHI-DEVD-GA^{NES}-XhoI*. The corresponding FastDigest restrictions enzymes (ThermoFisher Scientific) and T4 ligase (ThermoFisher Scientific) were used to replace one of the A copies with a new version.

Cell culture and imaging

HeLa cell culture and imaging were performed with previously described procedures with some modifications[298]. The HeLa cells were cultured in Dulbecco's modified Eagle medium (DMEM) supplemented with 10% fetal bovine serum (FBS) at 37°C and 5% CO_2. Transient transfections of pcDNA3.1 expression plasmid carrying caspase-3 triple ddFP or CaM-RS20 triple ddFP were performed with Turbofect (Thermo Scientific) according to the manufacturer's instruction. After 24–48 hours of incubation, the cells are subject to three washes with PBS buffer and then treated with histamine or TNF-α in HHBSS for CaM-RS20 triple ddFP construct and Caspase-3 triple ddFP construct, respectively. For CaM-RS20, cells were imaged immediately

after the treatment. For Caspase-3, cells were incubated 20–30 min at 37°C in TNF-α before being imaged. The imaging was performed on a Zeiss Axiovert 200M equipped with a 75-W xenon-arc lamp, a 40× objective lens, and a 14-bit CoolSnap HQ2 cooled charge-coupled device (CCD) camera (Photometrics) driven by MetaMorph software. Filter sets had the following wavelengths/bandwidths: excitation 470/40 nm, dichroic mirror 495-nm dclp, and emission 525/50 nm (GFP), and excitation 535/50 nm, dichroic mirror 565-nm dclp, and emission 585/29 nm (RFP).

Chapter 6 Development of dimerization dependent FRET pair

6.1 Introduction

The project of DipdTFP was inspired by ddFP project[298–300]. The weak binding of ddFP's A copy to B copy allows them to identify protein-protein interactions with a measurable intensiometric or ratiometric fluorescence change. The ratiometric measurement provided by FPX is less likely to be influenced by photobleaching in the cells, making it an attractive option for protein-protein interaction. The drawback of FPX is the requirement of at least three ddFPs, which led to the proposal of this project: to create a dimerization dependent FRET pair that enables a double FP ratiometric measurement instead of a triple FP ratiometric measurement with FPX, and potentially with better brightness.

6.2 Results

6.2.1 Modify dTFP surface to generate a new TFP that can interact with dTomato

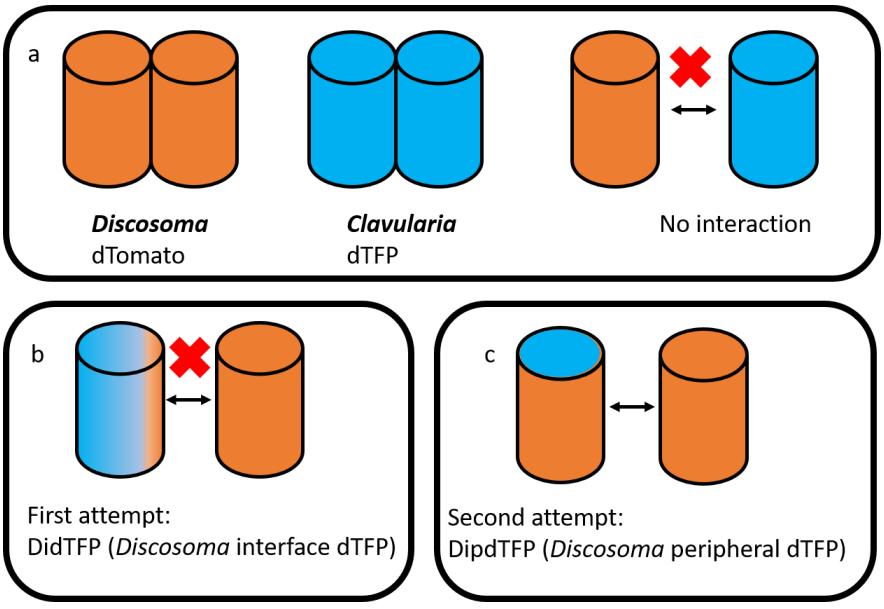

Figure 6.1. The dimerization dependent FRET fluorescent protein design with *Clavularia* dTFP and *Discosoma* dTomato.

(a) Both FPs are homodimers that do not form any heterodimers. (b) DidTFP was generated by changing the contacting interface of dTFP to that of dTomato, but it does not form heterodimer with dTomato. (c) DipdTFP was generated by changing all the exterior residues to those of dTomato and it interacts with dTomato.

This project started with a bold design of making two FPs from different organisms to interact through modification of the interface. I chose dTomato[302], a dimer red FP derived from *Discosoma* DsRed, to be one of the FRET pair because ddFPs were based on dTomato[299,300]. The other fluorescent proteins need to have an excitation or emission spectrum overlapping with the emission or excitation spectrum of dTomato to form a FRET pair. The candidates include dimer teal fluorescent protein (dTFP) engineered from *Clavularia sp.* cFP484 (Ref. 303), dimer Azami Green derived from *Galaxeidae* tetrameric Azami Green[304], as well as dScarlet evolved from *Discosoma* DsRed[258]. The first two have an emission spectrum overlapping with the excitation spectrum of dTomato, making them a potential FRET donor for dTomato. On the other hand, the spectra of dScarlet makes it a suitable FRET acceptor for dTomato. Because dScarlet and dTomato are both DsRed derived, they could be more likely to form heterodimers with some engineering. Fusing dTomato with any of the FRET partner fails to provide any substantial FRET signal possible due to the lack of interactions (**Fig. 6.1a**). To create an interaction like the one in ddFP, I sought to produce interactions for heterodimers and reduce the homodimer interaction at the same time.

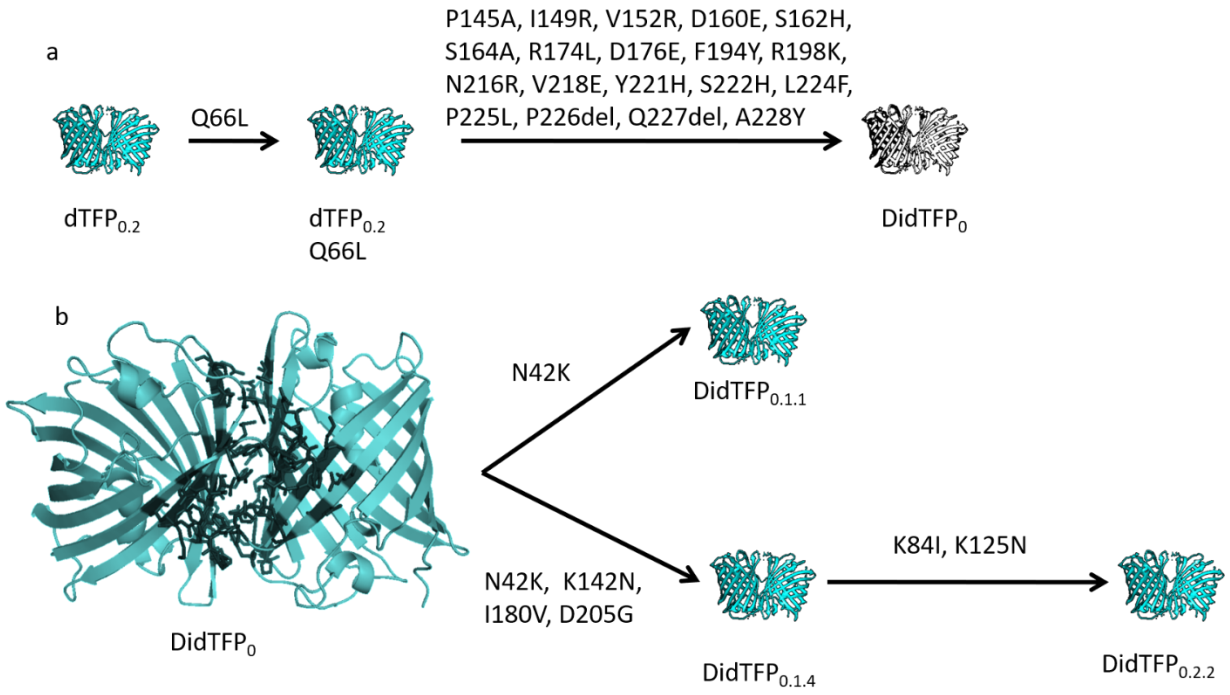

Figure 6.2. The mutations involved in the design and fluorescence rescue of DidTFP.

(a) The dTFP0.2 was used as the template for making DidTFP0. dTFP0.2 was generated by Dr. Huiwang Ai in his work to monomerize TFP from a tetramer and subsequent improvements came with a mutation of Q66L by Dr. Tam Tran. (b) The $DidTFP_0$ underwent two rounds of directed evolution for fluorescence rescue.

The first approach to make such change was to swap all the interface residues of the target FP to those of dTomato. Subsequently, target residues were identified after aligning the available structures (**Fig. 6.1b**). The changes were so detrimental that they led to dark FP in all cases, which necessitated rescues of fluorescence (**Fig. 6.2a**). I recovered the fluorescence with one round of directed evolution for TFP, but not for Azami Green or dScarlet. The newly derived TFP was denoted as DidTFP for *Discosoma* interface dTFP. The best variant from the first round of evolution, $DidTFP_{0.1.4}$, was further improved with another to yield $DidTFP_{0.2.2}$ (**Fig. 6.2b**). DidTFP forms homodimers according to its FPLC elution time when compared with the elution time of the

monomer control mCherry and the dimer control tdTomato (**Fig. 6.3**). However, DidTFPs do not interact with dTomato in a tandem dimer and their FRET response was not satisfactory as a potential FRET ddFP pair.

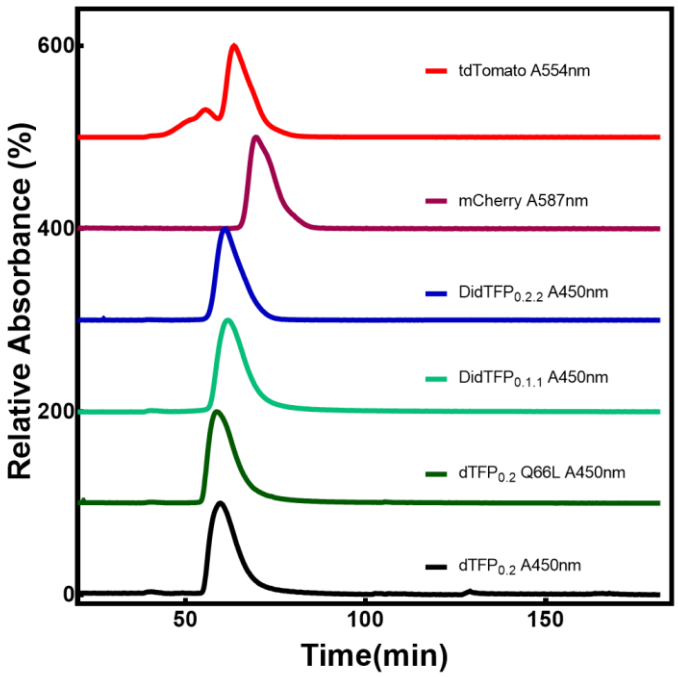

Figure 6.3. FPLC analysis of DidTFP variants.

tdTomato served as a dimer control and mCherry served as a monomer control. All dTFPs and DidTFPs eluted at the same time as tdTomato.

The second approach was used to swap all the exterior residues of dTFP to those of dTomato (**Fig. 6.1c**). The swapping is more dramatic than the first approach and inevitably led to a dark FP (**Fig. 6.4a and b**). Fortunately, the fluorescence was rescued by one round of directed evolution with several bright variants (**Fig. 6.4c**). They are named as DipdTFP for *Discosoma* peripheral dTFP. All bright variants contain a mutation at K83 (**Table 6.1**). The position of this residue is right above the chromophore, therefore, may serve an essential role in the chromophore environment (**Fig 6.4b** and **6.5a**). The brightest ones, DipdTFP$_{0.1.5}$ and DipdTFP$_{0.1.10}$, were visibly brighter on a plate (**Fig. 6.5b**) and were used for further characterization with dTomato.

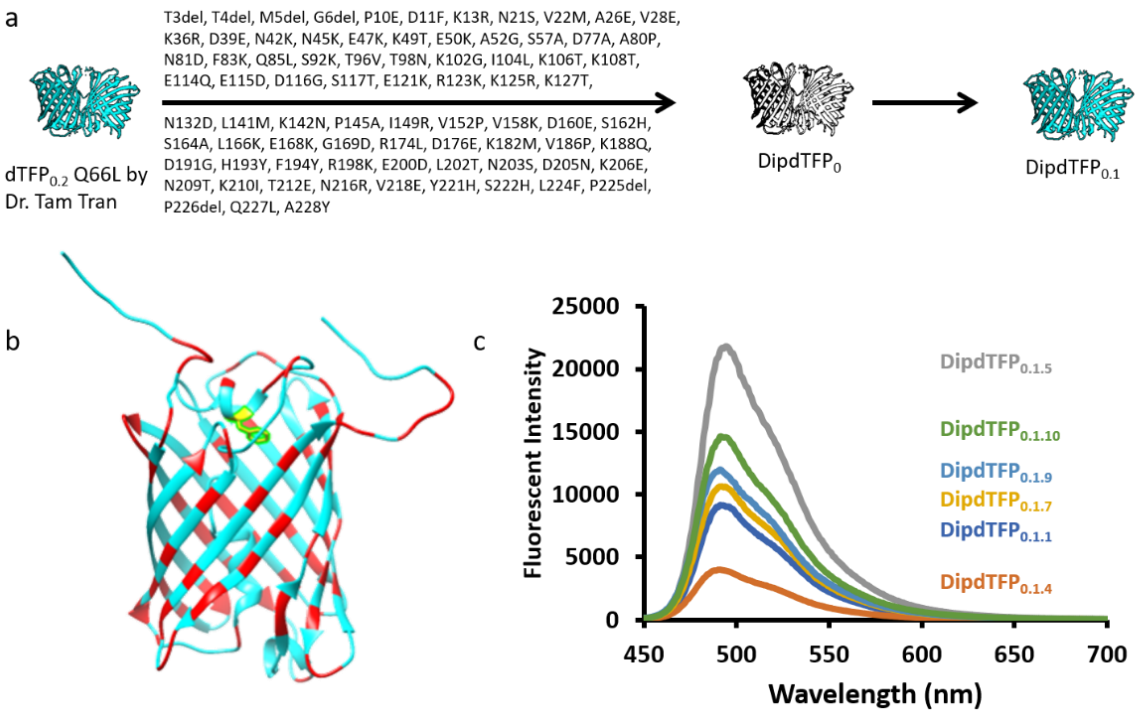

Figure 6.4. DipdTFP mutations and fluorescence rescue.

(a) The list of mutations on dTFP0.2 Q66L to generate DipdTFP0. (b) Structure of a dTFP monomer in cyan with DipdTFP mutation sites in red. F83K is labelled in yellow. (c) The lysate emission spectra of fluorescent variants of DipdTFP0.1 library.

6.2.2 Characterize DipdTFP$_{0.1}$ variants with dTomato

I characterize the interaction between DipdTFPs and dTomato with two designs: a tandem dimer (**Fig 6.6a**) and a co-expression system (**Fig. 6.6b**). The tandem dimers, DipdTFP$_{0.1.5}$-dTomato and DipdTFP$_{0.1.10}$-dTomato, yield good FRET response. When excited at 410nm for DipdTFP, they yield an emission spectrum similar to that of dTomato (**Fig. 6.6e**). Deconvolution analysis reveals a FRET efficiency of 99% for DipdTFP$_{0.1.10}$-dTomato (**Fig. 6.8d**). The absorbance spectra show a major peak for dTomato at ~560 nm and a minor peak for DipdTFP at ~460 nm (**Fig. 6.6d**) indicating both FPs are present. The 3D scan of the tandem dimers reveals two peaks for DipdTFP and dTomato as well (**Fig 6.7a and b**). A WELQut construct was designed to observe

the FRET change upon the dissociation of the tandem dimer DipdTFP$_{0.1.10}$ -WELQG-dTomato (**Fig 6.8a**). WELQut protease cuts specifically at the sequence WELQX, but the dimer does not dissociate after the cutting according to its emission and excitation spectra (**Fig 6.8b and c**). This suggests a strong affinity for the heterodimer. A pseudonative gel was performed to examine the oligomerization state (**Fig 6.6c**). DipdTFP$_{0.1.5}$ and DipdTFP$_{0.1.10}$ shows two thinner bands above the dimer size, one of which corresponds to the tetramer size. The tandem dimers dTomato-DipdTFP$_{0.1.5}$ and dTomato-DipdTFP$_{0.1.10}$ also shows bands of the same sizes indicating both cyan and red fluorescence but the tetramer band is much thicker. This suggests a possible higher state of oligomerization of DipdTFPs.

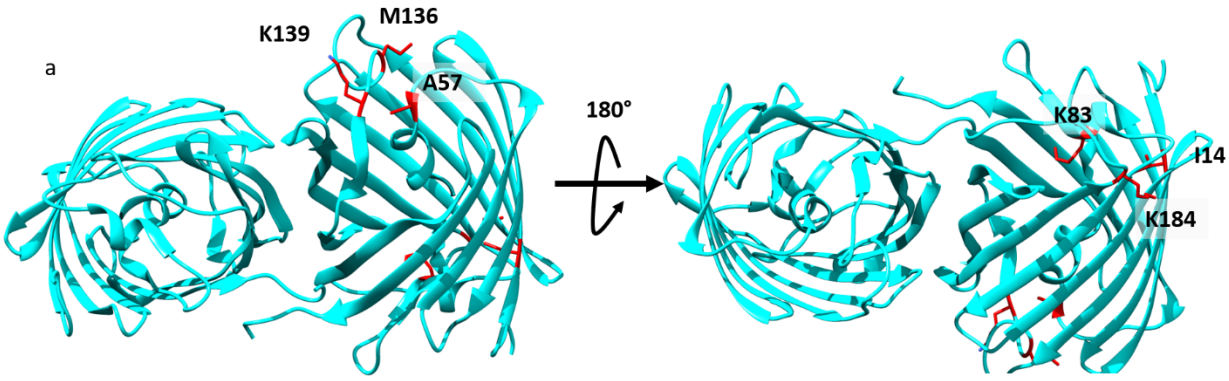

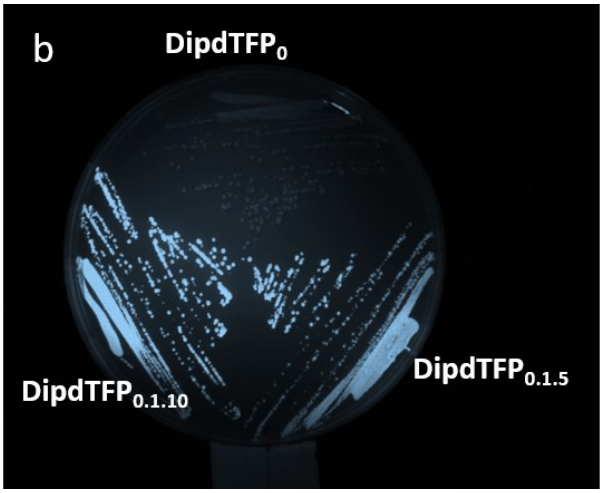

Figure 6.5. Mutations of selected variants in the DipdTFP0.1 library.

(a) The location of mutations involved in the library. (b) The streaked plate of *E. coli* expressing DipdTFP shows much better fluorescence for the new variants in the DipdTFP$_{0.1.5}$ and DipdTFP$_{0.1.10}$.

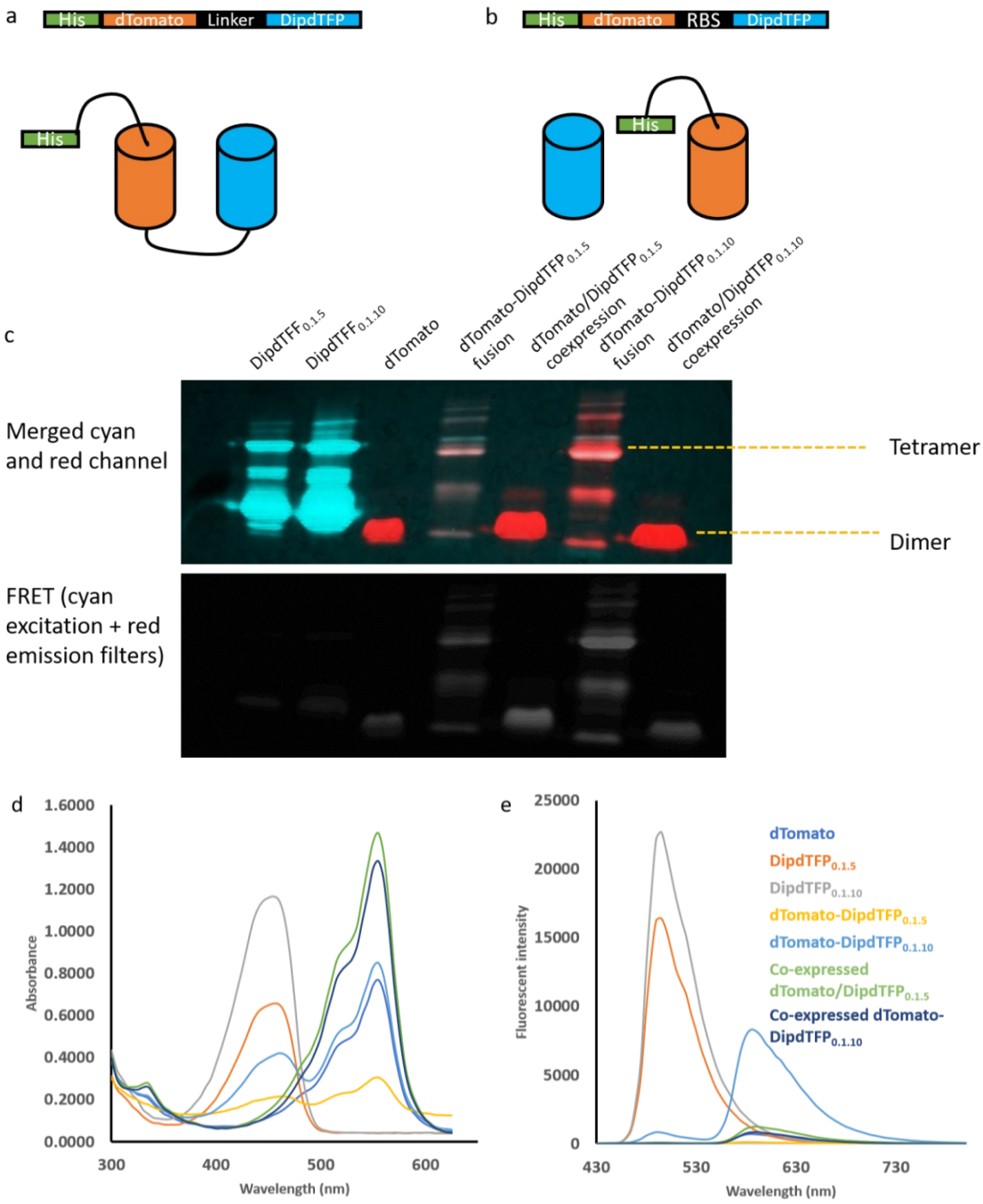

Figure 6.6. Characterize DipdTFP$_{0.1.5}$ and DipdTFP$_{0.1.10}$ co-expressed with dTomato or fused with dTomato.

The sequence of (a) dTomato-DipdTFP tandem dimer and (b) coexpressed dTomato and DipdTFP. (c) Fluorescence images of pseudonative gels, (d) absorbance spectra, and (e)

emission spectra of DipdTFPs, dTomato, DipdTFP-dTomato tandem dimer, and co-expressed DipdTFP and dTomato.

In the DipdTFP and dTomato co-expression system, only dTomato contains an N-terminal His tag. With the His tag binding to Ni-NTA beads, dTomato can be purified from the cell lysate; without the His tag, DipdTFP can only be retained in a Ni-NTA purified sample if bound to dTomato. Findings from the pseudonative gel (**Fig. 6.6c**), absorbance spectra (**Fig. 6.6d**), emission spectra (**Fig. 6.6e**), and the 3D scan (**Fig. 6.7c** and **d**) of the purified protein indicate that the majority of DipdTFP was washed away. The pseudonative gel shows a marginal band above the dTomato dimer band for co-expressed dTomato/DipdTFP$_{0.1.5}$, which was absent for dTomato only. This finding suggests a negligible amount of DipdTFP$_{0.1.5}$ in the sample. These results offer that homodimers are much more preferred than heterodimers. Future experiments need to address this by lowering the affinity for the homodimers to prevent homodimers and for the heterodimers to only allow weak dimerization of heterodimers.

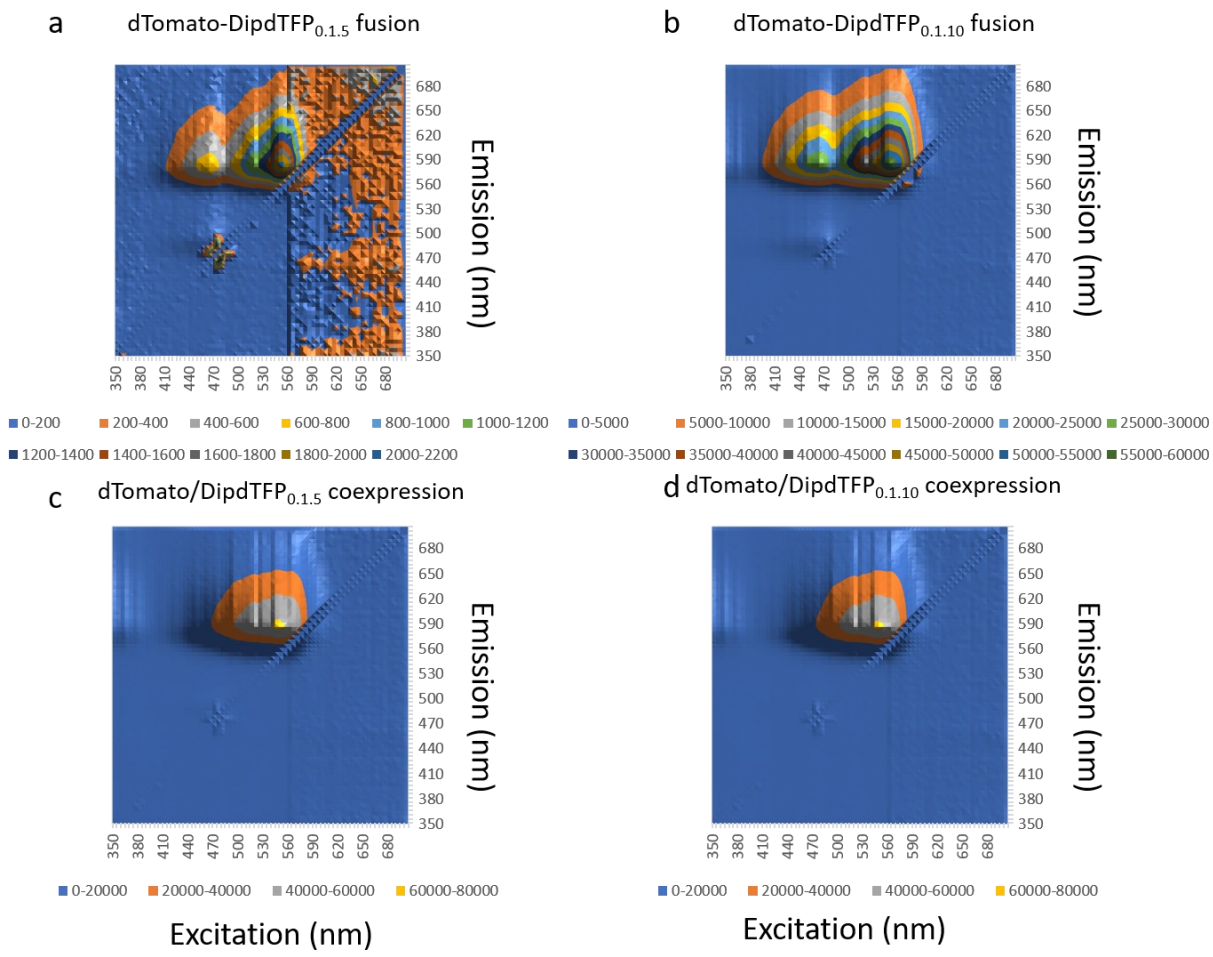

Figure 6.7. 3D scan of dTomato-DipdTFP fusion and co-expressed dTomato-DipdTFP.

The intensities are colored coded. (a) and (b) are tandem dimer constructs and (c) and (d) are co-expressed version.

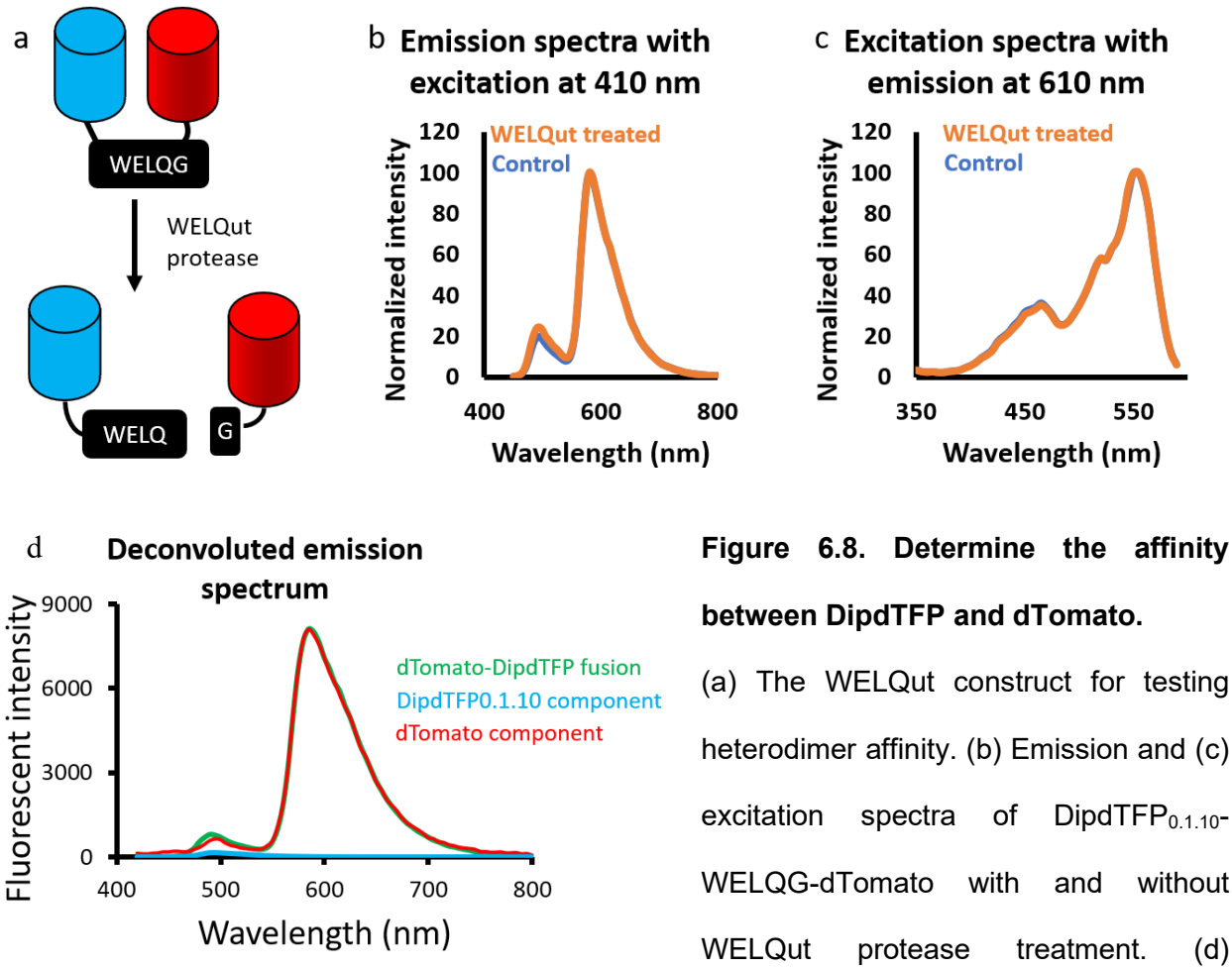

Figure 6.8. Determine the affinity between DipdTFP and dTomato. (a) The WELQut construct for testing heterodimer affinity. (b) Emission and (c) excitation spectra of DipdTFP$_{0.1.10}$-WELQG-dTomato with and without WELQut protease treatment. (d) Deconvoluted emission spectrum of DipdTFP$_{0.1.10}$-dTomato.

6.2.3 Further engineering of DipdTFP

DipdTFP$_{0.1.10}$ with K83M is used for further engineering with directed evolution. There are multiple selection criteria for the directed evolution: (a) better overall brightness as this was the main objective for ddFP optimization in Chapter 5 and (b) brighter DipdTFP relative to dTomato. The excitation spectrum of DipdTFP$_{0.1.10}$ indicates much lower DipdTFP peaks, suggesting DipdTFP$_{0.1.10}$ is dimmer than dTomato. DipdTFP$_{0.2.3}$ was selected because of its increased brightness in the *E. coli* lysate.

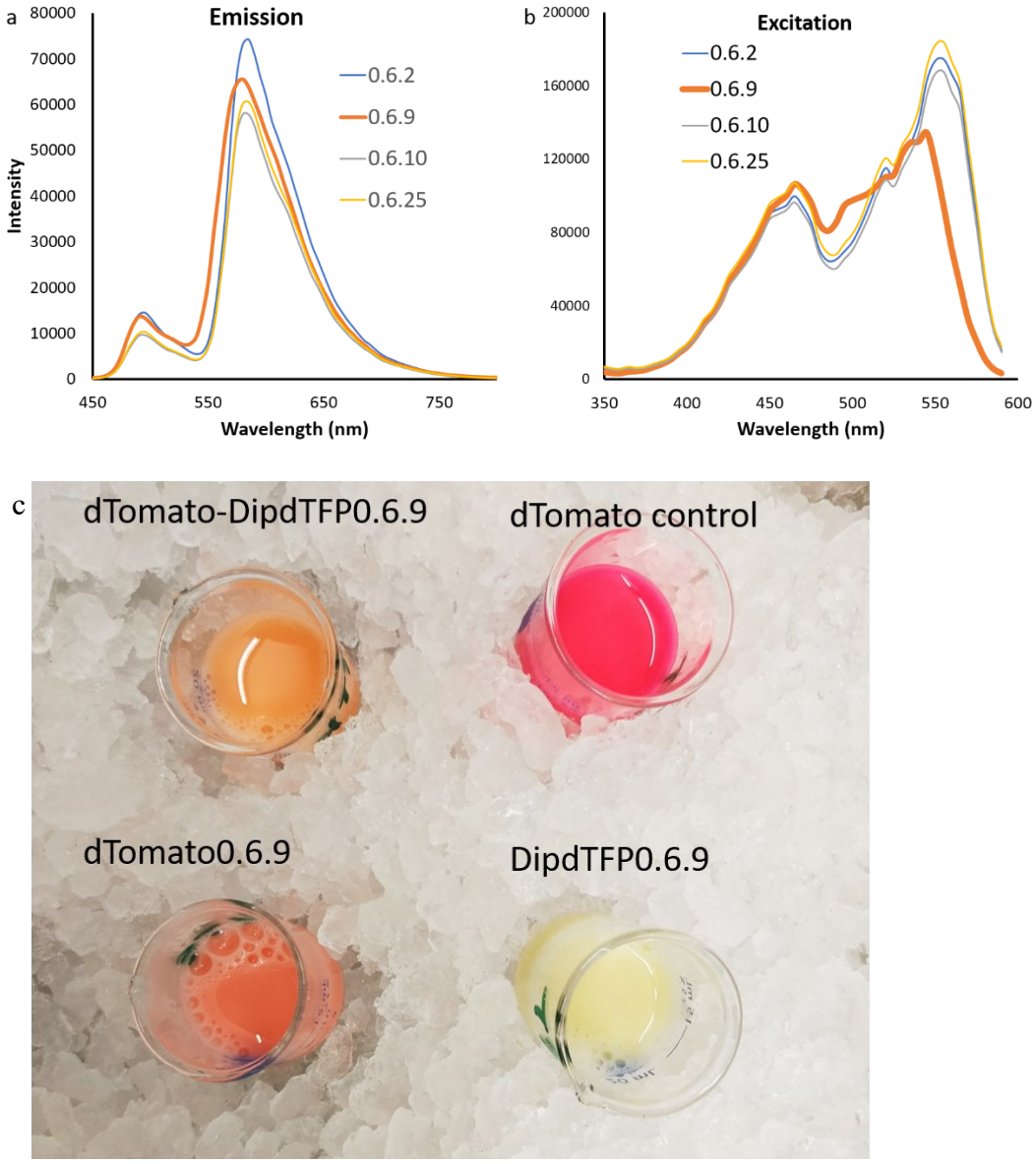

Figure 6.9. The spectra of the fusion protein of dTomato and DipdTFP.

The dTomato-DipdTFP$_{0.6.9}$ shows a similar emission spectrum (a), but a very different excitation spectrum (b) with lowered dTomato excitation peak. (c) The cell lysate expressing DipdTFP$_{0.6.9}$, dTomato$_{0.6.9}$, or fused tandem dimer shows visible differences in colour.

Charge flipping was subsequently performed on DipdTFP$_{0.2.3}$-dTomato to reduce the homodimer affinity as introduced to ddFPs by Dr Alford. E100R on DipdTFP$_{0.2.3}$ and R153E on

dTomato are introduced simultaneously as shown in **Fig 6.10a**. These mutations allow heterodimer formation with opposite charges but introduce charge repulsions during homodimer formation.

Two rounds of directed evolution on dTomato-DipdTFP$_{0.2.3}$ CF (charge-flipped) yield DipdTFP$_{0.4.28}$, which reverted the charge flipping. The new DipdTFP$_{0.4.28}$ was subjected to a site saturation at position 83 to determine a mutation for the best brightness as its mutation was important in making DipdTFP fluorescent in the first library. The variants selected contained either H, I, or M at Residue 83 (**Fig 6.11**). This result suggests hydrophobicity is important for the site, possibly for interacting with the chromophore.

The most interesting mutation occurs in dTomato-DipdTFP$_{0.6.9}$. This variant contains mutation in dTomato that lower its excitation peak thus making its height comparable to that of DipdTFP$_{0.6.9}$ (**Fig 6.9b**). Although its emission spectrum (**Fig. 6.9a**) experiences unremarkable change, purified dTomato$_{0.6.9}$ and dTomato-DipdTFP$_{0.6.9}$ produces a visible colour change (**Fig 6.9c**). dTomato$_{0.6.9}$ contains two mutations: F177C and M288L (**Table 6.2**). M288L is unlikely to contribute to the change in the spectrum because M288 in the C terminal flexible region that is not shown in the crystal structure adapted from DsRed structure. F177 is on the β-barrel, pointing towards the chromophore (**Fig. 6.10b**). The location makes F177C most likely to cause the excitation spectral change of dTomato.

Although the affinity issue was not addressed by the mutations accumulated, dTomato-DipdTFP$_{0.6.9}$ is better suited than dTomato-DipdTFP$_{0.1.10}$ for making the FRET ddFP pair.

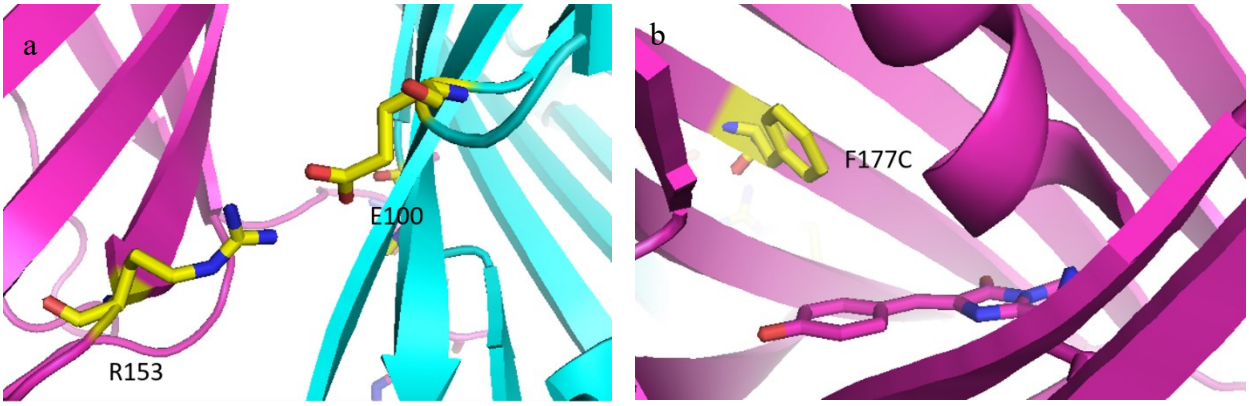

Figure 6.10. Important mutations on DipdTFP.

(a) Charge flipping residues: E100 of DipdTFP and R153 of dTomato. (b) The unique mutation in DipdTFP$_{0.6.9}$, F177C.

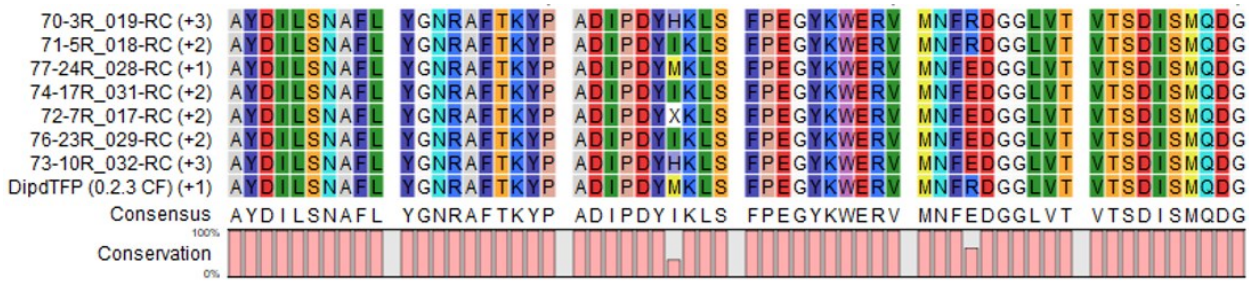

Figure 6.11. The alignment of selected variants in the library saturating position 83.

6.2.4 Characterize DipdTFP$_{0.6.9}$ with dTomato$_{0.6.9}$

I purified and characterized dTomato$_{0.6.9}$, DipdTFP$_{0.6.9}$, as well as the tandem dimer dTomato-DipdTFP$_{0.6.9}$ to determine the brightness of them. The absorbance spectrum of dTomato-DipdTFP$_{0.6.9}$ shows comparable peak heights for dTomato and DipdTFP (**Fig. 6.12a**). The emission spectra show a slightly blue-shifted emission peak for dTomato$_{0.6.9}$ and dTomato-DipdTFP$_{0.6.9}$ when compared to the dTomato control (**Fig. 6.12b**).

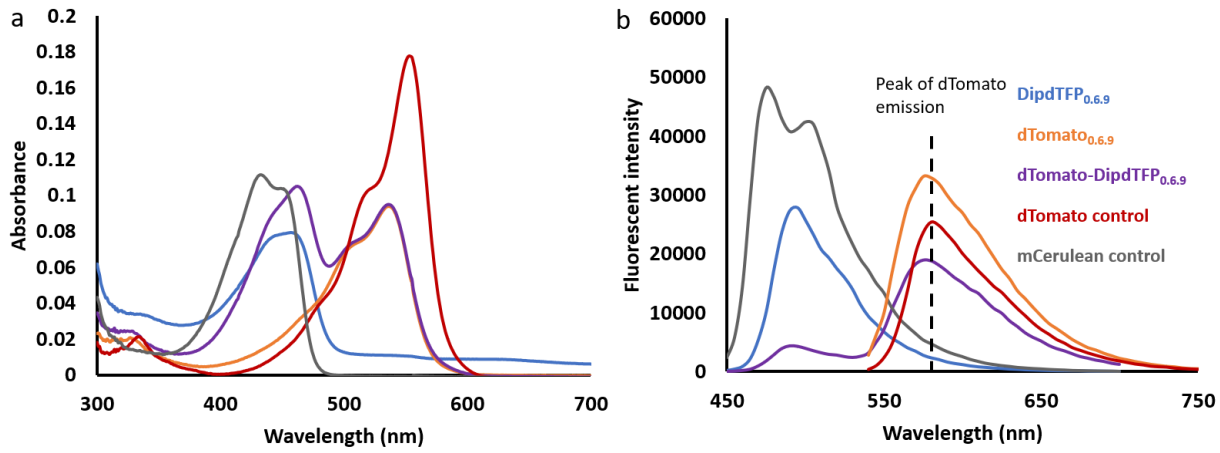

Figure 6.12. The absorbance and emission spectra of dTomato-DipTFP and controls.

The (a) absorbance spectra and (b) emission spectra of dTomato$_{0.6.9}$, DipdTFP$_{0.6.9}$, dTomato-DipdTFP$_{0.6.9}$ with controls. The emission spectra of DipdTFP$_{0.6.9}$, dTomato-DipdTFP$_{0.6.9}$ and mCerulean were measured with excitation at 420 nm; those of dTomato and dTomato$_{0.6.9}$ were measured with excitation at 520 nm.

Through measurement of extinction coefficient and the quantum yield of the purified proteins, the brightness of DipdTFP$_{0.6.9}$ was calculated to be 17.8, which is lower than that of cerulean (27.8.) and much lower than that of dTFP0.2 (40.8). dTomato$_{0.6.9}$ has a brightness of 49.3, which is comparable to that of dTomato (47.6) (**Table 6.3**). The tandem dimer dTomato-DipdTFP$_{0.6.9}$ has a brightness of 43.0 per two chromophores when the TFP component is excited and a brightness of 45.3 per two chromophores when the dTomato component is excited. The difference is very small, indicating a high FRET efficiency.

The brightness numbers obtained shows DipdTFP$_{0.6.9}$ has a potential to become brighter, dTomato$_{0.6.9}$ requires no brightness improvement, and the tandem dimer has achieved a improved brightness.

6.3 Conclusions and Future work

dTomato-DipdTFP$_{0.6.9}$ displayed high FRET efficiency as an engineering result of modifying dTFP0.2 interface to that of dTomato. It is common to disrupt an existing interface interaction, but rare to build such an interaction for FPs from different origins. The tandem dimer, as a proof of concept, shows this is possible although obstacles remain to make such dimers into a FRET ddFP pair. There is the primary challenge of affinity: the charge flipping may need to be re-introduced and more interface residues need to be examined. The ddFP project by Dr Alford reflected this part of the engineering to be time consuming and labour intensive. Additionally, there is the challenge of brightness: Although a brightness of 43.0 for the tandem dimer dTomato-DipdTFP$_{0.1.10}$ is acceptable, improvement is still necessary given the low brightness of DipdTFP$_{0.6.9}$.

6.5 Methods

Directed evolution

The directed evolution procedure is as described by Ai and coworkers[303]. The library was generated by either error-prone PCR or site-directed mutagenesis. The error-prone PCR is performed on DipdTFP for the first few rounds of directed evolution, and on the tandem dimer dTomato-DipdTFP for later rounds in a pBAD vector. Error-prone PCR reactions were performed in duplicate with 15 and 30 μM $MnCl_2$ to make a library with two different mutation rates. Products of the two error-prone reactions are combined for ligation. Site directed mutagenesis was performed with Agilent lightning site-directed mutagenesis kit following the manufacturer's instruction with 1 hour of DpnI digestion at 37°C. The colonies were picked based on their FRET response for lysate screening after being cultured in LB with 100 μg/mL ampicillin and 0.02% arabinose at 37°C overnight. The cells were lysed with BPER reagent from Thermo-Fisher at room

temperature with vortexing. After spinning at 10K rpm for 20 min, the supernatant is transferred to a 96-well plate for the excitation and emission measurement in a Tecan Safire2 microplate reader.

Protein purification and peudo-native gel

ddFP monomers and heterodimers linked to a His tag were expressed by *E. coli* DH10B and purified with Ni-NTA as previously described[296]. The purified proteins were run on a 12.5% polyacrylamide gel without denaturation as previously described[296,301]. The pre-stained molecular weight marker (Bio-Rad) was used as a size standard. The gel is excited with the light from a 175 W xenon arc lamp (Sutter). The photons emitted were collected with a Retiga 1300i 12-bit CCD camera (charge-coupled-device camera) (QImaging).

Fast protein liquid chromatography

The oligomeric structure of TFP variants was determined by gel filtration chromatography as previously described[303]. Samples of the TFP variants were loaded with the size standards (the monomeric mCherry and the tandem dimer tdTomato[302]. The AKTAbasic liquid chromatography system (GE Healthcare) can monitor multiple wavelengths. The elution profiles of TFP variants were monitored at 450 nm; those of mCherry and tdTomato were monitored at 587 nm and 554 nm, respectively.

Table 6.1. Lys83 mutation rescued the fluorescence of DipdTFP.

The list of mutations of each variant in the first round of directed evolution of DipdTFP, which aims to rescue the fluorescence. K83 mutations (bold) were shared among all of them.

Variants of DipdTFP	Mutations
0.1.1	**K83M**
0.1.4	A57S, **K83M**, K184E
0.1.5	**K83I**
0.1.7	**K83M**, M136L, K139N
0.1.9	I14F, **K83M**
0.1.10	**K83M**

Table 6.2. The mutations generated by directed evolution or introduced by site-directed evolution.

Directed evolution (DE) was performed on DipdTFP for first two rounds and the fusion construct of dTomato-DipdTFP later. Charge flipping on dTomato-DipdTFP was achieved by site-directed mutagenesis. The flipping was reversed after two rounds of directed evolution. Randomization on residue 83 was performed and the selected variants contain any of His, Ile, or Met at the position 83.

Variants		Mutation (dTomato)	Mutation (DipdTFP)
0.1.10		None	K83M
0.2.3		None	M22I, A144T
0.2.3	CF	**R153E**	**E100R**
0.4.28		E153R	R100E
0.4.28	83X	None	M83 to H/I/M
0.6.9		F177C, M228L	M83H, G190V

Table 6.3. Characterization of dTomato$_{0.6.9}$, DipdTFP$_{0.6.9}$, and dTomato-DipdTFP$_{0.6.9}$.

The parameters listed are extinction coefficient (ε), quantum yield (φ), brightness (the product of extinction coefficient and quantum yield), and brightness of a FRET pair if applicable.

*Data for dTomato and mCerulean were taken from referenced works.

	ε ($M^{-1}cm^{-1}$)	**φ**	**Brightness ($mM^{-1}cm^{-1}$)**	**per FRET pair**
DipdTFP0.6.9	52299	0.34	17.83	NA
dTomato0.6.9	64893	0.76	49.30	NA
dTom-DipdTFP0.6.9 2 15 (cyan)	35891	0.74	26.50	53.01
dTom-DipdTFP0.6.9 2 15 (red)	32435	0.87	28.16	56.33
*dTomato[302]	69,000	0.69	47.61	NA
*mCerulean[231]	43000	0.64	27.52	NA

Chapter 7 Conclusions and future work

In this thesis, I described my work on the genetically encoded K^+ indicators, dimerization-dependent fluorescent proteins (ddFPs), dimerization-dependent FRET pair, as well as indicators for insulin and BDNF described in Appendix. These FP-based tools can potentially provide opportunities for imaging molecules and protein-protein interactions (PPI) in live cells

7.1. K^+ indicators: general perspective and the future directions.

As the most abundant intracellular cation, K^+ plays essential roles in many cell processes[305]. The homeostasis of K^+ is readily maintained by the Na^+/K^+ pump and other K^+ channels and transporters to create a steep outward concentration gradient at the resting state of activatable cells[206]. During an action potential, the voltage-gated Na^+ channels open to allow Na^+ ions to enter the cell along the Na^+ concentration gradient and produce cell depolarization[306]. Subsequently, the voltage-gated K^+ channels open to allow K^+ to exit the cells and repolarize cells while concurrently the voltage-gated Na^+ channels close. The action potentials generally last for a few milliseconds[306]. Tools to monitor the transient K^+ change include the K^+ specific electrode[215] and the K^+ indicators[90]. The K^+ specific electrode, although accurate and sensitive, is invasive and time-consuming. Imaging with K^+ indicators, on the other hand, is less invasive and more convenient to use. The small molecule-based K^+ indicators in general lacks specificity as they often binds Na^+ (Ref. 90).

The structural determination of Kbp[94], an *E. coli* potassium binding protein, provided an opportunity for genetically encoded indicators described in Chapter 2, 3, and 4. Kbp undergoes a substantial conformational change upon K^+ binding, making it suitable for indicator development, because the conformational change can alter the chromophore environment in genetically encoded K^+ indicators.

In Chapter 2, I described FRET-based potassium indicators KIRIN1 and KIRIN-GR, and a GFP-based potassium indicator GINKO1 (Ref. 1). KIRIN1 incorporated a mCerulean and cpVenus FRET pair and allowed a dynamic range (R_{max}/R_{min}) of 2.3. KIRIN-GR provided an alternative colour pair of Clover and mRuby2 but also a lower dynamic range of 1.2. GINKO1 has a dynamic range (F_{max}/F_{min}) of 2.5 and it is more compatible in multiplex imaging, as demonstrated with a red Ca^{2+} indicator K-GECO.

In Chapter 3, I optimized GINKO1 to GINK2a and 2b. Through structural-guided optimization and directed evolution, GINKO2a and 2b were generated with a better sensitivity and specificity. They have a dynamic range of ~15 and do not respond to Na^+ at a concentration up to 150 mM. At the same time, GINKO2a and 2b have a reduced K^+ affinity (K_d values: 0.42 mM for GINKO1, 15.3 mM for GINKO2a, and 9.3 mM for GINKO2b).

The focus of Chapter 4 is on achieving anchoring of GINKOs to the extracellular side of the plasma membrane. This is important because the extracellular K^+ concentration is critical in the nervous system[294]. After trying with many leader peptides and membrane anchoring domains, I found the leader peptide of frizzled protein receptor 7 (Fzd7) led to membrane localization. The membrane bound GINKO2a failed to respond to K^+ and required further troubleshooting. I tested on potential sites for *N*-glycosylation, disulfide, and phosphorylation. There is a lack of evidence that these post-translational modifications cause the loss of GINKO function. Using SpyTag and SpyCatcher, I succeeded on anchoring purified SpyTag-GINKO2a protein to the membrane of HeLa cells expressing SpyCatcher. However, substantial reduction of GINKO2a was observed, suggesting the membrane environment a possible cause for the lack of K^+ response of the membrane bound GINKO2a. This lack of function can be caused by an inappropriate orientation or link length that restrict the conformational change that necessitate the fluorescence change,

potential Kbp interaction with membrane components, or unwanted Kbp modification by membrane enzymes.

To make the membrane bound GINKO2a functional, I propose several approaches: altering the SpyTag construct to test whether the orientation and linker length make a difference; testing for proteolytic events on the membrane; targeting GINKO to the endoplasmic reticulum and the Golgi apparatus to examine whether the functional loss occurred earlier in the secretory pathway; and trying different leader peptides.

At the same time, the affinity of GINKO2a also needs to be addressed for extracellular K^+ concentration. The site saturation on the sites identified by proline scan may yield variants with stronger affinity. Directed evolution is also an effective approach demonstrated in previous work on GECIs[47,48,62].

7.2 ddFPs and DipdTFP: general perspective and future directions

Detection of protein-protein interactions (PPIs) is a common theme in biomedical research. FRET pairs[307] and bimolecular fluorescence complementation[308] (BiFC) are examples of techniques for PPI detection in live cells. As an alternative, ddFPs were developed in three colours: red (ddRFP), yellow (ddYFP), and green (ddGFP)[299,300]. Every ddFP pair contains a fluorescent A copy and a dark B copy. They can form heterodimers of which the fluorescence intensity is enhanced by the dimerization. Fluorescent protein exchange (FPX) was developed when the B copy of ddRFP can bind to the A copies of ddRFP and ddGFP with similar affinity[298]. The triple-ddFP design allows ratiometric detection of protein-protein interactions.

The main goal of ddFP optimization is to increase the brightness of ddFP. Using rounds of directed evolution, new variants of ddRFP and ddGFP presented improved brightness on the agar plate and in the cell lysate. $ddRFP_{1.7.16}$ (the 16th colony picked in the 7th round of optimization)

showed 60% improvement on the brightness and ddGFP$_{1.4.33}$ showed 30% improvement on the brightness. The new variants were tested in mammalian cells, but the improvement was not sufficient to show a difference.

DipdTFP was generated from an attempt to make FRET-based dimerization dependent fluorescent proteins. The external residues of dTFP$_{0.2}$ were replaced by those of dTomato according to alignment. The resulting protein, DipdTFP, showed a remarkable FRET response when fused dTomato. However, the pair was challenged by a high homodimeric affinity and a heterodimeric affinity. Further engineering reduced the brightness of dTomato that resulted in similar excitation intensities for DipdTFP and dTomato.

Further engineering efforts on ddFP and DipdTFP are required to achieve ddFPs with improved brightness and a dTomato/DipdTFP pair with lower affinity for dimerization. Successful engineering of these dimerization-dependent fluorescent proteins can potentially lead to new tools for detecting protein-protein interaction or reporter domains for new biosensors.

References

1. Shen, Y. *et al.* Genetically encoded fluorescent indicators for imaging intracellular potassium ion concentration. *Commun. Biol.* **2**, 18 (2019).
2. Frieden, E. The chemical elements of life. *Sci. Am.* **227**, 52–60 (1972).
3. Ainscough, E. W. & Brodie, A. M. The role of metal ions in proteins and other biological molecules. *J. Chem. Educ.* **53**, 156 (1976).
4. Cerchiaro, G., Manieri, T. M. & Bertuchi, F. R. Analytical methods for copper, zinc and iron quantification in mammalian cells. *Metallomics* **5**, 1336–1345 (2013).
5. Ammann, A. A. Inductively coupled plasma mass spectrometry (ICP MS): a versatile tool. *J. Mass Spectrom.* **42**, 419–427 (2007).
6. Prange, D. P., Andreas. Inductively Coupled Plasma–Mass Spectrometry (ICP-MS) for Quantitative Analysis in Environmental and Life Sciences: A Review of Challenges, Solutions, and Trends - Daniel Pröfrock, Andreas Prange, 2012. *Appl. Spectrosc.* (2012).
7. Qin, Z., A. Caruso, J., Lai, B., Matusch, A. & Sabine Becker, J. Trace metal imaging with high spatial resolution: Applications in biomedicine. *Metallomics* **3**, 28–37 (2011).
8. Russell, J. T. Imaging calcium signals *in vivo*: a powerful tool in physiology and pharmacology. *Br. J. Pharmacol.* **163**, 1605–1625 (2011).
9. Clapham, D. E. Calcium Signaling. *Cell* **131**, 1047–1058 (2007).
10. Brini, M., Calì, T., Ottolini, D. & Carafoli, E. Neuronal calcium signaling: function and dysfunction. *Cell. Mol. Life Sci. CMLS* **71**, 2787–2814 (2014).
11. Bagur, R. & Hajnóczky, G. Intracellular Ca^{2+} Sensing: Its Role in Calcium Homeostasis and Signaling. *Mol. Cell* **66**, 780–788 (2017).

12. Carter, K. P., Young, A. M. & Palmer, A. E. Fluorescent Sensors for Measuring Metal Ions in Living Systems. *Chem. Rev.* **114**, 4564–4601 (2014).
13. Tsien, R. Y. New calcium indicators and buffers with high selectivity against magnesium and protons: design, synthesis, and properties of prototype structures. *Biochemistry* **19**, 2396–2404 (1980).
14. Tsien, R. & Pozzan, T. [14] Measurement of cytosolic free Ca^{2+} with quin2. in *Methods in Enzymology* vol. 172 230–262 (Academic Press, 1989).
15. Grynkiewicz, G., Poenie, M. & Tsien, R. Y. A new generation of Ca^{2+} indicators with greatly improved fluorescence properties. *J. Biol. Chem.* **260**, 3440–3450 (1985).
16. Malgaroli, A., Milani, D., Meldolesi, J. & Pozzan, T. Fura-2 measurement of cytosolic free Ca^{2+} in monolayers and suspensions of various types of animal cells. *J. Cell Biol.* **105**, 2145–2155 (1987).
17. Minta, A., Kao, J. P. & Tsien, R. Y. Fluorescent indicators for cytosolic calcium based on rhodamine and fluorescein chromophores. *J. Biol. Chem.* **264**, 8171–8178 (1989).
18. Gee, K. R. *et al.* Chemical and physiological characterization of fluo-4 Ca^{2+}-indicator dyes. *Cell Calcium* **27**, 97–106 (2000).
19. Lock, J. T., Parker, I. & Smith, I. F. A comparison of fluorescent Ca^{2+} indicators for imaging local Ca^{2+} signals in cultured cells. *Cell Calcium* **58**, 638–648 (2015).
20. Hyrc, K. L. *et al.* Synthesis and properties of Asante Calcium Red—A novel family of long excitation wavelength calcium indicators. *Cell Calcium* **54**, 320–333 (2013).
21. Heim, R., Prasher, D. C. & Tsien, R. Y. Wavelength mutations and posttranslational autoxidation of green fluorescent protein. *Proc. Natl. Acad. Sci. U. S. A.* **91**, 12501–12504 (1994).

22. Tung, J. K., Berglund, K., Gutekunst, C.-A., Hochgeschwender, U. & Gross, R. E. Bioluminescence imaging in live cells and animals. *Neurophotonics* **3**, 025001 (2016).

23. Shimomura, O., Johnson, F. H. & Saiga, Y. Extraction, purification and properties of aequorin, a bioluminescent protein from the luminous hydromedusan, Aequorea. *J. Cell. Comp. Physiol.* **59**, 223–239 (1962).

24. Bonora, M. *et al.* Subcellular calcium measurements in mammalian cells using jellyfish photoprotein aequorin-based probes. *Nat. Protoc.* **8**, 2105–2118 (2013).

25. Rodriguez-Garcia, A. *et al.* GAP, an aequorin-based fluorescent indicator for imaging Ca^{2+} in organelles. *Proc. Natl. Acad. Sci.* **111**, 2584–2589 (2014).

26. Bakayan, A., Vaquero, C. F., Picazo, F. & Llopis, J. Red Fluorescent Protein-Aequorin Fusions as Improved Bioluminescent Ca^{2+} Reporters in Single Cells and Mice. *PLOS ONE* **6**, e19520 (2011).

27. Koldenkova, V. P., Matsuda, T. & Nagai, T. MagIC, a genetically encoded fluorescent indicator for monitoring cellular Mg^{2+} using a non-Förster resonance energy transfer ratiometric imaging approach. *J. Biomed. Opt.* **20**, 101203 (2015).

28. Suzuki, K. *et al.* Five colour variants of bright luminescent protein for real-time multicolour bioimaging. *Nat. Commun.* **7**, 13718 (2016).

29. Takai, A. *et al.* Expanded palette of Nano-lanterns for real-time multicolor luminescence imaging. *Proc. Natl. Acad. Sci.* **112**, 4352–4356 (2015).

30. Saito, K. *et al.* Auto-Luminescent Genetically-Encoded Ratiometric Indicator for Real-Time Ca^{2+} Imaging at the Single Cell Level. *PLOS ONE* **5**, e9935 (2010).

31. Yang, J. *et al.* Coupling optogenetic stimulation with NanoLuc-based luminescence (BRET) Ca^{++} sensing. *Nat. Commun.* **7**, 1–10 (2016).

32. Miyawaki, A. *et al.* Fluorescent indicators for Ca^{2+}based on green fluorescent proteins and calmodulin. *Nature* **388**, 882–887 (1997).

33. Miyawaki, A., Griesbeck, O., Heim, R. & Tsien, R. Y. Dynamic and quantitative Ca^{2+} measurements using improved cameleons. *Proc. Natl. Acad. Sci. U. S. A.* **96**, 2135–2140 (1999).

34. Kerr, R. *et al.* Optical Imaging of Calcium Transients in Neurons and Pharyngeal Muscle of C. elegans. *Neuron* **26**, 583–594 (2000).

35. Evanko, D. S. & Haydon, P. G. Elimination of environmental sensitivity in a cameleon FRET-based calcium sensor via replacement of the acceptor with Venus. *Cell Calcium* **37**, 341–348 (2005).

36. Romoser, V. A., Hinkle, P. M. & Persechini, A. Detection in Living Cells of Ca^{2+}-dependent Changes in the Fluorescence Emission of an Indicator Composed of Two Green Fluorescent Protein Variants Linked by a Calmodulin-binding Sequence A NEW CLASS OF FLUORESCENT INDICATORS. *J. Biol. Chem.* **272**, 13270–13274 (1997).

37. Heim, N. & Griesbeck, O. Genetically Encoded Indicators of Cellular Calcium Dynamics Based on Troponin C and Green Fluorescent Protein. *J. Biol. Chem.* **279**, 14280–14286 (2004).

38. Mank, M. *et al.* A FRET-Based Calcium Biosensor with Fast Signal Kinetics and High Fluorescence Change. *Biophys. J.* **90**, 1790–1796 (2006).

39. Mank, M. & Griesbeck, O. Genetically Encoded Calcium Indicators. *Chem. Rev.* **108**, 1550–1564 (2008).

40. Thestrup, T. *et al.* Optimized ratiometric calcium sensors for functional *in vivo* imaging of neurons and T lymphocytes. *Nat. Methods* **11**, 175–182 (2014).

41. Baird, G. S., Zacharias, D. A. & Tsien, R. Y. Circular permutation and receptor insertion within green fluorescent proteins. *Proc. Natl. Acad. Sci.* **96**, 11241–11246 (1999).

42. Nagai, T., Sawano, A., Park, E. S. & Miyawaki, A. Circularly permuted green fluorescent proteins engineered to sense Ca^{2+}. *Proc. Natl. Acad. Sci.* **98**, 3197–3202 (2001).

43. Nakai, J., Ohkura, M. & Imoto, K. A high signal-to-noise Ca $^{2+}$ probe composed of a single green fluorescent protein. *Nat. Biotechnol.* **19**, 137–141 (2001).

44. Ohkura, M., Matsuzaki, M., Kasai, H., Imoto, K. & Nakai, J. Genetically Encoded Bright Ca^{2+} Probe Applicable for Dynamic Ca^{2+} Imaging of Dendritic Spines. *Anal. Chem.* **77**, 5861–5869 (2005).

45. Tallini, Y. N. *et al.* Imaging cellular signals in the heart *in vivo*: Cardiac expression of the high-signal Ca^{2+} indicator GCaMP2. *Proc. Natl. Acad. Sci.* **103**, 4753–4758 (2006).

46. Tian, L. *et al.* Imaging neural activity in worms, flies and mice with improved GCaMP calcium indicators. *Nat. Methods* **6**, 875–881 (2009).

47. Zhao, Y. *et al.* An Expanded Palette of Genetically Encoded Ca^{2+} Indicators. *Science* **333**, 1888–1891 (2011).

48. Akerboom, J. *et al.* Optimization of a GCaMP Calcium Indicator for Neural Activity Imaging. *J. Neurosci.* **32**, 13819–13840 (2012).

49. Chen, T.-W. *et al.* Ultrasensitive fluorescent proteins for imaging neuronal activity. *Nature* **499**, 295–300 (2013).

50. Dana, H. *et al.* High-performance calcium sensors for imaging activity in neuronal populations and microcompartments. *Nat. Methods* **16**, 649–657 (2019).

51. Shaner, N. C. *et al.* A bright monomeric green fluorescent protein derived from Branchiostoma lanceolatum. *Nat. Methods* **10**, 407–409 (2013).

52. Zarowny, L. *et al.* Bright and High-Performance Genetically Encoded Ca^{2+} Indicator Based on mNeonGreen Fluorescent Protein. *ACS Sens.* **5**, 1959–1968 (2020).

53. Subach, O. M. *et al.* Novel Genetically Encoded Bright Positive Calcium Indicator NCaMP7 Based on the mNeonGreen Fluorescent Protein. *Int. J. Mol. Sci.* **21**, (2020).

54. Ash, C., Dubec, M., Donne, K. & Bashford, T. Effect of wavelength and beam width on penetration in light-tissue interaction using computational methods. *Lasers Med. Sci.* **32**, 1909–1918 (2017).

55. Sandell, J. L. & Zhu, T. C. A review of in-vivo optical properties of human tissues and its impact on PDT. *J. Biophotonics* **4**, 773–787 (2011).

56. Wu, J. *et al.* Improved Orange and Red Ca^{2+} Indicators and Photophysical Considerations for Optogenetic Applications. *ACS Chem. Neurosci.* **4**, 963–972 (2013).

57. Wu, J. *et al.* A long Stokes shift red fluorescent Ca^{2+} indicator protein for two-photon and ratiometric imaging. *Nat. Commun.* **5**, (2014).

58. Akerboom, J. *et al.* Genetically encoded calcium indicators for multi-color neural activity imaging and combination with optogenetics. *Front. Mol. Neurosci.* **6**, (2013).

59. Inoue, M. *et al.* Rational design of a high-affinity, fast, red calcium indicator R-CaMP2. *Nat. Methods* **12**, 64–70 (2015).

60. Dana, H. *et al.* Sensitive red protein calcium indicators for imaging neural activity. *eLife* **5**, (2016).

61. Shen, Y. *et al.* A genetically encoded Ca^{2+} indicator based on circularly permutated sea anemone red fluorescent protein eqFP578. *BMC Biol.* **16**, 9 (2018).

62. Qian, Y. *et al.* A genetically encoded near-infrared fluorescent calcium ion indicator. *Nat. Methods* **16**, 171–174 (2019).

63. Qian, Y. *et al.* Improved genetically encoded near-infrared fluorescent calcium ion indicators for *in vivo* imaging. *bioRxiv* 2020.04.08.032433 (2020) doi:10.1101/2020.04.08.032433.

64. Frassinetti, S., Bronzetti, G., Caltavuturo, L., Cini, M. & Croce, C. D. The role of zinc in life: a review. *J. Environ. Pathol. Toxicol. Oncol. Off. Organ Int. Soc. Environ. Toxicol. Cancer* **25**, 597–610 (2006).

65. Chen, M. *et al.* Genetically Encoded, Photostable Indicators to Image Dynamic Zn^{2+} Secretion of Pancreatic Islets. *Anal. Chem.* **91**, 12212–12219 (2019).

66. Assaf, S. Y. & Chung, S.-H. Release of endogenous Zn^{2+} from brain tissue during activity. *Nature* **308**, 734–736 (1984).

67. Gee, K. R., Zhou, Z.-L., Ton-That, D., Sensi, S. L. & Weiss, J. H. Measuring zinc in living cells. A new generation of sensitive and selective fluorescent probes. *Cell Calcium* **31**, 245–251 (2002).

68. Walkup, G. K., Burdette, S. C., Lippard, S. J. & Tsien, R. Y. A New Cell-Permeable Fluorescent Probe for Zn^{2+}. *J. Am. Chem. Soc.* **122**, 5644–5645 (2000).

69. Chang, C. J. *et al.* Bright Fluorescent Chemosensor Platforms for Imaging Endogenous Pools of Neuronal Zinc. *Chem. Biol.* **11**, 203–210 (2004).

70. Burdette, S. C., Frederickson, C. J., Bu, W. & Lippard, S. J. ZP4, an Improved Neuronal Zn^{2+} Sensor of the Zinpyr Family. *J. Am. Chem. Soc.* **125**, 1778–1787 (2003).

71. Chang, C. J. *et al.* ZP8, a Neuronal Zinc Sensor with Improved Dynamic Range; Imaging Zinc in Hippocampal Slices with Two-Photon Microscopy. *Inorg. Chem.* **43**, 6774–6779 (2004).

72. Zhang, X., Hayes, D., Smith, S. J., Friedle, S. & Lippard, S. J. New Strategy for Quantifying Biological Zinc by a Modified Zinpyr Fluorescence Sensor. *J. Am. Chem. Soc.* **130**, 15788–15789 (2008).

73. Hirano, T., Kikuchi, K., Urano, Y., Higuchi, T. & Nagano, T. Highly Zinc-Selective Fluorescent Sensor Molecules Suitable for Biological Applications. *J. Am. Chem. Soc.* **122**, 12399–12400 (2000).

74. Hirano, T., Kikuchi, K., Urano, Y. & Nagano, T. Improvement and Biological Applications of Fluorescent Probes for Zinc, ZnAFs. *J. Am. Chem. Soc.* **124**, 6555–6562 (2002).

75. Wu, Y. *et al.* Boron dipyrromethene fluorophore based fluorescence sensor for the selective imaging of Zn(II) in living cells. *Org. Biomol. Chem.* **3**, 1387–1392 (2005).

76. Du, P. & Lippard, S. J. A Highly Selective Turn-On Colorimetric, Red Fluorescent Sensor for Detecting Mobile Zinc in Living Cells. *Inorg. Chem.* **49**, 10753–10755 (2010).

77. Koide, Y., Urano, Y., Hanaoka, K., Terai, T. & Nagano, T. Evolution of Group 14 Rhodamines as Platforms for Near-Infrared Fluorescence Probes Utilizing Photoinduced Electron Transfer. *ACS Chem. Biol.* **6**, 600–608 (2011).

78. Ghazvini Zadeh, E. H. *et al.* ZIGIR, a Granule-Specific Zn^{2+} Indicator, Reveals Human Islet α Cell Heterogeneity. *Cell Rep.* **32**, 107904 (2020).

79. Dittmer, P. J., Miranda, J. G., Gorski, J. A. & Palmer, A. E. Genetically encoded sensors to elucidate spatial distribution of cellular zinc. *J. Biol. Chem.* **284**, 16289–16297 (2009).

80. Vinkenborg, J. L. *et al.* Genetically encoded FRET sensors to monitor intracellular Zn^{2+} homeostasis. *Nat. Methods* **6**, 737–740 (2009).

81. Qin, Y., Dittmer, P. J., Park, J. G., Jansen, K. B. & Palmer, A. E. Measuring steady-state and dynamic endoplasmic reticulum and Golgi Zn^{2+} with genetically encoded sensors. *Proc. Natl. Acad. Sci. U. S. A.* **108**, 7351–7356 (2011).

82. Miranda, J. G. *et al.* New Alternately Colored FRET Sensors for Simultaneous Monitoring of Zn^{2+} in Multiple Cellular Locations. *PLOS ONE* **7**, e49371 (2012).

83. Evers, T. H., Appelhof, M. A. M., de Graaf-Heuvelmans, P. T. H. M., Meijer, E. W. & Merkx, M. Ratiometric Detection of Zn(II) Using Chelating Fluorescent Protein Chimeras. *J. Mol. Biol.* **374**, 411–425 (2007).

84. Hessels, A. M. *et al.* eZinCh-2: A Versatile, Genetically Encoded FRET Sensor for Cytosolic and Intraorganelle Zn^{2+} Imaging. *ACS Chem. Biol.* **10**, 2126–2134 (2015).

85. Chen, Z. & Ai, H. Single Fluorescent Protein-Based Indicators for Zinc Ion (Zn^{2+}). *Anal. Chem.* **88**, 9029–9036 (2016).

86. Qin, Y., Sammond, D. W., Braselmann, E., Carpenter, M. C. & Palmer, A. E. Development of an optical Zn^{2+} probe based on a single fluorescent protein. *ACS Chem. Biol.* **11**, 2744–2751 (2016).

87. Fudge, D. H., Black, R., Son, L., LeJeune, K. & Qin, Y. Optical Recording of Zn^{2+} Dynamics in the Mitochondrial Matrix and Intermembrane Space with the GZnP2 Sensor. *ACS Chem. Biol.* **13**, 1897–1905 (2018).

88. Minckley, T. F. *et al.* Sub-nanomolar sensitive GZnP3 reveals TRP1-mediated neuronal Zn^{2+} signals. *Nat. Commun.* **10**, 4806 (2019).

89. Humphries, E. S. A. & Dart, C. Neuronal and Cardiovascular Potassium Channels as Therapeutic Drug Targets. *J. Biomol. Screen.* **20**, 1055–1073 (2015).

90. Minta, A. & Tsien, R. Y. Fluorescent indicators for cytosolic sodium. *J. Biol. Chem.* **264**, 19449–19457 (1989).

91. Rimmele, T. S. & Chatton, J.-Y. A Novel Optical Intracellular Imaging Approach for Potassium Dynamics in Astrocytes. *PLoS ONE* **9**, (2014).

92. Rana, P. S. *et al.* Calibration and characterization of intracellular Asante Potassium Green probes, APG-2 and APG-4. *Anal. Biochem.* **567**, 8–13 (2019).

93. Wang, Z., Detomasi, T. C. & Chang, C. A Dual-Fluorophore Sensor Approach for Ratiometric Fluorescence Imaging of Potassium in Living Cells. (2020) doi:10.26434/chemrxiv.12649730.v1.

94. Ashraf, K. U. *et al.* The Potassium Binding Protein Kbp Is a Cytoplasmic Potassium Sensor. *Struct. Lond. Engl. 1993* **24**, 741–749 (2016).

95. Bischof, H. *et al.* Live-Cell Imaging of Physiologically Relevant Metal Ions Using Genetically Encoded FRET-Based Probes. *Cells* **8**, 492 (2019).

96. Pilchova, I., Klacanova, K., Tatarkova, Z., Kaplan, P. & Racay, P. The Involvement of Mg^{2+} in Regulation of Cellular and Mitochondrial Functions. *Oxidative Medicine and Cellular Longevity* vol. 2017 e6797460 https://www.hindawi.com/journals/omcl/2017/6797460/ (2017).

97. Grubbs, R. D. Intracellular magnesium and magnesium buffering. *Biometals* **15**, 251–259 (2002).

98. Romani, A. M. P. Magnesium Homeostasis in Mammalian Cells. in *Metallomics and the Cell* (ed. Banci, L.) vol. 12 69–118 (Springer Netherlands, 2013).

99. Kolisek, M. *et al.* Mrs2p is an essential component of the major electrophoretic Mg^{2+} influx system in mitochondria. *EMBO J.* **22**, 1235–1244 (2003).

100. London, R. E. Methods for measurement of intracellular magnesium: NMR and fluorescence. *Annu. Rev. Physiol.* **53**, 241–258 (1991).

101. Csernoch, L., Bernengo, J. C., Szentesi, P. & Jacquemond, V. Measurements of intracellular Mg^{2+} concentration in mouse skeletal muscle fibers with the fluorescent indicator mag-indo-1. *Biophys. J.* **75**, 957–967 (1998).

102. Shmigol, A. V., Eisner, D. A. & Wray, S. Simultaneous measurements of changes in sarcoplasmic reticulum and cytosolic [Ca^{2+}] in rat uterine smooth muscle cells. *J. Physiol.* **531**, 707–713 (2001).

103. Zhao, M., Hollingworth, S. & Baylor, S. M. Properties of tri- and tetracarboxylate Ca^{2+} indicators in frog skeletal muscle fibers. *Biophys. J.* **70**, 896–916 (1996).

104. Dong, X. *et al.* Dual-Color Imaging of Magnesium/Calcium Ion Activities with Two-Photon Fluorescent Probes. *Anal. Chem.* **84**, 8110–8113 (2012).

105. Fujii, T. *et al.* Design and Synthesis of a FlAsH-Type Mg^{2+} Fluorescent Probe for Specific Protein Labeling. *J. Am. Chem. Soc.* **136**, 2374–2381 (2014).

106. Lindenburg, L. H., Vinkenborg, J. L., Oortwijn, J., Aper, S. J. A. & Merkx, M. MagFRET: The First Genetically Encoded Fluorescent Mg^{2+} Sensor. *PLoS ONE* **8**, (2013).

107. Maeshima, K. *et al.* A Transient Rise in Free Mg^{2+} Ions Released from ATP-Mg Hydrolysis Contributes to Mitotic Chromosome Condensation. *Curr. Biol.* **28**, 444-451.e6 (2018).

108. Reynolds, R. M., Padfield, P. L. & Seckl, J. R. Disorders of sodium balance. *BMJ* **332**, 702–705 (2006).

109. Wilck, N., Balogh, A., Markó, L., Bartolomaeus, H. & Müller, D. N. The role of sodium in modulating immune cell function. *Nat. Rev. Nephrol.* **15**, 546–558 (2019).

110. Chahine, M. & O'Leary, M. E. Regulation/Modulation of Sensory Neuron Sodium Channels. in *Voltage Gated Sodium Channels* (ed. Ruben, P. C.) 111–135 (Springer, 2014). doi:10.1007/978-3-642-41588-3_6.

111. Strazzullo, P. & Leclercq, C. Sodium1. *Adv. Nutr.* **5**, 188–190 (2014).

112. Amorino, G. P. & Fox, M. H. Intracellular Na^{+} measurements using sodium green tetraacetate with flow cytometry. *Cytometry* **21**, 248–256 (1995).

113. Meier, S. D., Kovalchuk, Y. & Rose, C. R. Properties of the new fluorescent Na^+ indicator CoroNa Green: Comparison with SBFI and confocal Na^+ imaging. *J. Neurosci. Methods* **155**, 251–259 (2006).

114. Iamshanova, O., Mariot, P., Lehen'kyi, V. & Prevarskaya, N. Comparison of fluorescence probes for intracellular sodium imaging in prostate cancer cell lines. *Eur. Biophys. J.* **45**, 765–777 (2016).

115. Roder, P. & Hille, C. ANG-2 for quantitative Na^+ determination in living cells by time-resolved fluorescence microscopy. *Photochem. Photobiol. Sci. Off. J. Eur. Photochem. Assoc. Eur. Soc. Photobiol.* **13**, 1699–1710 (2014).

116. Futai, M. Acidification of organelles by V-ATPase. 10.

117. Nelson, N. Proton-motive force generation by V-ATPases. 7.

118. Farsi, Z., Jahn, R. & Woehler, A. Proton electrochemical gradient: Driving and regulating neurotransmitter uptake. *BioEssays News Rev. Mol. Cell. Dev. Biol.* **39**, (2017).

119. Reid, R. A., Moyle, J. & Mitchell, P. Synthesis of Adenosine Triphosphate by a Protonmotive Force in Rat Liver Mitochondria. *Nature* **212**, 257–258 (1966).

120. Rink, T. J., Tsien, R. Y. & Pozzan, T. Cytoplasmic pH and free Mg^{2+} in lymphocytes. *J. Cell Biol.* **95**, 189–196 (1982).

121. Whitaker, J. E., Haugland, R. P. & Prendergast, F. G. Spectral and photophysical studies of benzo[c]xanthene dyes: dual emission pH sensors. *Anal. Biochem.* **194**, 330–344 (1991).

122. Martinez-Zaguilan, R., Martinez, G. M., Lattanzio, F. & Gillies, R. J. Simultaneous measurement of intracellular pH and Ca^{2+} using the fluorescence of SNARF-1 and fura-2. *Am. J. Physiol.-Cell Physiol.* **260**, C297–C307 (1991).

123. Marcotte, N. & Brouwer, A. M. Carboxy SNARF-4F as a Fluorescent pH Probe for Ensemble and Fluorescence Correlation Spectroscopies. *J. Phys. Chem. B* **109**, 11819–11828 (2005).

124. Overly, C. C., Lee, K. D., Berthiaume, E. & Hollenbeck, P. J. Quantitative measurement of intraorganelle pH in the endosomal-lysosomal pathway in neurons by using ratiometric imaging with pyranine. *Proc. Natl. Acad. Sci.* **92**, 3156–3160 (1995).

125. Lindner, B., Burkard, T. & Schuler, M. Phagocytosis assays with different pH-sensitive fluorescent particles and various readouts. *BioTechniques* **68**, 245–250 (2020).

126. Godfrey, W. L. *et al.* Evaluation of granulocyte phagocytic activity using pHrodo™ dye, a novel fluorogenic pH indicator. *FASEB J.* **22**, 569–569 (2008).

127. Kneen, M., Farinas, J., Li, Y. & Verkman, A. S. Green fluorescent protein as a noninvasive intracellular pH indicator. *Biophys. J.* **74**, 1591–1599 (1998).

128. Llopis, J., McCaffery, J. M., Miyawaki, A., Farquhar, M. G. & Tsien, R. Y. Measurement of cytosolic, mitochondrial, and Golgi pH in single living cells with green fluorescent proteins. *Proc. Natl. Acad. Sci.* **95**, 6803–6808 (1998).

129. Tojima, T. *et al.* Attractive axon guidance involves asymmetric membrane transport and exocytosis in the growth cone. *Nat. Neurosci.* **10**, 58–66 (2007).

130. Johnson, D. E. *et al.* Red fluorescent protein pH biosensor to detect concentrative nucleoside transport. *J. Biol. Chem.* **284**, 20499–20511 (2009).

131. Rupprecht, C. *et al.* A novel FbFP-based biosensor toolbox for sensitive *in vivo* determination of intracellular pH. *J. Biotechnol.* **258**, 25–32 (2017).

132. Hellwig, N. *et al.* TRPV1 Acts as Proton Channel to Induce Acidification in Nociceptive Neurons. *J. Biol. Chem.* **279**, 34553–34561 (2004).

133. Gjetting, K. S. K., Ytting, C. K., Schulz, A. & Fuglsang, A. T. Live imaging of intra- and extracellular pH in plants using pHusion, a novel genetically encoded biosensor. *J. Exp. Bot.* **63**, 3207–3218 (2012).

134. Bizzarri, R. *et al.* Development of a Novel GFP-based Ratiometric Excitation and Emission pH Indicator for Intracellular Studies. *Biophys. J.* **90**, 3300–3314 (2006).

135. Hanson, G. T. *et al.* Green Fluorescent Protein Variants as Ratiometric Dual Emission pH Sensors. 1. Structural Characterization and Preliminary Application. *Biochemistry* **41**, 15477–15488 (2002).

136. Miesenböck, G., De Angelis, D. A. & Rothman, J. E. Visualizing secretion and synaptic transmission with pH-sensitive green fluorescent proteins. *Nature* **394**, 192–195 (1998).

137. Mahon, M. J. pHluorin2: an enhanced, ratiometric, pH-sensitive green florescent protein. *Adv. Biosci. Biotechnol. Print* **2**, 132–137 (2011).

138. Sankaranarayanan, S., De Angelis, D., Rothman, J. E. & Ryan, T. A. The Use of pHluorins for Optical Measurements of Presynaptic Activity. *Biophys. J.* **79**, 2199–2208 (2000).

139. Tantama, M., Hung, Y. P. & Yellen, G. Imaging intracellular pH in live cells with a genetically encoded red fluorescent protein sensor. *J. Am. Chem. Soc.* **133**, 10034–10037 (2011).

140. Li, Y. & Tsien, R. W. pHTomato: A genetically-encoded indicator that enables multiplex interrogation of synaptic activity. *Nat. Neurosci.* **15**, 1047–1053 (2012).

141. Shen, Y., Rosendale, M., Campbell, R. E. & Perrais, D. pHuji, a pH-sensitive red fluorescent protein for imaging of exo- and endocytosis. *J. Cell Biol.* **207**, 419–432 (2014).

142. Valdivieso, Á. G. & Santa-Coloma, T. A. The chloride anion as a signalling effector. *Biol. Rev.* **94**, 1839–1856 (2019).

143. Goetz, T., Arslan, A., Wisden, W. & Wulff, P. GABAA receptors. *Prog. Brain Res.* **160**, 21–41 (2007).

144. Verkman, A. S., Sellers, M. C., Chao, A. C., Leung, T. & Ketcham, R. Synthesis and characterization of improved chloride-sensitive fluorescent indicators for biological applications. *Anal. Biochem.* **178**, 355–361 (1989).

145. Biwersi, J., Tulk, B. & Verkman, A. S. Long-Wavelength Chloride-Sensitive Fluorescent Indicators. *Anal. Biochem.* **219**, 139–143 (1994).

146. Krapf, R., Berry, C. A. & Verkman, A. S. Estimation of intracellular chloride activity in isolated perfused rabbit proximal convoluted tubules using a fluorescent indicator. *Biophys. J.* **53**, 955–962 (1988).

147. Biwersi, J. & Verkman, A. S. Cell-permeable fluorescent indicator for cytosolic chloride. *Biochemistry* **30**, 7879–7883 (1991).

148. Wachter, R. M. & James Remington, S. Sensitivity of the yellow variant of green fluorescent protein to halides and nitrate. *Curr. Biol.* **9**, R628–R629 (1999).

149. Arosio, D. *et al.* Spectroscopic and Structural Study of Proton and Halide Ion Cooperative Binding to GFP. *Biophys. J.* **93**, 232–244 (2007).

150. Jayaraman, S., Haggie, P., Wachter, R. M., Remington, S. J. & Verkman, A. S. Mechanism and cellular applications of a green fluorescent protein-based halide sensor. *J. Biol. Chem.* **275**, 6047–6050 (2000).

151. Galietta, L. J. V., Haggie, P. M. & Verkman, A. S. Green fluorescent protein-based halide indicators with improved chloride and iodide affinities. *FEBS Lett.* **499**, 220–224 (2001).

152. Zhong, C. & Schleifenbaum, J. Genetically Encoded Calcium Indicators: A New Tool in Renal Hypertension Research. *Front. Med.* **6**, (2019).

153. Kuner, T. & Augustine, G. J. A genetically encoded ratiometric indicator for chloride: capturing chloride transients in cultured hippocampal neurons. *Neuron* **27**, 447–459 (2000).

154. Markova, O., Mukhtarov, M., Real, E., Jacob, Y. & Bregestovski, P. Genetically encoded chloride indicator with improved sensitivity. *J. Neurosci. Methods* **170**, 67–76 (2008).

155. Grimley, J. S. *et al.* Visualization of Synaptic Inhibition with an Optogenetic Sensor Developed by Cell-Free Protein Engineering Automation. *J. Neurosci.* **33**, 16297–16309 (2013).

156. Arosio, D. *et al.* Simultaneous intracellular chloride and pH measurements using a GFP-based sensor. *Nat. Methods* **7**, 516–518 (2010).

157. Tutol, J. N., Peng, W. & Dodani, S. C. Discovery and Characterization of a Naturally Occurring, Turn-On Yellow Fluorescent Protein Sensor for Chloride. *Biochemistry* **58**, 31–35 (2019).

158. Tutol, J. N., Kam, H. C. & Dodani, S. C. Identification of mNeonGreen as a pH-Dependent, Turn-On Fluorescent Protein Sensor for Chloride. *ChemBioChem* **20**, 1759–1765 (2019).

159. Saari, J. T. Copper deficiency and cardiovascular disease: role of peroxidation, glycation, and nitration. *Can. J. Physiol. Pharmacol.* **78**, 848–855 (2000).

160. Percival, S. S. Copper and immunity. *Am. J. Clin. Nutr.* **67**, 1064S-1068S (1998).

161. Opazo, C. M., Greenough, M. A. & Bush, A. I. Copper: from neurotransmission to neuroproteostasis. *Front. Aging Neurosci.* **6**, (2014).

162. Festa, R. A. & Thiele, D. J. Copper: an Essential Metal in Biology. *Curr. Biol. CB* **21**, R877–R883 (2011).

163. Baker, Z. N., Cobine, P. A. & Leary, S. C. The mitochondrion: a central architect of copper homeostasis. *Met. Integr. Biometal Sci.* **9**, 1501–1512 (2017).

164. Macomber, L. & Imlay, J. A. The iron-sulfur clusters of dehydratases are primary intracellular targets of copper toxicity. *Proc. Natl. Acad. Sci. U. S. A.* **106**, 8344–8349 (2009).

165. Stohs, S. J. & Bagchi, D. Oxidative mechanisms in the toxicity of metal ions. *Free Radic. Biol. Med.* **18**, 321–336 (1995).

166. Kaplan, J. H. & Maryon, E. B. How Mammalian Cells Acquire Copper: An Essential but Potentially Toxic Metal. *Biophys. J.* **110**, 7–13 (2016).

167. Yang, L. *et al.* Imaging of the intracellular topography of copper with a fluorescent sensor and by synchrotron x-ray fluorescence microscopy. *Proc. Natl. Acad. Sci.* **102**, 11179–11184 (2005).

168. Morgan, M. T., Bagchi, P. & Fahrni, C. J. Designed To Dissolve: Suppression of Colloidal Aggregation of Cu(I)-Selective Fluorescent Probes in Aqueous Buffer and In-Gel Detection of a Metallochaperone. *J. Am. Chem. Soc.* **133**, 15906–15909 (2011).

169. Zeng, L., Miller, E. W., Pralle, A., Isacoff, E. Y. & Chang, C. J. A Selective Turn-On Fluorescent Sensor for Imaging Copper in Living Cells. *J. Am. Chem. Soc.* **128**, 10–11 (2006).

170. Dodani, S. C. *et al.* Calcium-dependent copper redistributions in neuronal cells revealed by a fluorescent copper sensor and X-ray fluorescence microscopy. *Proc. Natl. Acad. Sci.* **108**, 5980–5985 (2011).

171. Dodani, S. C., Leary, S. C., Cobine, P. A., Winge, D. R. & Chang, C. J. A Targetable Fluorescent Sensor Reveals That Copper-Deficient SCO1 and SCO2 Patient Cells Prioritize Mitochondrial Copper Homeostasis. *J. Am. Chem. Soc.* **133**, 8606–8616 (2011).

172. Domaille, D. W., Zeng, L. & Chang, C. J. Visualizing Ascorbate-Triggered Release of Labile Copper within Living Cells using a Ratiometric Fluorescent Sensor. *J. Am. Chem. Soc.* **132**, 1194–1195 (2010).

173. Su Lim, C. *et al.* A copper(i)-ion selective two- photon fluorescent probe for *in vivo* imaging. *Chem. Commun.* **47**, 7146–7148 (2011).

174. Cao, X., Lin, W. & Wan, W. Development of a near-infrared fluorescent probe for imaging of endogenous Cu^{+} in live cells. *Chem. Commun. Camb. Engl.* **48**, 6247–6249 (2012).

175. Wegner, S. V., Arslan, H., Sunbul, M., Yin, J. & He, C. Dynamic Copper(I) Imaging in Mammalian Cells with a Genetically Encoded Fluorescent Copper(I) Sensor. *J. Am. Chem. Soc.* **132**, 2567–2569 (2010).

176. Wegner, S. V., Sun, F., Hernandez, N. & He, C. The tightly regulated copper window in yeast. *Chem. Commun.* **47**, 2571–2573 (2011).

177. Koay, M. S., Janssen, B. M. G. & Merkx, M. Tuning the metal binding site specificity of a fluorescent sensor protein: from copper to zinc and back. *Dalton Trans.* **42**, 3230–3232 (2013).

178. Liang, J. *et al.* A genetically encoded copper(I) sensor based on engineered structural distortion of EGFP. *Chem. Commun.* **48**, 3890–3892 (2012).

179. Liu, J., Karpus, J., Wegner, S. V., Chen, P. R. & He, C. Genetically Encoded Copper(I) Reporters with Improved Response for Use in Imaging. *J. Am. Chem. Soc.* **135**, 3144–3149 (2013).

180. Mazzolini, M., Traverso, S. & Marchetti, C. Multiple pathways of Pb^{2+} permeation in rat cerebellar granule neurones. *J. Neurochem.* **79**, 407–416 (2001).

181. Kerper, L. E. & Hinkle, P. M. Lead uptake in brain capillary endothelial cells: activation by calcium store depletion. *Toxicol. Appl. Pharmacol.* **146**, 127–133 (1997).

182. Martinez-Finley, E. J., Chakraborty, S., Fretham, S. & Aschner, M. Admit One: How Essential and Nonessential Metals Gain Entrance into the Cell. *Met. Integr. Biometal Sci.* **4**, 593–605 (2012).

183. Bridges, C. C. & Zalups, R. K. Molecular and ionic mimicry and the transport of toxic metals. *Toxicol. Appl. Pharmacol.* **204**, 274–308 (2005).

184. Clarkson, T. W. & Magos, L. The Toxicology of Mercury and Its Chemical Compounds. *Crit. Rev. Toxicol.* **36**, 609–662 (2006).

185. Medda, N., Patra, R., Ghosh, T. K. & Maiti, S. Neurotoxic Mechanism of Arsenic: Synergistic Effect of Mitochondrial Instability, Oxidative Stress, and Hormonal-Neurotransmitter Impairment. *Biol. Trace Elem. Res.* **198**, 8–15 (2020).

186. Na Kim, H., Xiu Ren, W., Seung Kim, J. & Yoon, J. Fluorescent and colorimetric sensors for detection of lead, cadmium, and mercury ions. *Chem. Soc. Rev.* **41**, 3210–3244 (2012).

187. Soleja, N., Manzoor, O., Khan, P. & Mohsin, M. Engineering genetically encoded FRET-based nanosensors for real time display of arsenic ($As\ 3^{+}$) dynamics in living cells. *Sci. Rep.* **9**, 11240 (2019).

188. Vijverberg, H. P. M. & Westerink, R. H. S. Sense in Pb^{2+} Sensing. *Toxicol. Sci.* **130**, 1–3 (2012).

189. He, Q., Miller, E. W., Wong, A. P. & Chang, C. J. A Selective Fluorescent Sensor for Detecting Lead in Living Cells. *J. Am. Chem. Soc.* **128**, 9316–9317 (2006).

190. Marbella, L., Serli-Mitasev, B. & Basu, P. Development of a Fluorescent Pb^{2+} Sensor. *Angew. Chem.* **121**, 4056–4058 (2009).

191. Chiu, T.-Y. & Yang, D.-M. Intracellular Pb^{2+} Content Monitoring Using a Protein-Based Pb^{2+} Indicator. *Toxicol. Sci.* **126**, 436–445 (2012).

192. Liu, W. *et al.* A Water-Soluble “Switching On” Fluorescent Chemosensor of Selectivity to Cd^{2+}. *Org. Lett.* **9**, 3829–3832 (2007).

193. Peng, X. *et al.* A Selective Fluorescent Sensor for Imaging Cd^{2+} in Living Cells. *J. Am. Chem. Soc.* **129**, 1500–1501 (2007).

194. Cheng, T. *et al.* A Highly Sensitive and Selective OFF-ON Fluorescent Sensor for Cadmium in Aqueous Solution and Living Cell. *J. Am. Chem. Soc.* **130**, 16160–16161 (2008).

195. Vinkenborg, J. L., Duijnhoven, S. M. J. van & Merkx, M. Reengineering of a fluorescent zinc sensor protein yields the first genetically encoded cadmium probe. *Chem. Commun.* **47**, 11879–11881 (2011).

196. Chiu, T.-Y., Chen, P.-H., Chang, C.-L. & Yang, D.-M. Live-Cell Dynamic Sensing of Cd^{2+} with a FRET-Based Indicator. *PLoS ONE* **8**, (2013).

197. Zhao, Y. *et al.* Rhodamine-based chemosensor for Hg^{2+} in aqueous solution with a broad pH range and its application in live cell imaging. *Org. Biomol. Chem.* **8**, 4143–4147 (2010).

198. Lin, W., Cao, X., Ding, Y., Yuan, L. & Yu, Q. A reversible fluorescent Hg^{2+} chemosensor based on a receptor composed of a thiol atom and an alkene moiety for living cell fluorescence imaging. *Org. Biomol. Chem.* **8**, 3618–3620 (2010).

199. Lu, H. *et al.* A highly selective and sensitive fluorescent turn-on sensor for Hg^{2+} and its application in live cell imaging. *Org. Biomol. Chem.* **7**, 2554–2558 (2009).

200. Bischof, H. *et al.* Novel genetically encoded fluorescent probes enable real-time detection of potassium *in vitro* and *in vivo*. *Nat. Commun.* **8**, 1422 (2017).

201. Raju, B., Murphy, E., Levy, L. A., Hall, R. D. & London, R. E. A fluorescent indicator for measuring cytosolic free magnesium. *Am. J. Physiol.-Cell Physiol.* **256**, C540–C548 (1989).

202. Meuwis, K., Boens, N., Gallay, J. & Vincent, M. Photophysics of Mag-fura-2: a fluorescent indicator for intracellular Mg^{2+}. *Chem. Phys. Lett.* **287**, 412–420 (1998).

203. Illner, H., McGuigan, J. A. S. & Lüthi, D. Evaluation of mag-fura-5, the new fluorescent indicator for free magnesium measurements. *Pflüg. Arch.* **422**, 179–184 (1992).

204. Claflin, D. R., Morgan, D. L., Stephenson, D. G. & Julian, F. J. The intracellular Ca^{2+} transient and tension in frog skeletal muscle fibres measured with high temporal resolution. *J. Physiol.* **475**, 319–325 (1994).

205. Lee, S., Lee, H. G. & Kang, S. H. Real-Time Observations of Intracellular Mg^{2+} Signaling and Waves in a Single Living Ventricular Myocyte Cell. *Anal. Chem.* **81**, 538–542 (2009).

206. Palmer, B. F. Regulation of Potassium Homeostasis. *Clin. J. Am. Soc. Nephrol.* **10**, 1050–1060 (2015).

207. Padmawar, P., Yao, X., Bloch, O., Manley, G. T. & Verkman, A. S. K^+ waves in brain cortex visualized using a long-wavelength K^+-sensing fluorescent indicator. *Nat. Methods* **2**, 825–827 (2005).

208. Florence, G., Pereira, T. & Kurths, J. Extracellular potassium dynamics in the hyperexcitable state of the neuronal ictal activity. *Commun. Nonlinear Sci. Numer. Simul.* **17**, 4700–4706 (2012).

209. Sica, D. A. *et al.* Importance of Potassium in Cardiovascular Disease. *J. Clin. Hypertens.* **4**, 198–206 (2002).

210. Warny, M. & Kelly, C. P. Monocytic cell necrosis is mediated by potassium depletion and caspase-like proteases. *Am. J. Physiol.-Cell Physiol.* **276**, C717–C724 (1999).

211. Yaron, J. R. *et al.* K^+ regulates Ca^{2+} to drive inflammasome signaling: dynamic visualization of ion flux in live cells. *Cell Death Dis.* **6**, e1954 (2015).

212. Groß, C. J. *et al.* K^+ Efflux-Independent NLRP3 Inflammasome Activation by Small Molecules Targeting Mitochondria. *Immunity* **45**, 761–773 (2016).

213. Rastergar, A. & Soleimani, M. Hypokalaemia and hyperkalaemia. *Postgrad. Med. J.* **77**, 759–764 (2001).

214. Chatterjee, R., Yeh, H.-C., Edelman, D. & Brancati, F. Potassium and risk of Type 2 diabetes. *Expert Rev. Endocrinol. Metab.* **6**, 665–672 (2011).

215. Frant, M. S. & Ross, J. W. Potassium ion specific electrode with high selectivity for potassium over sodium. *Science* **167**, 987–988 (1970).

216. Zhou, X. *et al.* A New Highly Selective Fluorescent K^+ Sensor. *J. Am. Chem. Soc.* **133**, 18530–18533 (2011).

217. Kong, X. *et al.* A Highly Selective Mitochondria-Targeting Fluorescent K^+ Sensor. *Angew. Chem. Int. Ed Engl.* **54**, 12053–12057 (2015).

218. Yeats, C. & Bateman, A. The BON domain: a putative membrane-binding domain. *Trends Biochem. Sci.* **28**, 352–355 (2003).

219. Buist, G., Steen, A., Kok, J. & Kuipers, O. P. LysM, a widely distributed protein motif for binding to (peptido)glycans. *Mol. Microbiol.* **68**, 838–847 (2008).

220. Carlson, H. J. & Campbell, R. E. Genetically encoded FRET-based biosensors for multiparameter fluorescence imaging. *Curr. Opin. Biotechnol.* **20**, 19–27 (2009).

221. Lindenburg, L. & Merkx, M. Engineering genetically encoded FRET sensors. *Sensors* **14**, 11691–11713 (2014).

222. Frommer, W. B., Davidson, M. W. & Campbell, R. E. Genetically encoded biosensors based on engineered fluorescent proteins. *Chem. Soc. Rev.* **38**, 2833–2841 (2009).

223. Campbell, R. E. Fluorescent-Protein-Based Biosensors: Modulation of Energy Transfer as a Design Principle. *Anal. Chem.* **81**, 5972–5979 (2009).

224. Miyawaki, A. *et al.* Fluorescent indicators for Ca^{2+} based on green fluorescent proteins and calmodulin. *Nature* **388**, 882–887 (1997).

225. Conley, J. M., Radhakrishnan, S., Valentino, S. A. & Tantama, M. Imaging extracellular ATP with a genetically-encoded, ratiometric fluorescent sensor. *PLOS ONE* **12**, e0187481 (2017).

226. Hires, S. A., Zhu, Y. & Tsien, R. Y. Optical measurement of synaptic glutamate spillover and reuptake by linker optimized glutamate-sensitive fluorescent reporters. *Proc. Natl. Acad. Sci.* **105**, 4411–4416 (2008).

227. Okumoto, S. *et al.* Detection of glutamate release from neurons by genetically encoded surface-displayed FRET nanosensors. *Proc. Natl. Acad. Sci.* **102**, 8740–8745 (2005).

228. Lundby, A., Mutoh, H., Dimitrov, D., Akemann, W. & Knöpfel, T. Engineering of a Genetically Encodable Fluorescent Voltage Sensor Exploiting Fast Ci-VSP Voltage-Sensing Movements. *PLOS ONE* **3**, e2514 (2008).

229. Gao, X. & Zhang, J. Spatiotemporal Analysis of Differential Akt Regulation in Plasma Membrane Microdomains. *Mol. Biol. Cell* **19**, 4366–4373 (2008).

230. Imamura, H. *et al.* Visualization of ATP levels inside single living cells with fluorescence resonance energy transfer-based genetically encoded indicators. *Proc. Natl. Acad. Sci.* **106**, 15651–15656 (2009).

231. Markwardt, M. L. *et al.* An Improved Cerulean Fluorescent Protein with Enhanced Brightness and Reduced Reversible Photoswitching. *PLOS ONE* **6**, e17896 (2011).

232. Nagai, T., Yamada, S., Tominaga, T., Ichikawa, M. & Miyawaki, A. Expanded dynamic range of fluorescent indicators for Ca^{2+} by circularly permuted yellow fluorescent proteins. *Proc. Natl. Acad. Sci. U. S. A.* **101**, 10554–10559 (2004).

233. Cranfill, P. J. *et al.* Quantitative assessment of fluorescent proteins. *Nat. Methods* **13**, 557–562 (2016).

234. Fritz, R. D. *et al.* A Versatile Toolkit to Produce Sensitive FRET Biosensors to Visualize Signaling in Time and Space. *Sci. Signal.* **6**, rs12–rs12 (2013).

235. Bajar, B. T. *et al.* Improving brightness and photostability of green and red fluorescent proteins for live cell imaging and FRET reporting. *Sci. Rep.* **6**, 20889 (2016).

236. Nakai, J., Ohkura, M. & Imoto, K. A high signal-to-noise Ca^{2+} probe composed of a single green fluorescent protein. *Nat. Biotechnol.* **19**, 137–141 (2001).

237. Barykina, N. V. *et al.* A new design for a green calcium indicator with a smaller size and a reduced number of calcium-binding sites. *Sci. Rep.* **6**, 34447 (2016).

238. Wu, J. *et al.* Genetically Encoded Glutamate Indicators with Altered Color and Topology. *ACS Chem. Biol.* **13**, 1832–1837 (2018).

239. Andersson, B., Janson, V., Behnam-Motlagh, P., Henriksson, R. & Grankvist, K. Induction of apoptosis by intracellular potassium ion depletion: using the fluorescent dye PBFI in a 96-well plate method in cultured lung cancer cells. *Toxicol. Vitro Int. J. Publ. Assoc. BIBRA* **20**, 986–994 (2006).

240. Ohtsuka, K. *et al.* Fluorescence imaging of potassium ions in living cells using a fluorescent probe based on a thrombin binding aptamer-peptide conjugate. *Chem. Commun. Camb. Engl.* **48**, 4740–4742 (2012).

241. Hösli, L., Hösli, E., Landolt, H. & Zehntner, Ch. Efflux of potassium from neurones excited by glutamate and aspartate causes a depolarization of cultured glial cells. *Neurosci. Lett.* **21**, 83–86 (1981).

242. Ballanyi, K. & Grafe, P. An intracellular analysis of gamma-aminobutyric-acid-associated ion movements in rat sympathetic neurones. *J. Physiol.* **365**, 41–58 (1985).

243. Grafe, P. & Ballanyi, K. Cellular mechanisms of potassium homeostasis in the mammalian nervous system. *Can. J. Physiol. Pharmacol.* **65**, 1038–1042 (1987).

244. Ballanyi, K., Grafe, P. & ten Bruggencate, G. Ion activities and potassium uptake mechanisms of glial cells in guinea-pig olfactory cortex slices. *J. Physiol.* **382**, 159–174 (1987).

245. Yu, S. P., Yeh, C.-H., Strasser, U., Tian, M. & Choi, D. W. NMDA Receptor-Mediated K^+ Efflux and Neuronal Apoptosis. *Science* **284**, 336–339 (1999).

246. Belhage, B., Hansen, G. H. & Schousboe, A. Depolarization by K^+ and glutamate activates different neurotransmitter release mechanisms in GABAergic neurons: vesicular versus non-vesicular release of GABA. *Neuroscience* **54**, 1019–1034 (1993).

247. Shen, Y. *et al.* A genetically encoded Ca^{2+} indicator based on circularly permutated sea anemone red fluorescent protein eqFP578. *BMC Biol.* **16**, 9 (2018).

248. Kuffler, S. W. Neuroglial cells: physiological properties and a potassium mediated effect of neuronal activity on the glial membrane potential. *Proc. R. Soc. Lond. B Biol. Sci.* **168**, 1–21 (1967).

249. Ransom, B. R. & Goldring, S. Ionic determinants of membrane potential of cells presumed to be glia in cerebral cortex of cat. *J. Neurophysiol.* **36**, 855–868 (1973).

250. Henn, F. A., Haljama¨e, H. & Hamberger, A. Glial cell function: Active control of extracellular K^+ concentration. *Brain Res.* **43**, 437–443 (1972).

251. Horio, Y. Potassium Channels of Glial Cells: Distribution and Function. *Jpn. J. Pharmacol.* **87**, 1–6 (2001).

252. Olsen, M. L. *et al.* New Insights on Astrocyte Ion Channels: Critical for Homeostasis and Neuron-Glia Signaling. *J. Neurosci. Off. J. Soc. Neurosci.* **35**, 13827–13835 (2015).

253. Horikawa, K. *et al.* Spontaneous network activity visualized by ultrasensitive Ca^{2+} indicators, yellow Cameleon-Nano. *Nat. Methods* **7**, 729–732 (2010).

254. Qin, Y. *et al.* Direct Comparison of a Genetically Encoded Sensor and Small Molecule Indicator: Implications for Quantification of Cytosolic Zn^{2+}. *ACS Chem. Biol.* **8**, 2366–2371 (2013).

255. Lam, A. J. *et al.* Improving FRET dynamic range with bright green and red fluorescent proteins. *Nat. Methods* **9**, 1005–1012 (2012).

256. Nguyen, A. W. & Daugherty, P. S. Evolutionary optimization of fluorescent proteins for intracellular FRET. *Nat. Biotechnol.* **23**, 355–360 (2005).

257. Grünberg, R. *et al.* Engineering of weak helper interactions for high-efficiency FRET probes. *Nat. Methods* **10**, 1021–1027 (2013).

258. Bindels, D. S. *et al.* mScarlet: a bright monomeric red fluorescent protein for cellular imaging. *Nat. Methods* **14**, 53–56 (2017).

259. Barnett, L. M., Hughes, T. E. & Drobizhev, M. Deciphering the molecular mechanism responsible for GCaMP6m's Ca^{2+}-dependent change in fluorescence. *PLOS ONE* **12**, e0170934 (2017).

260. Epstein, W. The roles and regulation of potassium in bacteria. *Prog. Nucleic Acid Res. Mol. Biol.* **75**, 293–320 (2003).

261. Wang, M., Zheng, Q., Shen, Q. & Guo, S. The Critical Role of Potassium in Plant Stress Response. *Int. J. Mol. Sci.* **14**, 7370–7390 (2013).

262. Yenush, L. Potassium and Sodium Transport in Yeast. in *Yeast Membrane Transport* (eds. Ramos, J., Sychrová, H. & Kschischo, M.) 187–228 (Springer International Publishing, 2016). doi:10.1007/978-3-319-25304-6_8.

263. Somjen, G. G. Extracellular potassium in the mammalian central nervous system. *Annu. Rev. Physiol.* **41**, 159–177 (1979).

264. Meuwis, K., Boens, N., De Schryver, F. C., Gallay, J. & Vincent, M. Photophysics of the fluorescent K^+ indicator PBFI. *Biophys. J.* **68**, 2469–2473 (1995).

265. Ding, J., Luo, A. F., Hu, L., Wang, D. & Shao, F. Structural basis of the ultrasensitive calcium indicator GCaMP6. *Sci. China Life Sci.* **57**, 269–274 (2014).

266. Tomlinson, S., Mathialagan, P. D. & Maloney, S. K. Special K: testing the potassium link between radioactive rubidium (86Rb) turnover and metabolic rate. *J. Exp. Biol.* **217**, 1040–1045 (2014).

267. Kato, S. *et al.* Restoration of the growth of *Escherichia coli* under K^+-deficient conditions by Cs^+ incorporation via the K^+ transporter Kup. *Sci. Rep.* **7**, 1965 (2017).

268. Halpern, Y. S., Barash, H., Dover, S. & Druck, K. Sodium and Potassium Requirements for Active Transport of Glutamate by *Escherichia coli* K-12. *J. Bacteriol.* **114**, 53–58 (1973).

269. Sokalingam, S., Raghunathan, G., Soundrarajan, N. & Lee, S.-G. A Study on the Effect of Surface Lysine to Arginine Mutagenesis on Protein Stability and Structure Using Green Fluorescent Protein. *PLOS ONE* **7**, e40410 (2012).

270. Tang, M. S. & Helmstetter, C. E. Coordination between chromosome replication and cell division in *Escherichia coli*. *J. Bacteriol.* **141**, 1148–1156 (1980).

271. Muñoz-Planillo, R. *et al.* K^+ efflux is the Common Trigger of NLRP3 inflammasome Activation by Bacterial Toxins and Particulate Matter. *Immunity* **38**, 1142–1153 (2013).

272. Wible, B. A. *et al.* Increased K^+ Efflux and Apoptosis Induced by the Potassium Channel Modulatory Protein KChAP/PIAS3β in Prostate Cancer Cells. *J. Biol. Chem.* **277**, 17852–17862 (2002).

273. Reichstein, E. & Rothstein, A. Effects of quinine on Ca^{++}-induced K^+ efflux from human red blood cells. *J. Membr. Biol.* **59**, 57–63 (1981).

274. Scheiner-Bobis, G., Heringdorf, D. M. zu, Christ, M. & Habermann, E. Palytoxin induces K^+ efflux from yeast cells expressing the mammalian sodium pump. *Mol. Pharmacol.* **45**, 1132–1136 (1994).

275. Larsson, O., Detsch, T. & Fredholm, B. B. VIP and forskolin enhance carbachol-induced K^+ efflux from rat salivary gland fragments by a Ca^{2+}-sensitive mechanism. *Am. J. Physiol.-Cell Physiol.* **259**, C904–C910 (1990).

276. Kabsch, W. Integration, scaling, space-group assignment and post-refinement. *Acta Crystallogr. D Biol. Crystallogr.* **66**, 133–144 (2010).

277. McCoy, A. J. Solving structures of protein complexes by molecular replacement with Phaser. *Acta Crystallogr. D Biol. Crystallogr.* **63**, 32–41 (2007).

278. Trigo-Mourino, P., Thestrup, T., Griesbeck, O., Griesinger, C. & Becker, S. Dynamic tuning of FRET in a green fluorescent protein biosensor. *Sci. Adv.* **5**, eaaw4988 (2019).

279. Emsley, P. & Cowtan, K. Coot: model-building tools for molecular graphics. *Acta Crystallogr. D Biol. Crystallogr.* **60**, 2126–2132 (2004).

280. Adams, P. D. *et al.* PHENIX: a comprehensive Python-based system for macromolecular structure solution. *Acta Crystallogr. D Biol. Crystallogr.* **66**, 213–221 (2010).

281. Ai, H., Baird, M. A., Shen, Y., Davidson, M. W. & Campbell, R. E. Engineering and characterizing monomeric fluorescent proteins for live-cell imaging applications. *Nat. Protoc.* **9**, 910–928 (2014).

282. Brown, S. D. & Jun, S. Complete Genome Sequence of *Escherichia coli* NCM3722. *Genome Announc.* **3**, (2015).

283. Köhling, R. & Wolfart, J. Potassium Channels in Epilepsy. *Cold Spring Harb. Perspect. Med.* **6**, (2016).

284. Sibille, J., Duc, K. D., Holcman, D. & Rouach, N. The Neuroglial Potassium Cycle during Neurotransmission: Role of Kir4.1 Channels. *PLOS Comput. Biol.* **11**, e1004137 (2015).

285. McIsaac, R. S., Bedbrook, C. N. & Arnold, F. H. Recent Advances in Engineering Microbial Rhodopsins for Optogenetics. *Curr. Opin. Struct. Biol.* **33**, 8–15 (2015).

286. Amann, T., Schmieder, V., Kildegaard, H. F., Borth, N. & Andersen, M. R. Genetic engineering approaches to improve posttranslational modification of biopharmaceuticals in different production platforms. *Biotechnol. Bioeng.* **116**, 2778–2796 (2019).

287. Liu, T. *et al.* Enhancing protein stability with extended disulfide bonds. *Proc. Natl. Acad. Sci.* **113**, 5910–5915 (2016).

288. Reily, C., Stewart, T. J., Renfrow, M. B. & Novak, J. Glycosylation in health and disease. *Nat. Rev. Nephrol.* **15**, 346–366 (2019).

289. Wang, Y.-C., Peterson, S. E. & Loring, J. F. Protein post-translational modifications and regulation of pluripotency in human stem cells. *Cell Res.* **24**, 143–160 (2014).

290. Ardito, F., Giuliani, M., Perrone, D., Troiano, G. & Muzio, L. L. The crucial role of protein phosphorylation in cell signaling and its use as targeted therapy (Review). *Int. J. Mol. Med.* **40**, 271–280 (2017).

291. Dephoure, N., Gould, K. L., Gygi, S. P. & Kellogg, D. R. Mapping and analysis of phosphorylation sites: a quick guide for cell biologists. *Mol. Biol. Cell* **24**, 535–542 (2013).

292. Shakin-Eshleman, S. H., Spitalnik, S. L. & Kasturi, L. The Amino Acid at the X Position of an Asn-X-Ser Sequon Is an Important Determinant of N-Linked Core-glycosylation Efficiency. *J. Biol. Chem.* **271**, 6363–6366 (1996).

293. Valnohova, J., Kowalski-Jahn, M., Sunahara, R. K. & Schulte, G. Functional dissection of the N-terminal extracellular domains of Frizzled 6 reveals their roles for receptor localization and Dishevelled recruitment. *J. Biol. Chem.* **293**, 17875–17887 (2018).

294. Cheng, C.-J., Kuo, E. & Huang, C.-L. Extracellular Potassium Homeostasis: Insights from Hypokalemic Periodic Paralysis. *Semin. Nephrol.* **33**, 237–247 (2013).

295. Thouta, S. *et al.* Proline Scan of the hERG Channel S6 Helix Reveals the Location of the Intracellular Pore Gate. *Biophys. J.* **106**, 1057–1069 (2014).

296. Baird, G. S., Zacharias, D. A. & Tsien, R. Y. Biochemistry, mutagenesis, and oligomerization of DsRed, a red fluorescent protein from coral. *Proc. Natl. Acad. Sci. U. S. A.* **97**, 11984–11989 (2000).

297. Switzer, R. C., Merril, C. R. & Shifrin, S. A highly sensitive silver stain for detecting proteins and peptides in polyacrylamide gels. *Anal. Biochem.* **98**, 231–237 (1979).

298. Ding, Y. *et al.* Ratiometric biosensors based on dimerization-dependent fluorescent protein exchange. *Nat. Methods* **12**, 195–198 (2015).

299. Alford, S. C., Abdelfattah, A. S., Ding, Y. & Campbell, R. E. A Fluorogenic Red Fluorescent Protein Heterodimer. *Chem. Biol.* **19**, 353–360 (2012).

300. Alford, S. C., Ding, Y., Simmen, T. & Campbell, R. E. Dimerization-Dependent Green and Yellow Fluorescent Proteins. *ACS Synth. Biol.* **1**, 569–575 (2012).

301. Laemmli, U. K. Cleavage of Structural Proteins during the Assembly of the Head of Bacteriophage T4. *Nature* **227**, 680–685 (1970).

302. Shaner, N. C. *et al.* Improved monomeric red, orange and yellow fluorescent proteins derived from *Discosoma* sp. red fluorescent protein. *Nat. Biotechnol.* **22**, 1567–1572 (2004).

303. Ai, H., Henderson, J. N., Remington, S. J. & Campbell, R. E. Directed evolution of a monomeric, bright and photostable version of Clavularia cyan fluorescent protein: structural characterization and applications in fluorescence imaging. *Biochem. J.* **400**, 531–540 (2006).

304. Karasawa, S., Araki, T., Yamamoto-Hino, M. & Miyawaki, A. A Green-emitting Fluorescent Protein from Galaxeidae Coral and Its Monomeric Version for Use in Fluorescent Labeling. *J. Biol. Chem.* **278**, 34167–34171 (2003).

305. Thier, S. O. Potassium physiology. *Am. J. Med.* **80**, 3–7 (1986).

306. Bean, B. P. The action potential in mammalian central neurons. *Nat. Rev. Neurosci.* **8**, 451–465 (2007).

307. Rainey, K. H. & Patterson, G. H. Photoswitching FRET to monitor protein–protein interactions. *Proc. Natl. Acad. Sci.* **116**, 864–873 (2019).

308. Kerppola, T. K. Design and implementation of bimolecular fluorescence complementation (BiFC) assays for the visualization of protein interactions in living cells. *Nat. Protoc.* **1**, 1278–1286 (2006).

309. Wilcox, G. Insulin and Insulin Resistance. *Clin. Biochem. Rev.* **26**, 19–39 (2005).

310. O'Connell, J. M. & Manson, S. M. Understanding the Economic Costs of Diabetes and Prediabetes and What We May Learn About Reducing the Health and Economic Burden of These Conditions. *Diabetes Care* **42**, 1609–1611 (2019).

311. Ward, C. W., Menting, J. G. & Lawrence, M. C. The insulin receptor changes conformation in unforeseen ways on ligand binding: Sharpening the picture of insulin receptor activation. *BioEssays* **35**, 945–954 (2013).

312. Shen, Y., Joachimiak, A., Rich Rosner, M. & Tang, W.-J. Structures of human insulin-degrading enzyme reveal a new substrate recognition mechanism. *Nature* **443**, 870–874 (2006).

313. Weis, F. *et al.* The signalling conformation of the insulin receptor ectodomain. *Nat. Commun.* **9**, 4420 (2018).

314. Patapoutian, A. & Reichardt, L. F. Trk receptors: mediators of neurotrophin action. *Curr. Opin. Neurobiol.* **11**, 272–280 (2001).

315. Johnson, D. *et al.* Expression and structure of the human NGF receptor. *Cell* **47**, 545–554 (1986).

316. Ahmed, S., Reynolds, B. A. & Weiss, S. BDNF enhances the differentiation but not the survival of CNS stem cell-derived neuronal precursors. *J. Neurosci. Off. J. Soc. Neurosci.* **15**, 5765–5778 (1995).

317. Yamada, K. & Nabeshima, T. Brain-Derived Neurotrophic Factor/TrkB Signaling in Memory Processes. *J. Pharmacol. Sci.* **91**, 267–270 (2003).

318. Lima Giacobbo, B. *et al.* Brain-Derived Neurotrophic Factor in Brain Disorders: Focus on Neuroinflammation. *Mol. Neurobiol.* **56**, 3295–3312 (2019).

319. Uegaki, K. *et al.* BDNF Binds Its Pro-Peptide with High Affinity and the Common Val66Met Polymorphism Attenuates the Interaction. *Int. J. Mol. Sci.* **18**, (2017).

320. Boute, N., Pernet, K. & Issad, T. Monitoring the Activation State of the Insulin Receptor Using Bioluminescence Resonance Energy Transfer. *Mol. Pharmacol.* **60**, 640–645 (2001).

321. Menting, J. G. *et al.* How insulin engages its primary binding site on the insulin receptor. *Nature* **493**, 241–245 (2013).

322. Edbauer, D., Willem, M., Lammich, S., Steiner, H. & Haass, C. Insulin-degrading enzyme rapidly removes the beta-amyloid precursor protein intracellular domain (AICD). *J. Biol. Chem.* **277**, 13389–13393 (2002).

323. KASUGA, M. Structure and function of the insulin receptor—a personal perspective. *Proc. Jpn. Acad. Ser. B Phys. Biol. Sci.* **95**, 581–589 (2019).

Appendix: Progress towards insulin and BDNF biosensors

Introduction

As an effort to expand the toolkit of genetically encoded fluorescent biosensors, I explored novel binding proteins for new biosensors including the insulin biosensor and the brain derived neurotropic factor (BDNF) biosensor.

Insulin is among the most important metabolic molecules and plays an essential role in regulating blood sugar in the human body[309]. After sensing elevated blood glucose level, the β cells of pancreatic islets secrete insulin to facilitate blood glucose uptake and metabolism to reduce the level of blood glucose. Diabetes arise when cells become insensitive to insulin or insulin secretion is compromised. The population affected by diabetes is increasing globally and this leads to an increasing financial burden for both individual families and the society[310]. As a result, diabetes research is attracting research attention and has shown to be a worthwhile investigative pursuit. An insulin biosensor has the potential to aid diabetes research by providing a tool to monitor insulin secretion and localization in the tissue.

For such a biosensor, an insulin binding protein with specific insulin molecule binding capacity is required to detect the presence of insulin. The binding proteins used in this project include the human insulin receptor (hIR) and the insulin degrading enzyme (IDE)[311,312]. The human insulin receptor forms homodimers on the membrane, with each monomer formed by an extracellular α subunit and a transmembrane β subunit linked by a disulfide bond[311]. Two αβ monomers are covalently linked by another disulfide bond to form the homodimer (**Fig. 1a**). The dimerization is important to facilitate the conformational change upon insulin binding to activate its β subunit tyrosine kinase domain in the cytoplasmic aspect of the membrane. Previous crystal structures have revealed global conformational changes at both extracellular and intracellular sides

that can utilized by a biosensor[311,313]. Unlike hIR that needs to be expressed in eukaryotic system, the human insulin degrading enzyme (IDE) is a cytosolic homodimer and can be expressed in *E. coli*[312]. It also undergoes substantial conformational change according to a structure study with cryo-EM. The N-terminal domain and the C-terminal domain of the IDE forms a clamp that closes upon insulin binding (**Fig. 1b**). This change makes it an ideal binding protein for insulin.

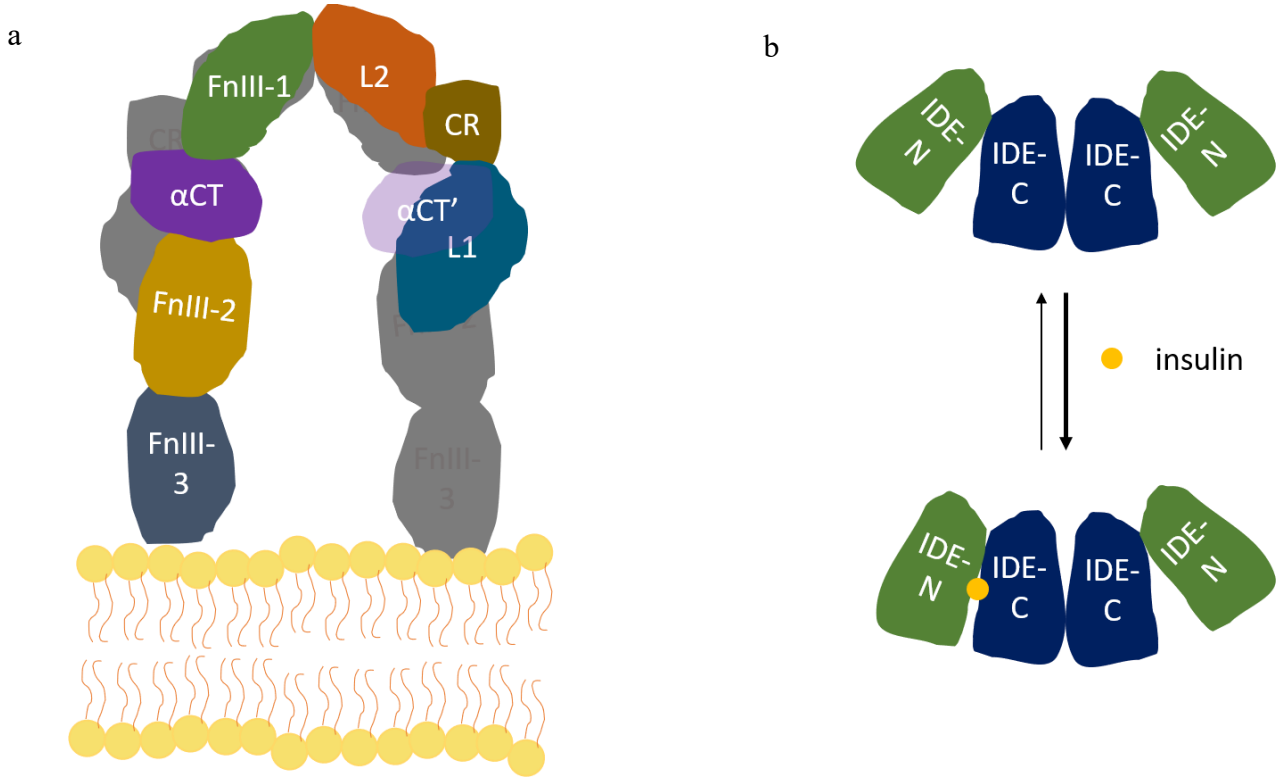

Figure 1. Structural illustration of the insulin receptor and the insulin degrading enzyme.

(a) The scheme of hIR above the membrane. The C-terminal part of FnIII-2 and the entire FnIII-3 are on the β subunit. L1 (leucine-rich repeat domain 1), CR, L2 (leucine-rich repeat domain 2), FnIII-1, αCT, and the N-terminal part of FnIII-2 form the α subunit. The homodimer of hIR forms an "A" shape above the membrane with CR and L1 interact with the αCT from the other α subunit. (b) IDE is a homodimeric cytosolic protein with well defined N-terminal domain and C-terminal domain. Binding of insulin shifts the equilibrium towards the closed form.

Like insulin, BDNF is also of physiological importance. As a nerve growth factor, BDNF binds TrkB[314] or the low-affinity nerve growth factor receptor[315] to stimulate nerve growth, which supports the existing neurons and promotes the growth and the differentiation of new neurons[316]. BDNF has also been reported to play a role in signal transmission[317]. It is of interest for researchers because it plays a role in schizophrenia, depression, Alzheimer's, and aging[317,318]. A biosensor for BDNF can provide a support for research on these conditions and could help to elucidate key mechanisms in neurophysiological compromise. The binding protein for BDNF is its pre-peptide. BDNF precursor is cleaved after its pre-peptide for maturation[319]. The pre-peptide cleaved off during post-translational modification is reported to bind to the mature BDNF, making it an excellent binding domain for a BDNF biosensor.

Results

Building a FRET-based insulin biosensor with the human insulin receptor

Inspired by a BRET insulin biosensor[320], the prototype construct of the insulin biosensor is built with the entire insulin receptor. A cpVenus or a mCerulean was linked at the C-terminus of the receptor in a mammalian expression vector (**Fig. 2**). Because hIR is membrane bound, the constructs were made in a mammalian vector to be tested on cell membrane directly. With co-transfection in mammalian cells, 50% of the dimers are cpVenus-hIR and mCerulean-hIR heterodimers assuming equal expression. Both cpVenus-hIR and mCerulean-hIR localize on the membrane. The images before and after adding insulin show a small but significant difference with the YFP to CFP ratio. This suggests that the conformational change at C terminus upon insulin binding is not substantial but enough to induce a detectable FRET change (**Fig. 3**). This FRET design has limited room for optimization because the hIR has a size of 1392 residues and only half

of the expressed proteins form heterodimer. Future effort will be dedicated to development of a design with smaller size with high sensitivity.

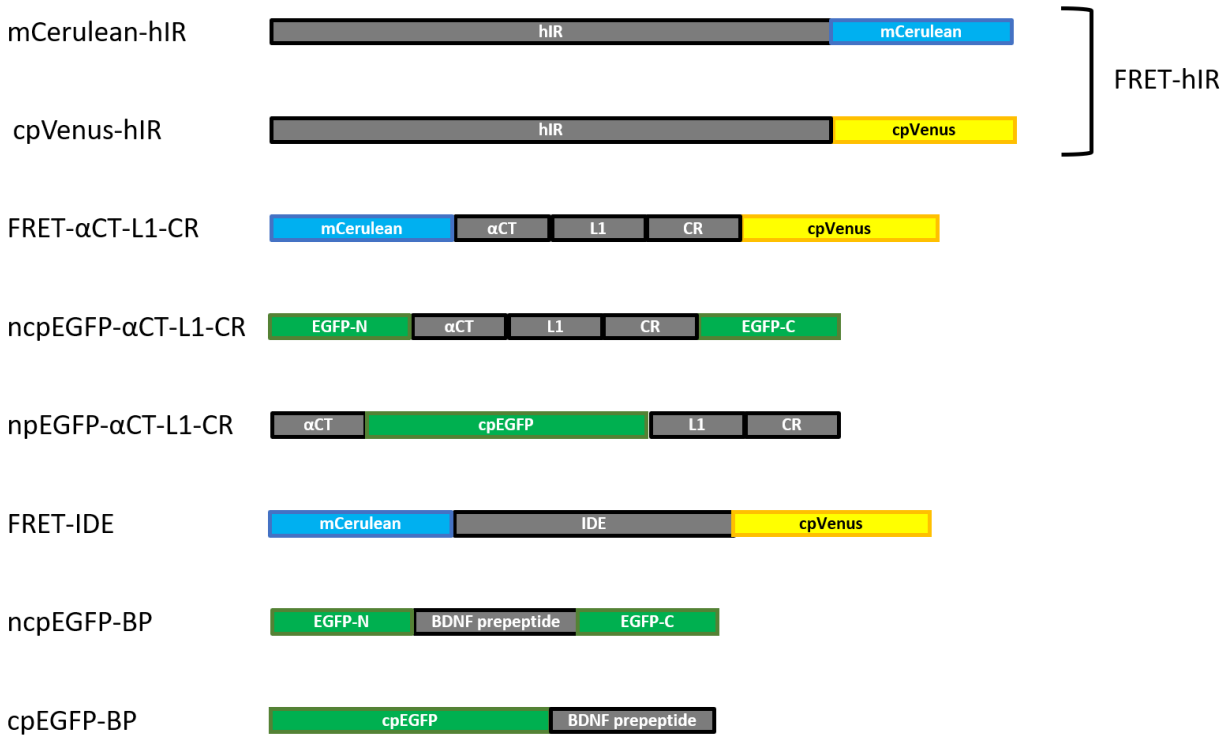

Figure 2. Construct designs for the insulin biosensors and BDNF biosensors

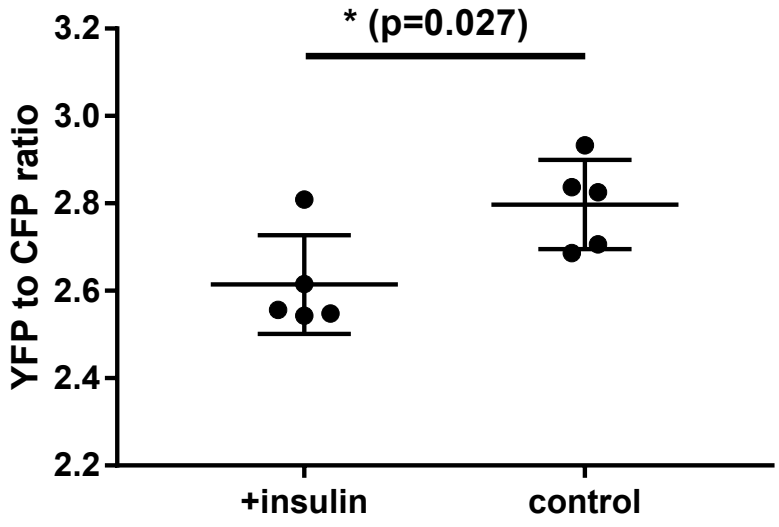

Figure 3. FRET-hIR on the membrane shows a small difference upon insulin binding.

The imaging was taken with YFP channel and CFP channel. Assuming YFP remains unaffected by FRET efficiency, a decrease in CFP to YFP ratio suggests a more efficient FRET as more photons are emitted as yellow light instead of cyan light, which is not detectable in the CFP channel.

Building an insulin biosensor with only the binding domain of the human insulin receptor

Research on the hIR suggests that the binding domain can bind to insulin without the rest of the hIR[311,313,321]. The αCT-L1-CR domain (**Fig. 1a**) of the α subunit alone could be purified according to structure studies and I designed several constructs that incorporate the αCT-L1-CR domain: a FRET construct with αCT-L1-CR flanked by mCerulean and cpVenus, a ncpEGFP construct with αCT-L1-CR flanked by EGFP N-terminal part and EGFP C-terminal part as in GINKO, and a cpEGFP construct with cpEGFP flanked by αCT and L1-CR as in GCaMP (**Fig. 2**). Because the αCT-L1-CR domain is in the extracellular part of hIR and requires additional work to target the membrane, all biosensor constructs were made in pBAD vector for *E. coli* expression. The purified mCerulean-αCT-L1-CR-cpVenus shows similar mCerulean and cpVenus emission peak heights when excited at 410 nm. The ratio of the two peaks remains unchanged after the addition of excess amount of insulin, but the overall fluorescence intensity is repressed by insulin for unknown reasons (**Fig. 4b**). Conversely, the emission spectra of ncpEGFP αCT-L1-CR shows no substantial intensity change with the addition of insulin (**Fig. 4a**). The cpEGFP design did not provide a better result (Data not shown).

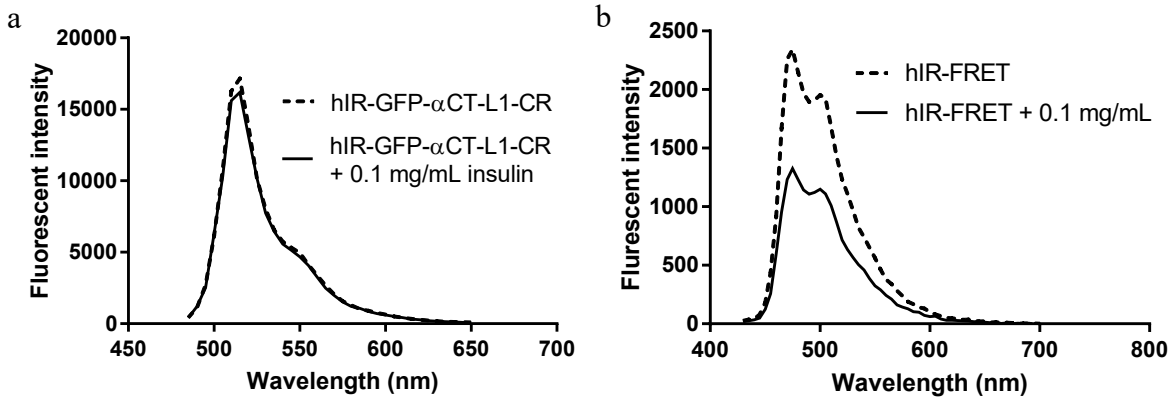

Figure 4. The emission spectra of insulin biosensors incorporating the binding domain of the insulin receptor.

The spectra of (a) ncpEGFP aCT-L1-CR and (b) FRET-aCT-L1-CR with and without addition of 0.1 mg/mL insulin.

Building an insulin biosensor with the insulin degradation enzyme

The insulin degrading enzyme (IDE) is an alternative insulin binding protein I used to build an insulin biosensor. A FRET design is an ideal start for this binding protein as the distance between its N and C termini changes substantially upon insulin binding[312] (**Fig. 2**). mCerulean-IDE-cpVenus does not respond to insulin according the insulin titration experiment (**Fig. 7.5**). I proposed the cause of this to be degradation of insulin by the active IDE. To address this concern, I made E111Q at IDE active site, as suggested by previous studies[312,322], to inhibit the catalytic activity of IDE. The insulin titration of mCerulean-IDE E11Q-cpVenus suggests the E111Q mutation is not sufficient to recover biosensor function (**Fig. 5**).

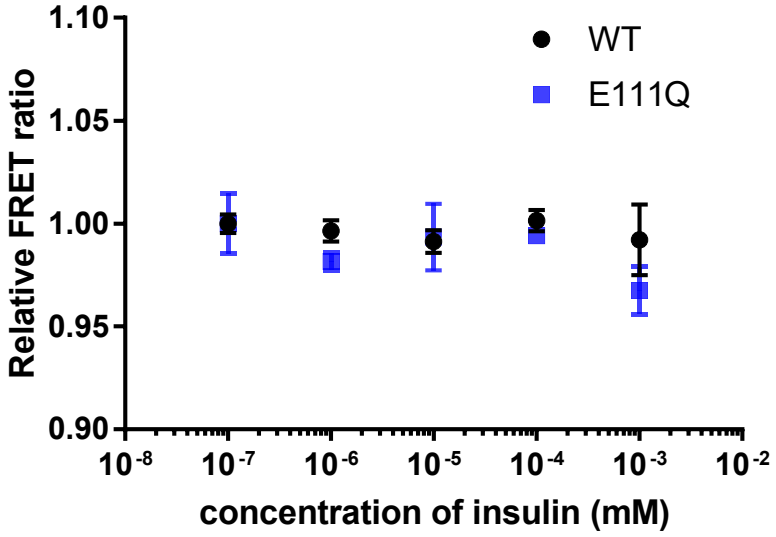

Figure 5. The insulin titration for FRET-IDE biosensor wildtype and the variant with E111Q

Building a BDNF biosensor with the BDNF pre-peptide

The BDNF biosensors was built with cpEGFP and ncpEGFP as illustrated (**Fig. 2**). Both cpEGFP-BP(BDNF pre-peptide) and ncpEGFP-BP were tested with BDNF purified in the lab. There is no substantial change according to the spectra (**Fig. 6**). This can be explained by the lack of conformational change of BDNF pre-peptide upon BDNF binding.

Conclusion

Insulin and BDNF are both pertinent biomolecules. Insulin regulates blood sugar and BDNF promotes neuron growth and differentiation. Insulin binding proteins used for the development of insulin biosensors include the human insulin receptor[323] (hIR) and the insulin degrading enzyme[312] (IDE). The full hIR has been reported in a BRET insulin biosensor[320]. I used the same design with a mCerulean3/cpVenus FRET pair to make hIR-mCerulean3 and hIR-

cpVenus, but the resulting indicators were not effective, partially because only half of co-expressed hIR proteins form heterodimers. Later, a binding domain containing L1-CR-αCT of hIR was used to build smaller indicators that cannot dimerize. These indicators failed to respond to insulin. An IDE-based FRET indicator was also generated but similarly failed to respond to insulin. The BDNF indicators were developed based a BDNF pre-peptide. Both cp- and ncpGFP were used but neither produced indicators that responded to BDNF.

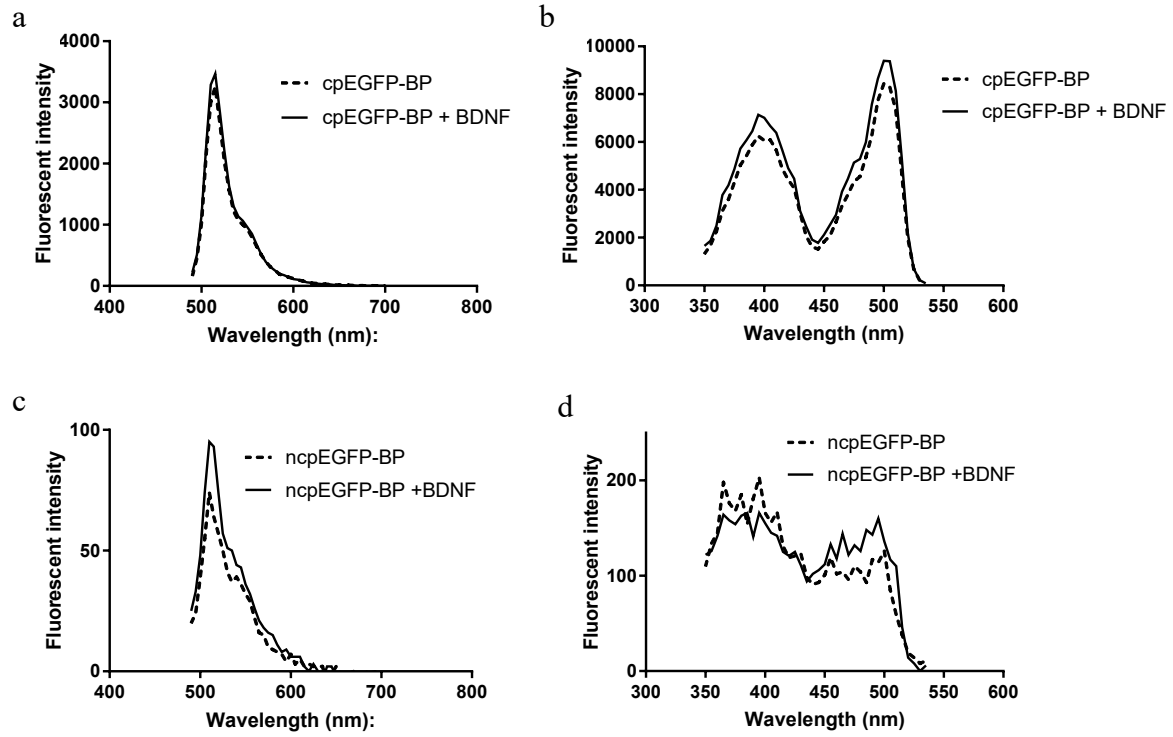

Figure 6. Spectra of BDNF biosensors.

(a) The emission spectrum and (b) the excitation spectrum of cpEGFP-BP with (solid lines) or without (dashes) shows a very small difference in spectra. (c) The emission spectrum and (d) the excitation spectrum of ncpEGFP-BP with (solid lines) or without (dashes) shows very low intensity due to low yield of purified protein.

Although the work on insulin indicators and BDNF indicators did not yield intended indicators, designing and creating the constructs was not a fruitless effort. With future research efforts and different angles of approach, the development of functional insulin and BDNF indicators is likely within reach. Developing a practical genetically encoded biosensor takes many steps: designing the constructs, testing first constructs, optimizations, and testing in cells and *in vivo*. It is common for prototype indicators to not be effective enough for further pursuit. Indicator development involves many trials and errors before generating working indictors. Considering the potential impact of effective insulin and BDNF biosensors, the development of these biosensors can be resumed when appropriate binding domains are identified.

Methods

Creating DNA plasmids

The FRET-hIR constructs were made based on an available hIR-GFP construct in a mammalian vector (Addgene #: 22286) by replacing GFP with mCerulean or cpVenus with Gibson assembly of vector and insert fragments amplified with Q5 polymerase.

Overlap PCR was used for construction of αCT-L1-CR constructs with cpEGFP, ncpEGFP, or FRET design. The complete linear fragments were inserted into a pBAD vector for expression.

Mature BDNF DNA fragment was ordered through the IDT. The synthesized DNA fragment was amplified by Q5 polymerase before being inserted into a pBAD vector for expression.

The BDNF pre-peptide (BP) sequence was cloned from a mammalian human BDNF vector from Addgene (Addgene #: 73036) with Q5 polymerase. The ncpEGFP fragments were cloned from GINKO1 and the cpEGFP fragment was cloned from GCaMP6s. The fragments were Gibson assembled into a pBAD vector for expression.